TECHNISCHE UNIVERSITÄT WIEN
Vienna University of Technology

Dissertation

Ordered Equilibrium Structures of Patchy Particle Systems

ausgeführt zum Zwecke der Erlangung des akademischen Grades eines Doktors der technischen Wissenschaften unter der Leitung von

Ao. Univ. Prof. Dr. Gerhard Kahl
Institut für Theoretische Physik
Technische Universität Wien

eingereicht an der Technischen Universität Wien
Fakultät für Physik

von

Dipl.-Ing. Günther Doppelbauer
Matrikelnummer 0225956
Franzensgasse 10/6, 1050 Wien

Wien, im Juli 2012

Günther Doppelbauer

Kurzfassung

Systeme der weichen Materie, die typischerweise aus mesoskopischen Teilchen in einem Lösungsmittel aus mikroskopischen Teilchen bestehen, können bei niedrigen Temperaturen im festen Aggregatzustand in einer Vielzahl von geordneten Strukturen auftreten. Die Vorhersage dieser Strukturen bei bekannten Teilchenwechselwirkungen und unter vorgegebenen thermodynamischen Bedingungen wurde in den letzten Jahrzehnten als eines der großen ungelösten Probleme der Physik der kondensierten (weichen) Materie angesehen. In dieser Arbeit wird ein Verfahren vorgestellt, das die geordneten Phasen dieser Systeme vorhersagt; dieses beruht auf heuristischen Optimierungsmethoden, wie etwa evolutionären Algorithmen. Um die thermodynamisch stabile geordnete Teilchenkonfiguration an einem bestimmten Zustandspunkt zu finden, wird das entsprechende thermodynamische Potential minimiert und die dem globalen Minimum entsprechende Phase identifiziert.

Diese Technik wird auf Modellsysteme für sogenannte kolloidale "Patchy Particles" angewandt. Die "Patches" sind dabei als begrenzte Regionen mit abweichenden physikalischen oder chemischen Eigenschaften auf der Oberfläche kolloidaler Teilchen definiert. "Patchy Particles" weisen, zusätzlich zur isotropen Hartkugelabstoßung der Kolloide, sowohl abstoßende als auch anziehende anisotrope Wechselwirkungen zwischen den "Patches" auf. Durch neue Synthetisierungsmethoden können solche Teilchen mit maßgeschneiderten Eigenschaften erzeugt werden. Deshalb werden "Patchy Particles" oft als neuartige Bausteine angesehen, die sich unter idealen Bedingungen ohne weitere äußere Einflussnahme zu wohldefinierten makroskopischen Strukturen zusammenfügen können. Die Systeme, die in dieser Arbeit (sowohl in zwei als auch in drei Dimensionen) behandelt werden reichen von aus wenigen Teilchen bestehenden Clustern bis hin zu unendlich ausgedehnten Kristallen.

Abstract

Soft matter systems, typically consisting of mesoscopic particles in a microscopic solvent, can form a surprisingly rich variety of solid, ordered structures at low temperature. A reliable prediction which solid phases will appear for given particle interactions under certain thermodynamic conditions has been considered a major problem in (soft) condensed matter physics for several decades. In this thesis, we present a prediction method based on heuristic global optimization schemes such as evolutionary algorithms. In order to find the most stable configuration of a system at a given thermodynamic state point, the particle arrangement corresponding to the global minimum of the appropriate thermodynamic potential, such as the (free) energy or enthalpy, is identified.

We apply these optimization methods to model systems for so-called patchy colloidal particles. Patches are defined as finite regions on the colloidal surface, which differ in their physical or chemical properties from the rest of the surface. Such particles are characterized, in addition to the isotropic excluded volume interactions of the colloids, by attractive as well as repulsive directional interactions induced by the patches. Novel synthesization techniques yield particles with desired properties. Thus, patchy particles are often seen as building blocks that are able to self-assemble into well-defined ordered macroscopic structures under certain external conditions. The systems we investigate range from finite clusters to bulk crystals in two as well as three dimensions.

Contents

1. Introduction

The work presented in this thesis is devoted to finding answers to some specific questions related to self-assembly scenarios in a particular class of soft matter systems, making use of modern computational tools.

Soft matter is an interdisciplinary field of science, transgressing the borders between physics, chemistry and biology. Soft matter systems are abundant in our daily lives, either occurring in nature, such as milk, blood or viruses or as man-made substances, such as ink, cosmetics, lubricants or plastics, some of them being of technological relevance.

Soft matter systems are typically governed by phenomena taking place at mesoscopic length scales ranging from 1 nm to 1 μm. Thus, the characteristic length scales are by orders of magnitude larger than in microscopic, pure atomic systems ($\sim$ 0.1 nm), but are still by orders of magnitude smaller than in macroscopic systems ($\sim$ 1 cm).

The fact that soft matter can indeed be considered as "soft", *i.e.*, exhibiting very small resistance against mechanical deformation or compression, can be understood by taking characteristic interaction energy (ϵ) and length (a) scales into account, as demonstrated in Ref. [1]: in soft matter systems at room temperature, the typical ϵ-values are of the same order of magnitude as in atomic systems ("hard matter", such as metallic crystals), while the length scales are by a factor of $\sim 10^1 - 10^4$ larger. Estimating, for instance, the respective shear moduli $G \propto \epsilon/a^3$ illustrates the striking difference between the mechanical properties of soft and hard matter.

The mesoscopic entities (*i.e.*, constituent particles) making up soft matter systems consist of large numbers of atoms themselves and often occur as a dispersed phase in a solvent of atomic particles. The resulting large disparity in length scales can lead to very complex and unexpected behavior in and out of equilibrium, where the internal architecture of the constituent particles of such systems plays, in general, an important role [2]. Of course this feature makes the general prediction of phenomena in soft matter systems complicated. As Pierre-Gilles DeGennes put forward in his Nobel lecture [3], "mild chemical action" can induce "drastic change in the mechanical properties". On the other hand, the disparity in length scales gives rise to the possibility to make a distinction between relevant (mesoscopic) and irrelevant (microscopic) degrees of freedom, which can be treated in a cumulative, averaged way. In so-called coarse-grained descriptions the irrelevant degrees of freedom are integrated out and the systems are described in terms of effective interactions between "effective particles " of a single component [1]. This often is the only practically feasible way to treat soft matter systems within theory and computer simulations, as the number of microscopic degrees of freedom is typically by orders of magnitude larger than the number of relevant ones, so that complete descriptions are beyond reach.

A specific class of soft matter systems are colloids, *i.e.*, mesoscopic particles usually suspended in a microscopic solvent. There are different kinds of colloidal suspensions, often categorized by the states of aggregation of the solute particles and the solvent. Examples for the mesoscopic solute are colloidal gold or silver nanoparticles or chemically synthesized polystyrene spheres, whose interactions can often be approximated by pure excluded volume models. The so-called depletion interaction, which is mediated by additional polymers in the solution, can introduce entropy-driven, short-range attractive forces between the colloidal particles. On one hand, colloids are interesting for their specific properties, which can conveniently be tuned in experiments, *e.g.*, by changing the concentration of polymers or salt in the solution. On the other hand, they can also act as models for atomic systems, as both classes of systems share many features, if the colloids are viewed from a coarse-grained perspective based on statistical physics. Colloidal model systems are more accessible than their atomic counterparts, to which they are mapped. Additionally, it is possible to directly observe colloids, *e.g.*, by confocal microscopy.

Not only observation, but also direct manipulation of colloidal particles by tailoring their shapes and interactions, is possible [2], a feature that can hardly be realized in atomic systems. This kind of experimental freedom has raised much attention from the scientific community in the past two decades.

One of the prospected applications of such manipulation techniques is the synthesis of specifically designed building blocks [4], which ideally self-assemble into desired target structures without further interference. Such "bottom up" fabrication methods of functional structures could lead to devices that are considerably cheaper to produce and are operational at much smaller length scales than those achievable with conventional "top down" assembly methods, such as optical lithography. Although it is a very challenging task to attain sufficient control over size, shape and interactions of the synthesized particles while being able to produce them in large quantities, many promising and successful steps in that direction have already been made [5].

In this work, we focus on so-called patchy particles, a class of novel nanoparticles with specific, anisotropic interactions. Such particles have well-defined areas with different physical or chemical properties on their, usually spherical, surfaces. These areas (*i.e.*, patches) induce anisotropy (for more details, *cf.* Chapter 2).

We investigate the relation between shape and interactions of these building blocks and the ordered macroscopic structures they can form under given thermodynamic conditions using computational optimization tools such as evolutionary algorithms (*cf.* Sec. 3.2). These tools are capable of locating global minima in vast search spaces in a reliable, efficient way and thus enable us to identify ordered structures corresponding to minimal values of thermodynamic potential functions. Such quantities, like energy, enthalpy or Gibbs free energy are treated as analytic functions of the structural parameters of the system in optimization approaches. However, within such a framework, it is difficult to evaluate entropic contributions to thermodynamic potential functions, which are relevant at non-zero-temperature values.

In order to evaluate the finite temperature behavior of the investigated systems, it is necessary to combine optimization tools with other methods, capable of incorporating entropic effects (*cf.* Sec. 3.3).

We perform studies on two- as well as three-dimensional systems of patchy particles. Concerning the former, we investigate a variety of systems containing particles with different patch numbers and patch decorations. We predict bulk structures into which these particles are expected to self-assemble under varying pressure by identifying global energy- and enthalpy minima of the systems at hand. Further, we explore the possibility of forming Archimedean tilings using suitably designed patchy particles. In the three-dimensional case, we thoroughly investigate systems consisting of particles with four patches, which have raised particular interest in recent years. Here, in addition to identifying global minima, we also search for further low-lying local minima characterizing the energy landscapes (*cf.* Sec. 3.1) of finite cluster and infinite bulk systems. Thereby, we suggest candidates for low-temperature ordered structures that could be formed via self-assembly and perform the first step of in-depth finite temperature investigations presented elsewhere [6, 7].

The thesis is organized as follows: In **Chapter 2**, we introduce patchy colloidal particles and provide a brief overview of available synthesization methods as well as interaction potentials utilized for modeling them in theoretical approaches and computer experiments. In **Chapter 3**, we describe the theoretical and computational tools we are making use of. **Chapter 4** is devoted to the results we obtained for the patchy particle systems sketched in the preceding paragraph. In **Chapter 5**, we provide conclusions and an outlook. Some mathematical derivations and a study on the performance of the optimization algorithm we use can be found in the **Appendices**.

2. Patchy Particle Systems

2.1. Experimental Overview

Immense progress in synthesizing colloidal particles with desired properties has been made in the last two decades. A sub-class of such processed colloids that have raised particular interest in recent years are so-called patchy particles, which are characterized by strongly anisotropic, highly directional interactions [8]. As argued in Ref. [9], there are some naturally occurring macromolecules, which could be described as patchy particles. Nevertheless, the predominant part of the scientific interest in this field is devoted to synthetic systems, whose features are obtained by patterning certain regions of the surfaces of the underlying colloids, using materials with different chemical or physical properties. As pointed out in Ref. [10], the resulting particles have potential applications in diverse fields, like the fabrication of photonic crystals* [11, 12] as well as drug delivery [13] and photovoltaics [14]. The reason why patchy particles are so attractive for such applications lies in the prospect of the "bottom up" self-assembly of functional structures: The appropriately synthesized particles are used as "building blocks", which are expected to assemble into desired structures without further intervention.

A number of distinct techniques for manipulating colloidal surfaces in order to obtain patchy particles has been introduced. These methods make use of very different interaction types, like electrostatic, magnetic, hydrophobic/hydrophilic, van-der-Waals or DNA base pair interactions are employed at strongly varying length scales, typically ranging from nanometers to micrometers, so that the denomination "patchy particles" can be seen as an umbrella term, describing a wide variety of systems. An extensive review of synthesization methods and their application can be found in Ref. [10].

In the following, we will give an introduction based on this review article, pointing out the specific advantages as well as the limitations of some fabrication techniques, where two key criteria are tunability (*i.e.*, the amount of control over the emerging particles that can be attained) and scalability (*i.e.*, the possibility of mass-production) of the methods.

- **Templating**: When synthesizing functional particles by templating, anisotropy in shape and interactions is obtained in a three-step procedure: first, the surface of the colloidal seed particles is partly covered by a "template", which often is represented by a liquid-air or liquid-liquid interface. The particles are partly immersed in the template. In the second step, the non-templated part of the particle surface is exposed to vapor deposition or chemical modification, while the covered part remains unchanged.

---

*A type of materials with band gaps in the photonic transmission spectrum.

Finally, the template has to be removed without further modifications to the desired particle constitution. A major advantage of templating is the possibility of synthesizing large quantities of uniform particles. On the other hand, the separation of the template from the end product is a rather delicate step and the versatility of such methods is limited: up to now, they are capable of yielding particles with one patch only. Examples for templating techniques are described in Ref. [15] and [16].

- **Colloidal assembly**: Clusters of polystyrene spheres, whose shape only depends on the particle number within the cluster can be obtained by the method described in Ref. [17]: Roughly speaking, in an oil-water emulsion, polystyrene spheres are bound to the water-interface within oil droplets. On evaporating the oil (*i.e.*, the droplets are shrinking), the spheres form spherical packings when the decreasing droplet size requires the densest possible configuration. Subsequently, after the oil has been completely removed, the particles are found to be organized in characteristically shaped clusters, which are stabilized by surface charges. Since the number of constituent particles within the oil droplets in the initial stage can not be controlled, the resulting clusters have to be separated according to their mass if monodisperse superparticles are desired. These structures show well-defined anisotropy in shape, but do not have strongly directional interparticle interactions. Colloidal assembly is scalable and allows for synthesis of large quantities of particles.

  Making use of so-called liquid protrusions on polystyrene spheres, a related method for synthesizing superparticles with controllable patch numbers and geometries has been introduced [18]. However, it is not yet possible to yield "sticky" patches with this method, the anisotropy is again only present in the shape of the resulting particles.

- **Glancing-angle deposition**: Deposition of vapor on a monolayer of close-packed spherical particles is used to produce so-called Janus particles, which are characterized by two hemispheres with different properties (*i.e.*, the upper hemisphere is covered by the evaporated substance, while the lower one remains unchanged after the process). If the vapor is not deployed at a vertical, but an inclined angle with respect to the monolayer, only a certain part of the surface of each particle is exposed to the reagent, since the particles act as shadow masks for their respective neighbors. This is a purely geometric effect, *i.e.* the size and shape of the generated patch on the particle surface depends only on the angle of incidence of the vapor relative to the monolayer and the orientation of the monolayer [19]. The method can be extended to produce particles with multiple patches when the monolayer is inverted or reoriented between multiple vapor deposition steps.

  One of the most striking examples of bottom-up fabrication of a target structure *via* patchy particles up to date was demonstrated using particles with two hydrophobic poles and an electrically charged middle band synthesized by glancing-angle deposition. These particles were shown to self-assemble into a two-dimensional Kagome-lattice under certain conditions [20].

The main limitation of this technique in the current state is the scalability, *i.e.* it is rather difficult to produce large amounts of uniform particles using this scheme.

- **DNA functionalized particles**: Attaching single- and double-stranded (ss and ds) DNAs to colloidal nanoparticles is another way to introduce selective anisotropic interactions [21]. The oligonucleotides of the ssDNA can reversibly bind to their complements attached to other particles *via* Watson-Crick base-pairing interactions. The method was explicitly introduced in order to direct assembly of the nanoparticles into desired structures. However, the target structures turned out to be stable in only a narrow region of temperature and are not very robust to perturbations like polydispersity of the nanoparticles; thus, success in fabricating such self-assembled structures has been limited so far. Nevertheless, some control over emerging crystalline structures has been demonstrated [22, 23]. Very recent theoretical and simulation studies suggest novel strategies, involving strong bonding between ssDNAs attached to different particles competing with weak bonding of DNA strands on the same particle, in order to increase the crystal forming abilities of such systems [24, 25].

- **Patchy magnetic particles**: As presented in Ref. [26], patchy particles can also be fabricated via a "dry self-assembly" technique. Similar to the colloidal assembly method described above, constituent particles are confined within a liquid droplet. Here, the droplet is deposited on a solid surface and dried in air. The method presented in [26] makes use of a mixture of magnetic and non-magnetic constituent particles within the droplet: during the drying process, a magnetic field is applied, which influences the spatial distribution of these particles. It has been demonstrated that magnetic super-particles with one, two or three patches can be obtained *via* this technique. The method is scalable using continuous droplet generation, however the obtained particle quantities are rather small.

- **Inverse patchy particles**: In a recent theoretical contribution [27], a new class of patchy particles has been introduced, which are termed "inverse" patchy, as their patches repel each other, while a patch-free region on the surface of each particle attracts the patches on nearby particles. The proposed system consists of positively charged polyelectrolyte stars, which are adsorbed on negatively charged colloidal particles in a solution. The charge ratio can be tuned, so that each colloid adsorbs only two polyelectrolyte stars, which then occupy opposite polar regions on the colloid, leading to repulsive polar-polar and attractive equatorial-polar interactions between the resulting complexes. The extent of the patches on the particle surface can be influenced by the salt concentration of the solution.

Even though the suggestion of such a system is based on promising experimental and simulation results (*e.g.*, Refs. [27, 28]), it has not yet been fully realized in an experimental multiparticle scenario. Therefore, it is hard to predict how scalable and tunable the technique will be.

2.1.1. Anisotropy Dimensions

The previous section focuses on patchy particle synthesis and mentions only a few examples for the wide spectrum of novel nanoparticles fabrication methods. Still, it hints on the fact that systems emerging from a more general class of novel particle synthesis techniques have very different features and are often not easy to put into relation. In Ref. [4], a well-received attempt to introduce a unified classification scheme based on anisotropy parameters is presented. These parameters, such as (A - patchiness), (B - aspect ratio), (C - faceting), (E - branching) or (H- roughness) are considered to be orthogonal dimensions, i. e., can be varied irrespective of each other, so that virtually any conceivable anisotropic building block can be represented as a vector in such a generalized coordinate system with a finite number of dimensions. As suggested in Ref. [4], the phase behavior of systems in dependence of the anisotropy parameters can be displayed in generalized phase diagrams, were the axes can represent thermodynamic as well as anisotropy parameters.

2.2. Models

Based on the review article Ref. [9], we briefly present different patchy particle models that have been proposed in the literature in this section. Here, we put a particular focus on the models that have been used for the investigations presented in Sec. 4. Most of these are *ad-hoc* models, introduced to investigate the generic behavior of patchy particles instead of trying to accurately represent the features of a specific system. An exception to this selection is the inverse patchy model, which results from a multi-step coarse graining procedure of a microscopic model specified in Sec. 2.2.3. For an extensive overview of both the models as well as the theoretical and computational investigations they have been involved in, we refer to Ref. [9].

2.2.1. Spot-like Models

In so-called spot-like potentials, patchy particles are composed of a (commonly spherical) excluded volume interaction

$$V_{\text{Colloid}}(r) = \begin{cases} \infty & r < \sigma_{\text{Colloid}} \\ 0 & r \geq \sigma_{\text{Colloid}} \end{cases}, \tag{2.1}$$

representing the interaction of repulsive colloids of radius σ_{Colloid} and additional, explicit attractive interaction sites located on the surface of the colloidal particle. These sites are usually represented by short-ranged square well interactions

$$V_{\text{Patch-Patch}}(r) = \begin{cases} -\epsilon & r < \sigma_{\text{Patch}} \\ 0 & r \geq \sigma_{\text{Patch}} \end{cases}, \tag{2.2}$$

where usually $\sigma_{\text{Patch}} \sim 0.1 - 0.2\sigma_{\text{Colloid}}$. The range of the patch-patch interaction as well as the spatial extent on the surface of the colloidal particle are both governed by σ_{Patch}.

These simple models have been extensively used in theoretical as well as in numerical studies, investigating the basic thermodynamic and dynamic properties of patchy systems in the fluid regime and the behavior of colloidal gels [29, 30]. Further investigations on gelation were done using hard ellipsoids as central entities [31].

2.2.2. Extended Patch Models

A second class of patchy models employs isotropic, short range-repulsive and medium-range attractive interaction potentials, which are modified by factors depending on particle orientations. In these models, the range of the patchy interaction is decoupled from the patches' extent on the surface of the central particle, as the range of the isotropic potential and the angular dependence of the orientational factor can be tuned irrespective of each other.

Kern-Frenkel Model

The first such model proposed in the literature [32] is also based on simple excluded volume and square well pair interactions. Its functional form is given as follows:

$$V_{\mathrm{KF}}(\mathbf{r}_{ij}, \widetilde{\Omega}_i, \widetilde{\Omega}_j) = V_{\mathrm{HSSW}}(r_{ij}) \cdot f(\hat{\mathbf{r}}_{ij}, \widetilde{\Omega}_i, \widetilde{\Omega}_j), \qquad (2.3)$$

where $\mathbf{r}_{ij}$ and r_{ij} represent the interparticle vector and its absolute value, $\widetilde{\Omega}_i$ stands for the spatial orientation of particle i and V_{HSSW} is the hard-core square well potential

$$V_{\mathrm{HSSW}}(r_{ij}) = \begin{cases} \infty & r < \sigma \\ -\epsilon & \sigma \leq r < \lambda\sigma \\ 0 & r \leq \lambda\sigma \end{cases} . \qquad (2.4)$$

The orientational factor $f(\widetilde{\Omega}_i, \widetilde{\Omega}_j)$ is defined by

$$f(\hat{\mathbf{r}}_{ij}, \widetilde{\Omega}_i, \widetilde{\Omega}_j) = \begin{cases} 1 & \text{if} & \begin{cases} (\hat{e}_\alpha \cdot \hat{r}_{ij} \leq \cos\delta) & \text{for some patch } \alpha \text{ on particle } i \\ \text{and} \ (\hat{e}_\beta \cdot \hat{r}_{ij} \leq \cos\delta) & \text{for some patch } \beta \text{ on particle } j \end{cases} \\ 0 & \text{otherwise} \end{cases} ,$$

$$\qquad (2.5)$$

i.e., the parameters λ and δ control the radial range and the angular width of the attractive interaction.

This freedom makes the Kern-Frenkel model very versatile, as it is possible to model particles with very focused, point-like patches as well as particles with large attractive regions, like so-called Janus-particles [33, 34], where the two hemispheres of each particle have different properties. Theoretical and simulation-based studies making use of the Kern-Frenkel model include calculations of phase diagrams and the gas-liquid critical behavior of patchy systems [35, 36].

Finally, we note that the functional form given in Eq. (2.3), as introduced in [32], is somewhat ambiguous. The excluded volume interaction is multiplied by the orientational factor, which can lead to a term $\infty \cdot 0$, which has to be interpreted as ∞ in order to retain the desired physical behavior. To resolve this issue, Eq. (2.3) should be rewritten if $r \geq \sigma$, so that V_{HSSW} is only multiplied by f.

Doye Model

This potential, first introduced by Doye and co-workers in Ref. [37], models patchy interactions by a modulated Lennard-Jones (LJ) potential. The steric, isotropic interaction of the central colloids is represented by the short-range ($r \leq \sigma$) repulsion of the LJ potential, while the patchy attraction is mapped onto the long-range ($r > \sigma$) attractive part of the LJ potential, multiplied by a factor $0 \leq V_{\mathrm{ang}} \leq 1$, depending on the orientation of the patches

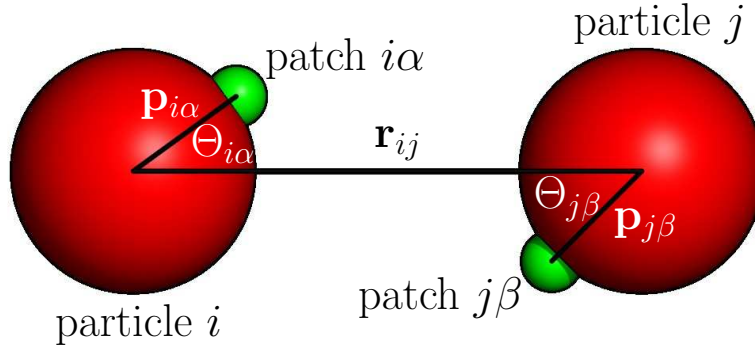with respect to the interparticle vector $\mathbf{r}_{ij}$ (*cf.* Fig. 2.1).

Figure 2.1.: Schematic representation of two interacting patchy particles, introducing the parameters of the interparticle potential of the Doye model [*cf.* Eqs. (2.6) – (2.8)].

The LJ potential is given by

$$V_{\mathrm{LJ}}(r) = 4\epsilon \left[\left(\frac{\sigma}{r} \right)^{12} - \left(\frac{\sigma}{r} \right)^{6} \right], \tag{2.6}$$

where σ and ϵ are defining the length- and energy-units. The orientational dependence is introduced *via* the modulating factor $V_{\mathrm{ang}} = V_{\mathrm{ang}}(\mathbf{r}_{ij}, \mathbf{p}_{i\alpha}, \mathbf{p}_{j\beta})$, which is given by

$$V_{\mathrm{ang}}(\mathbf{r}_{ij}, \mathbf{p}_{i\alpha}, \mathbf{p}_{j\beta}) = \exp\left[-(\Theta_{i\alpha}^2 + \Theta_{j\beta}^2)/w^2 \right]. \tag{2.7}$$

Here $\mathbf{r}_{ij} = \mathbf{r}_i - \mathbf{r}_j$ is the vector between the centers of masses of particles i and j; the patch vector, $\mathbf{p}_{i\alpha}$, connects the center of mass of particle i with patch α of particle i, $\Theta_{i\alpha}$ is the angle enclosed by $\mathbf{r}_{ij}$ and $\mathbf{p}_{i\alpha}$. The parameter w specifies the extent of the patch along the circumference (in two dimensions) or on the surface (in three dimensions), respectively (see Fig. 2.1) and thus plays a role similar to δ in the Kern-Frenkel model (*cf.* above). If not otherwise stated, we chose $w = 2\pi \cdot 0.05$. In total, the functional form of the potential reads

$$V_{\mathrm{Doye}}(\mathbf{r}_{ij}, \mathbf{p}_{i\alpha}, \mathbf{p}_{j\beta}) = \begin{cases} V_{\mathrm{LJ}}(r_{ij}) & r_{ij} \leq \sigma \\ V_{\mathrm{LJ}}(r_{ij}) V_{\mathrm{ang}}(\mathbf{r}_{ij}, \mathbf{p}_{i\alpha}, \mathbf{p}_{j\beta}) & \sigma < r_{ij} \end{cases}. \tag{2.8}$$

Although the Doye model has been successfully applied in numerous studies (including the calculation of phase diagrams [6, 38, 39], self-assembly of patchy particles into large target structures [40–43], and the possible formation of quasicrystals [44] or Archimedean tilings [45] by patchy systems) there are some problems and drawbacks related to describing patchy interactions in this coarse-grained way. In the following we are going to list these issues and we will either show approaches to resolve them or discuss the range of parameters for which these problems become negligible.
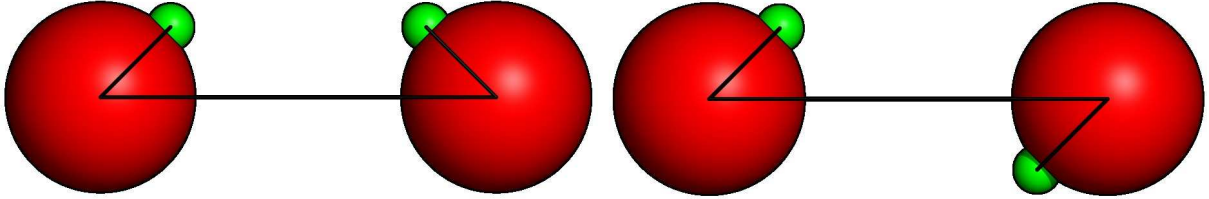
Figure 2.2.: Two distinctively different configurations of patchy particles that are character-ized by the same energy in the Doye model [based on the interparticle potential defined in Eqs. (2.6) – (2.8)].
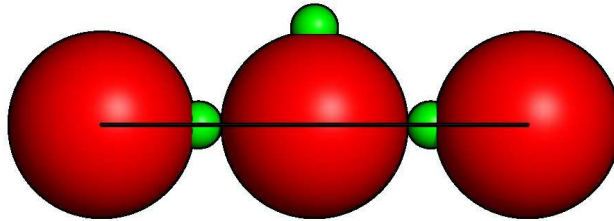

Figure 2.3.: Example for a configuration which gives rise to an unphysical contribution to the system's binding energy, emerging from an interaction between the outer particles, if r_{cut} is chosen larger than two particle diameters (*i.e.*, $r_{\mathrm{cut}} < 2\sigma$).

- Unphysical energy degeneracy: Considering the two particle arrangements shown in Fig. 2.2, we note that, based on the interaction potential specified in Eqs. (2.6) – (2.8), these configurations are characterized by the same energy, however, as a particle arrangement in a realistic system, they are definitely not equivalent. Obviously, this feature of the model originates from the simplification that V_{ang} – *cf.* Eq. (2.7) – can be split into two orientational factors that are independent of each other and both are separate functions of the orientation of only one patch in addition to $\mathbf{r}_{ij}$. However, for patch width values w that are sufficiently small, this artifact will not play a significant role, at least in investigations of equilibrium configurations.

- Long range interactions: Since the Lennard-Jones potential is of medium range, while patchy interactions are usually considered to be short-ranged (like in the models treated above), V_{LJ} has to be cut (and possibly shifted) at some cut-off distance r_{cut} in order to represent a realistically short-ranged attraction. This truncation is of particular im-portance, as unphysical patch-patch interactions between particles that are not near-est neighbors have to be prevented; as discussed in Fig. 2.3, with a cutoff distance $r_{\mathrm{cut}} \geq 2.2\sigma$, the interaction between the leftmost and the rightmost particle would still yield a binding energy of 0.035ϵ, even though the interaction should be completely screened by the colloidal particle located at the center. In our calculations, we have chosen $r_{\mathrm{cut}} = 1.9\sigma$ in order to make interactions across particles (*cf.* Fig. 2.3) impos-sible; nevertheless, we use $r_{\mathrm{cut}} = 2.5\sigma$ in many of the calculations in three dimensions in order to compare our results with the ones available in the literature [38, 39].

- In many studies of patchy particle systems (*e.g.* in theoretical approaches based on the Wertheim theory of association [29, 46]) it is required that patches can only form one bond and that there are no closed loops of bonds. This requirement is not fulfilled *a priori* within the Doye model. In order to prevent bonding *via* multiple pairs of patches that belong to the same pair of particles, only the patch-patch interaction which minimizes $\Theta_{i\alpha} + \Theta_{j\beta}$ is taken into account for each pair of particles. However, this criterion does not prevent bonding of a particular patch with multiple patches from different particles. Nevertheless, the single bonding condition can be retained if the potential cutoff r_{cut} and the patch width w are chosen to be sufficiently short and narrow, respectively.

- Discontinuous first derivatives: Unlike the Kern-Frenkel potential, the present interaction potential $V_{\mathrm{Doye}}(\mathbf{r}_{ij}, \mathbf{p}_{i\alpha}, \mathbf{p}_{j\beta})$ is continuous in all variables. However, its first derivative with respect to r, $\partial V_{\mathrm{Doye}}/\partial r$ is not continuous at $r = \sigma$ (*i.e.*, at the crossover between isotropic repulsion and patchy attraction) for $\Theta_{i\alpha} + \Theta_{j\beta} \neq 0$. The optimization algorithms we use to identify ordered equilibrium structures (*cf.* Sec. 3.2) heavily rely on local optimization steps and thus on the availability of first derivatives of the energy function*. Therefore, we replaced $V_{\mathrm{LJ}}(r)$ in Eq. (2.8) by a cubic polynomial for $r_0 \leq r < \sigma$:

$$P_{\mathrm{core}}(r) = b_3 r^3 + b_2 r^2 + b_1 r + b_0, \tag{2.9}$$

where r_0 is typically chosen to be 0.9σ. The coefficients b_i are determined by requiring continuity of function values and derivatives at $r = r_0$ and $r = \sigma$, *i.e.*

$$P_{\mathrm{core}}(r_0) = V_{\mathrm{LJ}}(r_0) \tag{2.10}$$

$$\frac{\partial P_{\mathrm{core}}}{\partial r}(r_0) = \frac{\partial V_{\mathrm{LJ}}}{\partial r}(r_0) \tag{2.11}$$

$$P_{\mathrm{core}}(\sigma) = V_{\mathrm{LJ}}(\sigma) \exp\left[-\min_{\alpha,\beta}(\Theta_{i\alpha}^2 + \Theta_{j\beta}^2)/w^2\right] = 0 \tag{2.12}$$

$$\frac{\partial P_{\mathrm{core}}}{\partial r}(\sigma) = \frac{\partial V_{\mathrm{LJ}}}{\partial r}(\sigma) \exp\left[-\min_{\alpha,\beta}(\Theta_{i\alpha}^2 + \Theta_{j\beta}^2)/w^2\right], \tag{2.13}$$

where the minimum $\min_{\alpha,\beta}$ is taken over all patch pairs (α, β) on a given pair of particles (i, j).

In addition, we use another cubic spline, $P_{\mathrm{cut}}(r)$, to ensure that the potential function vanishes smoothly at the long-distance cutoff $r = r_{\mathrm{cut}}$. In summary, our modifications can be expressed as the following substitution of Eq. (2.8):

$$V_{\mathrm{LJ}}(r) \rightarrow \begin{cases} V_{\mathrm{LJ}}(r), & r \leq r_0, \\ P_{\mathrm{core}}(\mathbf{r}_{ij}, \mathbf{p}_{i\alpha}, \mathbf{p}_{j\beta}), & r_0 < r \leq \sigma, \\ V_{\mathrm{LJ}}(r), & \sigma < r \leq r_{\mathrm{join}}, \\ P_{\mathrm{cut}}(r), & r_{\mathrm{join}} < r \leq r_{\mathrm{cut}}, \end{cases} \tag{2.14}$$

---

*Analytical derivatives of the potential function are computed in App. B.
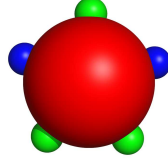
with $r_{\text{join}} = 0.9 r_{\text{cut}}$.

Figure 2.4.: Five-patch particle, decorated with two A and three B patches; in this model like patches attract each other, while unlike patches repel each other.

Repulsive Interactions between Patches   We have also considered the situation of both attractive and repulsive patches on a colloidal particle: in this model the particles are decorated by two different types of patches, denoted by indices A or B (*cf.* Fig. 2.4). Interactions between different kinds of patches are considered to be attractive, their potential is given by Eqs. (2.6) – (2.8). The interactions between like patches are assumed to be repulsive; they are modeled in the following way:

$$
V_{II}(\mathbf{r}_{ij}, \mathbf{p}_{i\alpha}, \mathbf{p}_{j\beta}) = \begin{cases} V(\mathbf{r}_{ij}, \mathbf{p}_{i\alpha}, \mathbf{p}_{j\beta}) & r_{ij} \leq r_1 \\ V_{\text{LJ}}(r_{ij}) + [V_1(r) - V_{\text{LJ}}(r)]V_{\text{ang}}(\mathbf{r}_{ij}, \mathbf{p}_{i\alpha}, \mathbf{p}_{j\beta}) & r_1 < r_{ij} \leq \sigma \\ V_1(r)V_{\text{ang}}(\mathbf{r}_{ij}, \mathbf{p}_{i\alpha}, \mathbf{p}_{j\beta}) & \sigma < r_{ij} \leq r_0 \\ -V(\mathbf{r}_{ij}, \mathbf{p}_{i\alpha}, \mathbf{p}_{j\beta}) & r_0 < r_{ij} \end{cases} \quad , \quad (2.15)
$$

with $I = A$ or B; further, $r_1 = 0.95\sigma$ and $r_0 = \sqrt[6]{2}\sigma$. The potential $V_1(r)$ is quadratic in r and is chosen in such a way that

$$
\begin{align}
V_1(r_1) &= V_{\text{LJ}}(r_1) \tag{2.16} \\
V_1(r_0) &= -V_{\text{LJ}}(r_0) = 1 \tag{2.17} \\
\frac{\partial V_1}{\partial r}(r_0) &= \frac{\partial V_{\text{LJ}}}{\partial r}(r_0). \tag{2.18}
\end{align}
$$

$V_{II}(\mathbf{r}_{ij}, \mathbf{p}_{i\alpha}, \mathbf{p}_{j\beta})$ is depicted in Fig. 2.5.

Patch Decoration   Considerable progress has been made in recent years in synthesizing patchy particle systems *via* a number of different experimental techniques. Encouraged by Refs. [10, 18, 26] we have introduced a geometry parameter g, allowing us to control the decoration of particles with patches in our calculations in a well-defined way. In the framework of the anisotropy dimensions introduced in [4] (*cf.* Sec. 2.1.1), we are able to vary the parameters (A - patchiness) *via* w, (B - aspect ratio) *via* g and (E - branching) *via* the number of patches.
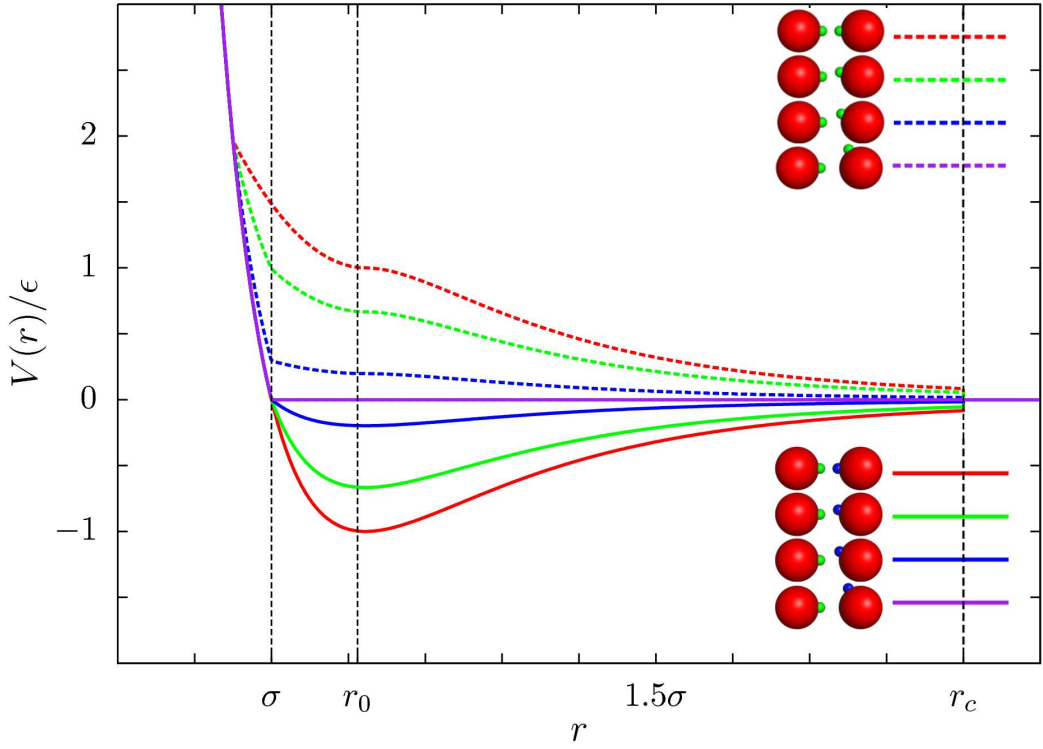
Figure 2.5.: Potentials for patchy particles with like and unlike patches, schematically represented in Fig. 2.4. The explicit expressions for these interactions are given in Eqs. (2.6) – (2.15). Symbols: dotted lines – repulsion between like patches, full lines – attraction between unlike patches. The potentials are displayed (from top to bottom for the repulsion and from bottom to top for the attraction) for patch width $w = 2\pi 0.05$ and the following angles Θ: 0 (red), 0.2 (green), 0.4 (blue), 1 (purple). The corresponding particle configurations are displayed schematically.

For the four-patch system, we define the geometry parameter as follows:

The first patch, specified by $\mathbf{p}_1$, is fixed at the north pole of the particle, while the locations of the remaining three patches, specified by $\mathbf{p}_i$, on the particle surface depend on the value

of g:

$$\mathbf{p}_1 = \frac{\sigma}{2} \begin{pmatrix} 0 \\ 0 \\ 1 \end{pmatrix} \tag{2.19}$$

$$\mathbf{p}_2 = \frac{\sigma}{2} \begin{pmatrix} \cos(0\pi/3)\sin(g\pi/180) \\ \sin(0\pi/3)\sin(g\pi/180) \\ \cos(g\pi/180) \end{pmatrix} \tag{2.20}$$

$$\mathbf{p}_3 = \frac{\sigma}{2} \begin{pmatrix} \cos(2\pi/3)\sin(g\pi/180) \\ \sin(2\pi/3)\sin(g\pi/180) \\ \cos(g\pi/180) \end{pmatrix} \tag{2.21}$$

$$\mathbf{p}_4 = \frac{\sigma}{2} \begin{pmatrix} \cos(4\pi/3)\sin(g\pi/180) \\ \sin(4\pi/3)\sin(g\pi/180) \\ \cos(g\pi/180) \end{pmatrix} \tag{2.22}$$

The patch decoration as a function of g is visualized in Fig. 2.6.
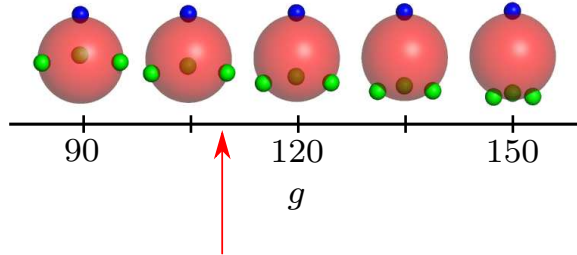
Figure 2.6.: Visualization of the decoration of the patchy particles (red sphere) by the four patches (small blue and green spheres) as the geometric parameter g varies over a representative range. Here and in the following figures the blue spheres specify the patch located on the north pole of the particle ($\mathbf{p}_1$), while the green spheres specify the remaining three patches ($\mathbf{p}_2$, $\mathbf{p}_3$ and $\mathbf{p}_4$). The red arrow represents the g value for which the patches form a regular tetrahedron.

2.2.3. Inverse Patchy Colloids (IPCs)

In a recent publication [47], a coarse-grained interaction potential for the inverse patchy particles introduced in Sec. 2.1 has been constructed in a two-step process: First, the electrostatic potential around one inverse patchy particle is derived analytically within the Debye-Hückel theory [48]. Subsequently, the resulting potential function is mapped onto an *ad-hoc* model, where the strength of interactions is determined by volume overlaps of spheres representing the patches and the naked colloids, respectively. Many properties of the exact model can be retained by suitable mapping, while pair interaction energies of the coarse-grained system can be evaluated at moderate computational cost.

Figure 2.7.: Schematic representation of the coarse-grained IPC model. For a description of the parameters, see text. Image courtesy of Emanuela Bianchi.
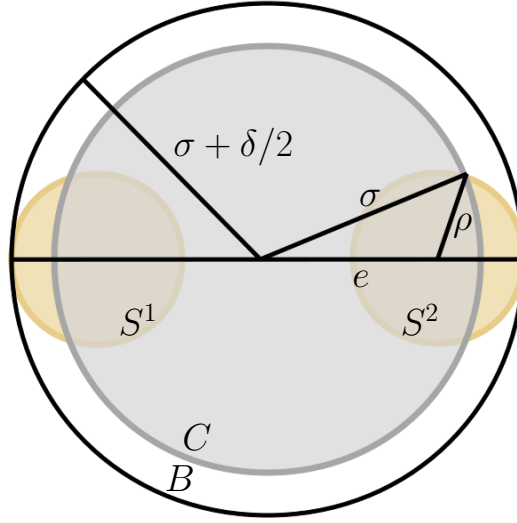
The coarse-grained model consists of two concentric spheres C and B with radii $r_C = \sigma$ and $r_B = \sigma + \delta/2$ and two additional spheres S^1 and S^2. These spheres of radius ρ are located at a distance $e \leq \sigma$ on two opposite positions along the diameter of the colloidal sphere (*cf.* Fig. 2.7). Since the surfaces of the larger central sphere B and each eccentric sphere S are required to intersect in one point, these numbers fulfill the relation

$$\delta = 2(e + \rho - \sigma). \tag{2.23}$$

The central sphere C mimics the steric repulsion between the colloids, which interact *via* simple excluded volume potentials with each other. On the other hand, the spheres S^i, representing the patches interact repulsively with their counterparts on neighboring particles and attractively with the larger central sphere B, representing the equatorial region of the respective particles. The relative strengths of these interactions are controlled by parameters, which are determined in the mapping procedure.

The spatial position and the orientation of an IPC i is given by vectors $\mathbf{r}_i$ and $\hat{\mathbf{n}}_i$*, respectively. With the interparticle vector $\mathbf{r}_{ij} = \mathbf{r}_j - \mathbf{r}_i$, interparticle distance $r_{ij} = |\mathbf{r}_{ij}|$ and the angles $\theta_i = \angle(\mathbf{r}_{ij}, \hat{\mathbf{n}}_i)$, $\theta_j = \angle(-\mathbf{r}_{ij}, \hat{\mathbf{n}}_j)$ and $\theta_{ij} = \angle(\hat{\mathbf{n}}_i, \hat{\mathbf{n}}_j)$, the coarse grained potential between a pair of interacting IPCs i, j reads

$$V_{\text{IPC}}(r_{ij}, \theta_i, \theta_j, \theta_{ij}) = \begin{cases} \infty & r_{ij} \leq 2\sigma \\ U(r_{ij}, \theta_i, \theta_j, \theta_{ij}) & 2\sigma \leq r_{ij} \leq 2\sigma + \delta \\ 0 & 2\sigma + \delta < r_{ij} \end{cases} . \tag{2.24}$$

---

*Since the model exhibits cylindrical symmetry, a single axis (*i.e.*, a unit vector $\hat{\mathbf{n}}_i$) is sufficient to describe its orientation.

$$U(r_{ij}, \theta_i, \theta_j, \theta_{ij}) = w_{BB}u_{BB} + w_{SS}u_{SS} + w_{BS}u_{BS}, \tag{2.25}$$

is determined by the weight factors $w_{\alpha\beta}$, which depend on the nine spherical overlap volumes

$$w_{BB} \propto \Omega_{BB}^{\text{SUM}} = \Omega(B_i B_j) \tag{2.26}$$

$$w_{SS} \propto \Omega_{SS}^{\text{SUM}} = \Omega(S_i^1 S_j^1) + \Omega(S_i^1 S_j^2) + \Omega(S_i^2 S_j^1) + \Omega(S_i^2 S_j^2) \tag{2.27}$$

$$w_{BS} \propto \Omega_{BS}^{\text{SUM}} = \Omega(B_i S_j^1) + \Omega(B_i S_j^2) + \Omega(S_i^1 B_j) + \Omega(S_i^2 B_j) \tag{2.28}$$

and the energy contributions $u_{\alpha\beta}$, which have to be determined in the mapping procedure. In order to obtain dimensionless weight factors, the overlap volumes are normalized by a reference value:

$$w_{\alpha\beta} = \frac{\Omega_{\alpha\beta}^{\text{SUM}}}{4/3\pi\sigma^3}. \tag{2.29}$$

The overlap volume of two spheres α, β with radii R_α, R_β and a center-center distance $r_{\alpha\beta}$ is given by

$$\Omega_{\alpha\beta}(r_{\alpha\beta}) = \begin{cases} 0 & r_{\text{max}} < r_{\alpha\beta} \\[2ex] \frac{\pi}{3}\left[\left(2R_\alpha + \frac{R_\alpha^2 - R_\beta^2 + r_{\alpha\beta}^2}{2r_{\alpha\beta}}\right)\left(R_\alpha - \frac{R_\alpha^2 - R_\beta^2 + r_{\alpha\beta}^2}{2r_{\alpha\beta}}\right)^2\right] + \\ \frac{\pi}{3}\left[\left(2R_\beta + \frac{R_\alpha^2 - R_\beta^2 - r_{\alpha\beta}^2}{2r_{\alpha\beta}}\right)\left(R_\beta - \frac{R_\alpha^2 - R_\beta^2 - r_{\alpha\beta}^2}{2r_{\alpha\beta}}\right)^2\right] & r_{\text{min}} \leq r_{\alpha\beta} \leq r_{\text{max}} \\[2ex] \frac{4}{3}\pi R_<^3 & r_{\alpha\beta} < r_{\text{min}} \end{cases} \tag{2.30}$$

where $R_< = \min(R_\alpha, R_\beta)$, $r_{\text{max}} = R_\alpha + R_\beta$ and $r_{\text{min}} = |R_\alpha - R_\beta|$. The inter-sphere distances $r_{\alpha\beta}$ can be calculated as functions of the values r_{ij}, θ_i, θ_j and θ_{ij} of the respective IPCs i, j.

For details on obtaining the $u_{\alpha\beta}$ and the mapping procedure, we refer to Ref. [47].

Since the derivatives of the $w_{\alpha\beta}$ with respect to the particle degrees of freedom $\mathbf{r}_i$, $\mathbf{r}_j$, $\hat{\mathbf{n}}_i$ and $\hat{\mathbf{n}}_j$ can be calculated analytically in a straightforward way (cf. App. C), this model is well suited for being studied with our optimization algorithm, as long as the interaction between the central hard spheres C is approximated by some suitable function.
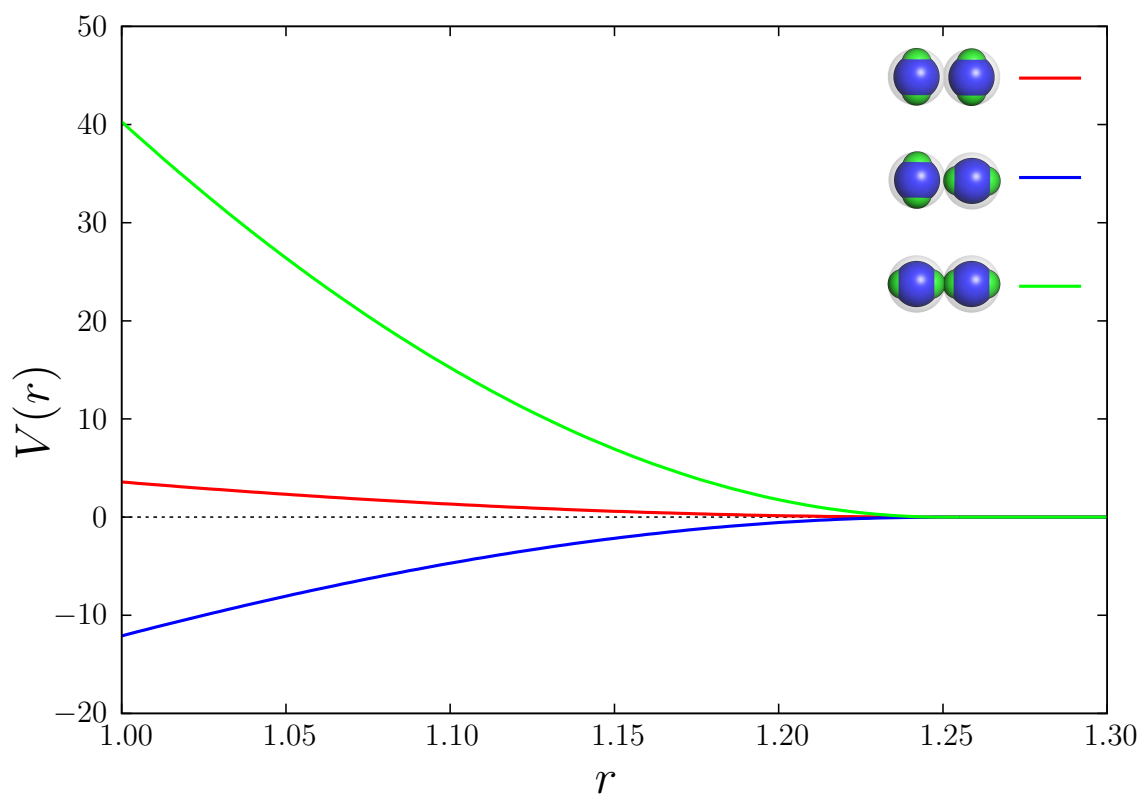
Figure 2.8.: Example for an interaction potential $V(r)$ of a pair of IPCs as a function of the interparticle distance r in the equatorial-equatorial (red line), equatorial-polar (blue line) and polar-polar (green line) configuration. Units and parameter values are chosen as given in Sec. 4.2.3, for geometry A with no overcharges.

3. Methods

3.1. Energy Landscapes

Following basic principles of thermodynamics, the equilibrium structure of a system at a given state point is the one that minimizes the governing thermodynamic potential. In the isothermal-isobaric ensemble (with constant particle number N, pressure P and temperature T), the Gibbs free energy

$$G = U + PV - TS \tag{3.1}$$

plays this role, with U representing the potential energy, V the volume and S the entropy of the system. At $T = 0$, G reduces to the enthalpy H.

In the canonical ensemble (with constant particle number N, volume V and temperature T and the Helmholtz free energy $F = U - TS$), the potential energy U remains the only relevant term in the thermodynamic potential at $T = 0$.

If we treat U as a function of the (Cartesian) particle coordinates $\{\mathbf{x}\}$, the function $\{\mathbf{x}\} \to U(\{\mathbf{x}\})$ is represented by a $\xi = dN$-dimensional hypersurface in a $\xi + 1$-dimensional space, d being the dimensionality of the system. For anisotropic rigid bodies, which have $d(d-1)/2$ additional rotational degrees of freedom per particle, we obtain

$$\xi = \left(1 + \frac{d-1}{2} \right) dN.$$

This hypersurface is often called the potential energy landscape (PES). Physical and chemical properties of many systems (*e.g.*, clusters, glassy systems or the folding of proteins) can be described in terms of their PES [49].

In the isothermal-isobaric ensemble, V can be treated as a function of $\{\mathbf{x}\}$ in a similar way, leading, together with $U(\{\mathbf{x}\})$, to the enthalpy landscape $H(\{\mathbf{x}\})$. For S and the (Gibbs) free energy landscape, the situation is more complicated, since in general, a reliable evaluation of $S(\{\mathbf{x}\})$ is very difficult. Nevertheless, these quantities can sometimes be approximated within a reduced system by functions of a small number of order parameters.

The key elements of the PES are stationary points *i.e.*, minima $\{\mathbf{x}\}_{\mathrm{MIN}}$ (points from which an infinitesimal step in any direction leads to an increase in energy) and transition states $\{\mathbf{x}\}_{\mathrm{TS}}$ (specified below). All stationary points are characterized by a vanishing gradient vector

$$\frac{\partial U(\{\mathbf{x}\})}{\partial x_i} = 0, \tag{3.2}$$

where the index i specifies a particle. These points can be classified into minima, transition states and higher-order stationary points by the number of negative eigenvalues (termed the index) of the Hessian matrix

$$\frac{\partial^2 U(\{\mathbf{x}\})}{\partial x_i \partial x_j}. \tag{3.3}$$

For minima, the Hessian matrix has only positive eigenvalues, while for transition states, there is exactly one negative eigenvalue (*i.e.*, for a TS, there is exactly one eigenvector, for which an infinitesimal step in the according direction decreases the energy, while it is increased by taking such steps in any perpendicular direction). The energetically lowest minimum is of particular interest and is called ground state or global minimum, as it determines the structure the system forms at zero temperature. The global minimum and additional local minima and their respective densities of states (*i.e.*, the vibrational entropy associated with the minima) govern the equilibrium behavior of the system at finite temperature, while the dynamics of the system also depend on the connection of local minima *via* TS. Fig. 3.1 displays a schematic two-dimensional energy landscape with four local minima and four TS.

Localizing arbitrary minima on a PES when analytic derivatives $\partial U(\{\mathbf{x}\})/\partial x_i$ are available is in principle a straightforward task, as search algorithms starting from random points can follow the direction of the steepest gradient descent until a local minimum is reached. The set of points in configuration space, from which a steepest descent minimization leads to the same local minimum is often called the "basin of attraction" of the corresponding minimum. However, there are several more sophisticated and much more efficient techniques than the steepest descent method available, the limited memory Broyden-Fletcher-Goldfarb-Shanno (L-BFGS) algorithm [50–52], being the one of our choice. This algorithm requires the evaluation of function values $U(\{\mathbf{x}\})$ and of derivatives $\partial U(\{\mathbf{x}\})/\partial x_i$ at each iteration and approximates the Hessian matrix by storing information obtained during a limited number M of previous optimization steps. As M can usually chosen to be rather small ($\sim 3 - 10$) and each iteration requires only $\mathcal{O}(M\xi)$ operations, this approach is computationally more efficient than algorithms which rely on the explicit calculation of the Hessian matrix (such as Newton's method).

Locating TS is a considerably more difficult task and in the following we will only give a very brief overview of the available methods to cope with those difficulties. The common techniques can generally be categorized into single-ended and double-ended methods: A single ended algorithm searches for a TS starting from a given point on the PES, while a double ended approach tries to identify a TS between two predefined points, often corresponding to local minima. Most single-ended algorithms are based on a method called "eigenvector following" [49]. In contrast to the standard Newton-Raphson method, which can converge to stationary points of arbitrary index, eigenvector following allows to locate points of a chosen index by introducing certain constraints and Lagrange multipliers in order to modify search step directions. For large systems, hybrid eigenvector-following plus minimization techniques can be employed in order to avoid explicit calculations of the Hessian. A double ended approach is the so-called nudged elastic band method, which is used in our pathway calculations
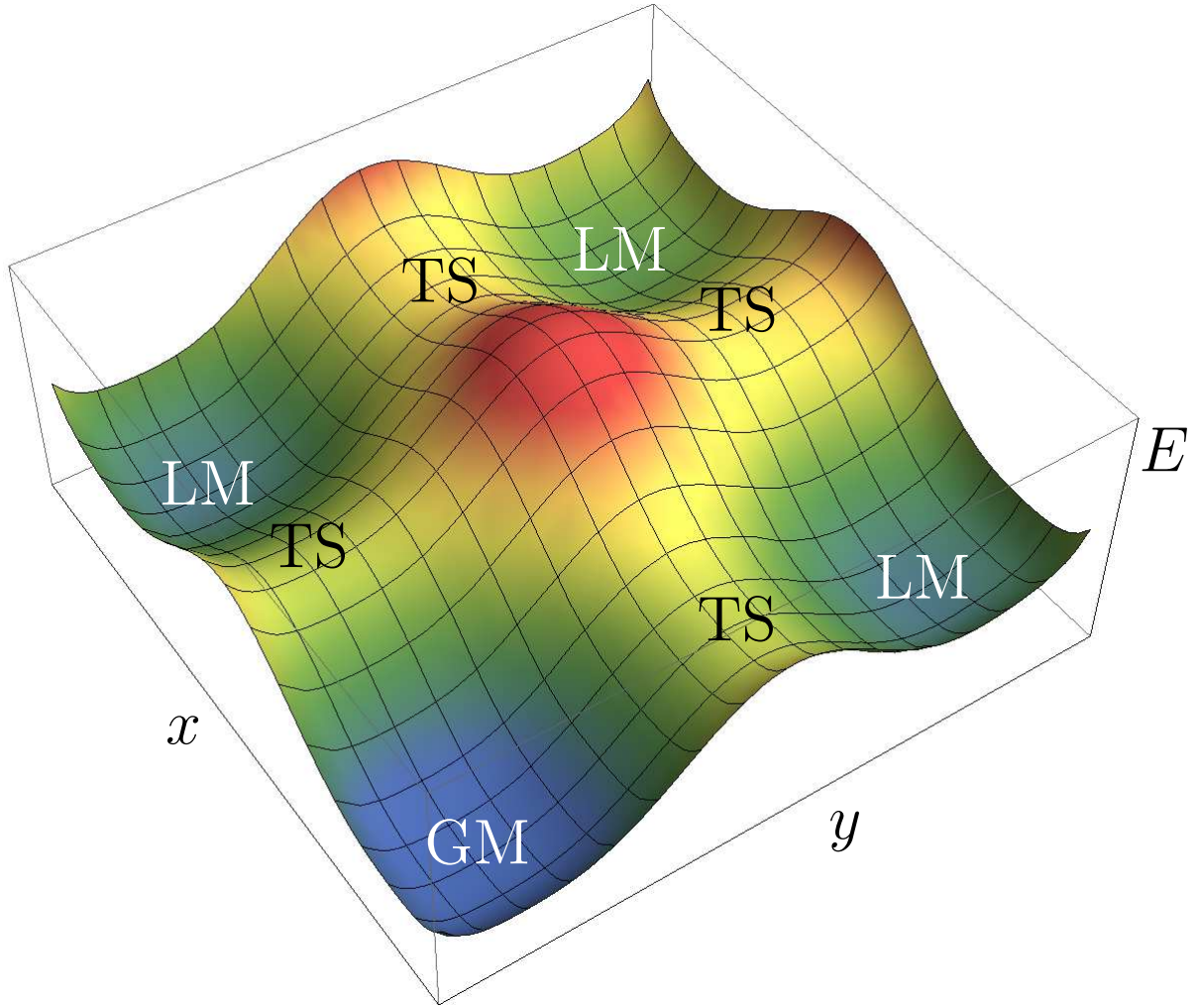
Figure 3.1.: Two-dimensional energy landscape with four local minima (LM; GM signifying the global minimum) and four transition states (TS).

presented in Sec. 4.2.1. Its basic principle is a geometric interpolation between the structures corresponding to the pre-defined endpoints. The interpolated structures are locally optimized, with an additional spring force parallel to the path between the endpoints. Any candidate TS found by this method are then further refined using the eigenvector-following method. For a much broader introduction on TS searches, we refer again to Ref. [49] and the references therein.

Once a representative database of minima and their connections *via* TS on a given energy landscape is available, this information can be used in order to characterize the landscape. In order to visualize the characteristics, some reduction of the generally multidimensional data is necessary. A very convenient two-dimensional representation are so-called disconnectivity graphs [53], which suppress any information about the actual location of minima and TS in configuration space, but rather visualize the (lowest possible) energetic cost of moving the system from one given local minimum A to a different minimum B. This cost is defined by the

energetically highest-lying TS that needs to be passed on the path AB. In a disconnectivity graph, local minima are assigned coordinates on the vertical axis proportional to their energy values, while the coordinates on the horizontal axis are chosen arbitrarily. TS are categorized into discrete energetic levels, and connections between minima are drawn according to the level of the highest TS on the path. Of course, these connections do not necessarily reflect the probability or rate constant of a transition from A to B, since any other TS on a path are ignored; nevertheless, disconnectivity graphs generated from representative databases are able to give a good impression of the general properties of an energy landscape. In Fig. 3.2, a simple one-dimensional energy landscape and the corresponding disconnectivity graph are displayed.
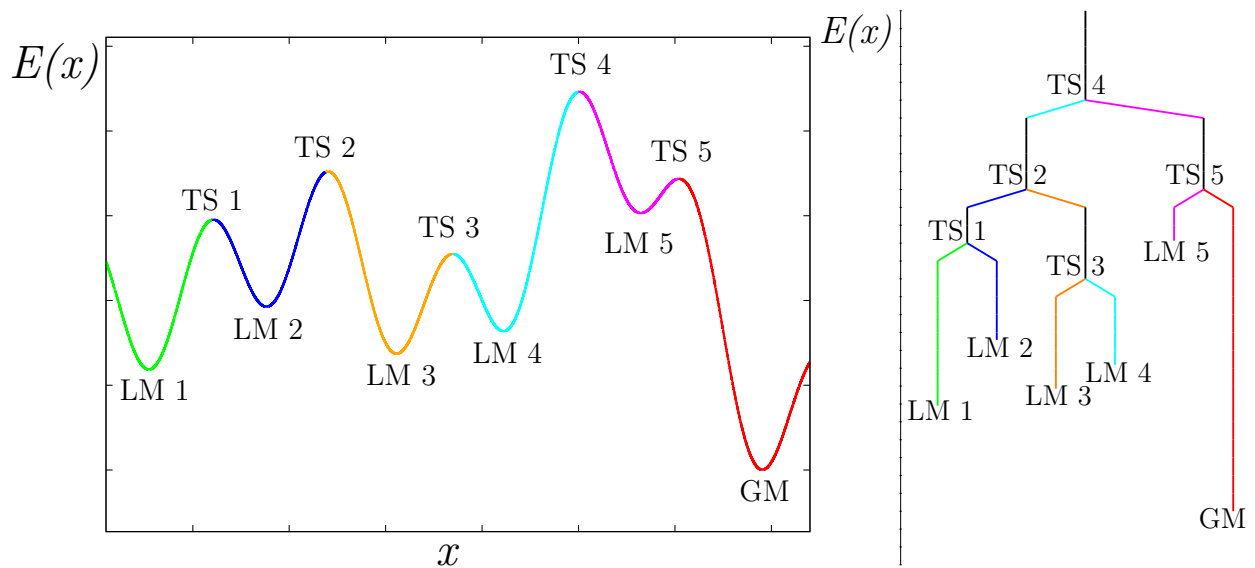
Figure 3.2.: Left: Sketch of a one-dimensional energy landscape with six minima (GM, LM n) and five transition states (TS n). Right: The same energy landscape represented as a disconnectivity graph; spacing between energy levels is chosen so that every TS is separately resolved (in real applications, where hundreds or thousands of transition states are present in a database, a much more coarse-grained spacing is chosen).

In Ref. [54], some "archetypal" forms of energy landscapes have been introduced. These are termed "palm tree", corresponding to a landscape consisting of a deep funnel with minima separated by low barriers, "weeping willow", corresponding to a shallow funnel with high barriers between minima and "banyan tree", corresponding to a rough landscape consisting of multiple, disconnected funnels. As it is argued in Ref. [49], palm-tree-like landscapes favor self-assembly of the global minimum structure, since pathways that go downhill in energy do not encounter comparably high energy barriers. For the same reason, solutions to global optimization problems on such landscapes should be comparably easy to find. Banyan-tree like landscapes on the other hand have strongly disconnected funnels, which can lead to multiple relaxation timescales and trapping in local minima.

In Sec. 4.2.1 we present disconnectivity graphs for clusters consisting of patchy particles.

3.2. Global Optimization

Identifying the global minimum on the PES, *i.e.*, solving the optimization problem

$$\underset{\{\mathbf{x}\}}{\text{minimize}} \quad U(\{\mathbf{x}\}) \tag{3.4}$$

is of course a much harder task than locating arbitrary minima from a given starting points (as discussed in the previous section).

In general, global optimization is a technique applied in a large number of scientific fields, as diverse as physics (*e.g.*, minimizing energy functionals in density functional theory [55]), chemistry (*e.g.*, the search for equilibrium configurations, *i.e.*, minimizing thermodynamic potentials), biochemistry (*e.g.*, protein folding [56–58]), mathematics and computer science (*e.g.*, the famous traveling salesman problem [59], problems in graph theory [60], packing problems like Kepler's conjecture and fitting problems) and economics (*e.g.*, scheduling problems).

Often, it is distinguished between deterministic, stochastic and heuristic global optimization algorithms. However, it can be argued [61] that a more accurate classification scheme should distinguish between the following types:

- incomplete - it is impossible to tell if the algorithm ever reaches the global minimum;

- asymptotically complete - the algorithm reaches the global minimum within an infinite amount of time with probability one, but it is impossible to tell if this already has happened during the run;

- complete/rigorous - such methods reach the global minimum with certainty given arbitrarily long running times and know after a finite time that an approximation to the global minimum has been found.

Complete and rigorous algorithms are guaranteed to identify the global minimum when they are run for a sufficient amount of time, which usually scales exponentially with system size, making them unfeasible for large and complex problems. In this case, incomplete – stochastic or heuristic – approaches have to be used. Stochastic algorithms sample the search space in a randomized way; heuristic ones try to incorporate information about the optimization problem acquired in preceding steps into the decision where to move next in search space. Such non-deterministic algorithms often provide good or "good enough" (*i.e.*, for some optimization problems finding a sufficiently low-lying local minimum is already an adequate solution) results within reasonable time scales. However it can never be guaranteed that an identified solution is indeed the global minimum and strictly, one has to speak of putative

solutions. The algorithms that will be discussed in the following are nondeterministic and have both stochastic and heuristic features.

An additional class of methods for addressing optimization problems are strategies based on deformations of the cost-function hypersurface [62]. By such deformations, one hopes to simplify the optimization problem by reducing the number of minima, lowering barriers between them and enlarging the basins of attraction of the lowest lying minima. Numerous problem-specific methods of how to perform a hypersurface deformation have been proposed. The method was first illustrated for specific graph partitioning problems [62]; for particle geometry optimization, altering the shape of the interaction potential [63, 64] or smoothing the potential by applying the diffusion equation [65, 66] have been proposed. However, in general, it cannot be guaranteed that the position of the global minimum of a deformed hypersurface corresponds to the global minimum on the original hypersurface.

A different kind of hypersurface deformation is defined by performing a steepest descent minimization* with respect to the cost function Φ at each point $\{\mathbf{x}\}$ the search algorithm encounters. As described in Ref. [67], the deformed hypersurface $\tilde{\Phi}$ is given as

$$\tilde{\Phi}(\{\mathbf{x}\}) = \text{localmin}[\Phi(\{\mathbf{x}\})]. \tag{3.5}$$

This deformation does not reduce the number of minima and keeps the size of the catchment basins constant, but still greatly simplifies the optimization problem by effectively reducing the cost function hypersurface to a number of plateaux, each corresponding to a catchment basin (*cf.* Fig. 3.3 for a one-dimensional sketch). Thereby, the cost function values and search space coordinates of all minima are kept intact, as well as the identity of the global minimum.

In order to construct an efficient optimization algorithm, an effective search strategy for low-lying minima on the (deformed) hypersurface needs to be employed. The choice for such a search strategy is of course very problem-specific and depends on the global structure of the cost function hypersurface. The search strategy should be able to exploit correlations of the positions of minima on the hypersurface [68] and detect "promising regions" in search space, in order to perform better than a completely random search. The two most widely used approaches in particle geometry optimization are basin-hopping Monte Carlo and evolutionary algorithms, which will be described below.

3.2.1. Basin-Hopping

The basin-hopping method was first introduced in Ref. [67], as an optimization method for the geometry of Lennard-Jones clusters. Local optimization steps are combined with global

---

*In practice, it is much more efficient to use L-BFGS minimization [50–52], although this might lead to a slightly different deformed hypersurface, as an L-BFGS minimization from a certain point does not necessarily lead to the same local minimum as a steepest descent path.
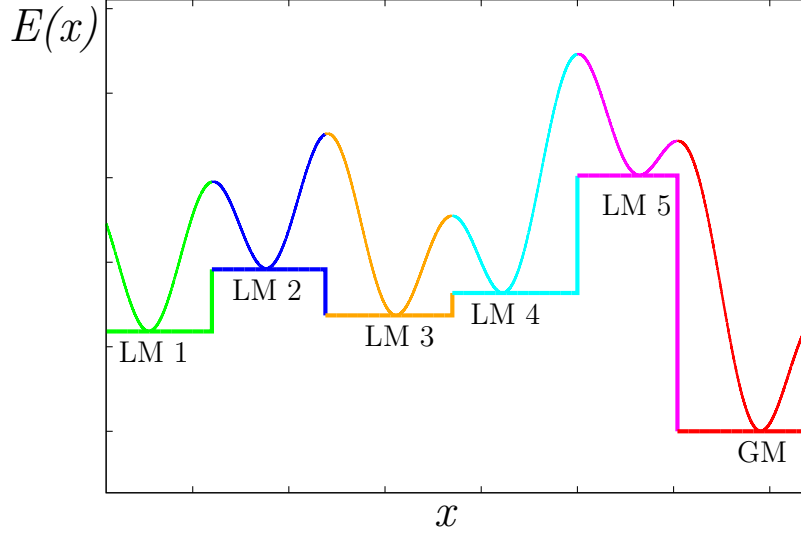
Figure 3.3.: Sketch of a one-dimensional energy landscape with six minima, their respective catchment basins (different colors) and the transformed landscape emerging from local minimizations at each point in search space (step function).

search based on canonical Monte Carlo (MC) sampling [69] of the energy landscape. Most importantly, for the Metropolis acceptance criterion

$$P_{\text{accept}} = \min(1, \exp -\Delta U/k_B T), \tag{3.6}$$

which determines the probability if a global search step is accepted or not, the energy values of the locally optimized configurations before and after the step are taken into account, *i.e.*

$$\Delta U = U_{\text{after MC step}}^{\text{optimized}} - U_{\text{before MC step}}^{\text{optimized}}. \tag{3.7}$$

Since the local optimizations are performed with respect to the energy only, the temperature T does not have a physical meaning within this approach, but rather is a parameter in the search algorithm; however, thermodynamic properties in the low temperature regime can be calculated subsequently, *e.g.*, by computing vibrational entropies for the identified minimum energy structures, *e.g. via* lattice dynamics, as shown in Ref. [70].

The size of trial steps is chosen to be much larger than in thermodynamic MC simulations, as these steps should be able to iterate the system from one catchment basin associated with a local minimum to another. For an efficient global search, the algorithm usually runs at a fixed acceptance probability P_{accept}, *i.e.*, the step size (or, alternatively, the temperature) is adjusted during the algorithm run, whenever P_{accept} differs from the desired value, which is usually 30 to 50 percent.

The basin-hopping technique has been optimized for structure prediction of finite clusters, introducing an additional type of moves: If the energy of the most weakly bound particle w in the system is higher than a certain threshold, depending on the value for the most tightly

bound particle, an "angular move" is performed: The particle is translocated to a random position on the surface of the cluster, *i.e.*, in spherical coordinates (r, θ, ϕ) with the center of mass of the cluster being the origin, r_w is set to the maximum distance between the origin and any other particle, while θ_w and ϕ_w are given random values.

In our investigations on patchy particle clusters (*cf.* Sec. 4.2.1), we employed the basin-hopping implementation "GMIN" [71], incorporating the Doye model potential (*cf.* Sec. 2.2.2) into the framework of the program.

3.2.2. Evolutionary Algorithms for Crystal Structure Prediction

In a previous work [72] we have described an evolutionary algorithm (EA) for the prediction of low energy (finite) cluster structures consisting of particles interacting *via* isotropic pair potentials. We use the concepts presented therein as a basis for the present work, where we extend the described framework for the prediction of low energy and low enthalpy three-dimensional crystal structures, consisting of anisotropic particles.

For crystalline structures, we exploit periodicity and are therefore able to predict infinitely extended configurations, working in a search space spanned by a finite number of dimensions. The parameter set of this optimization problem* consists at least of six parameters $(a, b, c, \alpha, \beta, \gamma)$ defining the primitive lattice vectors [73]

$$\mathbf{a} = \begin{pmatrix} a_x \\ a_y \\ a_z \end{pmatrix} = a \begin{pmatrix} 1 \\ 0 \\ 0 \end{pmatrix} \tag{3.8}$$

$$\mathbf{b} = \begin{pmatrix} b_x \\ b_y \\ b_z \end{pmatrix} = b \begin{pmatrix} \cos\gamma \\ \sin\gamma \\ 0 \end{pmatrix} \tag{3.9}$$

$$\mathbf{c} = \begin{pmatrix} c_x \\ c_y \\ c_z \end{pmatrix} = c \begin{pmatrix} \cos\beta \\ (\cos\alpha - \cos\beta\cos\gamma)/\sin\gamma \\ w/\sin\gamma \end{pmatrix}, \tag{3.10}$$

with
$$w = (1 - \cos^2\alpha - \cos^2\beta - \cos^2\gamma + 2\cos\alpha\cos\beta\cos\gamma)^{1/2}, \tag{3.11}$$

plus, for non-simple lattices with a basis of N particles, the positions $\mathbf{x}_i$ and orientations $\mathbf{o}_i$† of the particles in the primitive cell. Thus, we have $6 + 6N - 3 = 6N + 3$ independent variables, as the translational coordinates of one basis particle can be chosen arbitrarily. Usually, the positions and orientations of the basis particles are given in fractional coordinates $\mathbf{f}_i, \mathbf{g}_i$, *i.e.*,

---

*In practice, we minimize the reduced enthalpy, *cf.* App. A.
†The index i indicates the particle. For a definition of the orientation vector $\mathbf{o}_i$, see below.

in terms of the coordinate system defined by the primitive lattice vectors:

$$\mathbf{x} = \begin{pmatrix} x \\ y \\ z \end{pmatrix} \tag{3.12}$$

$$\mathbf{f} = \begin{pmatrix} f_a \\ f_b \\ f_c \end{pmatrix} \tag{3.13}$$

$$\mathbf{x} = \begin{pmatrix} a_x & b_x & c_x \\ a_y & b_y & c_y \\ a_z & b_z & c_z \end{pmatrix} \mathbf{f}. \tag{3.14}$$

The number of particles within the unit cell, N, is a constant parameter of each global optimization run. The operations that are performed by the optimization algorithm have to be adapted to this new set of variables and will be described below. Before that we will introduce a few terms frequently used in the context of EAs.

Definitions:

- Individuals: Any candidate solution (*i.e.*, a point in search space) that the algorithm is operating on is considered an individual taking part in the evolutionary process.

- Population: EAs are working on a number of candidate solutions simultaneously. The collection of individuals (usually a constant number) that are currently taking part in the simulated evolutionary process is called the population. New individuals can enter the population by replacing existing ones.

- Fitness: Each individual is assigned a fitness value f as a measure for its quality with respect to the underlying optimization problem. This value determines the individuals' chances for surviving within the population along the evolutionary process and being allowed to pass on its features by mating. To guarantee efficiency of the algorithm, the fitness value has to be related to the cost function of the optimization problem. There are many feasible choices for a useful fitness function [74]; in our approach, we calculate fitness values *via* an exponential function of the thermodynamic potential; the latter is considered with respect to the best and worst values within the population, as described in [72, 75, 76]:

$$f_i = \exp\left(-\alpha \frac{H_i - H_{\min}}{H_{\max} - H_{\min}}\right), \tag{3.15}$$

where α is a parameter (we usually set $\alpha = 3$), H_i represents the enthalpy of the current individual and $H_{\min}, H_{\max}$ are the lowest and highest enthalpy values within the population.

Operations:

- Selection and Mating: The central operation in an EA is the creation of new candidate solutions by recombination of features of existing ones. Before being able to perform this so-called mating step, the individuals taking part in this process have to be selected from the population. We employ a well-established [72, 75, 77] selection scheme, based on fitness values attributed to the individuals. For convenience, the fitness values of all individuals within the population are mapped onto the interval $[0, 1]$. Each individual is assigned a unique sub-interval, where higher fitness values correspond to longer subintervals. Subsequently, a random number $c \in [0, 1]$ is chosen and the individual occupying the sub-interval containing c is selected for mating. This procedure is repeated to select a second parent; if the same individual is chosen twice, the whole selection operation is restarted.

Once two unique parent individuals have been selected, they are recombined using a real-space crossover operation. Real space crossover, as a radical change from crossover operations based on encoded genotypes (*e.g.*, [75–77]), was initially implemented for cluster geometry optimization [78], as a "cut and splice" operation: Both clusters are split along a plane and two of the emerging fragments – one from each parent – are reassembled in order to from a child cluster, ensuring that the new cluster contains the same number of particles as the old ones. In this way, a large fraction of the information gained during local optimizations is retained in the child individual, as the local environment of particles is only perturbed along the splicing plane.

This scheme was extended later to crystal structures, which are described by primitive lattice vectors and a basis [79, 80]. It is most convenient to perform the crossover operation for the basis particles in fractional coordinates, *i.e.*, the particle positions are described in terms of the primitive lattice vectors and the cut and splice operation is carried out in the same way as for finite clusters, the cutting plane being perpendicular to a randomly chosen primitive lattice vector. As pointed out in Ref. [79], it is preferable to randomly shift the fractional coordinates of both parent individuals before splicing, *i.e.*, to add a random number $r_s \in [0, 1]$ to the fractional coordinates $x_{f,i}$; if a shifted component $x_{f,i}^s$ exceeds one or lies below zero, it is set to $x_{f,i}^s - 1$ or $1 - x_{f,i}^s$, respectively. The authors of Ref. [79] recommend to perform the shifting in the direction of the lattice vector defining the cutting plane with high probability (~ 95 percent) and in the two remaining directions with low probability (~ 5 percent); other investigators always perform shifts in all three directions [81]. The shifted configuration is physically indistinguishable from the unshifted one; the operation should increase diversity within the population by avoiding preferred positions of particles within the primitive cell. Unfortunately, it is less obvious how to perform a crossover for the primitive lattice vectors. The methods that have been proposed [79, 80, 82] include defining the primitive lattice vectors of the child individual by taking randomly weighted averages over the ones of the parents or inheriting the complete set of vectors from a single, randomly chosen, parent. Both of these approaches cannot be considered ideal, since changes in the lattice vectors of course can have large effects

on the particle positions (as they are stored in fractional coordinates), heavily distorting the local environment of all the particles in the system. We have implemented both proposed techniques and observed slightly faster convergence rates (*cf.* App. E) when using the averaging approach. A schematic, two-dimensional representation of a real-space crossover operation can be found in Fig. 3.4.

- Mutation: In a real space encoded EA, random mutation seems to be a less important operation. Nevertheless, it can be used to prevent premature convergence to local minima, which is mainly an issue concerning the primitive lattice vectors. Therefore, Oganov *et al.* [79, 83] defined a mutation operator, which performs a strain on the primitive lattice vectors. In matrix notation, this operation can be written as

$$\mathbf{a}' = (\mathbb{1} + \epsilon_{ij})\mathbf{a}, \tag{3.16}$$

where $\mathbf{a}$ and $\mathbf{a}'$ represent a lattice vector before and after the mutation operation and the strain matrix is given by

$$\mathbb{1} + \epsilon_{ij} = \begin{pmatrix} 1 + \epsilon_{11} & \epsilon_{12}/2 & \epsilon_{13}/2 \\ \epsilon_{21}/2 & 1 + \epsilon_{22} & \epsilon_{23}/2 \\ \epsilon_{31}/2 & \epsilon_{32}/2 & 1 + \epsilon_{33} \end{pmatrix}. \tag{3.17}$$

The matrix is symmetric, *i.e.*, $\epsilon_{ij} = \epsilon_{ji}$; ϵ_{ij} are zero-mean Gaussian random variables.

- Volume Scaling: For each newly created configuration – either randomly, by mating or by mutation –, the lattice vectors are uniformly rescaled, so that the volume of the primitive cell $V_{\mathrm{PC}} = |\mathbf{c} \cdot (\mathbf{a} \times \mathbf{b})|$ matches a predefined value V_{PC}^0, which has to be defined in advance, with respect to the investigated system. In the subsequent local optimization, V_{PC} is allowed to (and will most likely) change. V_{PC}^0 can be chosen to be constant during the algorithm run or to be adaptive with respect to the most successful individuals. In the latter case, at regular intervals, V_{PC}^0 is redefined as a weighted average of the current value and the values of the n most favorable individuals in the population:

$$V_{\mathrm{PC}}^{0,\mathrm{new}} = a V_{\mathrm{PC}}^{0,\mathrm{current}} + \sum_{i=1}^{n} \frac{1-a}{n} V_{\mathrm{PC}}^i. \tag{3.18}$$

In our calculations, we usually employ an adaptive unit cell volume; the weighting factor $0 \leq a \leq 1$ is chosen to be 0.6, and $0 \leq n \leq n_{\mathrm{ind}}$ is defined as half the total number of individuals in the population n_{ind}.

- Local Optimization: In the context of EAs, local optimizations (*cf.* Sec. 3.1) can be interpreted as "learning operations". Since individuals pass on features they acquired through learning to their offspring, these types of algorithms rather mimic Lamarckian evolution* or epigenetics [84] than Darwinian evolution, where individuals only pass on

---

*Within the theory of Lamarckian evolution, individuals can not only pass on their genetic material, but also characteristics they acquired during their lifetime.

their predefined genetic material. Another frequently used term for evolutionary algorithms with local optimization is "memetic algorithms" [68], referring to the neologism "meme" [85], signifying a "unit of cultural transmission".

In our particular L-BFGS-based local optimization routine (*cf.* Sec. 3.1 and Refs. [50–52]), we allow all nine components a_i, b_i, c_i of the primitive lattice vectors to vary freely, instead of the six parameters $a, b, c, \alpha, \beta, \gamma$. In our experience, this leads to faster convergence rates of the algorithm.

Crystal Boundary Conditions

When calculating energies *via* pair interaction potentials $U(r)$ with a finite range $r_{\max}$, for which $U(r > r_{\max}) = 0$, in a crystal lattice specified by the primitive vectors $\{\mathbf{a}, \mathbf{b}, \mathbf{c}\}$, all periodic images of the primitive cell within a distance $r \leq r_{\max}$ from the origin have to be taken into account. The distance r of an image cell specified by a lattice vector $\mathbf{l}$, or alternatively by a triplet $\{n_a, n_b, n_c\}$, is given by

$$r(n_a, n_b, n_c) = |\mathbf{l}| = |n_a\mathbf{a} + n_b\mathbf{b} + n_c\mathbf{c}|. \tag{3.19}$$

Identifying each triplet, which fulfills the condition $r(n_a, n_b, n_c) \leq r_{\max}$ is not completely trivial if all components of the primitive lattice vectors can be varied arbitrarily. We are using the following protocol (which is an extension of the method described in Ref. [73]) in order to solve this problem in an efficient way.

First, the orthonormal vectors

$$\hat{\mathbf{v}}_1 = \mathbf{b} \times \mathbf{c}/|\mathbf{b} \times \mathbf{c}| \tag{3.20}$$

$$\hat{\mathbf{v}}_2 = \hat{\mathbf{v}}_1 \times \mathbf{c}/|\hat{\mathbf{v}}_1 \times \mathbf{c}| \tag{3.21}$$

$$\hat{\mathbf{v}}_3 = \hat{\mathbf{v}}_1 \times \hat{\mathbf{v}}_2 \tag{3.22}$$

are calculated. These vectors define an orthonormal system; only the primitive lattice vector $\mathbf{a}$ can have components parallel to $\hat{\mathbf{v}}_1$, while $\mathbf{a}$ and $\mathbf{b}$ can have components parallel to $\hat{\mathbf{v}}_2$ and all three primitive lattice vectors can have components parallel to $\hat{\mathbf{v}}_3$:

$$\mathbf{a} \cdot \hat{\mathbf{v}}_1 = a_{v_1} \tag{3.23}$$

$$\mathbf{a} \cdot \hat{\mathbf{v}}_2 = a_{v_2} \quad \mathbf{b} \cdot \hat{\mathbf{v}}_2 = b_{v_2} \tag{3.24}$$

$$\mathbf{a} \cdot \hat{\mathbf{v}}_3 = a_{v_3} \quad \mathbf{b} \cdot \hat{\mathbf{v}}_3 = b_{v_3} \quad \mathbf{c} \cdot \hat{\mathbf{v}}_3 = c_{v_3}. \tag{3.25}$$

An arbitrary lattice vector $\mathbf{l}$ can be expressed in terms of the orthonormal system $\{\hat{\mathbf{v}}_i\}$:

$$\mathbf{l} = (\mathbf{l} \cdot \hat{\mathbf{v}}_1)\hat{\mathbf{v}}_1 + (\mathbf{l} \cdot \hat{\mathbf{v}}_2)\hat{\mathbf{v}}_2 + (\mathbf{l} \cdot \hat{\mathbf{v}}_3)\hat{\mathbf{v}}_3 \tag{3.26}$$

$$= (n_a a_{v_1})\hat{\mathbf{v}}_1 + (n_a a_{v_2} + n_b b_{v_2})\hat{\mathbf{v}}_2 + (n_a a_{v_3} + n_b b_{v_3} + n_c c_{v_3})\hat{\mathbf{v}}_3. \tag{3.27}$$

Now, a sphere with radius $r = r_{\max}$ is intersected with the lattice described in the orthogonal system defined by $\{\hat{\mathbf{v}}_i\}$ in order to calculate $n_a^{\max/\min}$, $n_b^{\max/\min}(n_a)$ and $n_c^{\max/\min}(n_a, n_b)$, for which

$$
\begin{align}
|\mathbf{l}|^2 &= (\mathbf{l} \cdot \hat{\mathbf{v}}_1)^2 + (\mathbf{l} \cdot \hat{\mathbf{v}}_2)^2 + (\mathbf{l} \cdot \hat{\mathbf{v}}_3)^2 \tag{3.28} \\
&= (n_a a_{v_1})^2 + (n_a a_{v_2} + n_b b_{v_2})^2 + (n_a a_{v_3} + n_b b_{v_3} + n_c c_{v_3})^2 \tag{3.29} \\
&\leq r_{\max}^2. \tag{3.30}
\end{align}
$$

First, we compute each n_a, which fulfills $|\mathbf{l} \cdot \hat{\mathbf{v}}_1| \leq r_{\max}$*. This leads to

$$
\begin{align}
n_a^{\max} &= \lceil +|r_{\mathrm{cut}}/a_{v_1}| \rceil \tag{3.31} \\
n_a^{\min} &= \lfloor -|r_{\mathrm{cut}}/a_{v_1}| \rfloor, \tag{3.32}
\end{align}
$$

where $\lceil x \rceil$ and $\lfloor x \rfloor$ represent for the ceiling and floor functions, which take the values of the smallest integer i_c, for which $i_c \geq x$ and the largest integer i_f, for which $i_f \leq x$, respectively.

Next, for all values $n_a \in \left[n_a^{\min}, n_a^{\max} \right]$, all $n_b(n_a)$ for which $(\mathbf{l} \cdot \hat{\mathbf{v}}_1)^2 + (\mathbf{l} \cdot \hat{\mathbf{v}}_2)^2 \leq r_{\max}^2$ are calculated:

$$
\begin{align}
n_b^{\max}(n_a) &= \left\lceil (+\sqrt{r_{\mathrm{cut}}^2 - (n_a a_{v_1})^2} - n_a a_{v_2})/b_{v_2} \right\rceil \tag{3.33} \\
n_b^{\min}(n_a) &= \left\lfloor (-\sqrt{r_{\mathrm{cut}}^2 - (n_a a_{v_1})^2} - n_a a_{v_2})/b_{v_2} \right\rfloor. \tag{3.34}
\end{align}
$$

Finally, for each pair

$$
n_a \in \left[n_a^{\min}, n_a^{\max} \right], n_b \in \left[n_b^{\min}(n_a), n_b^{\max}(n_a) \right], \tag{3.35}
$$

we can calculate all $n_c(n_a, n_b)$, which are allowed by inequality (3.30)[†]

$$
n_c^{\max}(n_a, n_b) = \left\lceil [+\sqrt{r_{\mathrm{cut}}^2 - (n_a a_{v_1})^2 - (n_a a_{v_2} + n_b b_{v_2})^2} - (n_a a_{v_3} + n_b b_{v_3})]/c_{v_3} \right\rceil \tag{3.36}
$$

$$
n_c^{\min}(n_a, n_b) = \left\lfloor [-\sqrt{r_{\mathrm{cut}}^2 - (n_a a_{v_1})^2 - (n_a a_{v_2} + n_b b_{v_2})^2} - (n_a a_{v_3} + n_b b_{v_3})]/c_{v_3} \right\rfloor. \tag{3.37}
$$

If there is more than one particle within the primitive cell, the maximum distance between any two particles i and j in the primitive cell has to be added to the cutoff distance in order to account for all possible interactions:

$$
r_{\max} \to r_{\max} + \max_{i,j}(|\mathbf{r}_j - \mathbf{r}_i|). \tag{3.38}
$$

---

*Any translation parallel to $\hat{\mathbf{v}}_2, \hat{\mathbf{v}}_3$ caused by the variation of n_a can be compensated for by variations of n_b and n_c, while the latter two variations will not change the projection $\mathbf{l} \cdot \hat{\mathbf{v}}_1$.

[†]The primitive lattice vector $\mathbf{c}$ is parallel to $\hat{\mathbf{v}}_3$, *i.e.*, variations of n_c do not change $\mathbf{l} \cdot \hat{\mathbf{v}}_1$ and $\mathbf{l} \cdot \hat{\mathbf{v}}_2$.

Handling Orientational Degrees of Freedom

In order to treat orientational degrees of freedom of rigid bodies in computer simulations, parametrization based on Euler angles [86] (three consecutive rotations about certain axes that are defined by convention), unit quarternions [69] (based on normalized vectors in four-dimensional space) or angle-axis representations (determined by an axis and an angle of rotation about that axis) have been used. Euler angles can lead to problems with singularities (a phenomenon known as "gimbal lock", which occurs when two of the three axes of rotation become parallel and one degree of freedom is lost); unit quaternion descriptions are singularity free and are used as a standard tool in MC and Molecular Dynamics (MD) simulations [69], but their components cannot be freely varied, since their norm is defined to be equal to unity. This makes them unsuitable for local optimization routines like L-BFGS, where it is required to vary all variables without constraints. A special implementation of an angle-axis description introduced in Ref. [87] has none of these limitations and has proved to be especially well-suited for geometry optimizations of anisotropic, rigid particles.

The method is described closely following the presentation in Ref. [87]: All information about the rotational state of a rigid body with one point fixed in space (*i.e.*, the center of mass fixed at r), can be stored in a vector

$$\mathbf{o} = \begin{pmatrix} o_1 \\ o_2 \\ o_3 \end{pmatrix} = \theta \hat{\mathbf{o}}, \text{ with} \tag{3.39}$$

$$\theta = \sqrt{o_1^2 + o_2^2 + o_3^2}. \tag{3.40}$$

The related unit vector $\hat{\mathbf{o}}$ is parallel to the axis of rotation, while its magnitude θ corresponds to the angle of rotation about this axis. We can calculate the corresponding rotation matrix $\mathbf{R}(\theta)$ in the following way: An arbitrary vector $\mathbf{v}$ that is to be rotated about $\hat{\mathbf{o}}$ by the angle θ, can be uniquely described as a sum of its projection on $\hat{\mathbf{o}}$ and its vector rejection from $\hat{\mathbf{o}}$:

$$\mathbf{v} = \hat{\mathbf{o}}(\hat{\mathbf{o}} \cdot \mathbf{v}) - \hat{\mathbf{o}} \times (\hat{\mathbf{o}} \times \mathbf{v}), \tag{3.41}$$

where the rotation will only affect the latter term. We perform the rotation in an orthonormal coordinate system (in which coordinates will be denoted by primed variables x' and $\rightarrow$ signifies a transformation from the original coordinate system to the primed one in the following), where the z-direction is chosen to be parallel to $\hat{\mathbf{o}}$:

$$\mathbf{v} \rightarrow \mathbf{v}' = \begin{pmatrix} v'_x \\ v'_y \\ v'_z \end{pmatrix}, \tag{3.42}$$

$$\hat{\mathbf{o}} \rightarrow \hat{\mathbf{o}}' = \begin{pmatrix} 0 \\ 0 \\ 1 \end{pmatrix}, \tag{3.43}$$

$$\hat{\mathbf{o}}' \times \mathbf{v}' = \begin{pmatrix} -v_y' \\ v_x' \\ 0 \end{pmatrix}, \tag{3.44}$$

$$-\hat{\mathbf{o}}' \times (\hat{\mathbf{o}}' \times \mathbf{v}') = \begin{pmatrix} v_x' \\ v_y' \\ 0 \end{pmatrix}, \tag{3.45}$$

$$\mathbf{R}(\theta) \rightarrow \mathbf{R}'(\theta) = \begin{pmatrix} \cos\theta & -\sin\theta & 0 \\ \sin\theta & \cos\theta & 0 \\ 0 & 0 & 1 \end{pmatrix}, \tag{3.46}$$

$$\mathbf{R}(\theta)(-\hat{\mathbf{o}} \times (\hat{\mathbf{o}} \times \mathbf{v})) \rightarrow \mathbf{R}'(\theta) \begin{pmatrix} v_x' \\ v_y' \\ 0 \end{pmatrix} = \cos\theta \begin{pmatrix} v_x' \\ v_y' \\ 0 \end{pmatrix} + \sin\theta \begin{pmatrix} -v_y' \\ v_x' \\ 0 \end{pmatrix}. \tag{3.47}$$

Thus, in the original coordinate system we have

$$\mathbf{R}(\theta)\mathbf{v} = \hat{\mathbf{o}}(\hat{\mathbf{o}} \cdot \mathbf{v}) - \cos\theta(\hat{\mathbf{o}} \times (\hat{\mathbf{o}} \times \mathbf{v})) + \sin\theta(\hat{\mathbf{o}} \times \mathbf{v}), \tag{3.48}$$

which is known as Rodrigues' rotation formula [88]; substituting Eq. (3.41) leads to

$$\mathbf{R}(\theta)\mathbf{v} = \mathbf{v} + (1 - \cos\theta)[\hat{\mathbf{o}} \times (\hat{\mathbf{o}} \times \mathbf{v})] + \sin\theta(\hat{\mathbf{o}} \times \mathbf{v}). \tag{3.49}$$

Writing the cross product as a matrix multiplication

$$\hat{\mathbf{o}} \times \mathbf{a} = \tilde{\mathbf{o}}\mathbf{a}, \tag{3.50}$$

with

$$\tilde{\mathbf{o}} = \frac{1}{\theta} \begin{pmatrix} 0 & -o_3 & o_2 \\ o_3 & 0 & -o_1 \\ -o_2 & o_1 & 0 \end{pmatrix}, \tag{3.51}$$

we end up with the rotation matrix

$$\mathbf{R}(\theta) = \mathbb{1} + (1 - \cos\theta)\tilde{\mathbf{o}}\tilde{\mathbf{o}} + \sin\theta\tilde{\mathbf{o}}. \tag{3.52}$$

Derivatives of $\mathbf{R}$ with respect to the components o_k of $\mathbf{o}$, denoted as $\partial\mathbf{R}/\partial o_k = \mathbf{R}_k$, can now easily be calculated using the chain rule:

$$\mathbf{R}_k = \frac{o_k \sin\theta}{\theta}\tilde{\mathbf{o}}^2 + (1 - \cos\theta)(\tilde{\mathbf{o}}_k\tilde{\mathbf{o}} + \tilde{\mathbf{o}}\tilde{\mathbf{o}}_k) + \frac{o_k \cos\theta}{\theta}\tilde{\mathbf{o}} + \sin\theta\tilde{\mathbf{o}}_k, \tag{3.53}$$

with $\theta = \sqrt{o_1^2 + o_2^2 + o_3^2}$, $\partial\theta/\partial o_k = o_k/\theta$ and

$$\tilde{\mathbf{o}}_1 = \frac{\partial\tilde{\mathbf{o}}}{\partial o_1} = \frac{1}{\theta}\begin{pmatrix} 0 & o_1 o_3/\theta^2 & -o_1 o_2/\theta^2 \\ -o_1 o_3/\theta^2 & 0 & -(1 - o_1^2/\theta^2) \\ o_1 o_2/\theta^2 & (1 - o_1^2/\theta^2) & 0 \end{pmatrix}, \tag{3.54}$$

$$\tilde{\mathbf{o}}_2 = \frac{\partial\tilde{\mathbf{o}}}{\partial o_2} = \frac{1}{\theta}\begin{pmatrix} 0 & o_2 o_3/\theta^2 & (1 - o_2^2/\theta^2) \\ -o_2 o_3/\theta^2 & 0 & o_1 o_2/\theta^2 \\ -(1 - o_2^2/\theta^2) & -o_1 o_2/\theta^2 & 0 \end{pmatrix}, \tag{3.55}$$

$$\tilde{\mathbf{o}}_3 = \frac{\partial\tilde{\mathbf{o}}}{\partial o_3} = \frac{1}{\theta}\begin{pmatrix} 0 & -(1 - o_3^2/\theta^2) & -o_2 o_3/\theta^2 \\ (1 - o_3^2/\theta^2) & 0 & o_1 o_3/\theta^2 \\ o_2 o_3/\theta^2 & -o_1 o_3/\theta^2 & 0 \end{pmatrix}. \tag{3.56}$$

Care has to be taken for $\theta = 0$, as Eq. (3.53) has a (removable) singularity at this value. In this case, we substitute the finite rotation matrix in Eq. (3.46) by an infinitesimal one:

$$\mathbf{R}'(\theta \to 0) \approx \begin{pmatrix} 1 & -\theta & 0 \\ \theta & 1 & 0 \\ 0 & 0 & 1 \end{pmatrix}. \tag{3.57}$$

The rotation formula given in Eq. (3.48) becomes

$$\mathbf{R}(\theta \to 0) \approx \mathbb{1} + \begin{pmatrix} 0 & -o_3 & o_2 \\ o_3 & 0 & -o_1 \\ -o_2 & o_1 & 0 \end{pmatrix}. \tag{3.58}$$

Now the derivatives can easily be calculated: $\mathbf{R}_k(\theta \to 0) \approx \tilde{\mathbf{o}}_k^0$ with

$$\tilde{\mathbf{o}}_1^0 = \begin{pmatrix} 0 & -o_3 & o_2 \\ o_3 & 0 & -1 \\ -o_2 & 1 & 0 \end{pmatrix}, \tag{3.59}$$

$$\tilde{\mathbf{o}}_2^0 = \begin{pmatrix} 0 & -o_3 & 1 \\ o_3 & 0 & -o_1 \\ -1 & o_1 & 0 \end{pmatrix}, \tag{3.60}$$

$$\tilde{\mathbf{o}}_3^0 = \begin{pmatrix} 0 & -1 & o_2 \\ 1 & 0 & -o_1 \\ -o_2 & o_1 & 0 \end{pmatrix}. \tag{3.61}$$

In practice, Eq. (3.53) can be implemented as a single subroutine in a computer program in order to efficiently and conveniently compute all derivatives with respect to the orientational degrees of freedom.

Population Control and Niches

Hard Constraints   The parameter subspace spanned by the primitive lattice vectors and the fractional coordinates of the particles in the primitive cell contains regions, which represent crystal structures that can immediately be discarded by physical intuition. Examples are configurations that (a) obviously lead to overlaps of the colloidal particles or (b) strongly distorted unit cells, which can always be described by an alternative set of primitive lattice vectors [76]. In the most extreme cases of distorted unit cells [*i.e.*, (c) the primitive lattice vectors lie within a plane], we end up with flat structures, which are undesirable for our system. By discarding unphysical configurations (corresponding to cases a and c) prior to the local optimization procedure computational time can be saved without biasing the evolutionary process. After local optimization, we also discard structures with at least one very small or very large angle α between the primitive lattice vectors (corresponding to case b; usually we allow $\pi/6 \leq \alpha \leq 5\pi/6$) in order to avoid exploring redundant, but computationally expensive regions of the parameter space (since such angles lead to a large number of image cells that have to be taken into account for each energy calculation, *cf.* Sec. 3.2.2).

Diversity   In order to prevent premature convergence to local minima and dominance of individuals corresponding to such minima within the population, we need to ensure that the population stays "diverse", *i.e.*, consists of individuals corresponding to sufficiently "different" local minima. Thus, we need a metric that can measure the "difference" between individuals. The most straightforward and widely used way to do this is to use the binding energy or enthalpy of the individuals as such a measure. In many implementations, only one individual within each energy interval (the typical length of these intervals ranges from 10^{-3} to 10^{-2} in the respective units) is allowed to stay in the population. In many cases this rather crude method of introducing "niches" to the evolutionary process, relying on the assumption that energy levels are not structurally degenerate, works just fine.

As soon as structurally different but energetically equivalent minima on the energy landscape come into play (which is particularly an issue for patchy particle systems), it is very desirable to introduce a refined measuring system that quantifies structural features of the individuals. For optimization problems involving finite clusters of particles, a method for measuring structural diversity of individuals and constructing niches has been presented in [89]. It uses a simple geometry parameter g_p, which measures the distribution of particles in two-dimensional projections of the three-dimensional clusters*. Only a certain percentage of the population is allowed to have similar g_p-values.

For crystal structures, there is an additional complication: the description of an (infinite) crystal by a set of primitive lattice vectors and a basis is very convenient, but not unique. Assessing if two given representations describe the same crystal is a non-trivial task. Many

---

*More specifically, the maximum number of coinciding particles in a two-dimensional projection is measured. Thereby, clusters with fcc-like symmetry, which have a large number of coinciding particles for certain cluster orientations, can easily be distinguished from clusters with icosahedral symmetry.

implementations of EAs for structure prediction make use of "fingerprint-based" structural identification, evaluating a set of characteristic parameters, in the spirit of the Hartke method for clusters. Examples are a cosine distance measure, based on a fingerprint functions measuring correlations between particle positions [90], a method based on scattering densities [91], or space group identification [81].

Another application of fingerprint distance measures lies in the analysis of a collection of local minima obtained by optimization techniques, in a subsequent post-processing step as described in Ref. [90].

Only recently, a non-fingerprint-based exact technique that allows the identification of representations describing the same infinite structure* has been introduced [92]. Thereby, unwanted duplicate structures can be detected and subsequently removed from the population with high accuracy, in order to keep the population diverse.

Bond Order Parameters   In our calculations, we rely on another fingerprint technique in order to prevent domination of the population by a small number of structures; thereby, we do not decide if two representations are equivalent (within some range of tolerance), but rather distinguish between classes of structures. In fact, we can employ a well-established approach that has been widely used for this task: the Steinhardt order parameters (also known as bond order parameters) [93]. These parameters are based on calculating spherical harmonics of bond angles and constructing third- and fourth order invariants out of these quantities. Using the Steinhardt order parameters leads to a number of advantages:

- Bond order parameters can precisely distinguish between liquid (isotropic) phases and solid phases, exhibiting discrete translational and orientational symmetries. (This powerful feature – the averaged parameters vanish for the isotropic phase – is not relevant in our case, since all our candidate structures are crystalline by design.)

- It is possible to distinguish between crystal structures by comparing sets of bond order parameters (*i.e.*, fingerprints) calculated for different individuals.

- Bond order parameters are insensitive to the representation in parameter space. Furthermore, second and third order averages (see below), which are invariant under spatial rotations of the whole system, can be calculated in a straightforward way.

- Finally, bond order parameters can be calculated with justifiable computational costs, which is especially relevant in our case, since we want to measure structural features of individuals after each local optimization step.

In the context of the Steinhardt parameters, the term "bond" does not strictly correspond to chemical bonds (or patch-patch interactions for the systems studied here), but rather refers to lines connecting the center of mass of a particle to the centers of masses of its

---

I.e., this does not measure a difference between structures, but reliably detects exact replicas even if they are represented by distant points in parameter space.

near neighbors. Of course, a criterion under which particles are to be considered near neighbors, has to be defined. As possible values for the maximum interparticle distance r_0 for near neighbors, the minimum of the interaction potential, or the first maximum of the radial distribution function have been proposed [93]. To account for small perturbations, r_0 is usually multiplied by a factor ~ 1.2. For arbitrary crystal structures, the "intrinsic" number of near neighbors can be very different (*e.g.*, in an fcc crystal each particle has twelve neighbors in the first coordination shell, while in a bcc crystal, each particle has eight neighbors in the first coordination shell and six further ones in the second coordination shell.) Thus, we chose r_0 (and thereby the number of neighbors N_n to be taken into account for the calculation of the bond order parameters) "on the fly" for each candidate structure: we evaluate N_n as a function of r_0 at discrete values within a given interval (typically 50 r_0-values between 1.0σ and 1.3σ); then we perform a histogram analysis for these values. The maximum in the histogram, *i.e.*, the N_n-value with the most occurrences and the smallest corresponding r_0-value, are chosen for this particular candidate structure.

Once r_0 is fixed, we compute for each particle i in the primitive cell and each of its neighbors $j = 1, ..., N_n$, with interparticle vector $\mathbf{r}_{ij} = (x_{ij}, y_{ij}, z_{ij})^T$ the spherical harmonics

$$Q_{lm}(\mathbf{r}_{ij}) \equiv Y_{lm}\left(\theta(\mathbf{r}_{ij}), \phi(\mathbf{r}_{ij})\right). \tag{3.62}$$

$\theta(\mathbf{r}_{ij}) = \mathrm{acos}\left(z_{ij}/(x_{ij}^2 + y_{ij}^2 + z_{ij}^2)^{1/2}\right)$ and $\phi(\mathbf{r}_{ij}) = \mathrm{atan2}(y_{ij}, z_{ij})^*$ represent the polar and azimuthal angles between the centers of mass of particle i and neighbor j (with respect to an arbitrary external coordinate system), respectively. The indices l of the spherical harmonics, for which we have to calculate Q_{lm} in order to get significant results depend on the symmetry of the crystal structures; for example, for cubic configurations, $l = 4$ is the lowest nonzero value with finite Q [93]. In our calculations, we compute $Q_{4,m}$ and $Q_{6,m}$. For each particle, we take an average over all neighbors

$$\bar{Q}_{lm}(i) = \frac{1}{N_n} \sum_{j=1}^{N_n} Q_{lm}(\mathbf{r}_{ij}). \tag{3.63}$$

In order to obtain rotationally invariant quantities (and remove the dependence on the chosen external coordinate system), we have to average over $|m| \leq l$ as well

$$Q_l(i) = \sqrt{\frac{4\pi}{2l+1} \sum_{m=-l}^{l} |\bar{Q}_{lm}(i)|^2}. \tag{3.64}$$

---

*atan2(y, x) computes the principal value of the argument function of the complex number $x + iy$. This function can be used to transform from Cartesian into polar coordinates and allows to determine the angle in the correct quadrant [94].

$Q_l(i)$ is an average of second order; a third order average can also be constructed:

$$\hat{W}_l(i) = \frac{\displaystyle\sum_{\substack{m_1,m_2,m_3 \\ m_1+m_2+m_3=0}} \begin{pmatrix} l & l & l \\ m_1 & m_2 & m_3 \end{pmatrix} \bar{Q}_{lm_1}\bar{Q}_{lm_2}\bar{Q}_{lm_3}}{\left(\displaystyle\sum_{m=-l}^{m=l} |\bar{Q}_{lm}|^2\right)^{3/2}}, \tag{3.65}$$

where the expression

$$\begin{pmatrix} l & l & l \\ m_1 & m_2 & m_3 \end{pmatrix} \tag{3.66}$$

stands for the so-called Wigner-3j-symbols [95], which are related to the Clebsch-Gordan coefficients $\langle j_1 m_1 j_2 m_2 | JM \rangle$ in the following way:

$$\begin{pmatrix} l & l & l \\ m_1 & m_2 & m_3 \end{pmatrix} = \frac{(-1)^{j_1-j_2-m_3}}{\sqrt{2j_3+1}} \langle j_1 m_1 j_2 m_2 | j_3 - m_3 \rangle. \tag{3.67}$$

Finally, we average these invariants over the basis particles:

$$\langle \bar{Q}_l \rangle = \frac{1}{N_{bb}} \sum_{i=1}^{N_{bb}} \bar{Q}_l(i) \tag{3.68}$$

$$\langle \hat{W}_l \rangle = \frac{1}{N_{bb}} \sum_{i=1}^{N_{bb}} \hat{W}_l(i). \tag{3.69}$$

Thereby, we obtain a "fingerprint vector"

$$f = \begin{pmatrix} \langle \bar{Q}_4 \rangle \\ \langle \bar{Q}_6 \rangle \\ \langle \hat{W}_4 \rangle \\ \langle \hat{W}_6 \rangle \end{pmatrix} \tag{3.70}$$

for each individual after local optimization, which can be used to determine if two given representations correspond to similar structures: Whenever an individual a is threatened to be rejected from the population because of the enthalpy criterion (*i.e.*, has an enthalpy value too close to the value of another individual b), the "distance" vector $\Delta f = f_b - f_a$ of the competing individuals a and b is taken into account: if at least one of its components is sufficiently large – we typically use

$$\Delta_{\min} \langle \bar{Q}_4 \rangle = \Delta_{\min} \langle \bar{Q}_6 \rangle = 0.1 \tag{3.71}$$

$$\Delta_{\min} \langle \hat{W}_4 \rangle = \Delta_{\min} \langle \hat{W}_6 \rangle = 0.01 \tag{3.72}$$

as minimum values – both individuals are allowed to coexist in the population, as they are occupying different structural niches.

Recording of Minima

During the evolution of the population, we want to record candidate structures corresponding to the global minimum as well as low-lying local minima on the enthalpy landscape, even if they are removed from the current population at a certain stage. Thus, we introduce a "vault", which stores individuals if their enthalpy lies below a certain threshold and they are sufficiently different in structure from already stored ones. Again, we use a combination of binding energy differences and bond order parameters to measure this difference: Within each energy interval of length δU, starting from the fully bonded configuration, we allow a number n_i of individuals. These individuals must have a sufficiently different set of bond order parameters. If two individuals are located within the same binding energy interval and have a similar bond order parameter-fingerprint, they compete for the same spot within the vault and the one with the lower enthalpy value will be stored, the other being discarded.

Parallelization of the Algorithm

Implementations of EAs involving local optimization steps are usually very good candidates for efficient parallelization. Since the local optimizations are very time-consuming (typically taking more than 90 percent of the algorithm runtime), but completely independent from each other, they can be carried out in parallel on different processor cores. The time duration of local optimization procedures varies strongly, as some newly created individuals are close to a local minimum in parameter space, while others are far away; naively parallelizing a synchronous, generation-based EA leads to the problem of very long waiting times for some processors, as all distinct local optimizations have to be finished before the algorithm advances to the next generation. This problem can be overcome by switching to an asynchronous algorithm: here the population is treated as a "pool" of individuals; candidate structures can be added to or removed from the pool at all times (while their total number is usually kept constant).

The concept of elitism has to be adjusted in an asynchronous algorithm: In a generation-based EA, the elitism parameter e defines how many of the fittest individuals of generation i are taken into generation $i + 1$ without any changes [72]. For the pool-based algorithm with population size n, we define elitism as a mechanism of protecting the fittest individuals from being removed from the population: Whenever a new individual enters the pool, it has to replace an existing one. The elitism parameter determines the e fittest individuals, which can only be replaced by individuals with even higher fitness. The remaining $n - e$ candidate solutions within the pool can be replaced by any new ones with uniform probability. This leads to the following special cases:

- $e = n$: A new individual can only enter the population if its cost function has a lower value than the least fit individual within the pool.

- $e = n - 1$: A new individual always replaces the least fit individual within the pool, regardless of its cost function value.

- $e = 0$: A new individual replaces a randomly determined individual, regardless of their cost function values.

The asynchronous scheme can be implemented conveniently using a "master-worker" approach, where a number of processes (workers) constantly create and locally optimize new individuals. The workers do not have to communicate with each other, but only with a single process (master), which is administrating the population. The workflow and communications within this protocol is illustrated schematically in Fig. 3.5.

When constructing the parallelized protocol, a compromise between minimized waiting times and accurate population control has to be found: since the population control routine might involve the creation of completely new individuals, including local optimization, it often turns out to be very time-consuming. Therefore running this routine within the master process can increase waiting times drastically. Running this routine within the worker processes, on the other hand, has the disadvantage that the population administered by the master process is continuously evolving, while the workers are only aware of the state the population was in at the last occurrence of communication with the master. Therefore, a worker process can only check if its newly created individual is compatible with the niche criteria applied on a previous state of the population. Nevertheless, we opted for the latter version, since we consider its drawbacks minor compared to the loss of efficiency connected to the former one. Since the workload of the master processor is much smaller than the one of the workers in this scheme, such an algorithm becomes more efficient when adding more workers, up to a certain threshold where the master process is working at full capacity. Typical numbers of processor cores that we used for running the parallel algorithm were ranging from twelve to 32.

In practice, the communication between the processor cores can be handled by making use of the so-called Message Passing Interface (MPI) [96].

Other Evolutionary Approaches

As a final note, we would like to mention that in the literature, there is a number of related geometry optimization techniques based on evolutionary approaches, which do not make use of hypersurface deformation by local optimization. Here the individuals are not represented by the real space or fractional coordinates of the particles, but rather a more abstract search space is explored. Examples are algorithms using genetic encoding for crossovers ([75, 77]) or algorithms describing the candidate solutions by lattice groups (which are a more precise classification of crystal structures than the usual space groups, *cf.* [97]).
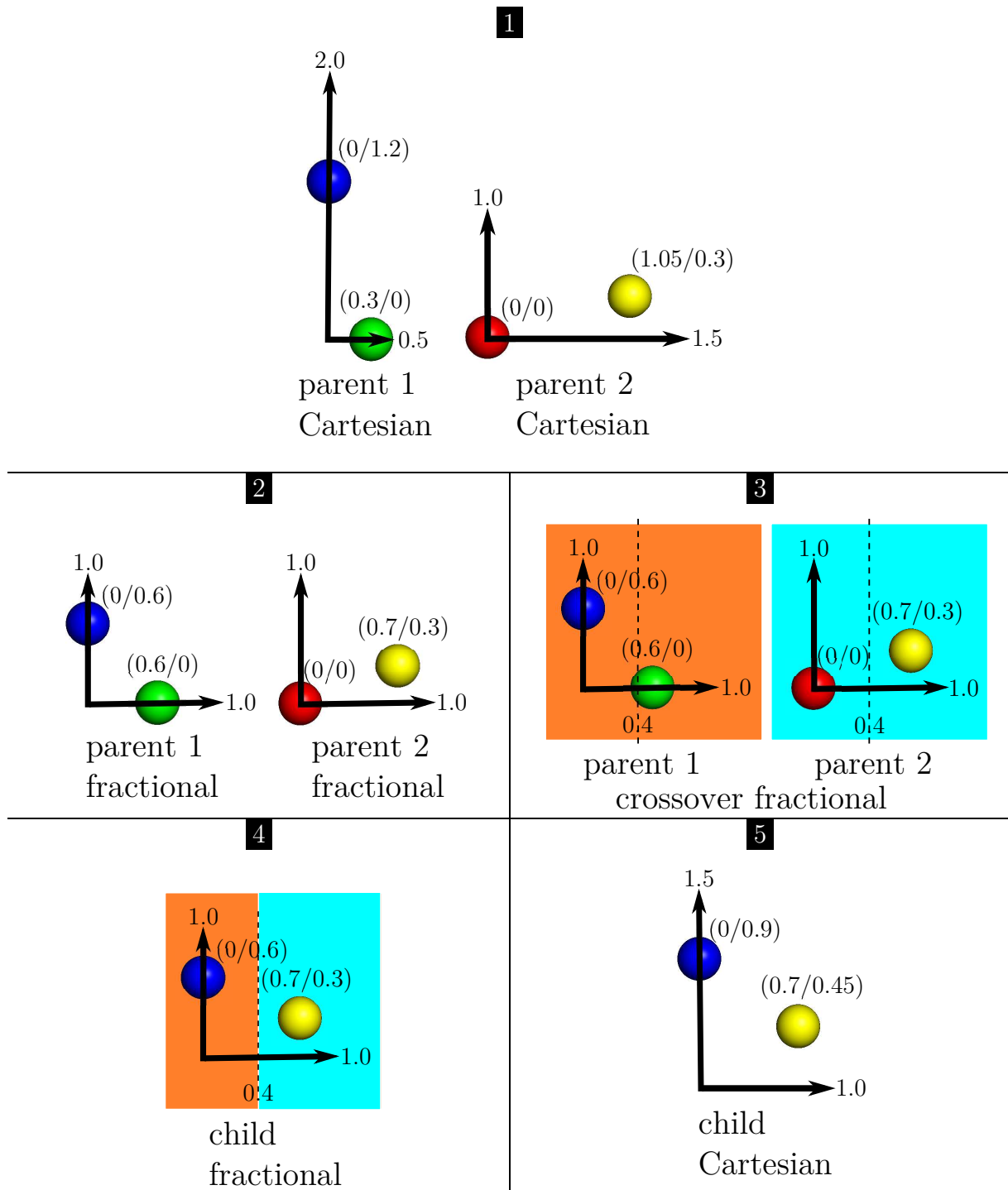
Figure 3.4.: Real space crossover. Panel ▮1▮ : Primitive cells of two parent individuals selected for mating, in Cartesian coordinates. Panel ▮2▮ : The same primitive cells, in fractional coordinates. Panel ▮3▮ : The crossover operation is performed in fractional coordinates - in this particular case, the cutting plane is defined by $x = 0.4$. Panel ▮4▮ : Two fragments are reassembled to form a new primitive cell in fractional coordinates. Panel ▮5▮ : The primitive lattice vectors of the new individual are computed as averages of the parent-lattice vectors in order to obtain the newly created primitive cell in Cartesian coordinates.

Figure 3.5.: Schematic representation of tasks (black) and flow of communication (red) in a parallel, asynchronous EA. For simplicity, only one worker process is visualized. In a typical implementation, the master process communicates with a large number (in our calculations around 30) of worker processes.

3.3. Finite Temperature

In the regime of self-assembly, interaction energies are significantly higher than the thermal energy $k_B T$ [98]. Thus, the knowledge of the zero-temperature equilibrium configurations of a self-assembling system (*i.e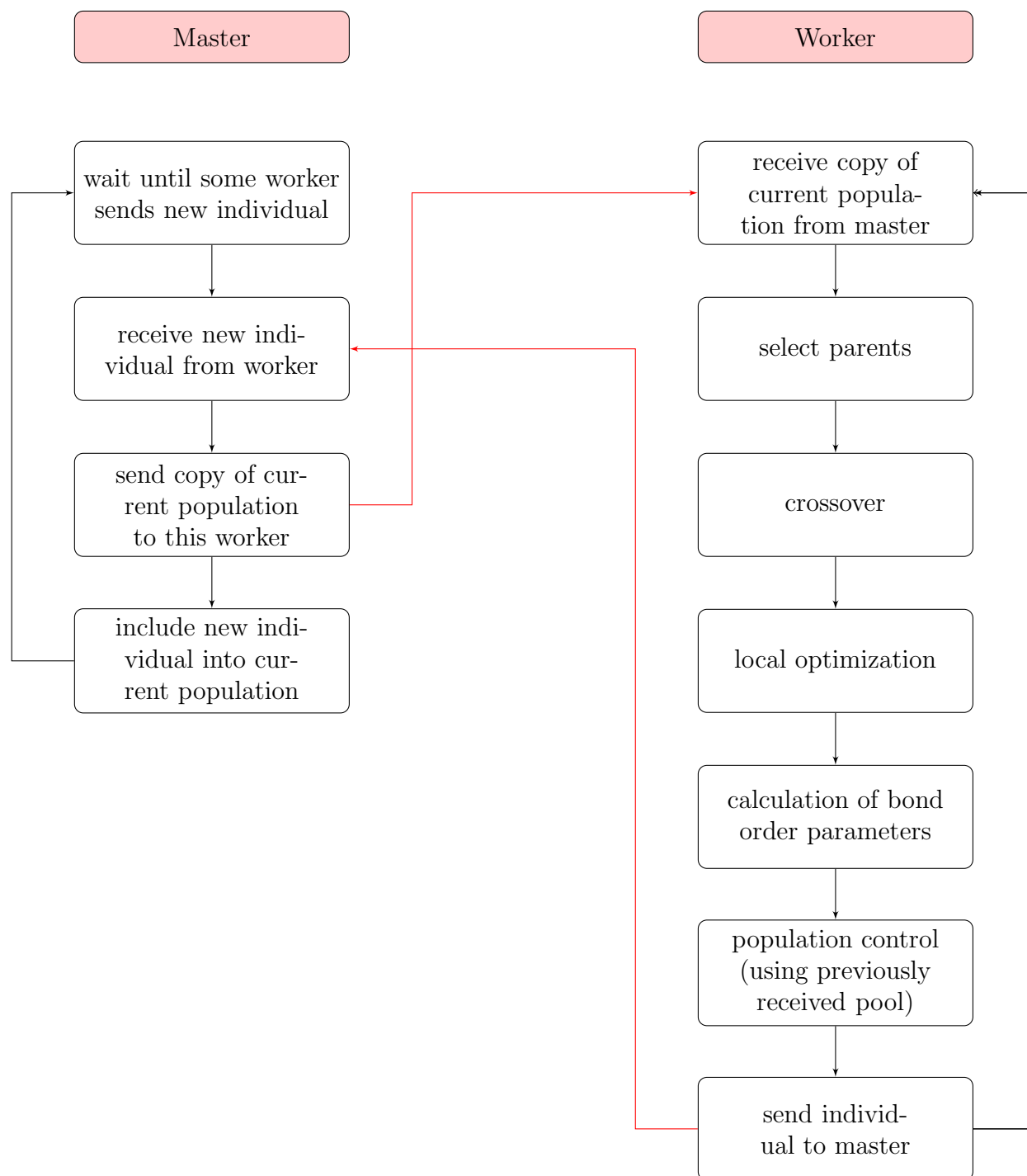.*, its likely target structures) is an important ingredient for understanding its characteristics. However, entropic effects, connected to the vibrational, and – in case of anisotropic interactions – rotational motions of particles about their equilibrium positions and orientations, can have an influence on the thermodynamic stability of self-assembling structures at finite temperature and have to be taken into account. Several methodologies for calculating free energies of ordered structures are available in the literature (*e.g.*, Refs. [69, 99–101]). For our purposes, each of these methods has specific advantages as well as limitations. In the following, we will briefly introduce three techniques that we consider most suitable for dealing with entropic effects within the structure identification framework presented above.

3.3.1. Theoretical Methods

Lattice Dynamics

Within the theory of lattice dynamics [99, 102, 103], thermodynamic properties of crystal structures are calculated by expressing all particle movements within a crystalline structure as superpositions of harmonic oscillations.

The scheme is based on the assumption that the fluctuating displacement $\mathbf{u}_i$ of particle i from its average position is small compared to the average distance $\mathbf{r}_0$ from a neighboring particle j. Then, a Taylor expansion of the pair interaction potential $V(\mathbf{r} = \mathbf{r}_0 - \mathbf{u}_i + \mathbf{u}_j)$ around the $\mathbf{r}_0$ can be truncated after the quadratic term. This is known as the harmonic approximation:

$$
\begin{aligned}
V(\mathbf{r}) = & V(\mathbf{r}_0) + \left.\frac{\partial V}{\partial \mathbf{r}}\right|_{\mathbf{r}=\mathbf{r}_0} \mathbf{u}_i + \left.\frac{\partial V}{\partial \mathbf{r}}\right|_{\mathbf{r}=\mathbf{r}_0} \mathbf{u}_j + \\
& + \left.\frac{\partial^2 V}{\partial \mathbf{r}\partial \mathbf{r}}\right|_{\mathbf{r}=\mathbf{r}_0} \mathbf{u}_i\mathbf{u}_i + 2\left.\frac{\partial^2 V}{\partial \mathbf{r}\partial \mathbf{r}}\right|_{\mathbf{r}=\mathbf{r}_0} \mathbf{u}_i\mathbf{u}_j + \left.\frac{\partial^2 V}{\partial \mathbf{r}\partial \mathbf{r}}\right|_{\mathbf{r}=\mathbf{r}_0} \mathbf{u}_j\mathbf{u}_j + \mathcal{O}(\mathbf{u}^3) \quad .
\end{aligned}
\tag{3.73}
$$

In the formalism, the energy of the whole system is written as a superposition of truncated Taylor expansions in a similar way. Since only configurations, which correspond to local minima on the energy landscape (*i.e.*, $\partial V/\partial \mathbf{r}|_{\mathbf{r}=\mathbf{r}_0} = \mathbf{0}$), are taken into account in this analysis, the linear terms in the expansion vanish per definition. In a bulk crystal, the equations of motion for the displacements $\mathbf{u}_i$ can conveniently be solved using a plane wave ansatz, after performing a transform to Fourier space with wave vectors $\mathbf{q}$ [102]. Thus, particle movements can be described as superpositions of vibrational normal modes with wave vector $\mathbf{q}$ and frequency $\omega(\mathbf{q})$. These normal modes (or phonons) are treated as pseudoparticles within a

classical grand canonical ensemble, with an analytically computable partition function. The vibrational contribution to the entropy can thus be calculated by solving an eigenvalue problem if the second derivatives of the potential with respect to the particle displacements are available (for details, see App. D and [104]).

As outlined in [104], it is also possible to compute derivatives of the (Gibbs) free energy with respect to the structural parameters within lattice dynamics. Thus, local structural optimization, as described for $T = 0$ in the previous sections, is also feasible at finite T within this formalism. This is known as the quasi-harmonic approximation (*i.e.*, the free energy of a structure is calculated within the harmonic approximation, but is treated as a function of the structural parameters [104]). However, upon implementing a lattice dynamics based global optimization scheme, we were confronted with major difficulties, arising from high computational costs, especially when treating anisotropic particles [105], as well as discontinuities in the second derivatives of many patchy particle potentials (such as the Kern-Frenkel or the Doye potential). Thus, we consider this approach in principle useful, but unsuitable for usage with the Doye potential of patchy particles (*cf.* Sec. 2.2.2), and discarded it in favor of a numerical approach described below.

Additional care has to be taken when using lattice dynamics on colloidal systems, as some differences from the more common usage within atomic crystals apply [76]. The influence of the solvent has to be taken into account, introducing (i) friction and thus damping of the vibrational motion of the colloidal particles, as well as (ii) hydrodynamic forces.

Classical Density Functional Theory

In classical density functional theory [100, 106], the Helmholtz free energy of a system is expressed as a functional $F[\rho(\mathbf{r})]$ of the one-particle density $\rho(\mathbf{r})$. In the grand canonical ensemble with the chemical potential μ and vanishing external forces, the thermodynamic grand potential

$$\Omega[\rho] = F[\rho] - \int d\mathbf{r}\mu\rho(\mathbf{r}) \tag{3.74}$$

is minimized by the equilibrium one-particle density $\rho_0(\mathbf{r})$. Since the explicit form of $F[\rho]$ is usually unknown, approximations have to be employed. As outlined in [106], the thermodynamic properties of structures identified by optimization algorithms can be evaluated *via* classical density functional theory for a variety of systems (*i.e.*, if a suitable approximation for $F[\rho]$ is available). To this end, the solid candidate structures are treated as inhomogeneous liquids by expressing $\rho(\mathbf{r})$ as a superposition of Gaussian distribution functions centered at the respective lattice positions. This method could be suitable for an *a posteriori* evaluation of free energies of structures obtained by $T = 0$ optimization methods.

3.3.2. Numerical Method - Frenkel-Ladd Approach

In a conceptually different approach based on Monte Carlo simulations, free energies are calculated by Hamiltonian integration from a reference system with an analytically computable free energy value. For systems with isotropic interactions, one of the most successful implementations of this concept is the Frenkel-Ladd method, which is described in detail in Refs. [69, 107]. The Einstein crystal, where particles do not interact with each other, but are coupled to their positions in the according crystal lattice by harmonic spring potentials, is used as a reference system. For each particle $i = 1, \ldots, N$, with current position $\mathbf{r}_i$, the energy contribution only depends on the distance from its equilibrium position $\mathbf{r}_i^0$:

$$U_{\mathrm{EC}} = \sum_{i=1}^{N} U_{\mathrm{harmonic}}(\mathbf{r}_i) = \sum_{i=1}^{N} \alpha_i (\mathbf{r}_i - \mathbf{r}_i^0)^2. \qquad (3.75)$$

With the switching parameter λ, a Hamiltonian

$$H(\lambda) = \lambda H_0 + (1 - \lambda) U_{\mathrm{EC}} \qquad (3.76)$$

that continuously varies between the original, interacting system H_0 and the reference system can be constructed (the explicit dependence on the coordinates $\mathbf{r_i}$ are suppressed here). With

$$\frac{\partial F}{\partial \lambda} = -\frac{1}{\beta} \frac{\partial}{\partial \lambda} \left\{ \ln \int \cdots \int \exp\left[-\beta H(\lambda)\right] d\mathbf{q}^N \right\} = \left\langle \frac{\partial H(\lambda)}{\partial \lambda} \right\rangle_\lambda, \qquad (3.77)$$

the Helmholtz free energy F of the interacting system can now be calculated numerically as

$$F = F(\lambda = 0) + \int_{\lambda=0}^{\lambda=1} \left\langle \frac{\partial H(\lambda)}{\partial \lambda} \right\rangle_\lambda, \qquad (3.78)$$

since the free energy of the reference system $F(\lambda = 0)$ is known analytically and the ensemble average $\langle \partial H(\lambda)/\partial \lambda \rangle_\lambda$ can be evaluated at each λ by performing a Monte Carlo simulation.

An extension of this method to systems with anisotropic interactions is described in Ref. [108]. In the reference system, the particles' rotational displacements are coupled to their equilibrium orientations by additional spring potentials, whose explicit form depends on the symmetry of the particles.

Calculating free energies by a Frenkel-Ladd based method is usually very accurate, but computationally rather expensive. Performing such a calculation and especially taking numerical derivatives of the free energy at each instance of a cost function evaluation within one of the optimization algorithms described in Sec. 3.2 is completely out of scope (while it seems feasible *via* lattice dynamics for certain systems). Nevertheless, the methods can be combined *a posteriori* in a two-step approach [6]: first, the global minimum and low-lying local minima of the enthalpy landscape are identified by the optimization method and taken into

account as candidate finite temperature equilibrium structures; subsequently, free energy calculations are performed for these proposed configurations in order to obtain the finite temperature phase diagram.

4. Results

4.1. Patchy Particle Systems in Two Dimensions

In this section, we investigate possible self-assembly scenarios of two dimensional patchy particle systems with varying geometry by identifying global enthalpy minima at different pressure values and zero temperature. Additionally, we briefly explore binary mixtures of particles with different patch numbers as well as systems with repulsive interactions between patches. Finally, we thoroughly study the possibility of realizing Platonic and Archimedean tilings in a bottom-up self-assembly strategy using patchy particle systems. In all of these investigation, we employ the Doye model of patchy particles (*cf.* Sec. 2.2.2) with the parameters $r_{\mathrm{cut}} = 1.9\sigma$ and $w = 2\pi \cdot 0.05$.

4.1.1. Ordered Equilibrium Structures for Varying Patch Decorations

Three Patch Systems
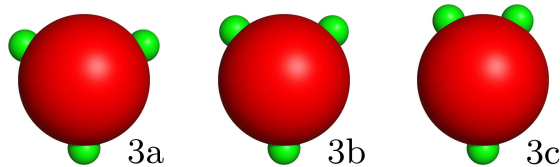
Figure 4.1.: Three-patch particles with three different decorations as they are investigated in the present study: left panel – type 3a, regular patch distribution, *i.e.*, with a set of inter-patch angles of $\{120^{\mathrm{o}}, 120^{\mathrm{o}}, 120^{\mathrm{o}}\}$, center panel – type 3b, with a set of inter-patch angles of $\{90^{\mathrm{o}}, 135^{\mathrm{o}}, 135^{\mathrm{o}}\}$, and right panel – type 3c, with a set of inter-patch angles of $\{60^{\mathrm{o}}, 150^{\mathrm{o}}, 150^{\mathrm{o}}\}$. The patch, which encloses the same angle with both other patches will be called "pole patch" in the following.

We consider particles carrying three patches in three different geometries, as shown in Fig. 4.1. For particle type 3a, with patches located on the vertices of an equilateral triangle, for which the colloidal particle represents the circumscribed circle, we identified two different ground state structures over the pressure range that we investigated (*cf.* Fig. 4.2, top panel). For low pressure values, a honeycomb lattice with full patch saturation (*i.e.*, $U^\star = 1.50$) and rather low area number density ($\eta \leq 0.50$) exhibits the lowest enthalpy value. On increasing pressure to $P^\star > 0.78$, an equilateral triangular (*i.e.*, hexagonal close

packed) lattice, with only two bonded patches per particle becomes dominant. With further increasing pressure, the lattice is compressed, ultimately leading to quasi close packing of the colloidal particles ($U^\star = 0.83$, $\eta = 0.87$ at $P^\star = 10.00$ – the highest possible packing fraction of hard disks is given by $\eta = \pi/\sqrt{12} \approx 0.907$ [109]).

For particle type 3b (the patches are located on the circumflex of the particle, with angles $\{90°, 135°, 135°\}$), the low-pressure equilibrium structure has the same bonding pattern as the honeycomb structure formed by 3a, but the cells are more elongated due to the changed geometry. Here, we observe two intermediate structures before reaching a close packed high pressure configuration: For pressure values between $P^\star = 0.51$ and $P^\star = 2.78$ a structure based on four-particle arrangements that are bound to each other *via* the patches separated by small angles and thereby forming tetragons. Two of the pole patches, located on diagonally opposite vertices of the tetragon, directly bond with neighboring tetragons, while the remaining two patches, again on opposite vertices, are interacting *via* longer-distance bonds. Thereby, this configuration achieves a binding energy of $U^\star = -1.29$, while increasing η by a factor of 1.36 compared to the fully bonded low-pressure lattice. On further increasing pressure, a structure based on zig-zag lanes of particles represents the ground state. Here, all the pole patches are fully bonded, while half of the small-angle patches engage in long-distance bonds (with interparticle distance $r = 1.67\sigma$ and a binding energy of 17.5 percent of a fully optimized bond). This leads to values of $U^\star = -1.05$ and η is increased by a further factor of 1.06. For pressure values above $P^\star = 5.13$, the bonds connecting pole patches are broken and the zig-zag pattern is rearranged, so that a (distorted) triangular lattice with almost close packing ($U^\star = -0.53$, $\eta = 0.88$ at $P^\star = 10.00$) is formed (*cf.* Fig. 4.3).

The particles of type 3c (with patches located on a triangle with angles $\{60°, 150°, 150°\}$) form only two different ground state structures again (*cf.* Fig. 4.2, bottom panel): For low pressure we observe an even more elongated, fully bonded honeycomb lattice. Due to the geometry of the patch locations, this lattice already has a considerably high area number density of $\eta = 0.67$. For pressure values above $P^\star = 4.25$, the minimum enthalpy configuration is of almost close packed triangular type, with bonded low-angle patches, while all the north-pole patches are unbonded; the particles themselves form close-packed trimers of equilateral triangles in this configuration ($U^\star = -0.83$, $\eta = 0.87$ at $P^\star = 10.00$).

Four Patch Systems

For systems containing particles with four patches, we have also considered three distinct types of patch decorations, shown in Fig. 4.4. For any of these systems, we observe at most two different minimum enthalpy configurations over the pressure range that we investigated. The fully bonded (*i.e.*, $U^\star = -2.00$) low-pressure configuration has the same, obvious bonding pattern for all three particle types, leading to square or rhombic lattices, depending on the patch decoration. The high pressure configurations on the other hand show some differences: The symmetric particles (4a) form a triangular lattice with two full and two
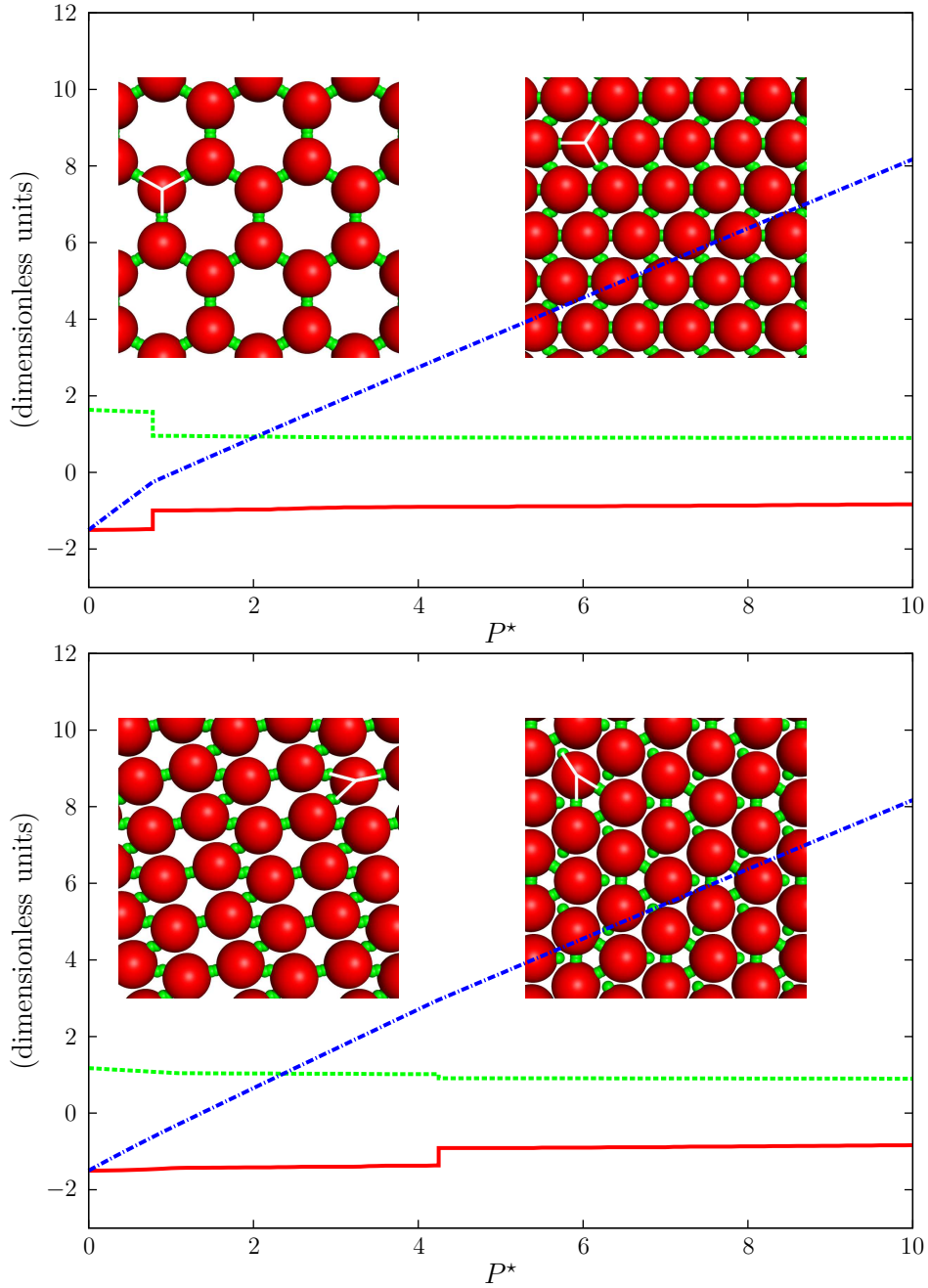
Figure 4.2.: Gibbs free energy [$G^\star = U^\star + P^\star/(\eta\sigma_0^2)$, dash-dotted blue line], lattice sum ($U^\star$, solid red line) and area [$1/(\eta\sigma_0^2)$, dashed green line] of the energetically most favorable structures formed by a system of patchy particles of type 3a (top) and 3c (bottom) as functions of pressure. Insets: low pressure configurations (regular/elongated hexagons, left) and high pressure configurations (triangular lattice/triangular packing of trimers, right).

Figure 4.3.: Top: Gibbs free energy, lattice sum and area of the energetically most favorable structures formed by a system of patchy particles of type 3b as functions of pressure. Insets: low pressure configuration (elongated hexagons, left) and high pressure configuration (triangular lattice, right). Bottom: intermediate pressure configurations, with increasing pressure from left to right. Line styles as in Fig. 4.2.
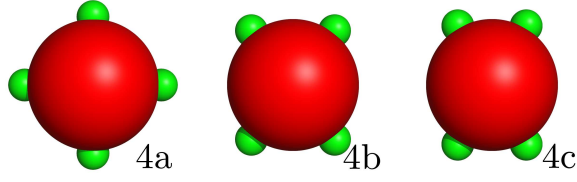
Figure 4.4.: Four-patch particles with three different decorations as they are investigated in the present study: left panel – type 4a, regular patch distribution, *i.e.*, with a set of inter-patch angles of $\{90^{\circ}, 90^{\circ}, 90^{\circ}, 90^{\circ}\}$, center panel – type 4b, with a set of inter-patch angles of $\{75^{\circ}, 105^{\circ}, 75^{\circ}, 105^{\circ}\}$, and right panel – type 4c, with a set of inter-patch angles of $\{60^{\circ}, 120^{\circ}, 60^{\circ}, 120^{\circ}\}$.

long-distance bonds per particle for pressure values above $P^{\star} = 2.84$ ($U^{\star} = -1.07$, $\eta = 0.87$ at $P^{\star} = 10.0$). Particles of type 4b form a configuration where each particle has two fully bonded and four close-packed neighbors for $P^{\star} \geq 4.33$ ($U^{\star} = -0.93$, $\eta = 0.87$ at $P^{\star} = 10.0$). Finally, particles of type 4c arrange in the same pattern over the whole investigated pressure range, with the lattice being gradually distorted and the bonds being slightly bent in order to achieve better packing at higher pressure ($U^{\star} = -1.64$, $\eta = 0.84$ at $P^{\star} = 10.0$).

Five Patch Systems

The case of five patches is expected to show interesting properties, since polygons with five-fold symmetry cannot fully cover a plane. Here we focus on a symmetrical patch distribution. For the standard value of the patch width (*i.e.*, patches with $w = 0.05$), we reproduce the results presented in Ref. [37]: The low pressure configuration is represented by the so-called σ-phase (in reference to the three-dimensional Frank-Kasper phases [110]). In this configuration, each patch is bonded, but because of the incompatibility between the five-fold symmetry and covering of a two-dimensional plane, four out of five bonds cannot be perfectly aligned and each of them has an energy $U^{\star}_{\text{Bond}}$ of only 60 percent of the optimal value. Increasing the pressure to values $P^{\star} > 4.30$, the minimum enthalpy structure is a variation of the σ-phase, as its central four particle-subunits are retained; however they do not bond to each other anymore, but arrange instead in a packed configuration, thereby reducing the binding energy from $U^{\star} = -1.45$ to $U^{\star} = -0.83$ and increasing the packing fraction by a factor of 1.16. Finally, the high pressure configuration which is stable for $P^{\star} > 9.23$ consists of trimers, which arrange in a close-packed way with $U^{\star} = -0.56$ and further increasing the packing fraction by a factor of 1.02.

On decreasing the patch width to $w = 0.03$, the low pressure configuration we find has a slightly lower enthalpy than the one presented in Ref. [37]. The difference between these two structures is rather subtle: both consist of closed interconnected five-particle loops, where each particle has three perfectly bonded patches and two completely unbonded ones. For the configuration shown in Ref. [37], these loops arrange parallel to each other (the so-called H-phase, again in reference to the Frank-Kasper phases [110]), while for the lattice predicted

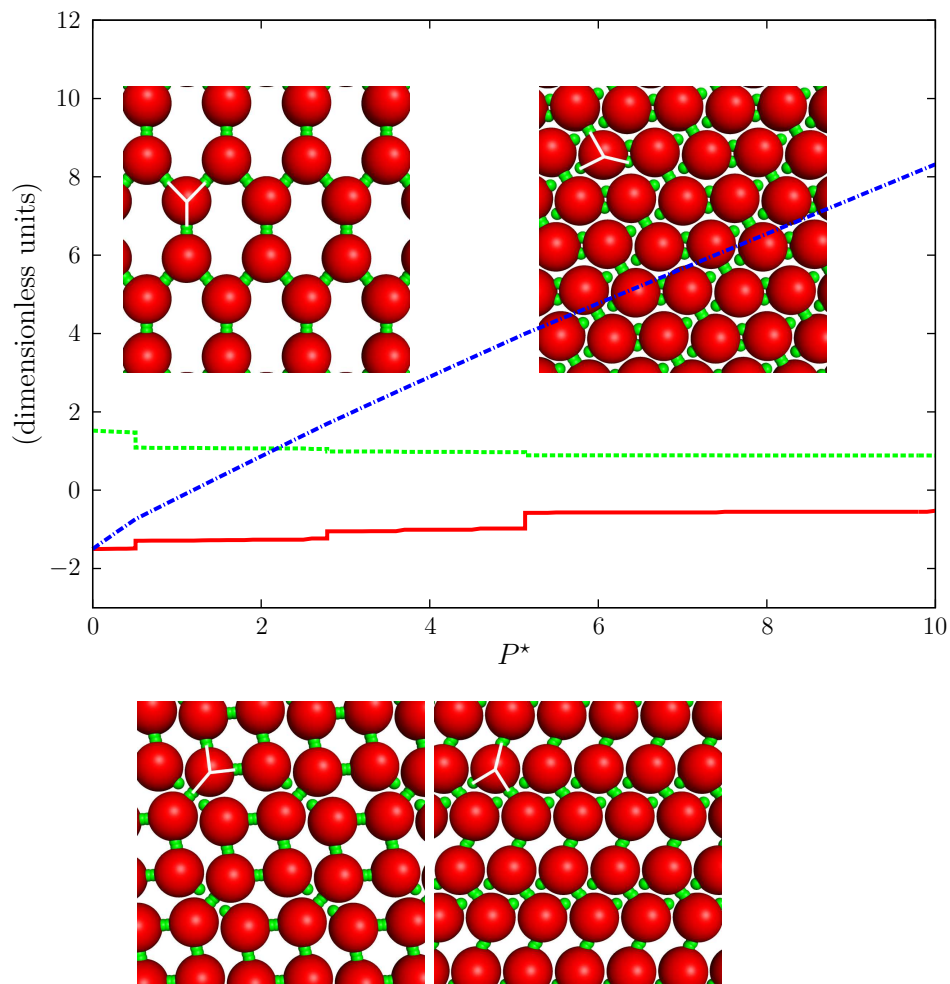Figure 4.5.: Gibbs free energy, lattice sum and area of the energetically most favorable structures formed by a system of patchy particles of type 4a (top) and 4b (bottom) as functions of pressure. Insets: low pressure configurations (square/rhombic lattice, left) and high pressure configurations (triangular lattices, right). Line styles as in Fig. 4.2.
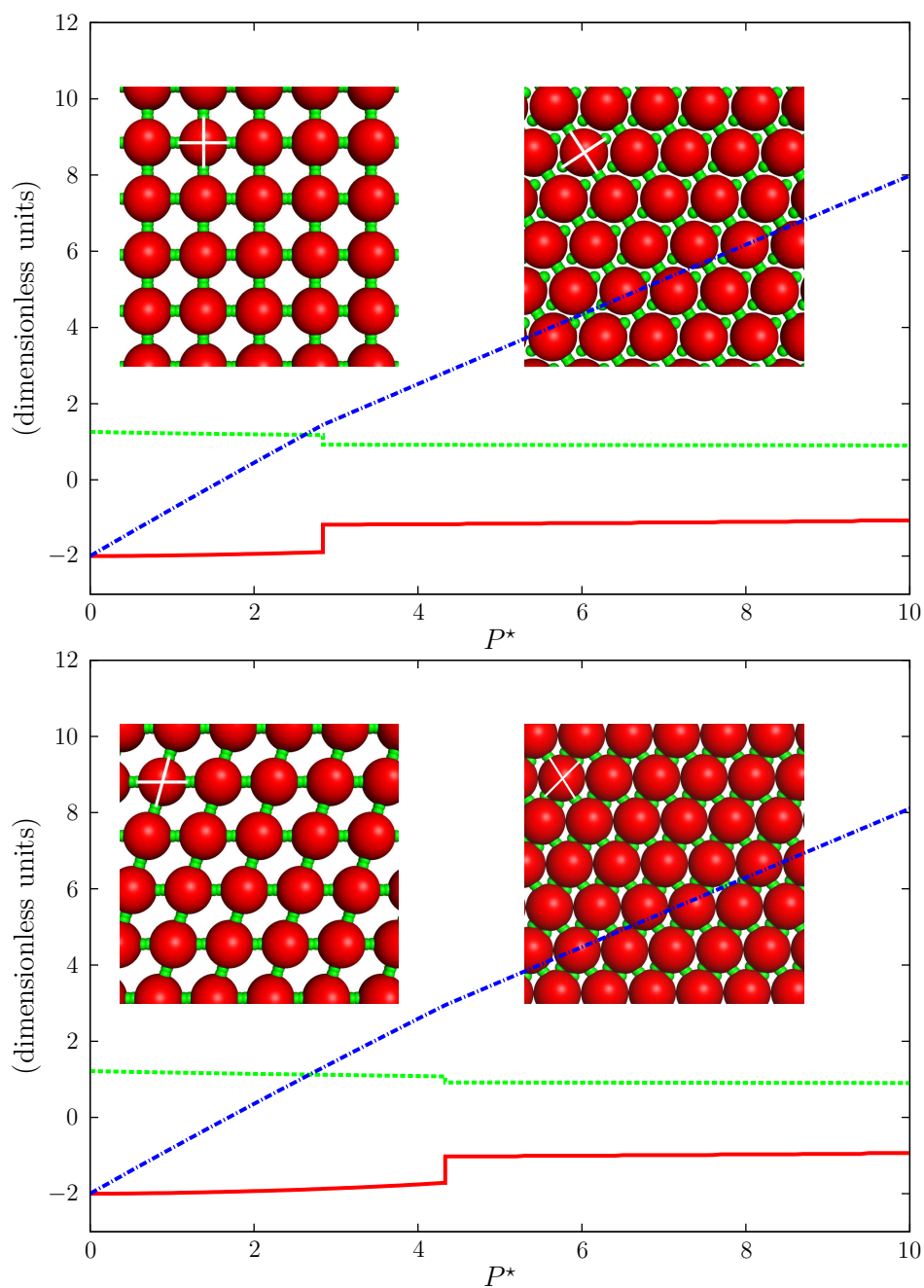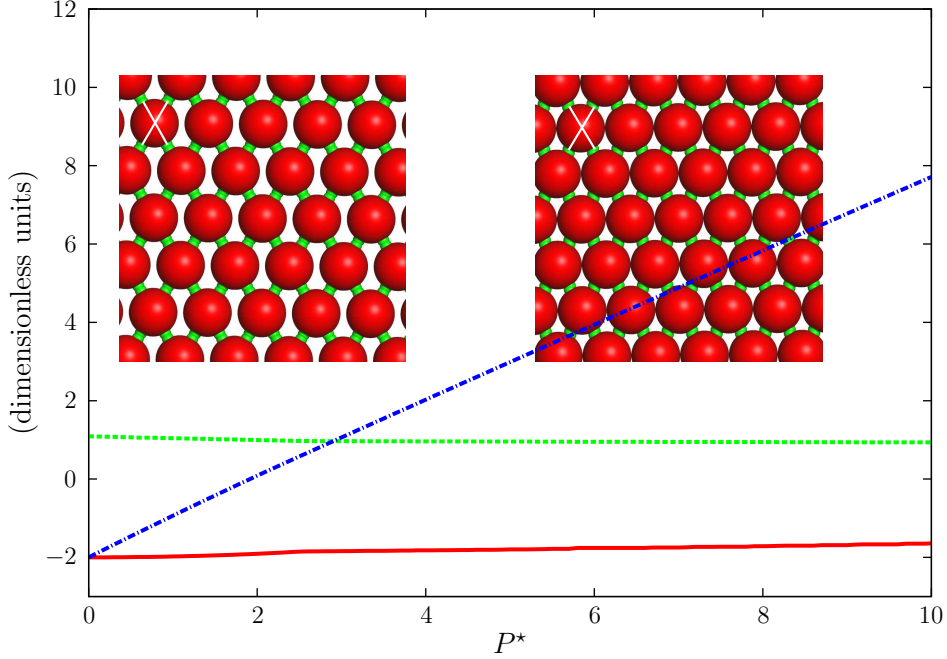
Figure 4.6.: Gibbs free energy, lattice sum and area of the energetically most favorable structures formed by a system of patchy particles of type 4c as functions of pressure. Insets: low pressure configuration (elongated hexagons, left) and high pressure configuration with the same bonding pattern (triangular, right). Line styles as in Fig. 4.2.

by our method, the loops are tilted against each other, leading to a slightly higher packing fraction ($\eta = 0.6177$ compared to $\eta = 0.6175$). For $P^\star > 1.64$, the equilibrium structure we identified consists of zig-zag lanes of particles, with two full bonds and two additional long-distance bonds per particle. The long-distance bonds have a binding energy of seven percent of the optimal value and could be seen as an artifact of the model, since their connection line crosses a colloidal particle (see Fig. 4.8, bottom). The high pressure configuration ($P^\star > 4.53$) is again triangular and almost close packed ($\eta = 0.89$ at $P^\star = 10.00$) and exhibits one full and one (more realistic) long-distance bond per particle.

Binary Mixtures

Additionally, we have considered an equimolar binary mixture of particles, where the different species are decorated with two and three regularly distributed patches, respectively. For this system, we identify three different minimum enthalpy configuration over the investigated pressure range: for very low pressure, we find a fully bonded lattice, which can be interpreted as hexagons that are elongated by incorporating the two-patch particles. For slightly higher pressure values, ($P^\star > 0.18$), an intermediate configuration, where two bonds per unit cell are given up in order to increase the packing fraction by a factor of 1.61. Here, the three-patch particles still arrange in fully bonded hexagons, while the two-patch particles form

Figure 4.7.: Top: Gibbs free energy, lattice sum and area of the energetically most favorable structures formed by a system of patchy particles with five regularly distributed patches of width $w = 0.05$ as functions of pressure. Insets: low pressure configuration (σ phase, left) and high pressure configuration (trimers, right). Bottom: intermediate pressure configuration. Line styles as in Fig. 4.2.
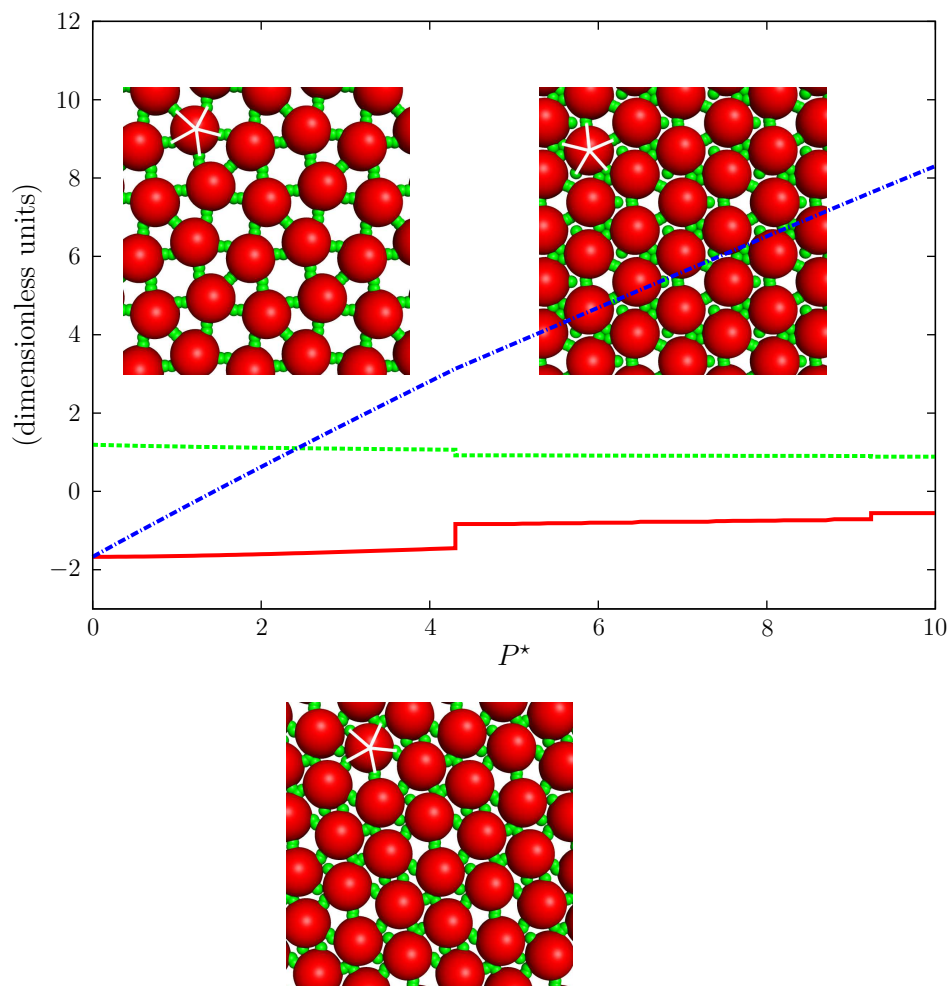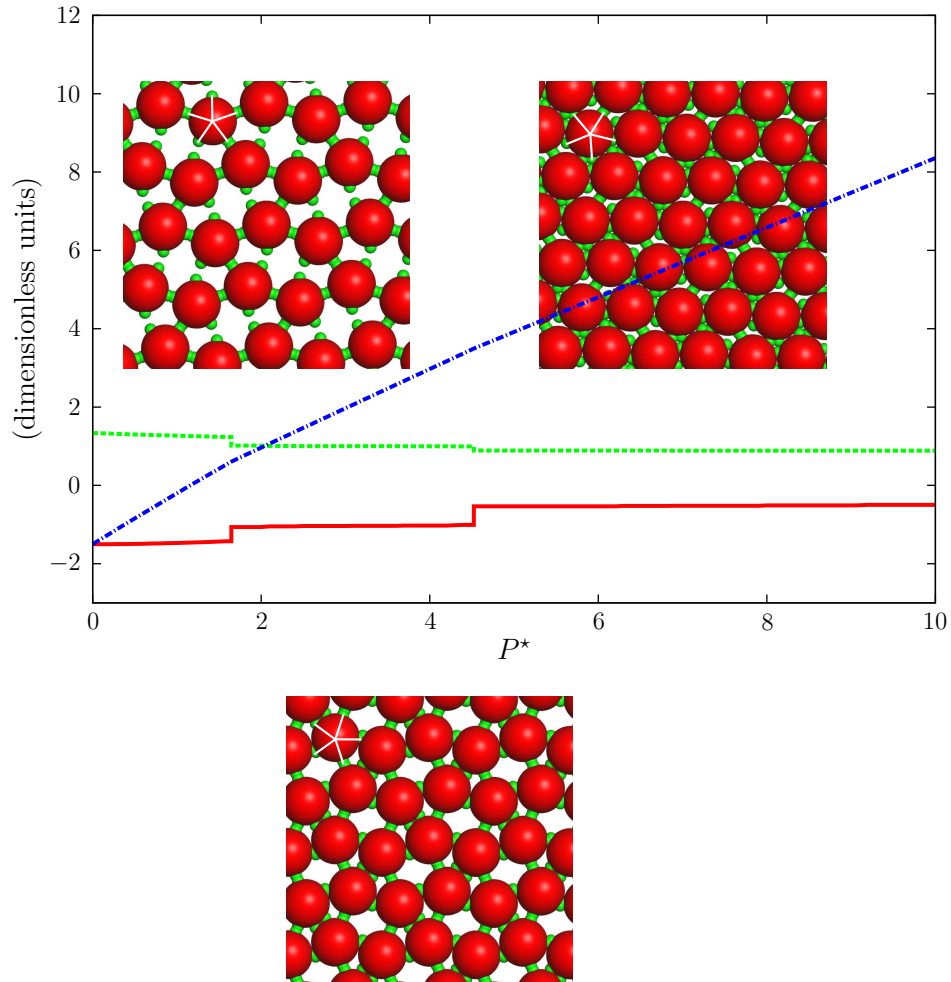
Figure 4.8.: Top: Gibbs free energy, lattice sum and area of the energetically most favorable structures formed by a system of patchy particles with five regularly distributed patches of width $w = 0.03$ as functions of pressure. Insets: low pressure configuration (left) and high pressure configuration (right). Bottom: intermediate pressure configuration. Line styles as in Fig. 4.2.

dimers, located in between parallel lanes of the hexagons. Interestingly, no single bond is formed between two neighboring "hexagons + dimers"-lanes (see Fig. 4.9) and therefore, they can freely move against each other (note the slight horizontal shift in the figure). The high pressure configuration, which is already formed at $P^\star > 0.53$ in this system, is an almost close-packed triangular lattice, where each particle, either having two or three patches, forms two bonds.

Systems with Repulsive Interactions

For the case of additional patch-patch repulsion, we restrict ourselves to a system, which seems particularly interesting: our particles are decorated by five patches (*cf.* Fig. 2.4) where two of them are of type A, while the other three are of type B. In this model, like patches attract each other, while unlike patches repel each other. The imparity in patch numbers of different type induces considerably more rich self-assembly scenarios than those encountered in systems where the numbers of A and B patches are equal.

By varying the pressure we identified three different MECs, depicted in Fig. 4.10. At low pressure, we observe a tiling of the two-dimensional space by triangular shaped, equilateral units that consist of six particles, with all tiles pointing in the same direction. Note that all A patches are saturated by a B patch, so that only one B patch per particle remains unbonded, which points towards the center of the triangular unit. As the pressure is increased, the emerging minimum enthalpy configuration can be divided into elongated, closed substructures, composed of six particles which cover the two-dimensional space in alternating orientations (see Fig. 4.10, bottom left panel). Still, almost all $A - B$ bonds are saturated, but the increased pressure forces the (mutually repulsive) B patches to approach each other. Finally, at the highest pressure, we observe hexagonal particle arrangements. At first sight, the system seems to be homogeneous. However, a substructure characterized by the orientation of the particles can easily be observed. The system forms double lanes: using the terminology introduced for the bonds in Fig. 4.10 (bottom right), adjacent pairs of lanes are stabilized *via* the strong B1 bonds, while inside each pair of lanes we observe B2 and B3 bonds, both of them being energetically less favorable. In a closer analysis of the energies of these bonds one recovers the following U/ϵ-values: $U_{B1}/\epsilon = -0.75$, $U_{B2}/\epsilon = -0.13$, and $U_{B3}/\epsilon = -0.06$. The strength of the B1 bond can be easily traced back to the small angles involved, while the weakness of the B3 bond is due to the large distances between the patches.
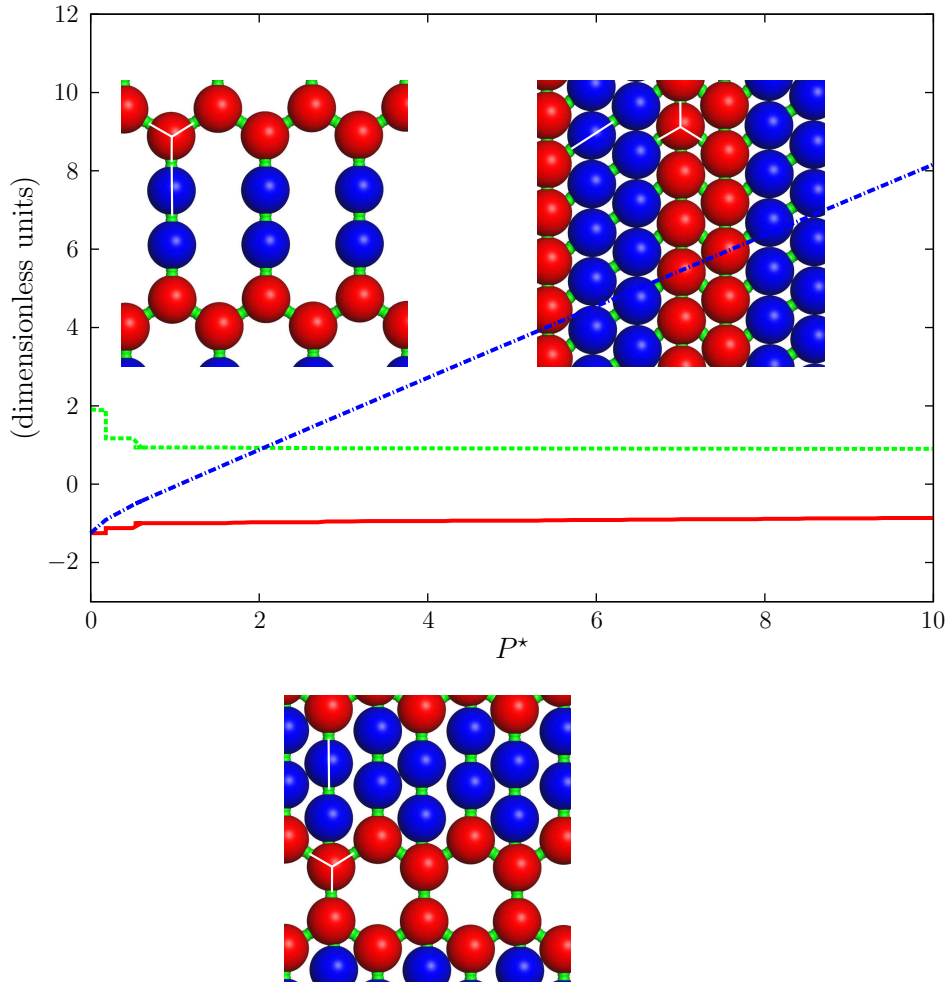
Figure 4.9.: Top: Gibbs free energy, lattice sum and area of the energetically most favorable structures as functions of pressure. The system is a binary mixture of patchy particles, where the particle species are decorated with two and three regularly distributed patches, respectively. Insets: low pressure configuration (elongated hexagons, left) and high pressure configuration (triangular lattice, right). Bottom: intermediate pressure configuration. Line styles as in Fig. 4.2.
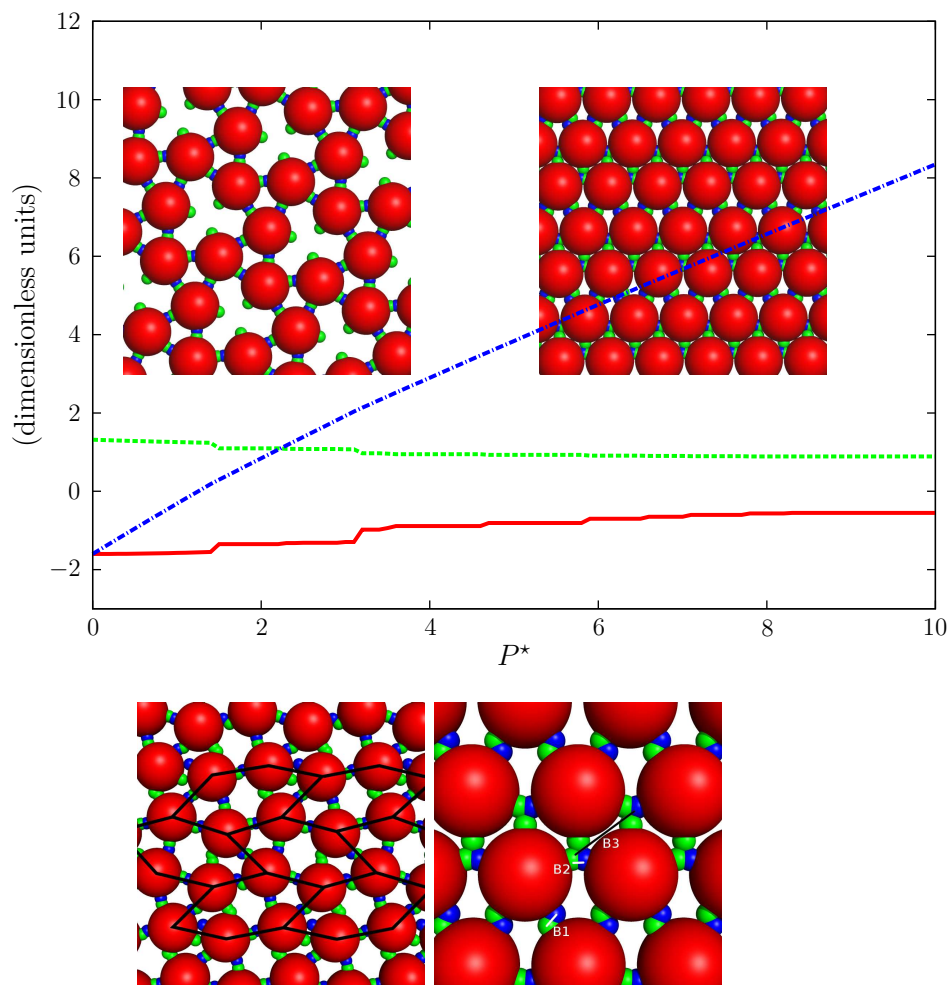
Figure 4.10.: Top: Gibbs free energy, lattice sum and area of the energetically most favorable structures formed by a system of patchy particles with attractive and repulsive patch interactions as functions of pressure. Differently colored patches are mutually attractive, while patches in the same color repel each other. Insets: low pressure configuration (left) and high pressure configuration (double layers/distorted triangular lattice, right). Bottom: intermediate pressure configuration (left, with tiling as a guide to the eye) and high pressure configuration, highlighting the bonds that are discussed in the text (right). Line styles as in Fig. 4.2.

4.1.2. Platonic and Archimedean Tilings Realized by Patchy Particles

Tesselations (or tilings) of a two-dimensional plane, have been under study in science and in use in art and construction since antiquity [111]. In general, a tiling covers a plane by repeating geometrical patterns (*i.e.*, tiles), without any overlaps or gaps between the individual tiles.

Tesselations with the highest degree of symmetry are the so-called Platonic, or regular, tilings. Each of them contains only one type of regular polygons of equal edge-length. Such tilings can be realized using either equilateral triangles (six polygons meet at each vertex, denoted as 3^6), squares (four at each vertex, 4^4) or regular hexagons (three at each vertex 6^3). If the restriction to use only one type of polygons is relaxed to requiring only one type of vertex, the Archimedean, or semiregular, tilings are obtained. These tilings contain five different types of regular polygons of equal edge-length (namely equilateral triangles, squares, hexagons, octagons and dodecagons). Besides the three regular tilings, there are eight different realizations of this type of tesselation, which can be characterized by their vertex type [*i.e.*, a listing of the polygons meeting (in the same sequence) at each vertex]. These tilings and their vertex descriptions are listed in Tables 4.1 and 4.2 and depicted in Fig. 4.11. In general, a given vertex of an Archimedean tiling can be mapped onto any other vertex of the same tiling by a proper rotation; an exception to this rule is the truncated trihexagonal tiling, where a reflection and a rotation are needed to achieve this mapping (*i.e.*, the tiling consist of chiral vertices that appear as two distinct enantiomers).

The regular and semi-regular tilings are ideal candidates for bottom-up self-assembly strategies using patchy particles: since all vertices are of the same type and the distances between neighboring vertices are the same, it is straightforward to make an appropriate guess for decorating particles with patches in such a way that they might self-assemble into one of the given target structures.

There are two options for decorating a tiling with patchy particles; the particles can either be placed on the vertices or on the centers of the inscribed circles of the polygons. In the following, these options will be called vertex representation and center representations, respectively. The former has the advantage that only one species of patchy particles (concerning particle size as well as patch decoration) has to be introduced for each Archimedean tiling to be constructed (with the exception of the truncated trihexagonal tiling, where enatiomeric particles are required), while the center representation requires particles with large size disparity for many tilings. Therefore, systems in the vertex representation are expected to be realize experimentally more easily. However, the vertex representation exhibits large voids for tilings involving polygons with a large number of vertices and therefore the structures representing these tilings have rather high unit cell volumes and might be unstable with respect to more closely packed configuration even at small pressure.

In the following, we present the results of our investigations where we have addressed the

question if suitable patch decorations can lead to the formation of Platonic and Archimedean tilings as equilibrium structures at $T = 0$ and varying pressure.

Vertex Representation

In the vertex representation, the patch decoration is chosen so that bonds are formed along the edges of a tiling when the centers of mass of the patchy particles are located at the vertices. This leads to the system parameters (*i.e.*, required number of particles in the primitive cell of a lattice and patch-angles) presented in Table 4.1.

vertex representation			
tiling	vertices	N	patch-angles [°]
triangular	3^6	1	$\{0, 60, 120, 180, 240, 300\}$
square	4^4	1	$\{0, 90, 180, 270\}$
hexagonal	6^3	2	$\{0, 120, 240\}$
elongated triangular	$3^3.4^2$	2	$\{0, 60, 120, 180, 270\}$
snub square	$3^2.4.3.4$	4	$\{0, 60, 120, 210, 270\}$
snub hexagonal	$3^4.6$	6	$\{0, 60, 120, 180, 240\}$
trihexagonal	$3.6.3.6$	3	$\{0, 60, 180, 240\}$
rhombitrihexagonal	$3.4.6.4$	6	$\{0, 60, 150, 270\}$
truncated square	4.8^2	4	$\{0, 90, 225\}$
truncated hexagonal	3.12^2	6	$\{0, 60, 210\}$
truncated trihexagonal	$4.6.12$	6	$\{0, 90, 240\}$
	$4.12.6$	6	$\{0, 90, 210\}$

Table 4.1.: List of the three Platonic and eight Archimedean tilings (first column) and their vertex specification (second column). In the two other columns parameters are collected that specify patchy particles for the *vertex* representation (see text): N stands for the number of particles required per unit cell (*cf.* Fig. 4.11). The last column specifies the patch positions along the circumference *via* the indicated angles. Note that in the vertex representation all particles have the same size; only for the truncated trihexagonal tiling two particle species of equal size but different chirality in their decoration are required.

In our study, we use our optimization algorithm in order to identify the structure with lowest enthalpy that can be formed by these systems. At $P^\star = 0$, the unit cell area does not contribute to the enthalpy and the tilings represent (one of) the stable structure(s) by construction, as they all minimize the binding energy of the system. We start our investigations at low pressure (*i.e.*, close to zero) and increase $P^\star$ stepwise. For sufficiently high pressure values, close-packed triangular lattices will be stable for all systems, as the packing term is completely dominating the bonding term in the enthalpy.

For the Platonic tesselations, the situation is not very complex and all of the tilings can be realized as equilibrium structures for sufficiently low pressure values: The *triangular*

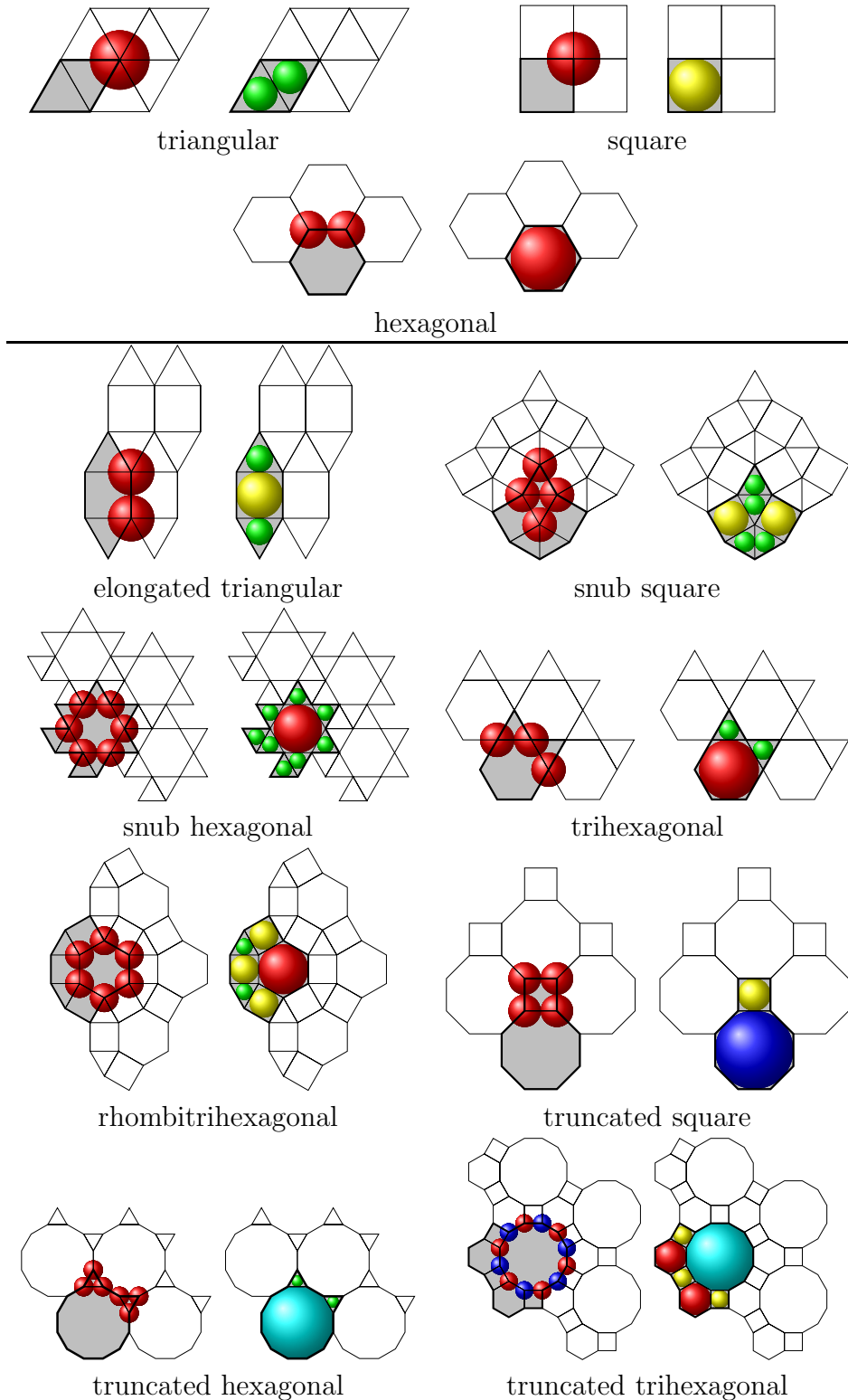Figure 4.11.: Representative sections of the three Platonic and the eight Archimedean tilings (as labeled) – thin lines. The left (right) panels visualize the vertex (center) representations, respectively. The grey-shaded areas, delimited by thick lines represent the respective unit cells. Different particle species (either distinguished *via* their patch decoration or their size) are displayed using different colors.

tiling, realized by particles with six patches already represents a close-packed structure and therefore is stable over the whole pressure range. The *square* tiling, on the other hand, is realized by a non-close packed lattice and is only stable until $P^\star \approx 2.9$. Above this value, a triangular lattice with a higher binding energy is identified as the equilibrium structure. Finally, the *hexagonal* tiling, which is represented by a honeycomb lattice of particles with three patches is only stable up to $P^\star \approx 0.8$ due to its comparatively large unit cell area. For higher pressures, we again encounter a close-packed, triangular lattice as the configuration with minimal enthalpy.

The Archimedean tilings, on the other hand are more difficult to be stabilized for non-vanishing pressure. The *elongated triangular* tiling corresponds to the equilibrium structure of a system with two five-patch particles in the unit cell for $P^\star \lesssim 3.5$. This structure can be viewed as parallel zig-zag lanes, characterized by strong bonding within the lanes (involving four of the five patches); the fifth patch of each particle is used to connect to the neighboring zig-zag lanes. As one passes the threshold value for the pressure, the four-fold bonding is able to resist while the inter-lane bonds are broken. In an effort to decrease the area, the now disconnected neighboring zig-zag lanes are shifted relative to each other (lowering thereby the thermodynamic potential), leading to a structure which closely resembles a triangular configuration, with a small deviation in order to retain bonds (*i.e.*, the interparticle distances of bonded particles are close to the minimum of the Lennard-Jones potential $2^{1/6}\sigma$, while distances between non-bonding neighboring particles are close to σ). This deviation continuously becomes smaller (*i.e.*, the bond lengths are decreased from the energetically optimal value, in order to minimize the area term) with increasing pressure. This configuration closely resembles the high pressure configuration of the system with attractive and repulsive interactions investigated in the previous section (*cf.* Fig. 4.12).

For the *snub square* tiling the pressure dependence of the emerging structures is even more complex. Five patch particles are required with the decoration as specified in Tab. 4.1. Again, the full saturation of all bonds of this tiling combined with a comparatively small area guarantees that the configuration is able to resist up to relatively high pressure values (*i.e.*, $P^\star \approx 6.5$). Only then a more close packed arrangement with approximately half of the minimum binding energy is more favorable with respect to the enthalpy. This configuration resembles the triangular high-pressure arrangement, like the high pressure configuration of the *elongated triangular* system, but has a more complicated bonding scheme, as only half of the particles have one completely unbonded patch and at two locations in the primitive cell, three patches (from three different particles) connect to each other (*cf.* Fig. 4.12, bottom panel).

The remaining six tilings never represent the minimum enthalpy structure of their respective systems in the vertex representation at finite pressure values.

The *snub hexagonal* and the *trihexagonal* systems arrange already at the lowest accessible pressure values in distorted triangular lattices, as these support full bonding while requiring a much smaller unit cell area than the respective tilings. Again, the distortion is caused by

larger distances between bonded nearest neighbors than for non-bonded ones and becomes less evident with increasing pressure (*cf.* Fig. 4.13).

The particles designed for the *rhombitrihexagonal* lattice arrange already at vanishingly small pressure values in a lattice similar to the *snub square* one, which remains stable for pressure values up to $P^\star \approx 5.3$. Note that the particles have one patch less than the particles designed for the snub square lattice, which explains the lower threshold value in pressure. At higher pressure, the system collapses into a triangular-like structure with two direct and two further long-distance bonds per particle (*cf.* Fig. 4.14, top).

Particles designed to self-assemble in a *truncated square* tiling assemble, instead, already at vanishingly small pressure in a distorted hexagonal lattice: again, the full bond saturation combined with a smaller area than the lattice corresponding to the tiling makes this structure more favorable with respect to the enthalpy. The system transforms at a relatively low pressure value ($P^\star \approx 0.5$) into a configuration consisting of square four-particle arrangements. In this configuration, all the patches engage in bonding, even though two of the bonds in each unit cell are long-distance ones. At $P^\star \approx 2.8$ and above, we identified a double-lane structure, where particles arrange in a zig-zag pattern, stabilized by strong internal bonds as the most favorable one; the zig-zag lanes, themselves are connected to their next-nearest neighbors *via* single long-distance bonds: a loss in bond-saturation is compensated by a relatively small unit cell area. Eventually, at $P^\star \approx 5.0$ the system collapses to a distorted triangular structure with one full, one long-distance and one wide-angle bond (*cf.* Fig. 4.15).

Patchy particles designed to form the *truncated hexagonal* tiling form at low pressure a distorted hexagonal lattice, where the distortion is induced by the patch decoration (in this configuration the centers of mass of the particles occupy the same locations as in the *elongated triangular* tiling, but there is a smaller number of bonds). At $P^\star \approx 4.4$ the system transforms into a triangular-like structure with two non-bonded patches per unit cell, which again induce the distortion (*cf.* Fig. 4.14, bottom).

Finally, the vertex representation of the *truncated trihexagonal* tiling suggests to use the two different enantiomers of a chiral patchy particle (six of each in the unit cell), to realize this ordered particle arrangement. Due to the large number of parameters that have to be optimized, it is difficult to give conclusive results on this system. We found lattices with lower enthalpy than the desired tiling at all pressure values due to the tiling's very large unit cell area (however, we are not entirely convinced if these identified lattices really represent the global minima on the enthalpy landscape).
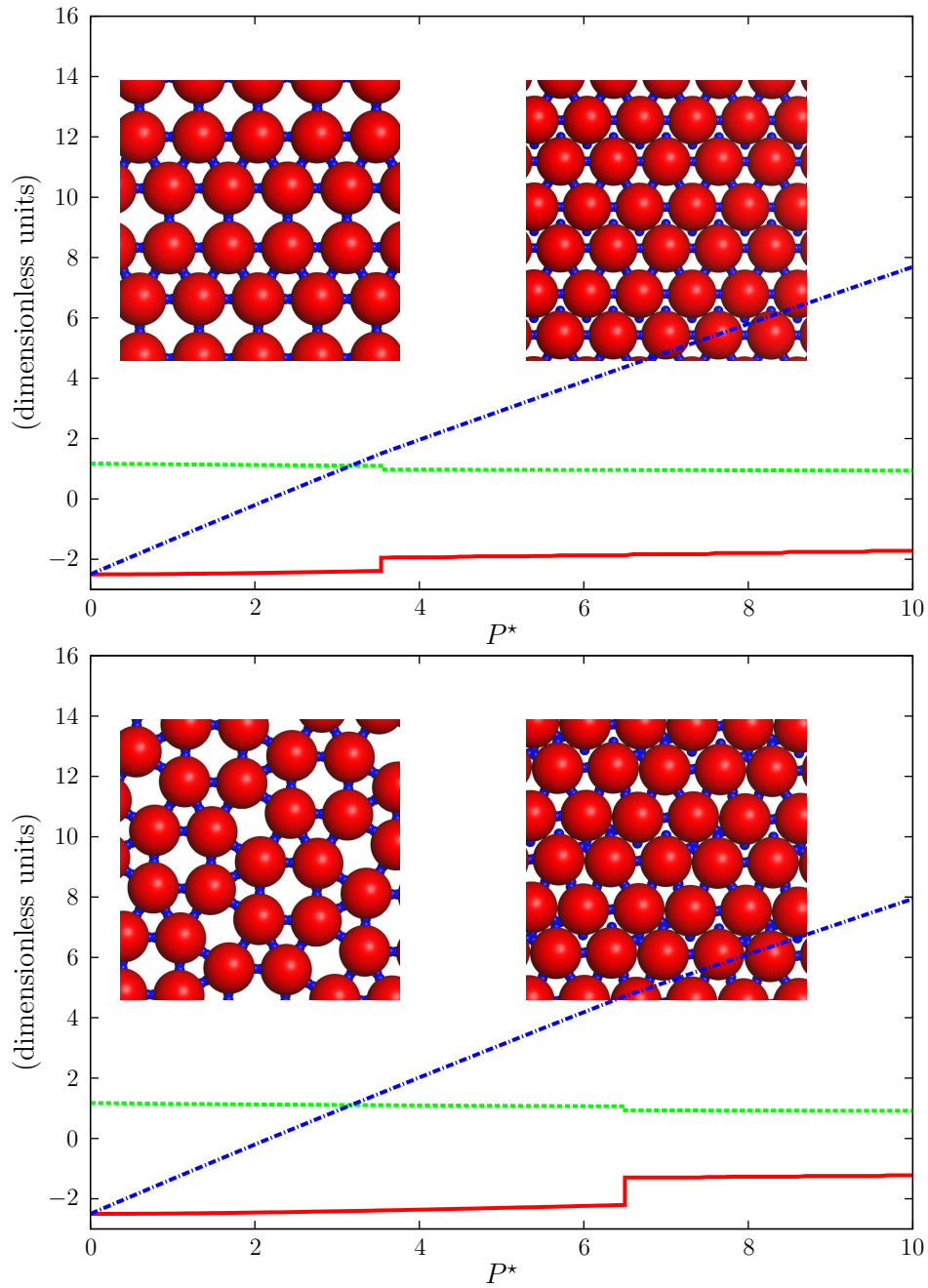
Figure 4.12.: Gibbs free energy [$G^\star = U^\star + P^\star/(\eta\sigma_0^2)$, dash-dotted blue line], lattice sum ($U^\star$, solid red line) and area [$1/(\eta\sigma_0^2)$, dashed green line) of the energetically most favorable structures formed by the particles designed for *elongated triangular* (top) and *snub square* (bottom) tilings in the vertex representation as functions of pressure $P^\star$. Insets: low pressure configurations (elongated triangular /snub square tilings, left) and high pressure configurations (distorted triangular lattices, right).
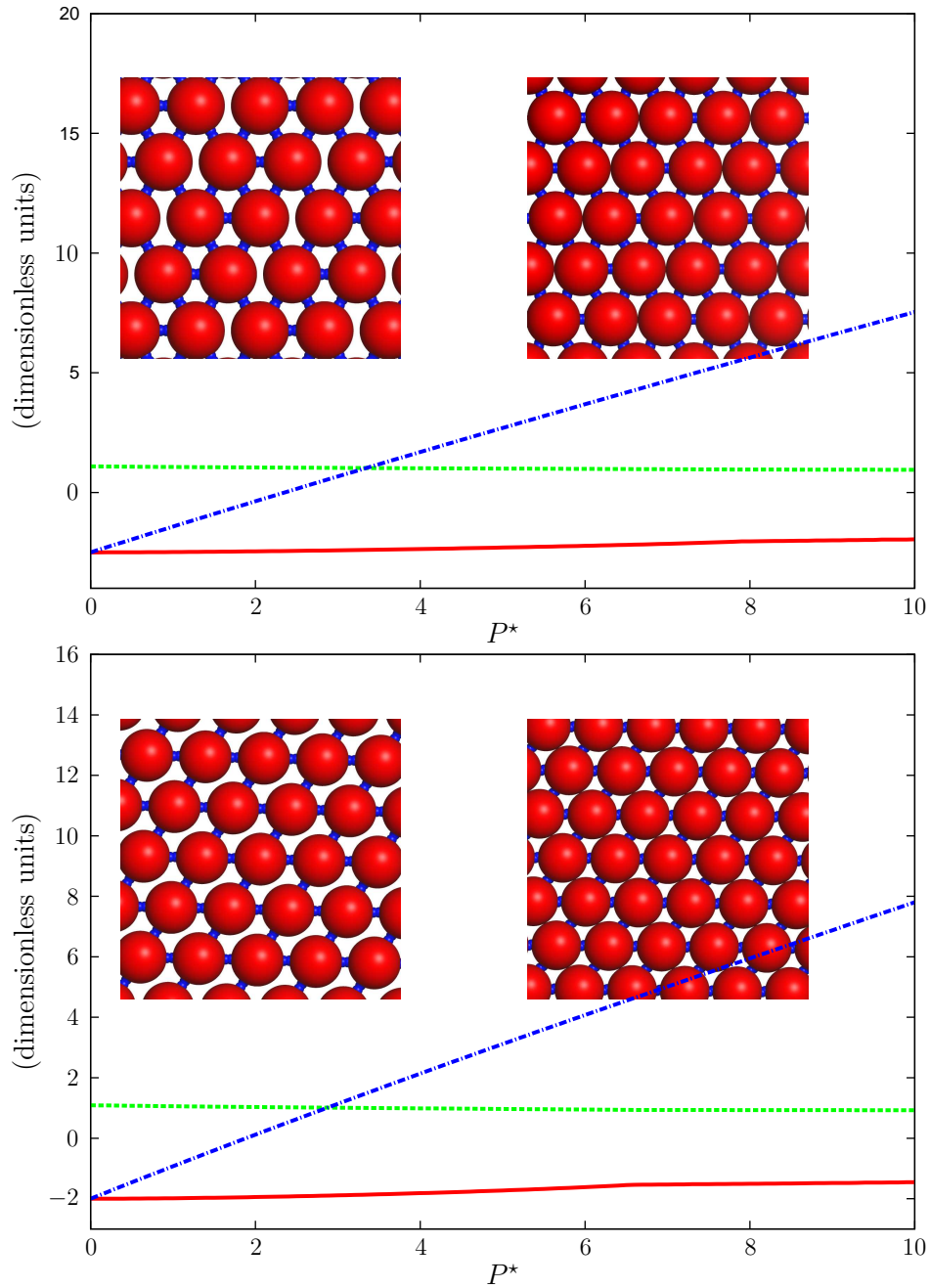
Figure 4.13.: Gibbs free energy, lattice sum and area of the energetically most favorable structures formed by the particles designed for *snub hexagonal* (top) and *tri-hexagonal* tilings in the vertex representation, as functions of pressure. Insets: low pressure configurations (distorted triangular lattices, left) and high pressure configurations (same respective configurations, optimized for high pressure, right). Line styles as in Fig. 4.12.
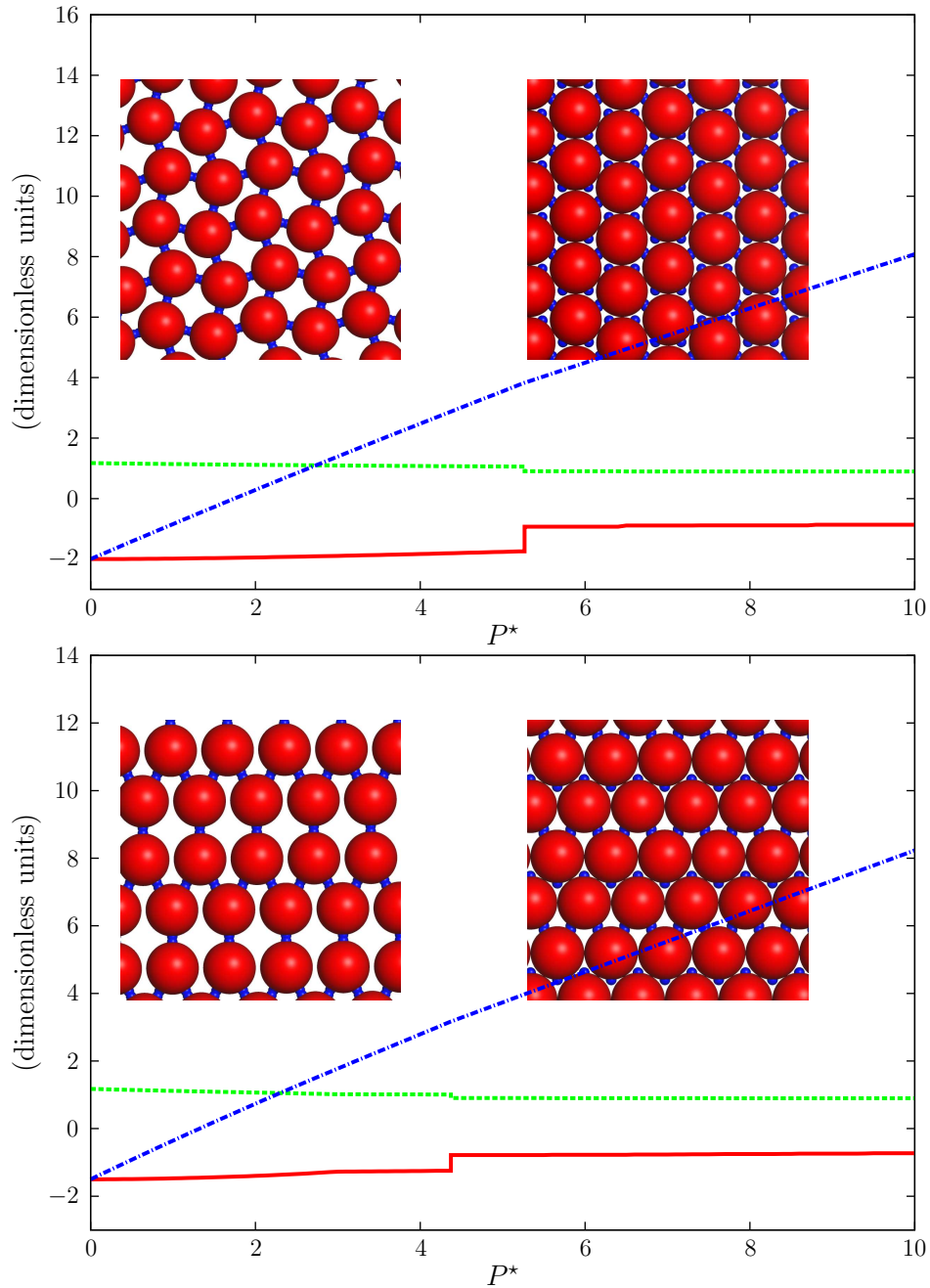
Figure 4.14.: Gibbs free energy, lattice sum and area of the energetically most favorable structures formed by the *rhombitrihexagonal* (top) and *truncated hexagonal* (bottom) systems in the vertex representation, as functions of pressure. Insets: low pressure configurations (snub square tiling/distorted triangular lattice, left) and high pressure configurations (distorted triangular lattices, right). Line styles as in Fig. 4.12.
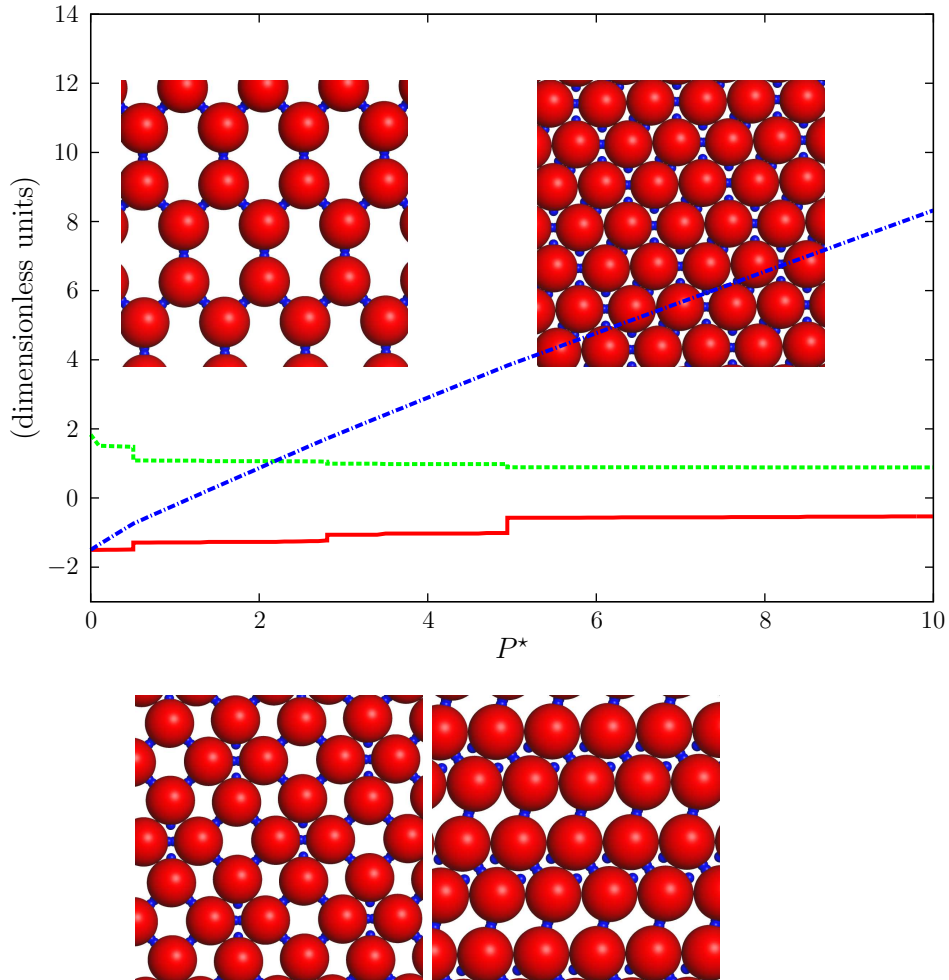
Figure 4.15.: Top: Gibbs free energy, lattice sum and area of the energetically most favorable structures formed by the particles designed for the *truncated square* tiling in the vertex representation, as functions of pressure. Insets: low pressure configuration (distorted hexagonal, left) and high pressure configuration (distorted triangular, right). Bottom: intermediate pressure configurations, with increasing pressure from left to right. Line styles as in Fig. 4.12.

Center Representation

The parameters that specify the size and the decoration of the patchy particles designed to self-assemble in the Platonic and Archimedean tilings within the center representation are summarized in Table 4.2, along with the number of particles of each species in the primitive cell that are required in order to realize the target lattice. Here, the particles are defined as inscribed circles of the polygonal building units of the respective tiling; their patch decoration is imposed by the requirement that each bond connecting two patches bisects the shared edge of neighboring polygonal units. In an attempt to realize the desired target structures in the center representation, at least two particle species of different size and decoration have to be introduced; we point out that, compared to the vertex representation, a relatively large number of patches is required. Again, we start our investigation at pressure values close to zero; we then gradually increase the pressure up to $P^\star = 10$. Note that due to the fact that at least two particle species are involved, the high-pressure phase is no longer the (monodisperse) triangular lattice.

Again, all the Platonic tilings can be stabilized for sufficiently low pressure; in fact, the *triangular* tesselation in the center representation corresponds to exactly the same system of patchy particles as the *hexagonal* tesselation in the vertex representation and vice versa. The *square* tiling corresponds to the same system in both representations. Therefore, the threshold pressure values up to which the tilings are stable are the same as the ones discussed in the section on the vertex representation.

Particles designed for the *elongated triangular* tiling show a size disparity of 0.577. At finite pressure values, the target structure is not realized; instead, lanes form: alternatingly, the larger particles populate a square lattice, while the smaller ones self-assemble in honeycomb-cells. This lattice is favored over the target structure with respect to the enthalpy, even though the unit cell area is only slightly smaller than the one of the lattice corresponding to the *elongated triangular* tesselation. This is due to the higher compressibility of the lane-based structure.

As the pressure is increased, the smaller particles form lanes as well, positioning themselves in increasingly more compact arrangements, breaking up more and more bonds. Since the lanes (consisting of alternating particle types) get broader as the number of particles in the unit cell is increased, we suspect that this behavior corresponds to a phase separation scenario, where the two phases are monodisperse triangular lattices consisting of the two subspecies of particles, respectively (*cf.* Fig. 4.16). Complete phase separation can of course only be realized in the limit of infinitely large primitive cells, which is clearly not reachable using the optimization algorithm.

For the *snub square* system we observe exactly the same phase behavior, since its unit cell in center representation consists of identical particle types and ratios as the *elongated triangular* one (*cf.* Tab. 4.2).

center representation				
tiling	N	size $[\sigma_0]$	N_p	inter-patch angles $360/N_\mathrm{p}$ [°]
triangular	2	$1/\sqrt{3} \approx \quad 0.577$	3	120
square	1	1.000	4	90
hexagonal	1	$\sqrt{3} \approx \quad 1.732$	6	60
elongated triangular	1	1.000	4	90
	2	$1/\sqrt{3} \approx \quad 0.577$	3	120
snub square	2	1.000	4	90
	4	$1/\sqrt{3} \approx \quad 0.577$	3	120
snub hexagonal	1	$\sqrt{3} \approx \quad 1.732$	6	60
	8	$1/\sqrt{3} \approx \quad 0.577$	3	120
trihexagonal	1	$\sqrt{3} \approx \quad 1.732$	6	60
	2	$1/\sqrt{3} \approx \quad 0.577$	3	120
rhombitrihexagonal	1	$\sqrt{3} \approx \quad 1.732$	6	60
	3	1.000	4	90
	2	$1/\sqrt{3} \approx \quad 0.577$	3	120
truncated square	1	$1 + \sqrt{2} \approx \quad 2.414$	8	45
	1	1.000	4	90
truncated hexagonal	1	$2 + \sqrt{3} \approx \quad 3.732$	12	30
	2	$1/\sqrt{3} \approx \quad 0.577$	3	120
truncated trihexagonal	1	$2 + \sqrt{3} \approx \quad 3.732$	12	30
	2	$\sqrt{3} \approx \quad 1.732$	6	60
	3	1.000	4	90

Table 4.2.: List of the three Platonic and eight Archimedean tilings and parameters that specify patchy particles for the *center* representation (see text): N stands for the number of particles required per unit cell (*cf.* Fig. 4.11). For all tilings at least two particle species with different size are required; their respective size (in units of σ_0) is given in the third column. The last two columns specify the number of patches N_p and the (uniform) inter-patch angles for each particle species, respectively.

In an effort to realize the *snub hexagonal* lattice we require one large six-patch and eight small three-patch particles per unit cell, with a size disparity characterized by a factor of three. The desired target structure is indeed stable for pressure values up to $P^\star \approx 2.0$. Then, upon increasing the pressure, four different lane structures emerge with increasing complexity and space filling factors, while the number of bonds decreases. The large particles remain fully bonded in the first two arrangements, while they lose one bond at each transition to the higher pressure arrangements.

Finally, the large particles form a highly compact square lattice, hosting the small particles in the interstitial regions. In this structure, the large particles have four, very weak wide-angle bonds with small particles, while each small particle exhibits one strong bond with a

neighboring particle of the same species (*cf.* Fig. 4.17).

Particles designed for the *trihexagonal* tiling (which also have a size disparity of three, but require a stoichiometry of 1 : 2) do not form the target lattice as an equilibrium structure. At low pressure values, the larger, six-patch particles instead arrange in a rectangular sublattice, while the smaller three-patch particles arrange in lanes of dimers between the larger particles. This configuration is fully bonded and has a smaller unit cell area than the target structure. Increasing the pressure leads to a lattice characterized by double-lanes of large particles, with four-particle arrangements of the smaller ones in between. The larger particles and 50 percent of the small particles are still fully bonded, while the remaining ones have no bonds at all. The high pressure arrangement is characterized by single lanes of large particles, with two small particles in each void. Each large particles has four bonds, each small particle has a single bond in this configuration (*cf.* Fig. 4.18).

In the construction of the *rhombitrihexagonal* lattice, three particle species (six-patch, four-patch and three-patch) are involved, the size disparity between the largest and the smallest species again being characterized by a factor three. Indeed, the desired target structure remains stable over a relatively large pressure range, *i.e.*, up to $P^\star \approx 3.8$, then transforming into a complex, more packed lane structure. Here, the six-patch particles have three bonds, half of the four-patch particles have three, the remaining half two bonds and all the three-patch particles have one bond (*cf.* Fig. 4.19, top panel).

Particles designed for the *truncated square* tiling (*i.e.*, one eight-patch and one four-patch particle with a size disparity of a factor 2.414) arrange in the desired target structure, two superposed square lattices decorated by the two particle species, respectively. This configuration is the only equilibrium structure that these particles form: as the pressure is increased, the system is homogeneously compressed (decreasing the bond lengths from the optimal value $2^{1/6}(\sigma_i + \sigma_j)/2$ towards $(\sigma_i + \sigma_j)/2$ and thereby increasing the energy from the fully bonded value towards zero) until a close-packed configuration is reached, maintaining the desired lattice structure (*cf.* Fig. 4.19, bottom panel).

In order to build up the *truncated hexagonal* tiling, two particle species (twelve-patch and three-patch) with a size disparity of a factor 6.46 are required. Again, the desired target structure represents the global enthalpy minimum at all pressure values investigated. The particle arrangement is gradually compressed with increasing pressure (*cf.* Fig. 4.20, top panel).

Finally, we require three particle species (twelve-patch, six-patch and four-patch) to realize the *truncated trihexagonal* tiling; the largest and the smallest of these particles differ in their size by a factor of 3.732. Similar to the two tilings discussed before, particles arrange for all investigated pressure values in one single structure, which represents the desired particle arrangement. An increase in pressure only reduces the lattice constants and bond lengths (*cf.* Fig. 4.20, bottom panel).

In conclusion, we note that all Platonic tilings represent the equilibrium configuration at

Figure 4.16.: Top: Gibbs free energy, lattice sum and area of the energetically most favorable structures formed by the particles designed for the *elongated triangular* and *snub square* tilings in the center representation, as functions of pressure. Insets: low pressure configuration (lanes I) and high pressure configuration (phase separation). Bottom: intermediate pressure configuration (lanes II). Particles with three patches are displayed in green, particles with four patches in yellow color. Line styles as in Fig. 4.12.

Figure 4.17.: Top: Gibbs free energy, lattice sum and area of the energetically most favorable structures formed by the particles designed for the *snub hexagonal* tiling in the center representation, as functions of pressure. Insets: low pressure configuration (snub hexagonal tiling, left) and high pressure configuration (right). Bottom: intermediate pressure configurations, with increasing pressure from left to right and from top to bottom. Particles with three patches are displayed in green, particles with six patches in red color. Line styles as in Fig. 4.12.
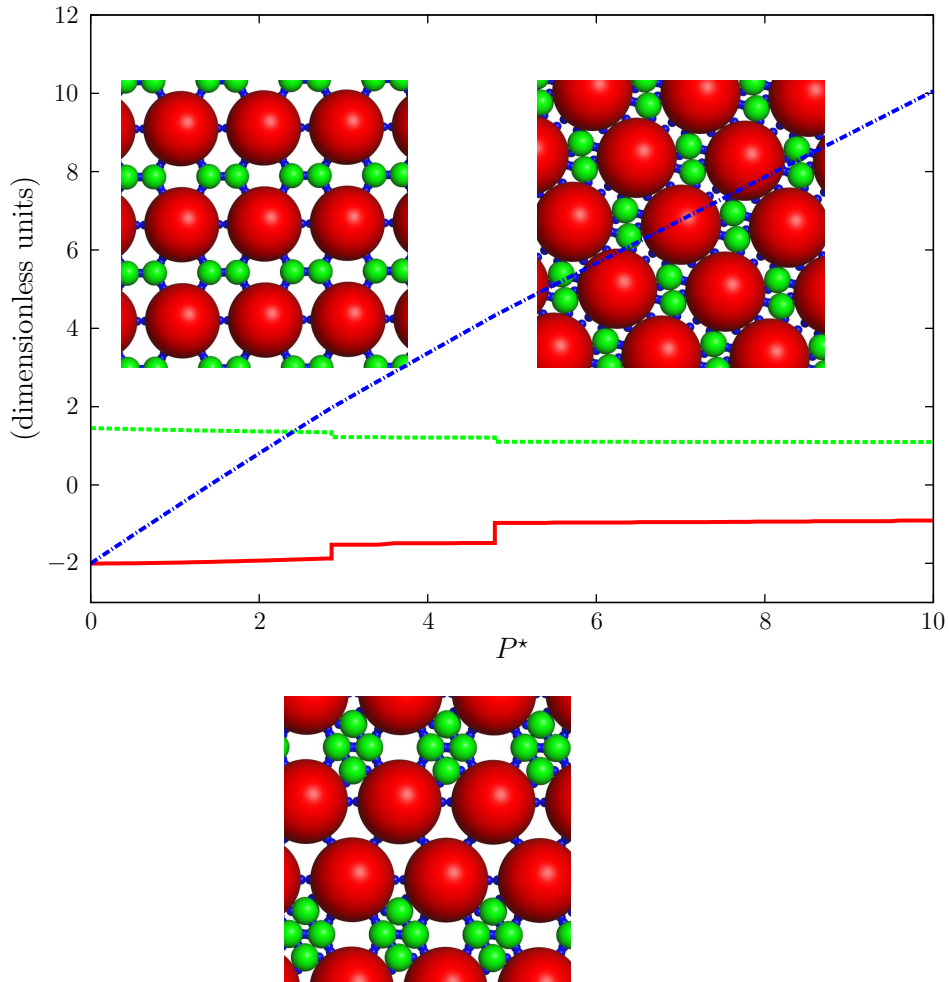
Figure 4.18.: Top: Gibbs free energy, lattice sum and area of the energetically most favorable structures formed by the particles designed for the *trihexagonal* tiling in the center representation, as functions of pressure. Insets: low pressure configuration (rectangular) and high pressure configuration (single lanes). Bottom: intermediate pressure configuration (double lanes). Particles with three patches are displayed in green, particles with six patches in red color. Line styles as in Fig. 4.12.
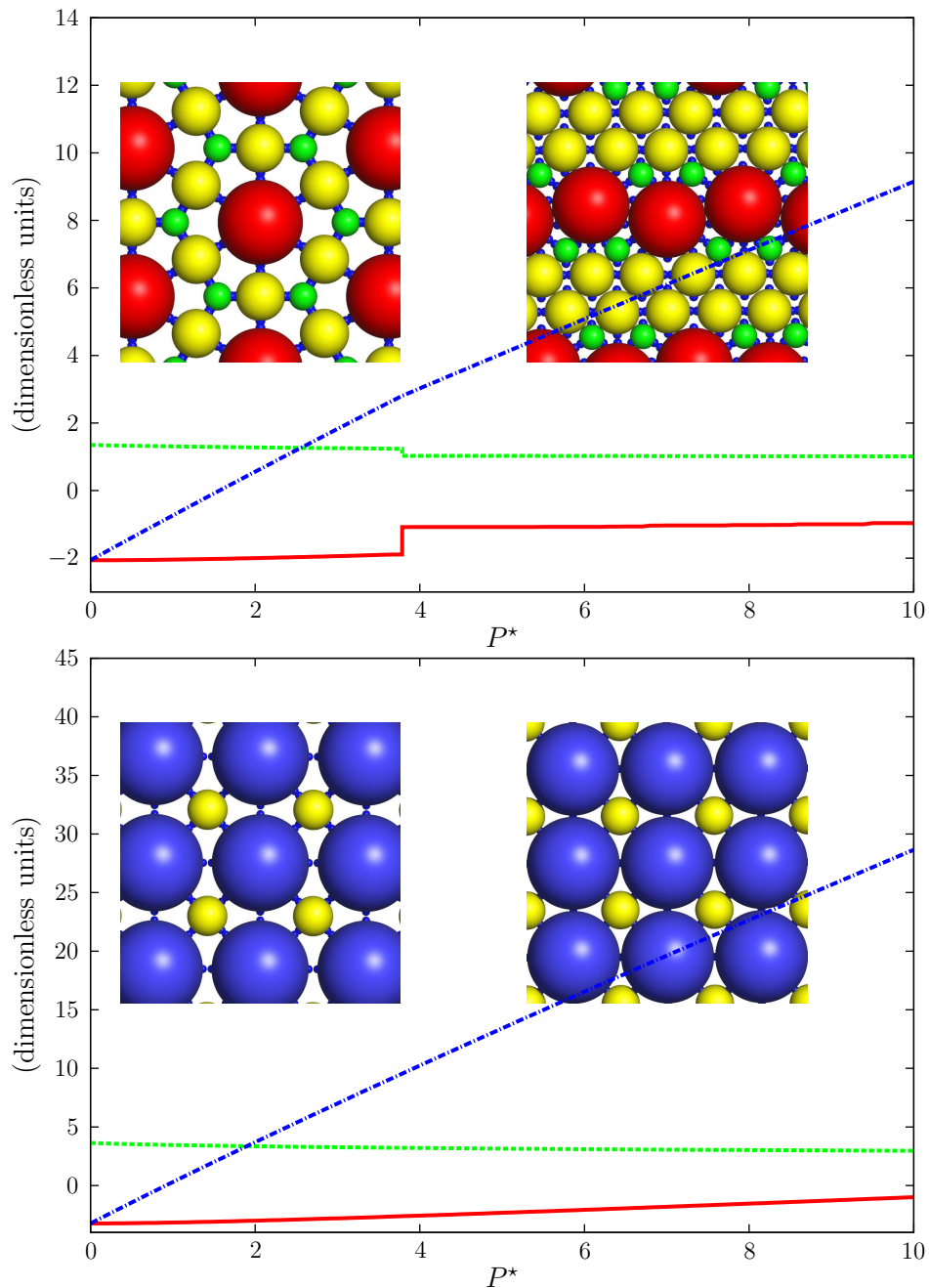
Figure 4.19.: Gibbs free energy, lattice sum and area of the energetically most favorable structures formed by the particles designed for the *rhombitrihexagonal* (top) and *truncated square* (bottom) tilings in the center representation, as functions of pressure. Insets: low pressure configurations (rhombitrihexagonal/truncated square tilings, left) and high pressure configurations (lane configuration/truncated square tiling, right). Particles with three patches are displayed in green, particles with four patches in yellow, particles with six patches in red and particles with eight patches in blue color. Line styles as in Fig. 4.12.
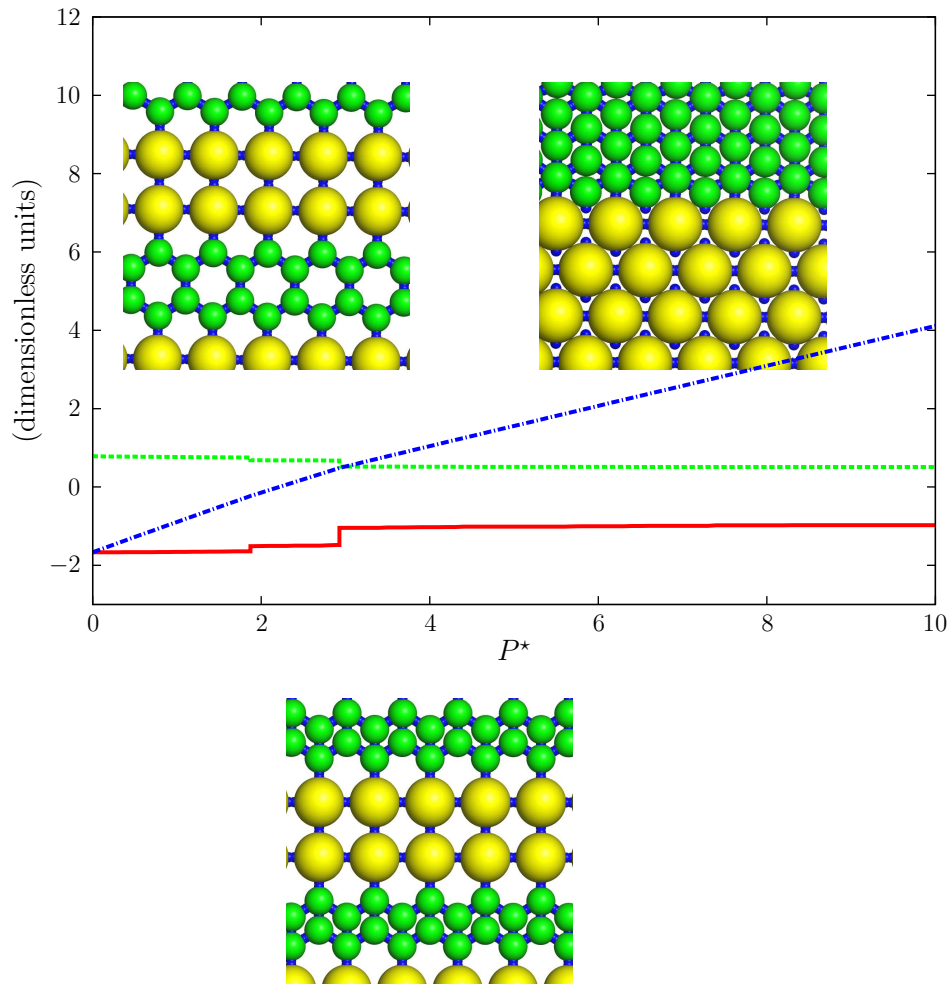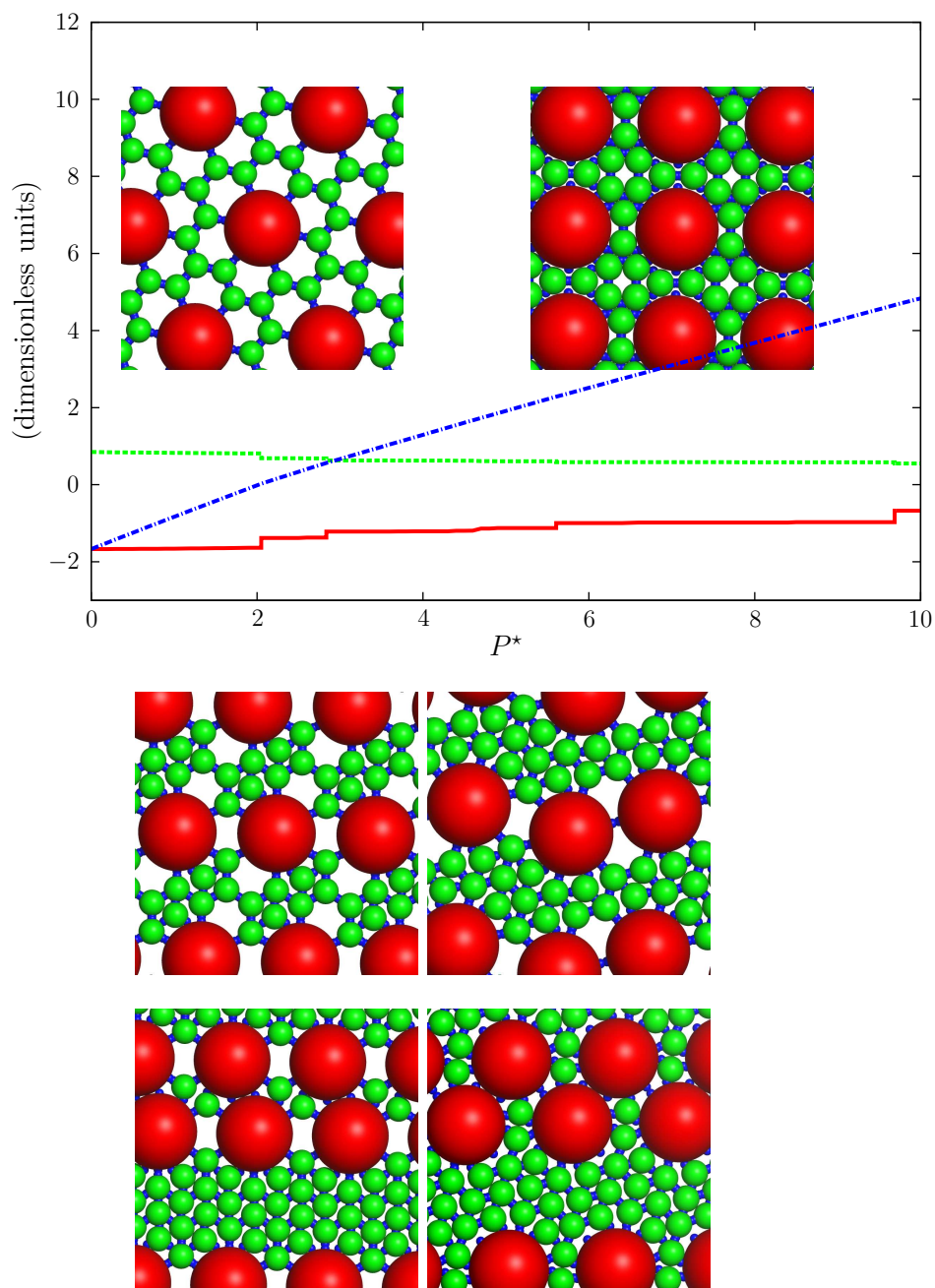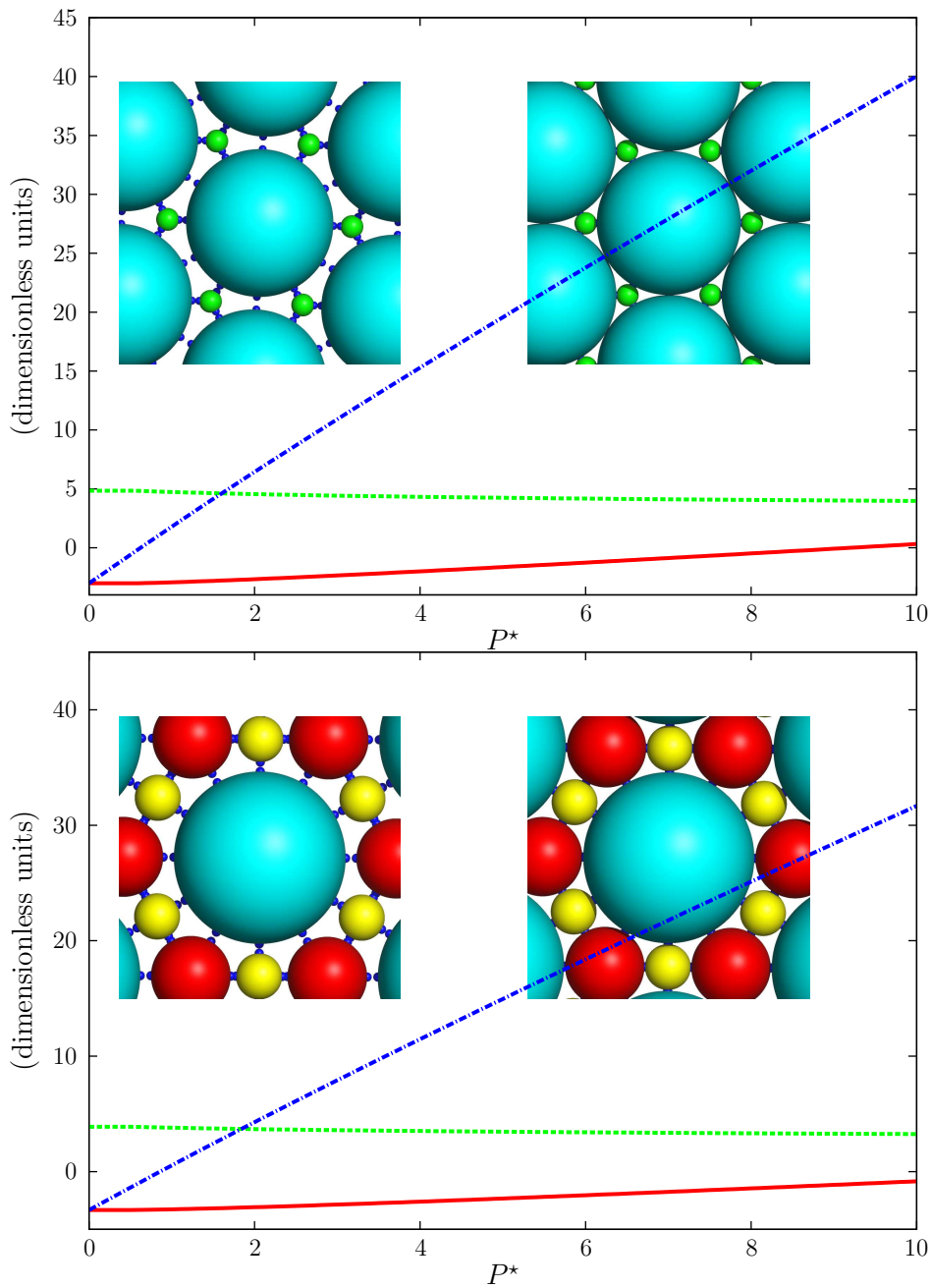
Figure 4.20.: Gibbs free energy, lattice sum and area of the energetically most favorable structures formed by the particles designed for the *truncated hexagonal* (top) and *truncated trihexagonal* (bottom) tilings in the center representation, as functions of pressure. Insets: low pressure configurations (truncated hexagonal/truncated trihexagonal tilings, left) and high pressure configurations (same respective configurations, with bond lengths optimized for close packing, right). Particles with three patches are displayed in green, particles with four patches in yellow, particles with six patches in red and particles with twelve patches in cyan color. Line styles as in Fig. 4.12.

$T = 0$ and some finite pressure value in both the vertex and the center representation. All Archimedean tilings except for the *trihexagonal* one represent the global enthalpy minimum at $T = 0$ and finite pressure in *one* of the representations. The *elongated triangular* and the *snub square* tilings can be stabilized only in the vertex representation, while the *snub hexagonal*, *rhombitrihexagonal*, *truncated square*, *truncated hexagonal* and *truncated trihexagonal* tilings where identified as equilibrium structures only in the center representation. This duality is not completely surprising, as polygonal building units correspond to voids in the vertex representation and to particles in the center representation. Therefore, tesselations with very large building units are strongly disfavored in the vertex representation, while they correspond to a rather good space filling factor in the center representation by definition (as an increasing number of edges makes the polygons more disk-like). For many of the systems, we have identified additional, sometimes very complex, global enthalpy minima at intermediate and high pressure values, which become favorable when the packing term in the enthalpy dominates over the bonding term. Only the *truncated square*, *truncated hexagonal* and *truncated trihexagonal* tilings (which all include octagonal or dodecagonal building units) in the center representation correspond to the global enthalpy minimum over the whole investigated pressure range.

4.2. Patchy Particle Systems in Three Dimensions

4.2.1. Clusters

The results in this section were obtained using the basin-hopping Monte Carlo global optimization algorithm [67], developed by David Wales and coworkers, during a visit to this group in Cambridge. Again, we are using the Doye model (*cf.* Sec. 2.2.2) with parameters $w = 2\pi \cdot 0.05$ and $r_{\text{cut}} = 1.9\sigma$.

The term "cluster" refers to cohesive arrangements of a finite number N of particles. Clusters can be seen as an intermediate state between an (ideal) gas phase (*i.e.*, single particles, separated by distances that are large compared to their intrinsic length scales, defined in the respective interaction potentials) and a condensed phase (*i.e.*, a liquid or a bulk solid, containing a huge number of particles that are separated by distances of the order of magnitude of their intrinsic length scales). There are no well-defined minimum or maximum particle number N above or below which such an arrangement can be considered a cluster, as entities consisting of as little as two or as many as millions of particles are termed in this way.

Global Energy Minima of Clusters of Patchy Particles

We have identified putative equilibrium structures in the NVT ensemble* for clusters of patchy particles containing up to $N = 47$ particles, each with four patches arranged in regular tetrahedral symmetry. By inspecting the identified configurations, we make the general observation that the minimum energy clusters contain substructures, which can be characterized as closed rings consisting of either five or six particles. This is in agreement with results presented in Ref. [37]. The six particle rings are never flat, but can be seen as finite sections of cubic and hexagonal diamond crystals (in Sec. 4.2.2, Fig. 4.36, panels C and D, these two crystal structures are depicted). For the five-particle rings, we can distinguish between flat (all centers of masses lie within a plane, representing the vertices of a regular pentagon) and warped arrangements (the vertices of the "pentagon" do not exactly lie within a plane). The six-particle rings are energetically slightly favored, as the bonding angles can be optimally aligned (*i.e.*, $\Theta_{i\alpha} = \Theta_{j\beta} = 0$) within those rings. The flat, pentagonal five-particle rings, where the patch alignments slightly deviate from the optimal angles due to geometric constraints, are better suited for supporting a larger number of total bonds in clusters with a higher number of particles by forming closed shells, based on the structure of the smallest possible fullerene, C_{20} [112, 113].

Thus, it is not surprising that the minimum energy clusters contain mostly six-particle rings for cluster sizes $5 < N < 11$ while five particle rings dominate for $N > 18$. In the intermediate region, we observe global minima corresponding to structures containing both types of rings. Plotting the energy per particle as a function of cluster size, we identify minimal values for

---

*At $T = 0$ and $V \gg NV_{\text{Particle}}$.

$N = 8, 10, 15, 20, 30, 35, 47$. These sizes represent "magic numbers", where a comparatively large number of patches can be saturated.

By examining the structures (*cf.* Figs. 4.22 and 4.22), we observe that $N = 6, 8, 10, 12$ are built up by six-particle rings only ($N = 10$ represents a section of a cubic diamond, $N = 8$ and 12 sections of a hexagonal diamond, while the minimum for $N = 6$ is degenerate and can be realized both by the cubic and the hexagonal diamond arrangements). For $N = 7$ and 9 we observe global energy minima represented by structures consisting of the $(N - 1)$ cluster plus an additional, weakly bonded particle; $N = 11$ combines a non-flat five-particle ring and cubic-type six-particle ring in order to maximize the number of saturated bonds. The $N = 15$ minimum energy cluster contains both five- and six-particle rings, the former in the flat version, the latter of hexagonal type. The minimum energy structures for $N = 13, 14$ and 17 are all based on this cluster, while the one for $N = 16$ is a particle arrangement with rather low symmetry, consisting mostly of five-particle rings. $N = 20$ represents a dodecahedral closed shell of flat five-particle rings. For $N > 17$ we observe a growth pattern, towards the 20 particle closed shell: The global minimum structures at $N = 18$ and 19 are represented by incomplete versions of this shell. Cluster with more than twenty particles always contain the shell as a substructure; for $N = 30$ and $32 - 34$ the shell is combined with the clusters observed at $N_0 = N - 15$, where one of the flat five-particle rings is shared between the shell and the additional subcluster. For cluster sizes $N = 21$ to 25, 27 to 29 and 31, the global minimum for N_0 particles does not contain a compatible five-particle ring and therefore the 20 particle shell is combined with an energetically higher local minimum structure of the N_0-particle system, which does include a five-particle ring that can be shared. A special case is the cluster with $N = 26$ particles, where the 20 particle shell is combined with the $N = 8$ cluster, where the subclusters share only two particles.

The global minimum for $N = 35$ is represented by a combination of two full closed shells, again sharing one five-particle ring. All clusters with $N > 35$ contain those two merged shells and another growth pattern can be observed for particle numbers up to $N = 47$, where the global minimum consists of three combined closed shells.

Transition States and Energy Landscapes

For cluster sizes $N = 10$, 12 15 and 20 we performed extensive searches for additional local minima and transition states, in order to characterize the energy landscape for these systems.

Examining the disconnectivity graph (*cf.* Sec. 3.1 and Ref. [53]) representation of the energy landscape at $N = 10$ (*cf.* Fig. 4.24, left panel), we find a local minimum that is energetically very close (within less than one percent of the total energy) to the global minimum ($U_{\mathrm{GM}} \approx -12.00$). This local minimum consists of five-particle rings only and is therefore structurally quite different from the global one, which is based on cubic diamond-type six-particle rings. The fastest reaction pathway between these two minima that we identified has to pass over a high-energy barrier ($U_{\mathrm{TS}} \approx -10.00$, *i.e.*, two bonds have to be broken on the pathway),
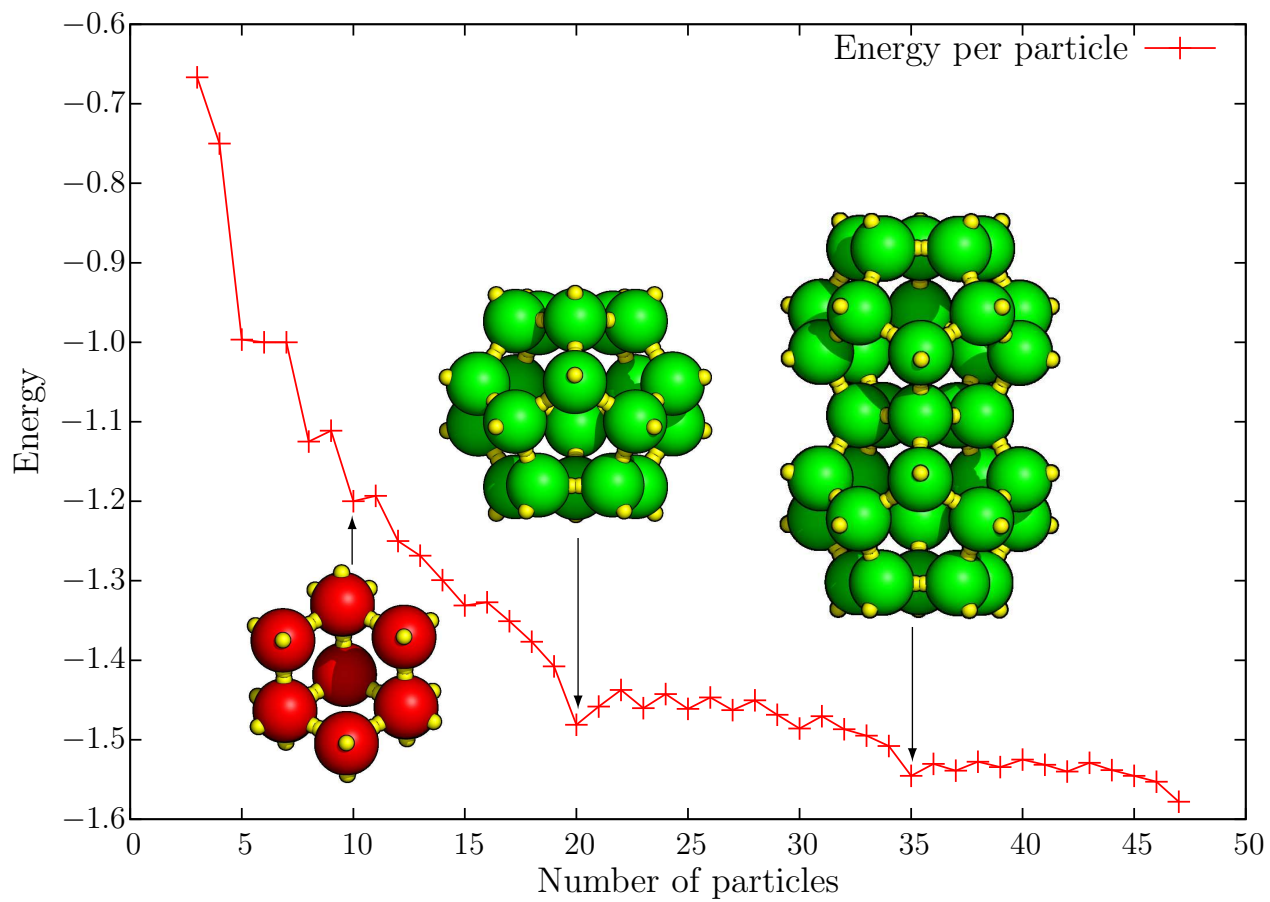
Figure 4.21.: Energy per particle as a function of cluster size. Insets: Minimal energy clusters with $N = 10, 20$ and 35 particles.

5 | **6 (cubic)** | **6 (hexagonal)**

8 | **10** | **11**

12 | **14** | **15**
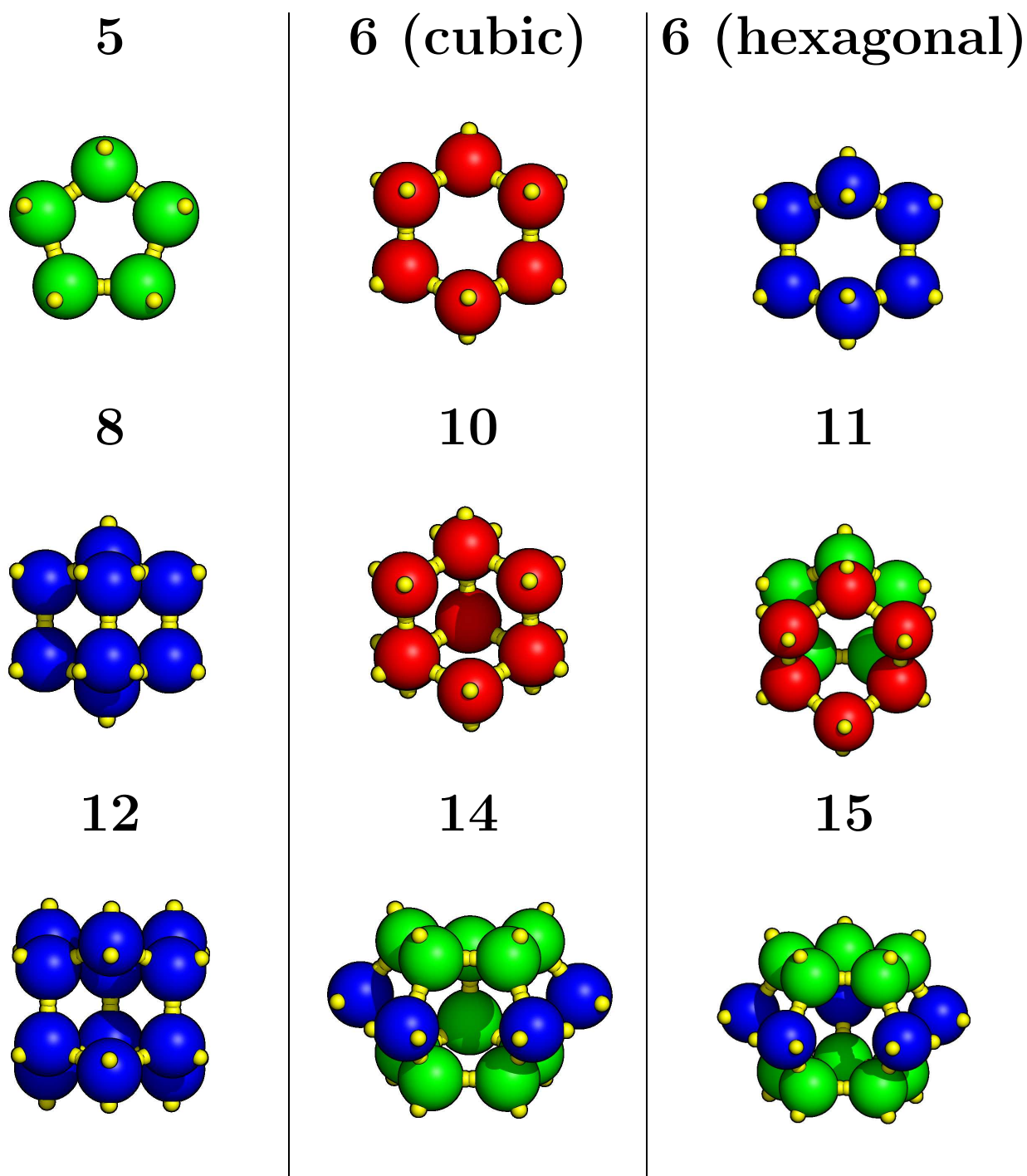
Figure 4.22.: Visualizations of the structures corresponding to global energy minima for selected cluster sizes. Particles that are parts of five-particle rings are colored green, those forming cubic diamond-type six-particle rings are shown in red and particles within hexagonal diamond-type six-particle rings are colored blue. Particles which are part of two different ring-types appear (somewhat arbitrarily) in one of the specified colors only, so that the illustration does not become unnecessarily complicated.
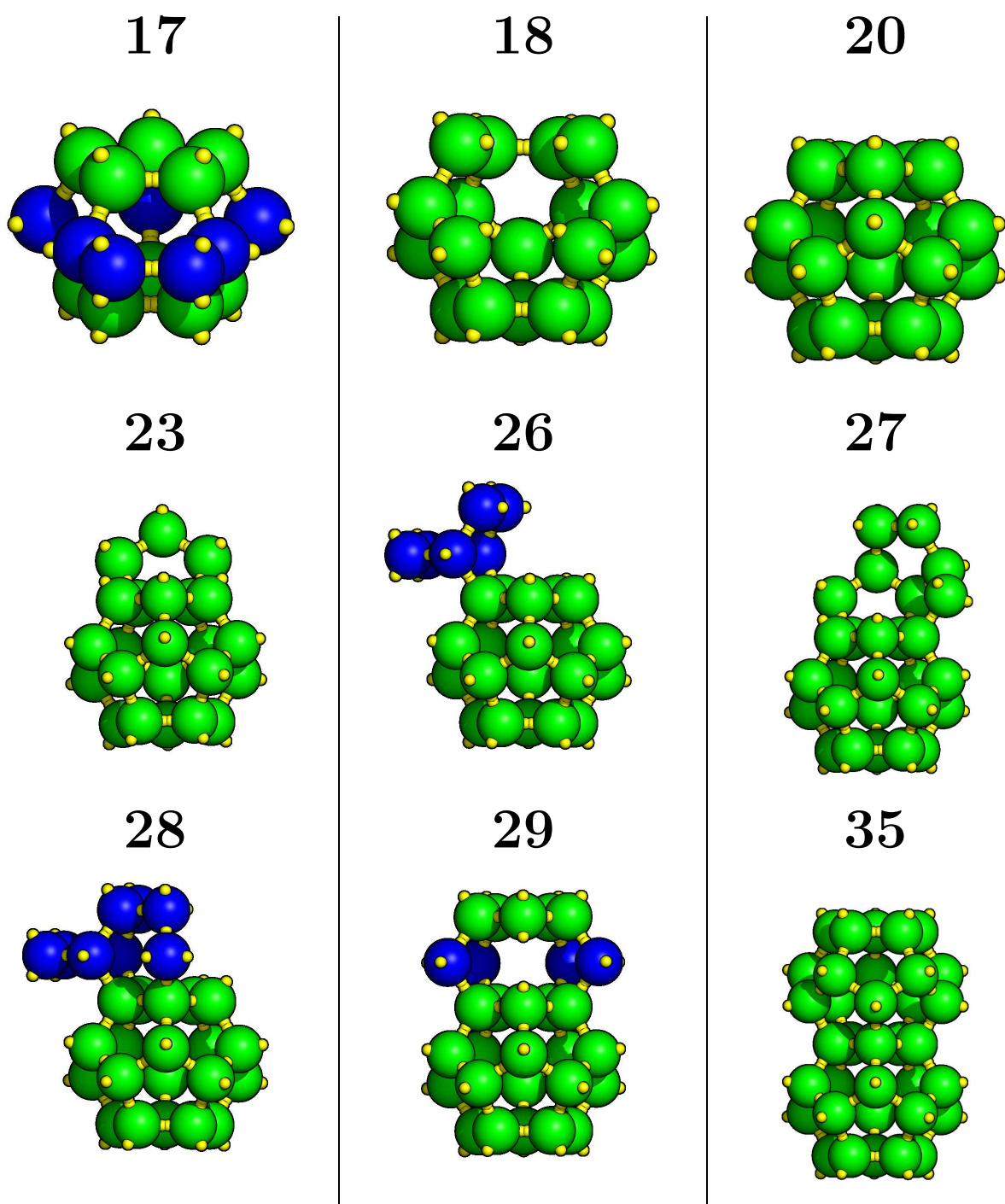
Figure 4.23.: Visualizations of the structures corresponding to global energy minima for selected cluster sizes. For the particle coloring scheme, *cf.* Fig. 4.22

in order to achieve the required structural rearrangement. We observe several, energetically slightly higher-lying minima ($U \approx -11.65$), which contain combinations of five- and six-particle rings and are connected to the global minimum *via* lower-lying transition states ($U_{\text{TS}} \approx -10.50$). All these *local* minima have the same number of bonds as the *global* minimum, the higher binding energy is due to non-optimal bond angles.

At $N = 12$, we have evaluated a disconnectivity graph with a broad funnel containing a large number of minima that are all separated by barriers of similar height (*cf.* Fig. 4.24, right panel). The three lowest minima all lie within this funnel, *i.e.*, are interconnected *via* pathways requiring the same, comparatively small amount of bond breaking.

For $N = 15$, the disconnectivity graph (*cf.* Fig. 4.25, left panel) looks more peculiar: The global minimum ($U_{\text{GM}} \approx -19.97$), consisting of flat five-particle and hexagonal diamond-type six-particle rings is not located within the dominating funnel of the energy landscape, which contains most of the low-lying local minima. More specifically, within the dominating funnel, there is one local minimum with $U \approx -19.84$, corresponding to a fragment of the 20 particle icosahedral shell and a number of additional minima that are represented by slight variations of this structure, with $-19.42 \lesssim U \lesssim -19.00$. To transform one of these structures to another, transition states with $U_{\text{TS}} \approx -18.50$ have to be overcome, while reaching the global minimum from this funnel requires passing a barrier with $U_{\text{TS}} \approx -18.00$. This shows that the $N = 15$ cluster system lies in an intermediate regime of cluster sizes, where local minima based on five particle rings already dominate the energy landscape, but the global minimum still corresponds to a structure largely based on six particle rings.

At $N = 20$, we observe a more regular, "weeping-willow"-type disconnectivity graph (*cf.* Fig. 4.25, right panel) with a single, broad funnel that is completely dominated by structures based on five-particle rings. The global minimum (with $U_{\text{GM}} \approx -29.62$) is separated from five structurally distinct local minima with degenerate energies ($U \approx -27.75$) by a rather large gap, which amounts to more than six percent of the total energy. These local minima can all be assembled by removing one particle from the global minimum structure (*i.e.*, the closed icosahedral shell) and reattaching it at a different place on the surface of the shell, thereby losing three (slightly non-optimal) bonds and regaining a single (optimal) one. Therefore, reaction pathways from the global minimum to any of these local minima have to pass transition states with the same energies ($U_{\text{TS}} \approx -26.50$), as reflected in the disconnectivity graph. However, there are a few slightly higher-lying minima ($U \approx -27.40$), which are connected to the global minimum *via* transition states that correspond to energetically less costly rearrangements of the structure ($U_{\text{TS}} \approx -27.00$, *i.e.*, these pathways do not require complete detachment of a particle from the cluster).

An interesting perspective for future investigations could be to study the influence of the patch width w on the shape of the energy landscapes for different cluster sizes. With decreasing w, minima in funnels corresponding to five-particle rings are expected to be shifted towards higher energies.

Figure 4.24.: Left: Disconnectivity graph showing the 50 lowest minima on the energy landscape of the ten particle cluster. Right: Disconnectivity graph showing the 100 lowest minima of the twelve particle cluster. Insets: structures representing the energetically lowest minima of each system. The ordinate shows the cluster energy in units of the Lennard-Jones ϵ.
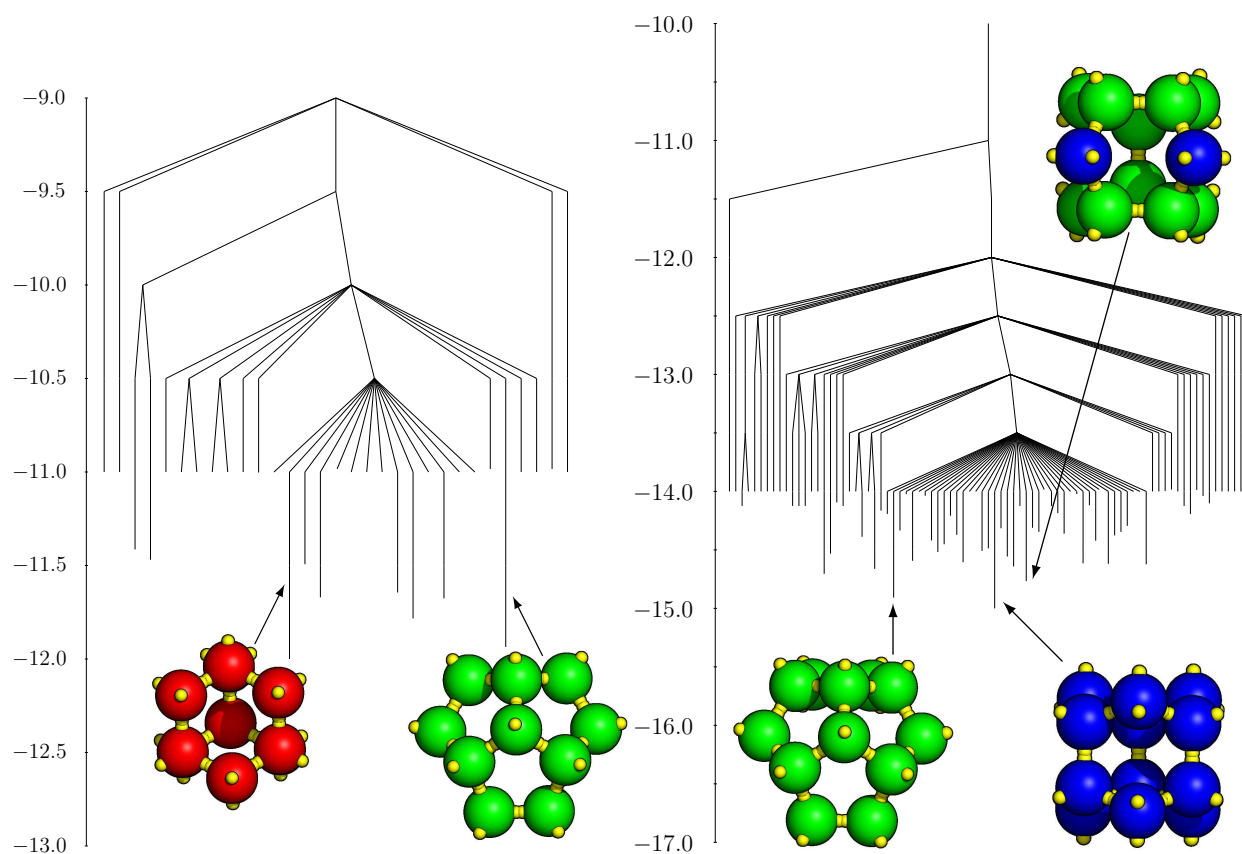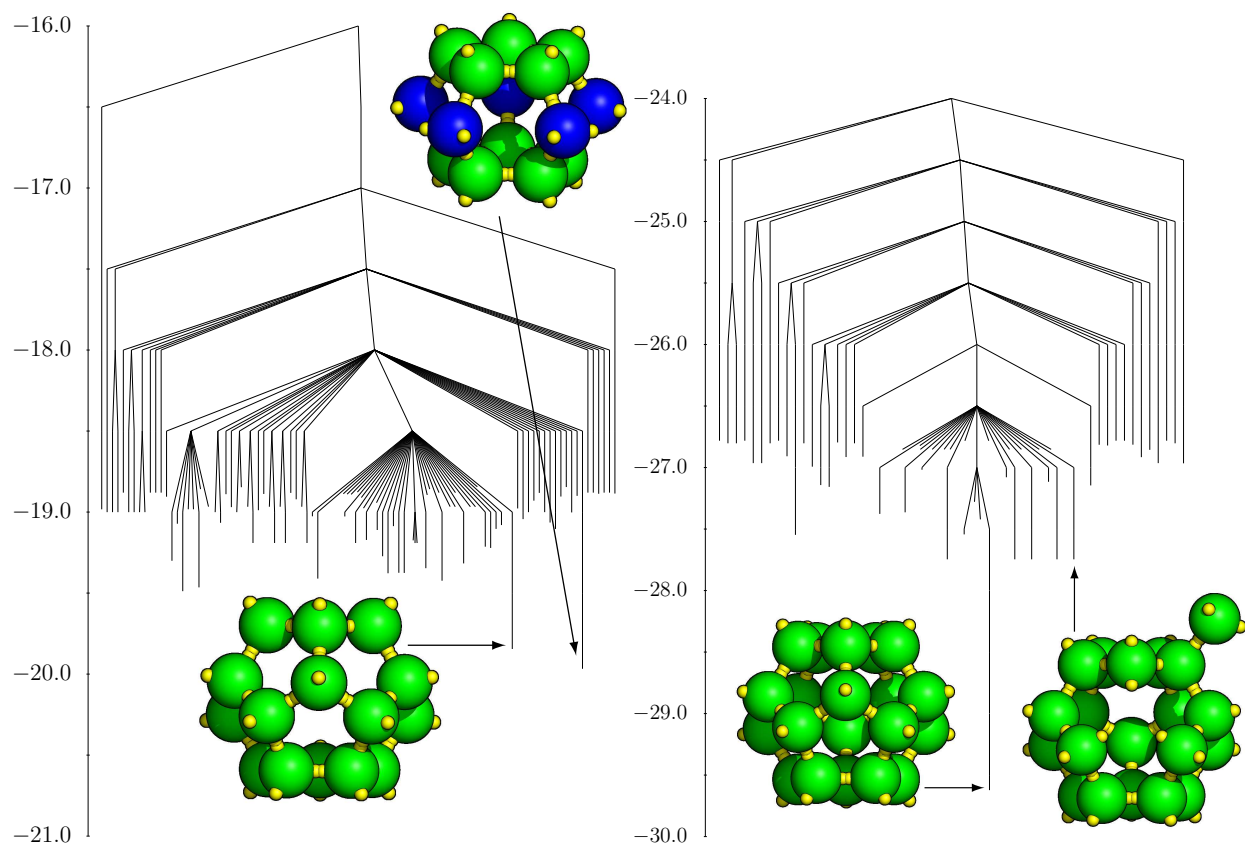
Figure 4.25.: Left: Disconnectivity graph showing the 100 lowest minima of the 15 particle cluster. Right: Disconnectivity graph showing the 100 lowest minima of the 20 particle cluster. Insets: structures representing the two energetically lowest minima of each system. The ordinate shows the cluster energy in units of the Lennard-Jones ϵ.

4.2.2. Crystals

In the following section, we present the generalized* zero-temperature phase diagram of the three-dimensional four-patch system, in dependence of system pressure $P^\star$ and the geometry of the patch decoration, *i.e.*, the anisotropy parameter g. Again, our calculations are based on the Doye model (*cf.* Sec. 2.2.2), here with parameters $w = 2\pi \cdot 0.06752$ and $r_{\mathrm{cut}} = 2.5\sigma$. We vary $P^\star$ between 0 and 10 and g between 90.00 and 150.00; to be specific, patches 2-4 are located on the equator for $g = 90.00$ and on the southern hemisphere of the colloidal particles for all other g values; for our calculations, we increase g in 16 steps of $\Delta g = 3.75$.

We give detailed insight into the structural features of the zero-temperature equilibrium configurations (*i.e.*, global minima on the enthalpy landscape) for each state point, specified by $(g, P^\star)$. Additionally, we present structures corresponding to competing *local* minima on the landscape, for selected values of g and $P^\star$. In certain cases, these local minima can be thermodynamically stabilized at finite temperature by entropic effects (*cf.* Sec. 3.3). In order to investigate this possibility in more detail, full free energy calculations [107, 114] have to be performed. As pointed out in Sec. 3.3, our search algorithm can not only be used to determine the zero-temperature behavior of such systems, but also to suggest candidate structures, for which free energy calculations are executed in order to determine the finite temperature phase diagram in a two-step approach [6, 7].

Note that for many values of the geometry parameter g, the patchy interactions lead to – sometimes strong – deviations from ideal lattices (such as bcc, fcc and hcp). Therefore we refer to the structures we identified as bcc-like, fcc-like or hcp-like in order to indicate such aberrations.

For the visual representations of the structures in the following figures, we introduce a color code as a guide to the eye:

- For layered honeycomb lattices and structures consisting of hexagonal layers, particles located in different layers are colored in an alternating pattern (*i.e.*, red-yellow-red-yellow-...).

- For bcc-like lattices, particles located on the vertices of the cubic unit cell appear in red, while the particles at the center of the unit cell are colored yellow.

- In the double diamond picture, particles belonging to different non-interacting diamond sublattices appear in different colors.

- For fcc-like structures, the particles located at the vertices of the cubic unit cell and the particles at the centers of the faces of the unit cell are colored red and yellow, respectively.

Additionally, patches located on the north pole of a particle are colored blue, while the patches with g dependent locations on the particle surface are colored green.

---

*With pressure and an anisotropy parameter as coordinate axes, *cf.* Sec. 2.1.1 and Ref. [4].

Minimum Enthalpy Structures

As shown in Figs. 4.26 and 4.27, we are able to identify a broad variety of zero-temperature equilibrium structures for varying patch geometries and pressures. These can crudely be categorized as open, very loosely packed configurations, hexagonally layered and body-centered (bc) configurations with medium packing fractions and (almost) close packed face centered and hexagonal configurations. The multitude of the observed configurations is the result of a complex competition between packing (maximizing the packing fraction η) and bond saturation (minimizing the energy $U^\star$). Accordingly, we can identify three regions in the $(g, P^\star)$-phase diagram:

- For pressure-values up to $P^\star \approx 4.00$ we observe structures that are characterized by full bond saturation (*i.e.*, $U^\star \approx -2.00$) and rather small packing fraction η, being by a factor of ≈ 2.75 (for open structures) to ≈ 1.16 (for distorted body-centered structures) smaller than the packing fraction of close-packed spheres ($\eta \approx 0.74$). Here, the spectrum of identified lattices ranges from open, layered structures ($g \approx 90.00$) over bc-like lattices (which dominate over a broad g range, *i.e.*, $93.75 \lesssim g \lesssim 135.00$) to layers of hexagonally arranged particles for $g \gtrsim 135.00$.

For intermediate and higher pressure-values a trend towards more compact structures is observed: non-close-packed hexagonal and bcc-like lattices are encountered, which, as $P^\star$ is further increased, eventually transform into close-packed hcp-like and fcc-like structures.

- For $g \lesssim 120.00$ the transition from low- to high-pressure structures is characterized by an abrupt change in the energy $U^\star$, increasing from nearly full saturation (*i.e.*, $U^\star \approx -2.00$) to a value of around -1.00. In this range of g, the location of the patches on the colloidal surface does not allow for the formation of strong bonds in denser configurations, thus pressure rather easily wins over bond saturation.

- In contrast, for $g \gtrsim 120.00$, $U^\star$ increases more smoothly with $P^\star$ and the identified ordered structures are the result of a delicate trade-off between saturation and packing. In particular we emphasize that for selected g values (*i.e.*, $g \approx 123.75$ and $g \approx 150.00$) the respective patch decorations support both a high degree of bond saturation and, at the same time, the formation of high density lattices. As a consequence, the identified structures are able to persist up to high pressure values (*i.e.*, $P^\star \approx 10.00$ in the former case, even higher in the latter) while maintaining a relatively low binding energy (*i.e.*, $U^\star \approx -1.65$).

In the following, we will provide detailed descriptions of the structural features of the identified equilibrium configurations.

As mentioned above, the calculations in this section have been carried out with a long-distance potential cutoff of $r_{\text{cut}} = 2.5\sigma$, in order to allow a comparison with previously published results [39] and a direct exchange of data with our collaborator Eva Noya. This rather high value causes additional attractive long-distance interaction to play a (though
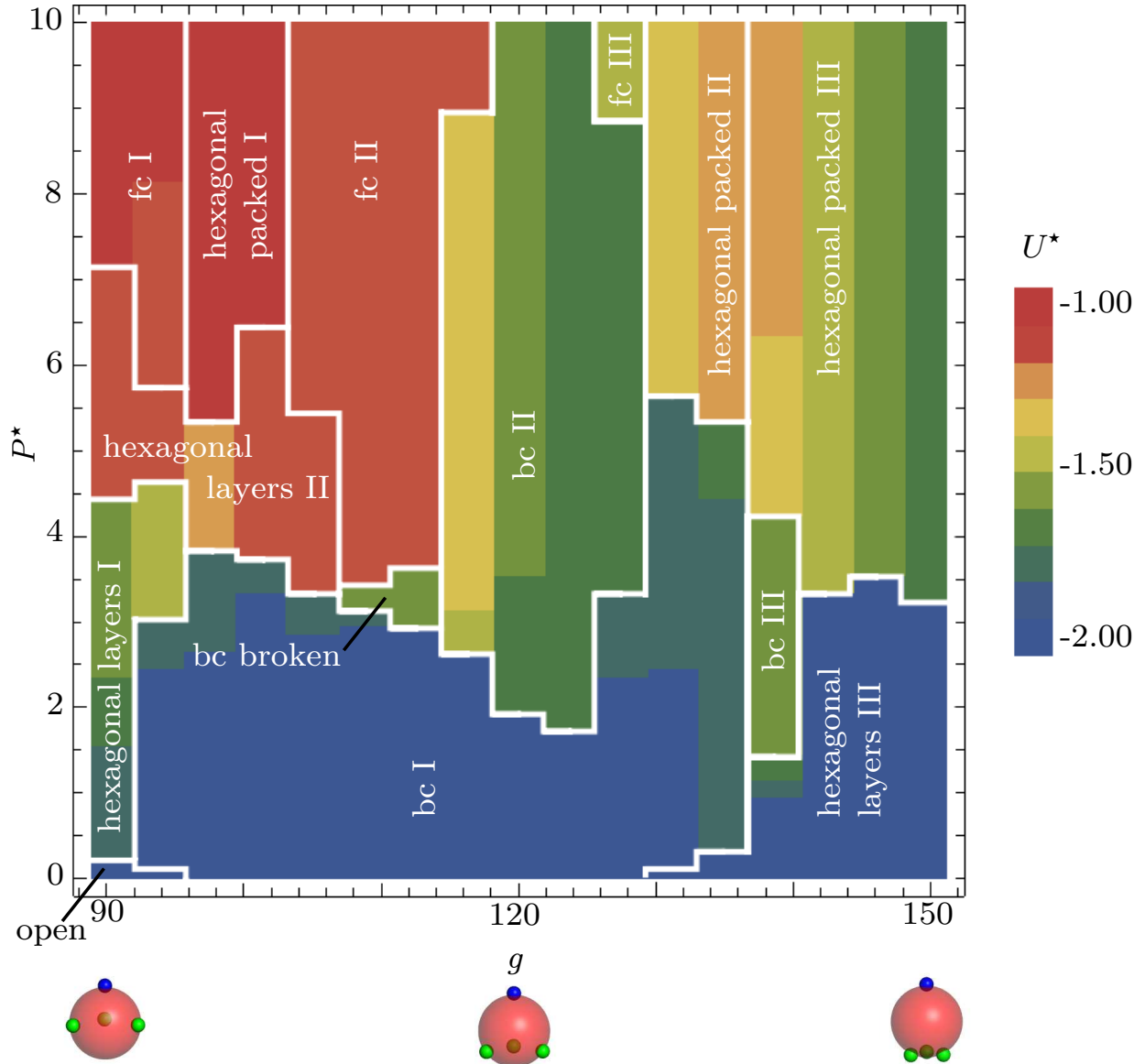
Figure 4.26.: Contour plot of the reduced energy $U^\star = U/(N\epsilon)$ of the identified minimum enthalpy structures as a function of the geometry parameter g and the reduced pressure $P^\star = P\sigma^3/\epsilon$; the color code is displayed on the right. White boundaries indicate the limits of stability of the respective ordered structures on the underlying $(g, P^\star)$-grid. "bc" stands for body-centered lattices, "fc" for face-centered lattices.
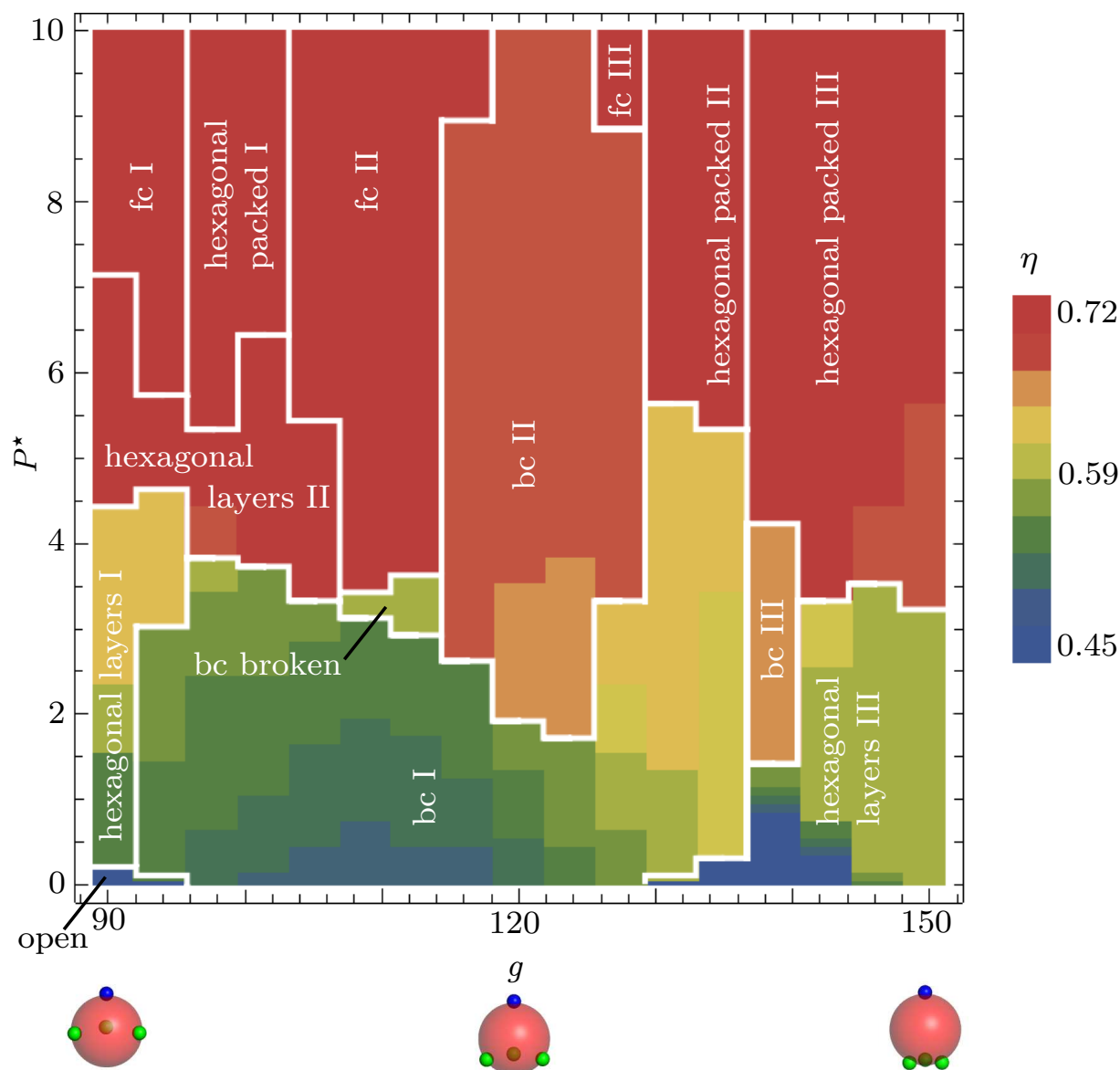
Figure 4.27.: Contour plot of the packing fraction η of the identified minimum enthalpy structures as a function of the geometry parameter g and the reduced pressure $P^\star = P\sigma^3/\epsilon$; the color code is displayed on the right (its range is cut off at $\eta = 0.45$, *i.e.*, all values below 0.45 appear in the same color). White boundaries indicate the limits of stability of the respective ordered structures on the underlying $(g, P^\star)$-grid. "bc" stands for body-centered lattices, "fc" for face-centered lattices.

marginal) role in the energy calculations, which can lead to $U^\star$ values slightly larger then 2.00 for fully bonded systems.

When the region of stability of an identified structure spans over a larger region in the phase diagram, the $U^\star$- and η values can considerably vary, especially on the g coordinate. Therefore we report intervals of values in such cases.

We will use the following abbreviations:

- NP: north pole patch

- SH: patches located on the southern hemisphere of a particle (on the equator for $g = 90$)

- % OBE: percent of the optimal binding energy (of a single bond)

- fc(c): face centered (cubic)

- bc(c): body centered (cubic)

- h(c)p: hexagonal (close) packed

As labeled in Figs. 4.26 and 4.27, we categorize the identified equilibrium structures into 14 types:

1. "**open**": For the lowest two values of g taken into account and very small pressure, we observe a fully bonded staggered honeycomb lattice with very low packing fraction (see Fig. 4.28, top panel) corresponding to the global enthalpy minimum. The honeycomb-pattern in the layers making up this structure is induced by the bonds formed between the SH patches; the layers are interconnected by NP-NP bonds.

g	stability	binding energy	packing fraction
90.00	$P^\star < 0.3$	$U^\star \approx -2.02$	$0.340 \lesssim \eta \lesssim 0.341$
93.75	$P^\star < 0.1$	$U^\star \approx -2.02$	$\eta \approx 0.269$

2. "**hexagonal layers I**": For $g = 90.00$, the open structure is transformed into a hexagonally layered configuration (see Fig. 4.28, center panel) at $P^\star \approx 0.3$. This configuration is also stable in an intermediate pressure region for $g = 93.75$ and is characterized by strong SH-SH inter-layer bonds and slightly weaker NP-SH intra-layer bonds ($U^\star_{\text{Bond}} \approx 85$ % OBE).

g	stability	binding energy	packing fraction
90.00	$0.3 < P^\star < 4.4$	$-1.86 \lesssim U^\star \lesssim -1.55$	$0.533 \lesssim \eta \lesssim 0.638$
93.75	$3.1 < P^\star < 4.6$	$-1.54 \lesssim U^\star \lesssim -1.52$	$0.641 \lesssim \eta \lesssim 0.645$

3. "**hexagonal layers II**": A further increase of pressure stabilizes a second, much denser and rather weakly bonded, hexagonally layered structure (see Fig. 4.28, bottom panel). Its region of stability spans over a large interval on the geometry-coordinate: $90.00 \lesssim g \lesssim 105.00$. As for all relatively dense configurations, the variations in energy and

especially packing fraction are small. The NP patches form strong inter-layer bonds, more specifically, each layer is bonded with one of its two adjacent layers in this way. One of the SH patches on each particle engages in an intra-layer bond of similar strength. The remaining SH patches interact only very weakly ($3 \lesssim U^\star_{\mathrm{Bond}} \lesssim 20$ % OBE).

g	stability	binding energy	packing fraction
90.00	$4.4 < P^\star < 7.1$	$U^\star \approx -1.19$	$0.708 \lesssim \eta \lesssim 0.709$
93.75	$4.6 < P^\star < 5.7$	$U^\star \approx -1.18$	$\eta \approx 0.709$
97.50	$3.8 < P^\star < 5.3$	$-1.23 \lesssim U^\star \lesssim -1.22$	$0.695 \lesssim \eta \lesssim 0.699$
101.25	$3.7 < P^\star < 6.4$	$-1.20 \lesssim U^\star \lesssim -1.19$	$0.698 \lesssim \eta \lesssim 0.700$
105.00	$3.3 < P^\star < 5.4$	$U^\star \approx -1.20$	$0.697 \lesssim \eta \lesssim 0.698$

4. "**fc I**": For the two lowest g values and for high pressure, we encounter an almost close packed, fcc-like structure (*i.e.*, an ABCABC.. stacking of hexagonal layers; see Fig. 4.29, top panel). In this configuration, the NP patches engage in long-distance bonds ($r \approx 1.32$, $U^\star_{\mathrm{Bond}} \approx 61$ % OBE); one of the SH patches on each particle forms a strong bond with one of its counterparts on a neighboring particle and the remaining two SH patches form wide-angle bonds, with $U^\star_{\mathrm{Bond}} \approx 20$ % OBE. The packing fraction of this structure is among the highest ones encountered in this phase diagram.

g	stability	binding energy	packing fraction
90.00	$P^\star > 7.1$	$-1.08 \lesssim U^\star \lesssim -1.07$	$\eta \approx 0.724$
93.75	$P^\star > 5.8$	$-1.11 \lesssim U^\star \lesssim -1.09$	$0.721 \lesssim \eta \lesssim 0.723$

5. "**hexagonal packed I**": For $g = 97.50$ and $g = 101.25$, the high pressure structure is hcp-like (*i.e.*, an ABAB.. stacking of hexagonal layers, see Fig. 4.29, center panel). This is the most weakly bonded equilibrium configuration encountered in the whole parameter space investigated. The packing fraction is only slightly lower than the value for close packed hard spheres. Similarly to the "hexagonal layers II" structure, the NP patches form bonds with each other, connecting neighboring layers. But unlike in the aforementioned configuration, the SH patches form only long-distance and wide-angle bonds with $10 \lesssim U^\star_{\mathrm{Bond}} 40$ % OBE.

g	stability	binding energy	packing fraction
97.50	$P^\star > 5.3$	$-1.09 \lesssim U^\star \lesssim -1.07$	$0.722 \lesssim \eta \lesssim 0.724$
101.25	$P^\star > 6.4$	$-1.04 \lesssim U^\star \lesssim -1.03$	$\eta \approx 0.724$

6. "**fc II**": The high pressure equilibrium configuration for $105.00 \lesssim g \lesssim 116.25$ is another face centered structure (see Fig. 4.29, bottom panel). Each particle has two bonded SH patches, which lead, with additional, very minor wide-angle contributions ($U^\star_{\mathrm{Bond}} \approx 4$ % OBE), to binding energies $-1.14 \lesssim U^\star \lesssim -1.11$. The density of this configuration is also near close packing, but slightly lower than for the two structure types described

before.

g	stability	binding energy	packing fraction
105.00	$P^\star > 5.4$	$-1.12 \lesssim U^\star \lesssim -1.11$	$0.711 \lesssim \eta \lesssim 0.713$
108.75	$P^\star > 3.4$	$-1.13 \lesssim U^\star \lesssim -1.12$	$0.709 \lesssim \eta \lesssim 0.710$
112.50	$P^\star > 3.6$	$-1.14 \lesssim U^\star \lesssim -1.11$	$0.709 \lesssim \eta \lesssim 0.712$
116.25	$P^\star > 8.9$	$U^\star \approx -1.13$	$\eta \approx 0.713$

7. "**bc I**": This structure covers by far the largest region of stability in the low-pressure domain of the $(g, P^\star)$-phase diagram, which extends within the intervals $93.75 \lesssim g \lesssim 135.00$ and $0.0 \lesssim P^\star \lesssim 5.6$. Because of these large variations, the structure type undergoes substantial particle rearrangements as g is increased (see Fig. 4.30, bottom panel for a comparison), and the characteristic values $U^\star$ and η vary within large intervals. Nevertheless, we categorize the emerging configurations as being of a single structure type, since the particles always bond in the same pattern: we observe two inter-penetrating, but virtually non-interacting, fully bonded sublattices, with NP-SH and SH-SH bonds. At $g \approx 109.47$ (*i.e.*, the patches are located on a perfectly symmetric tetrahedron), the two sublattices are perfect diamond cubic structures and the full lattice is body centered cubic (bcc). As the sublattices do not interact attractively, they can freely move relative to each other (the movement is only restricted by the repulsion of the colloidal particle cores). Indeed, we observe a slight shifting of the sublattices against each other at geometries close to the symmetric tetrahedron, which leads to a slightly lower enthalpy than the perfectly symmetrical bcc configuration (see Fig. 4.30, top panel). This is due to more optimal bond lengths (*i.e.*, $r = \sqrt[6]{2} \approx 1.122$), which can be retained at higher densities in the shifted configuration.

g	stability	binding energy	packing fraction
93.75	$0.1 < P^\star < 3.0$	$-1.84 \lesssim U^\star \lesssim -2.01$	$0.529 \lesssim \eta \lesssim 0.571$
97.50	$P^\star < 3.8$	$-2.02 \lesssim U^\star \lesssim -1.81$	$0.509 \lesssim \eta \lesssim 0.581$
101.25	$P^\star < 3.7$	$-2.02 \lesssim U^\star \lesssim -1.85$	$0.497 \lesssim \eta \lesssim 0.567$
105.00	$P^\star < 3.3$	$-2.03 \lesssim U^\star \lesssim -1.83$	$0.487 \lesssim \eta \lesssim 0.560$
108.75	$P^\star < 3.1$	$-2.03 \lesssim U^\star \lesssim -1.87$	$0.482 \lesssim \eta \lesssim 0.546$
112.50	$P^\star < 2.9$	$-2.03 \lesssim U^\star \lesssim -1.87$	$0.484 \lesssim \eta \lesssim 0.547$
116.25	$P^\star < 2.6$	$-2.03 \lesssim U^\star \lesssim -1.92$	$0.493 \lesssim \eta \lesssim 0.550$
120.00	$P^\star < 1.9$	$-2.03 \lesssim U^\star \lesssim -1.94$	$0.508 \lesssim \eta \lesssim 0.566$
123.75	$P^\star < 1.7$	$-2.03 \lesssim U^\star \lesssim -2.00$	$0.533 \lesssim \eta \lesssim 0.570$
127.50	$P^\star < 3.3$	$-2.03 \lesssim U^\star \lesssim -1.85$	$0.553 \lesssim \eta \lesssim 0.637$
131.25	$0.1 < P^\star < 5.6$	$-1.94 \lesssim U^\star \lesssim -1.83$	$0.593 \lesssim \eta \lesssim 0.638$
135.00	$0.3 < P^\star < 5.3$	$-1.82 \lesssim U^\star \lesssim -1.74$	$0.606 \lesssim \eta \lesssim 0.632$

8. "**bc broken**": In a very small region ($g = 108.75, 112.50, 2.9 \lesssim P^\star \lesssim 3.6$) of the zero-temperature phase diagram, we observe a variation of the bc-like structure, which we term "bc-broken" (see Fig. 4.30, center panel). Compared to the "bc I" configuration

in the double-diamond description, bonds between two oppositely located pairs of particles within each six-particle ring are broken (also *cf.* Fig. 4.38, panels I and L); the emerging half-rings are slightly distorted and displaced with respect to each other. This results in a higher packing fraction (increased by 9.8 %) but a substantially weaker bonding term (decreased by 14.2 %).

g	stability	binding energy	packing fraction
108.75	$3.1 < P^\star < 3.4$	$U^\star \approx -1.63$	$\eta \approx 0.593$
112.50	$2.9 < P^\star < 3.6$	$U^\star \approx -1.63$	$\eta \approx 0.599$

9. "**bc II**": This structure spans over a wide range on the pressure coordinate and is observed for geometries $116.25 \lesssim g \lesssim 127.50$. These patch geometries (*i.e.*, the SH patch-vectors form angles close to 90 degrees between each other) allow for three and a half bonds per particle in a dense bcc-like configuration: all the SH patches are able to bond with their counterparts on neighboring particles, while only half of the NP patches engage in NP-NP bonding. This configuration is the only one with a packing fraction $\eta < 0.70$, which represents the global enthalpy minimum in its g region, even at the highest pressure value we considered in our calculations. A visual representation can be found in Fig. 4.31, top panel.

g	stability	binding energy	packing fraction
116.25	$2.6 < P^\star < 8.9$	$-1.44 \lesssim U^\star \lesssim -1.41$	$0.675 \lesssim \eta \lesssim 0.684$
120.00	$P^\star > 1.9$	$-1.66 \lesssim U^\star \lesssim -1.59$	$0.670 \lesssim \eta \lesssim 0.685$
123.75	$P^\star > 1.7$	$-1.75 \lesssim U^\star \lesssim -1.68$	$0.671 \lesssim \eta \lesssim 0.685$
127.50	$3.3 < P^\star < 8.8$	$U^\star \approx -1.66$	$0.683 \lesssim \eta \lesssim 0.684$

10. "**fc III**": The third fcc-like structure (see Fig. 4.31, center panel) we identified represents the global enthalpy minimum for only one geometry value and at high pressures. We observe three SH-SH bonds per particle, one of them being of long-distance type and therefore considerably weaker ($U^\star_{\text{Bond}} \approx 67\ \%$ OBE). The NP patches are unbonded in this configuration.

g	stability	binding energy	packing fraction
127.50	$P^\star > 8.8$	$U^\star \approx -1.44$	$\eta \approx 0.706$

11. "**hexagonal packed II**": For more elongated patch geometries ($g \approx 131.25, 135.00$), the high pressure configuration is hcp-like again (see Fig. 4.31, bottom panel). The bonding pattern of this structure is very peculiar: all the patches form bonds, but none of these is fully optimized. Within the hexagonal layers, NP and SH patches form wide-angle bonds with $U^\star_{\text{Bond}} \approx 65\ \%$ OBE, while the remaining patches form long-distance inter-layer bonds with $U^\star_{\text{Bond}} \approx 53\ \%$ OBE.

g	stability	binding energy	packing fraction
131.25	$P^\star > 5.6$	$U^\star \approx -1.34$	$0.711 \lesssim \eta \lesssim 0.712$
135.00	$P^\star > 5.3$	$-1.26 \lesssim U^\star \lesssim -1.23$	$0.711 \lesssim \eta \lesssim 0.714$

12. "**hexagonal layers III**": The low pressure equilibrium structure for the most elongated geometries ($g \gtrsim 131.25$) is a stacking of hexagonally arranged layers (see Fig. 4.32, top panel). All the patches are fully bonded and adjacent layers are alternatingly connected *via* three SH-SH bonds or one NP-NP bond per particle. This bonding pattern controls the packing fraction within the hexagonal layers, which strongly increases with g. Consequently, the region of stability of this structure on the pressure coordinate also heavily depends on g. At $g = 138.75$, the binding energy increases with pressure considerably faster than at higher g values. This is caused by the SH-SH bonds arranging in less optimal angles ($7° \lesssim \Theta_i \lesssim 10°$, leading to bonds with 67 to 80 % OBE), in order to increase the packing fraction.

g	stability	binding energy	packing fraction
131.25	$P^\star < 0.1$	$U^\star \approx -2.03$	$\eta \approx 0.306$
135.00	$P^\star < 0.3$	$-2.03 \lesssim U^\star \lesssim -2.01$	$0.336 \lesssim \eta \lesssim 0.356$
138.75	$P^\star < 1.4$	$-2.04 \lesssim U^\star \lesssim -1.73$	$0.378 \lesssim \eta \lesssim 0.566$
142.50	$P^\star < 3.3$	$-2.06 \lesssim U^\star \lesssim -1.90$	$0.438 \lesssim \eta \lesssim 0.601$
146.25	$P^\star < 3.5$	$-2.10 \lesssim U^\star \lesssim -2.06$	$0.535 \lesssim \eta \lesssim 0.597$
150.00	$P^\star < 3.2$	$-2.15 \lesssim U^\star \lesssim -2.12$	$0.580 \lesssim \eta \lesssim 0.594$

13. "**bc III**": For $g \approx 138.75$, we observe an additional body-centered intermediate pressure configuration (see Fig. 4.32, center panel). This configuration shows three bonds per particle, one connecting NP patches and two connecting SH patches to each other.

g	stability	binding energy	packing fraction
138.75	$1.4 < P^\star < 4.2$	$-1.56 \lesssim U^\star \lesssim -1.54$	$0.650 \lesssim \eta \lesssim 0.655$

14. "**hexagonal packed III**": Finally, the high pressure minimum enthalpy structure for $g \gtrsim 138.75$ is another hcp-like configuration (see Fig. 4.32, bottom panel). This structure is closely related to the "hexagonal layers III"-configuration: starting from the fully bonded configuration, the particles are tilted (in alternating directions in adjacent layers), thereby making one of the SH-SH bonds on each particle long-range and wide-angle, so that it retains only ≈ 13 % of its binding energy. The total energy of the configuration is strongly decreasing with g. The beneficial effect of this tilting is a considerable reduction of the inter-layer distance, leading to a packing fraction of $\eta \approx 0.70$.

g	stability	binding energy	packing fraction
138.75	$P^\star > 4.2$	$-1.33 \lesssim U^\star \lesssim -1.29$	$0.699 \lesssim \eta \lesssim 0.704$
142.50	$P^\star > 3.3$	$-1.49 \lesssim U^\star \lesssim -1.44$	$0.697 \lesssim \eta \lesssim 0.703$
146.25	$P^\star > 3.5$	$-1.61 \lesssim U^\star \lesssim -1.57$	$0.695 \lesssim \eta \lesssim 0.701$
150.00	$P^\star > 3.2$	$-1.71 \lesssim U^\star \lesssim -1.66$	$0.694 \lesssim \eta \lesssim 0.700$

1
"open"

2
"hexagonal layers I"

3
"hexagonal layers II"

Figure 4.28.: Perpendicular views of ordered structures with regions of stability in the $T = 0$ phase diagram (Figs. 4.26 and 4.27). Particular configurations obtained for $g = 93.75$, $P^\star = 0.00$ (top), $g = 93.75$, $P^\star = 4.00$ (center) and $g = 93.75$, $P^\star = 5.00$ (bottom) are displayed.

4
"fc I"

5
"hexagonal packed I"

6
"fc II"

Figure 4.29.: Perpendicular views of ordered structures with regions of stability in the $T = 0$ phase diagram (Figs. 4.26 and 4.27). Particular configurations obtained for $g = 93.75$, $P^\star = 6.00$ (top), $g = 101.25$, $P^\star = 8.00$ (center) and $g = 108.75$, $P^\star = 6.00$ (bottom) are displayed.

7
"bc I"

8
"bc
broken"

Figure 4.30.: Perpendicular views of ordered structures with regions of stability in the $T = 0$ phase diagram (Figs. 4.26 and 4.27). Particular configurations obtained for $g = 108.75$, $P^\star = 2.00$ (top) and $g = 108.75$, $P^\star = 3.20$ (center) are displayed. Bottom: Views of the structure "bc I" with increasing values of the geometry parameter (from left to right): $g = 93.75$ (the flattest geometry for which the structure is stable), $g = 109.47$ (tetrahedral symmetry of the patch decoration/true bcc structure), $g = 135$ (the most elongated geometry for which the structure is stable).

9
"bc II"

10
"fc III"

11
"hexagonal
packed
II"

Figure 4.31.: Perpendicular views of ordered structures with regions of stability in the $T = 0$ phase diagram (Figs. 4.26 and 4.27). Particular configurations obtained for $g = 123.75$, $P^\star = 6.00$ (top), $g = 127.50$, $P^\star = 9.00$ (center) and $g = 135.00$, $P^\star = 8.00$ (bottom) are displayed.

12
"bc III"

13
"hexagonal layers III"
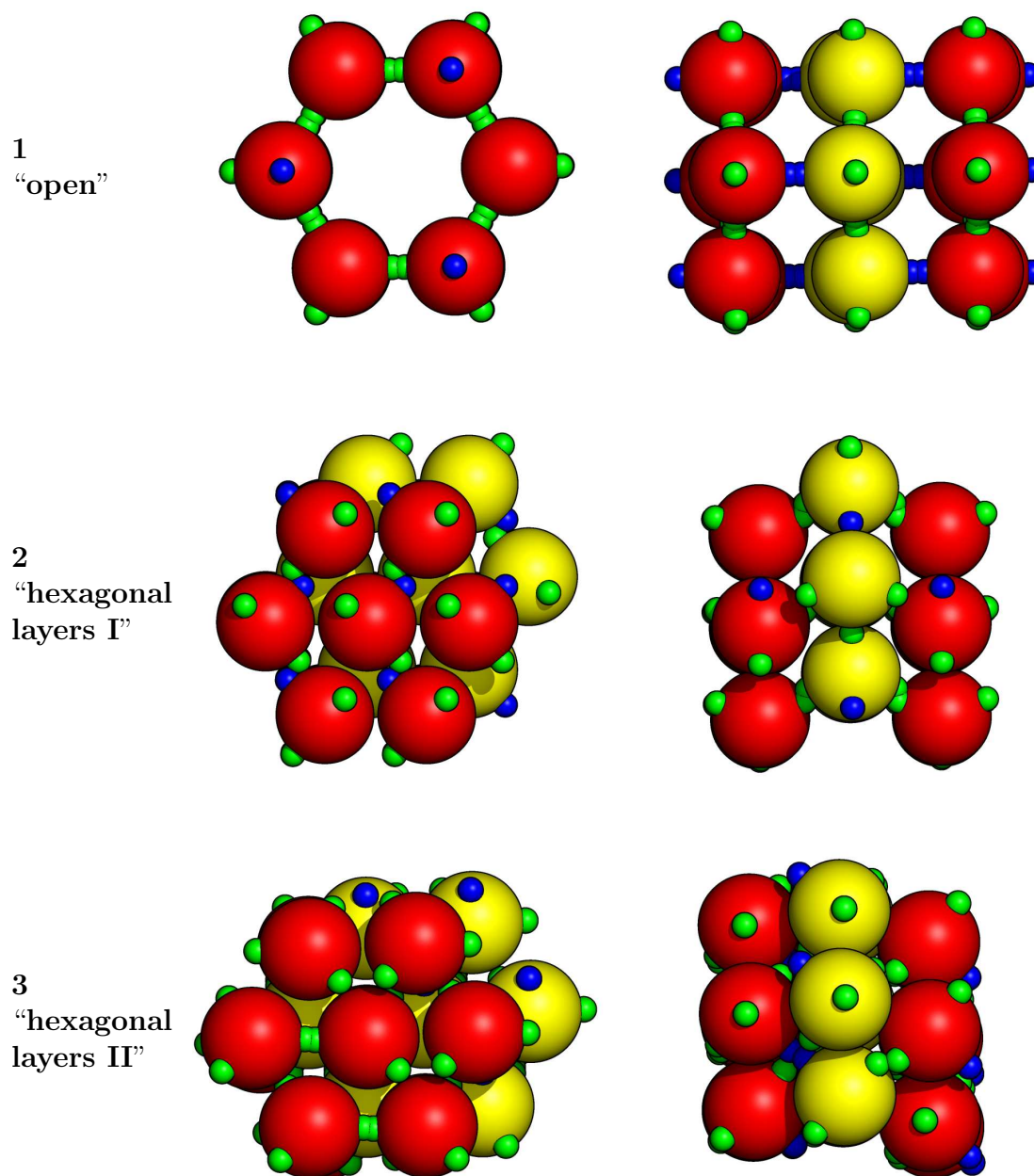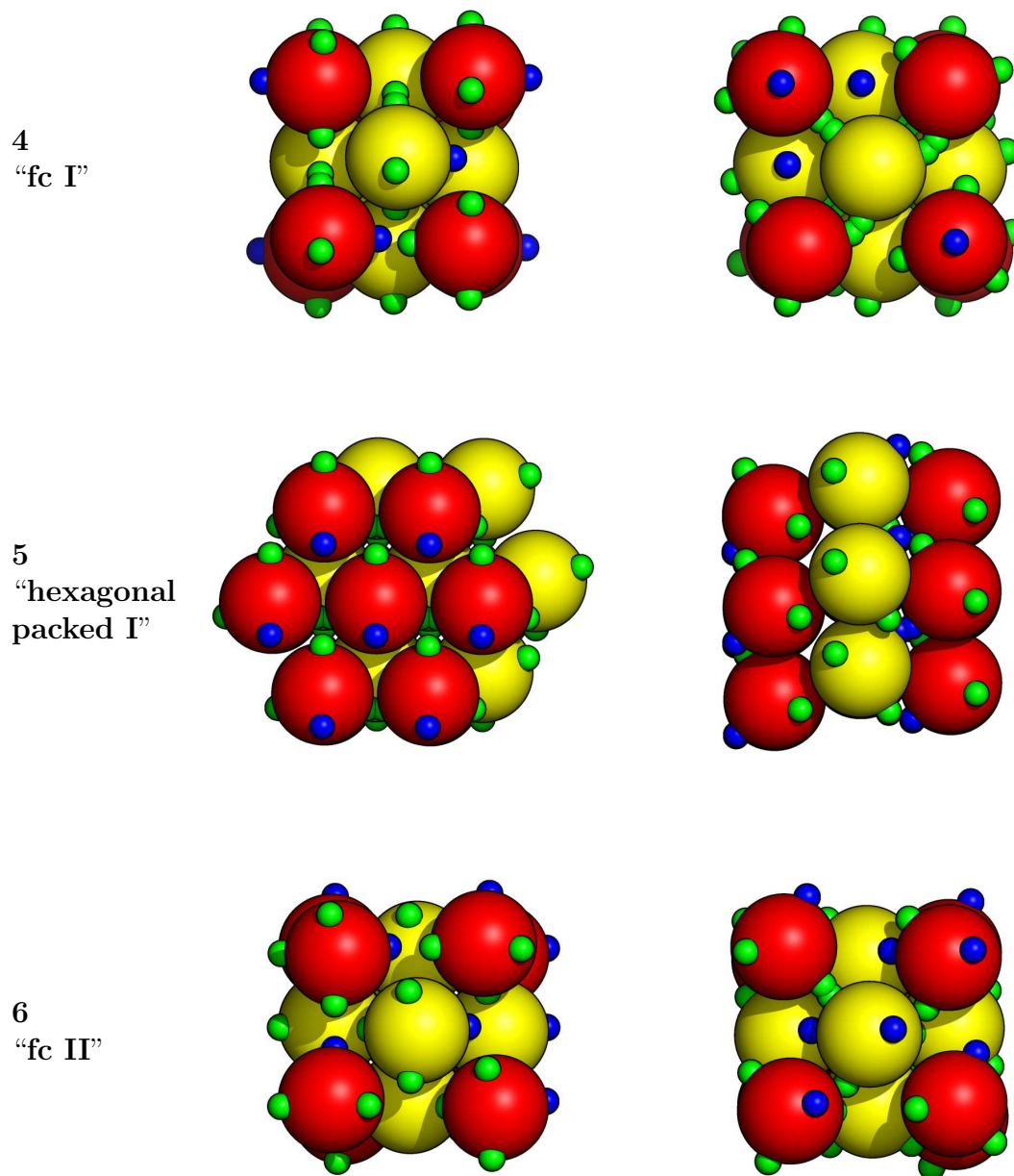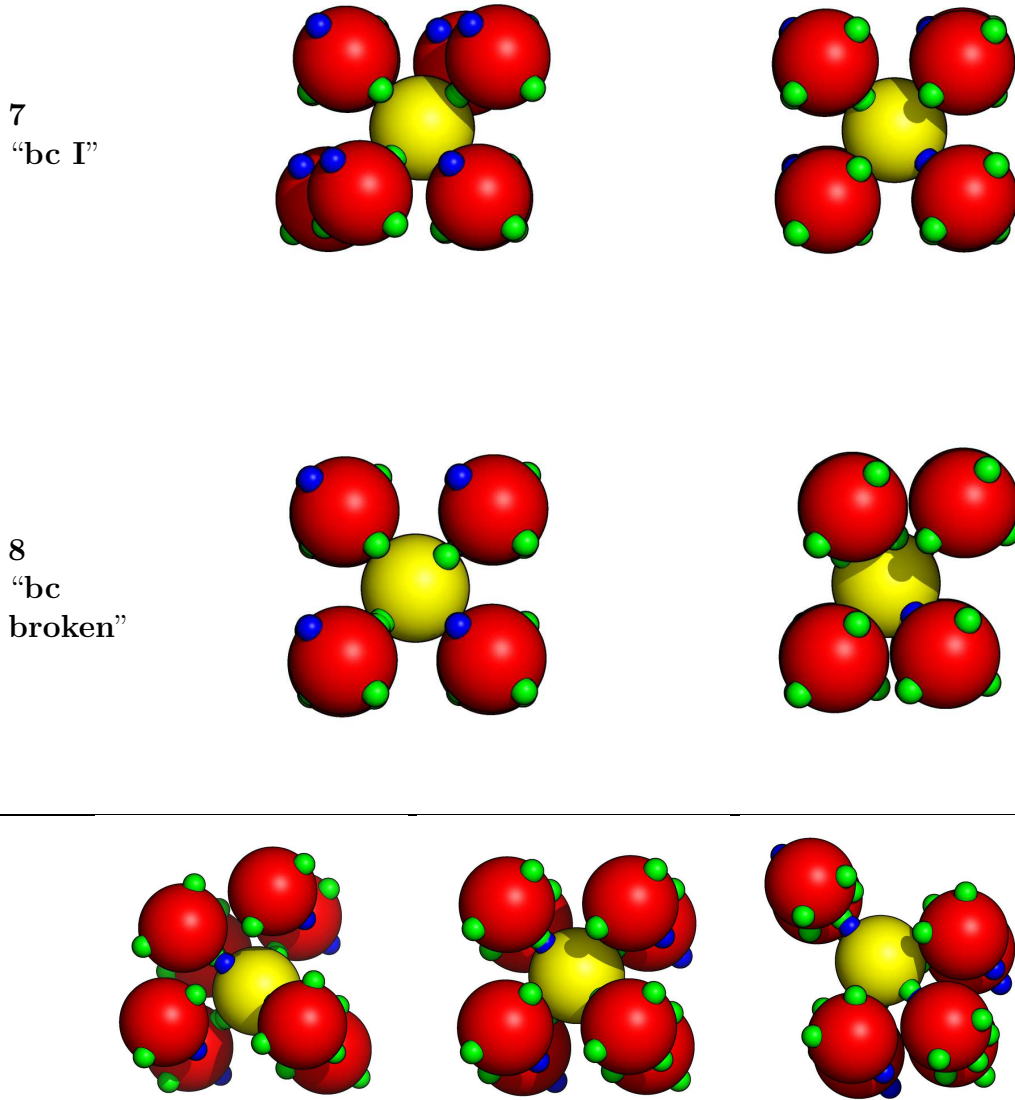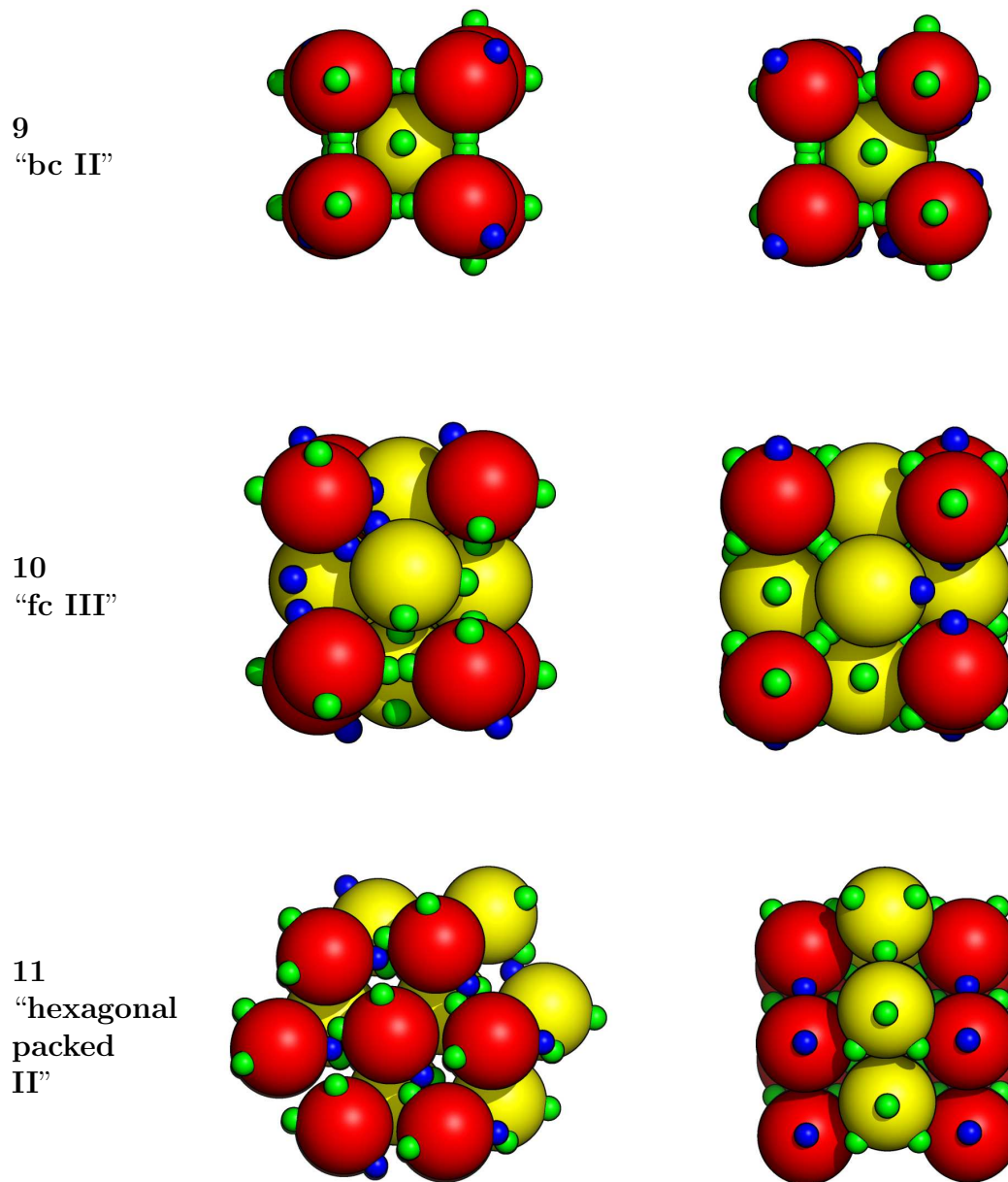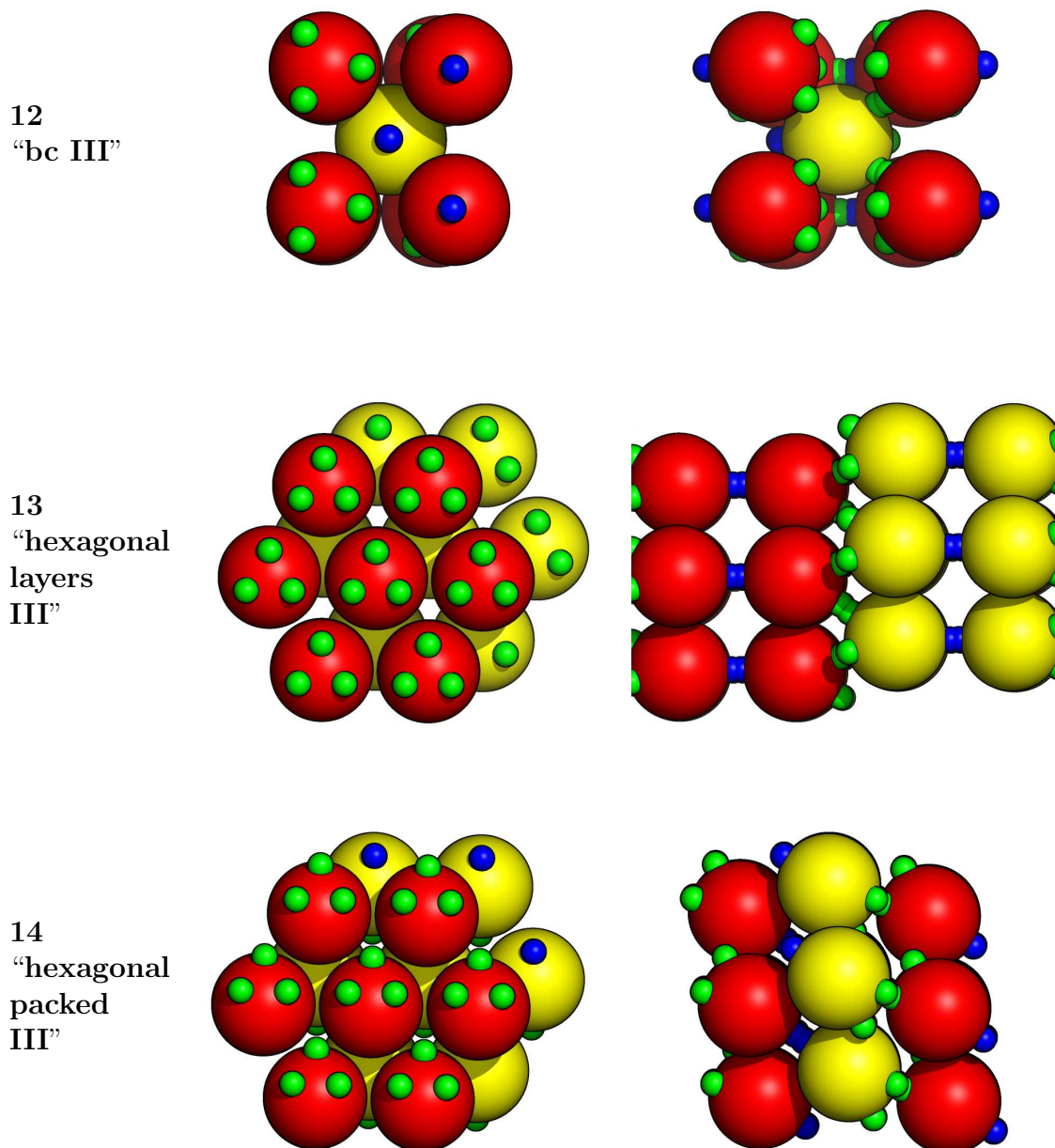

14
"hexagonal packed III"

Figure 4.32.: Perpendicular views of ordered structures with regions of stability in the $T = 0$ phase diagram (Figs. 4.26 and 4.27). Particular configurations obtained for $g = 138.75$, $P^\star = 3.00$ (top), $g = 150.00$, $P^\star = 2.00$ (center) and $g = 150.00$, $P^\star = 6.00$ (bottom) are displayed.

Competing Local Minima

In this section, we extend our focus from the global minima on the enthalpy landscape to competing local minima. These local minima can become essential at finite temperature, as entropic contributions to the Gibbs free energy $G = H - TS$ start to play an important role. As sketched in Sec. 3.3, it is very hard to take these entropic effects directly into account in an optimization algorithm. Instead, we employed the two-step scheme described in Sec. 3.3: enthalpy optimizations and subsequent Frenkel-Ladd type full free energy calculations [108, 114] are carried out, in order to obtain the finite temperature phase diagram of the studied system.

Since the free energy calculations were entirely performed by our collaborator Eva Noya, we will keep our focus in this thesis on the first step of this approach, namely the identification of candidate structures. The finite temperature results have been published in Refs. [6, 7]. Some of the following results have also been compared to structures obtained from a variable box shape simulation-based optimization method, as described in Ref. [115].

In Figs. 4.33-4.40 we display visual representations of the lowest-lying local enthalpy minima for four different geometries g, at three different pressure values $P^\star$ for each g. The first figure in each group (*i.e.*, the barchart) shows the enthalpy values for each minimum, along with the two relevant contributions to this quantity. These are the lattice sums and the packing fractions. These quantities are shown separately for each selected pressure value, in relative units of the corresponding values of the most favorable lattice structures with respect to the enthalpy. Thus, $U_i/U_{opt} > 1 (< 1)$ - where the index "i" stands for any of the considered structures and the index "opt" indicates the most favorable lattice - correspond to a higher (lower) degree of bond saturation than realized in the optimal particle configuration. Similarly, $\eta_i/\eta_{opt} > 1$ (< 1) indicates a better (worse) packing of particles as compared to the most favorable lattice.

In an effort to introduce order into the zoo of emerging structures, we label configurations, which have already been identified as global minima in the previous section by the numbers introduced there; on the other hand, the newly encountered structures that only occur as local enthalpy minima are labeled by capital letters.

g = 90.00

$\underline{P^\star = 0.5:}$ For the flattest patch decoration (*i.e.*, with three patches on the equator) and rather low pressure, the global minimum corresponds to, as reported in the previous section, the "hexagonal layers I" configuration. The second-lowest enthalpy minimum is represented by the "open" structure, which is, as reported, the equilibrium configuration for even lower pressure. As the third-lowest minimum, which is very close to the "open" configuration in enthalpy, we identify a structure first mentioned in Ref. [115] and termed "honeycomb double layered" (*cf.* Fig. 4.34, label A). Here, the particles arrange in honeycomb cells with additional particles located in the central voids of the cells. In each layer, one bond per

particle with one of the neighboring layers (either NP-NP or NP-SH) and no bonds at all with the other one are formed. The bonding pattern in two adjacent honeycomb layers is quite different: in a type A layer, the six particles on the rim of each honeycomb cell bond to each other (SH-SH), while the central particle does not bond with them at all. In a type B layer, the particles on the rim do not bond with each other, while three of them engage in bonding with the central particle (SH-SH). In this rather complex pattern, eleven out of twelve possible bonds in the six-particle primitive cell can be realized. The fourth local enthalpy minimum corresponds to the fully bonded* "bc I" structure, which has a wide region of stability for higher g values; at $g = 90.00$ however, many of the bonds can not be sufficiently optimized in this arrangement, therefore the structure is not stable at zero temperature for this patch geometry.

index	classification	$H^\star$	$U^\star$	η
2	hexagonal layers I	-1.37	-1.88	0.52
1	open	-1.26	-2.01	0.35
A	honeycomb double layered	-1.25	-1.77	0.50
7	bc I	-1.17	-1.70	0.50

$\underline{P^\star = 2.5:}$ On increasing pressure, we observe three competing structures. The global minimum corresponds to the "hexagonal layers I" configuration. "Hexagonal layers II" already represents the second-lowest minimum here. Notably, at this pressure, the structure forms an additional inter-layer SH-SH bond, which is traded off by a lower packing fraction compared to the version representing the global minimum at higher pressure; in Fig. 4.34, label 3, we show the low $P^\star$ version, for the high $P^\star$ version, we refer to Fig. 4.28, bottom panel). Finally, the third local minimum corresponds to a bc-like structure that has not been previously identified. Here, the NP patch and one of the SH patches on each particle strongly bond with their respective counterparts on neighboring particles. The remaining SH patches contribute to the binding energy *via* long-distance and slightly wide-angle bonds ($r \approx 1.56$, $U^\star_{\rm Bond} \approx 0.18$ % OBE). This structure has a considerably higher packing fraction than the competing ones, but due to its rather high energy value it is never stable at vanishing temperature.

index	classification	$H^\star$	$U^\star$	η
2	hexagonal layers I	0.47	-1.65	0.62
3	hexagonal layers II (low $P^\star$)	0.54	-1.52	0.64
B	bc-like	0.65	-1.25	0.69

$\underline{P^\star = 4.5:}$ At intermediate pressure, the "hexagonal layers II" structure in its denser version represents the global enthalpy minimum, while the very close second-lowest minimum corresponds to the bc-like structure already identified at $P^\star = 2.5$. The almost close packed "fc I" configuration differs only slightly in reduced enthalpy as well. The "hexagonal layers

---

*In a sense that all patches engage in bonds with $U^\star > 50$ % OBE.

I" structure corresponds only to the fourth-lowest local minimum here and its enthalpy is considerably higher.

index	classification	$H^\star$	$U^\star$	η
3	hexagonal layers II (high $P^\star$)	2.14	-1.19	0.71
B	bc-like	2.15	-1.25	0.69
4	fc I	2.16	-1.15	0.71
2	hexagonal layers I	2.23	-1.37	0.65
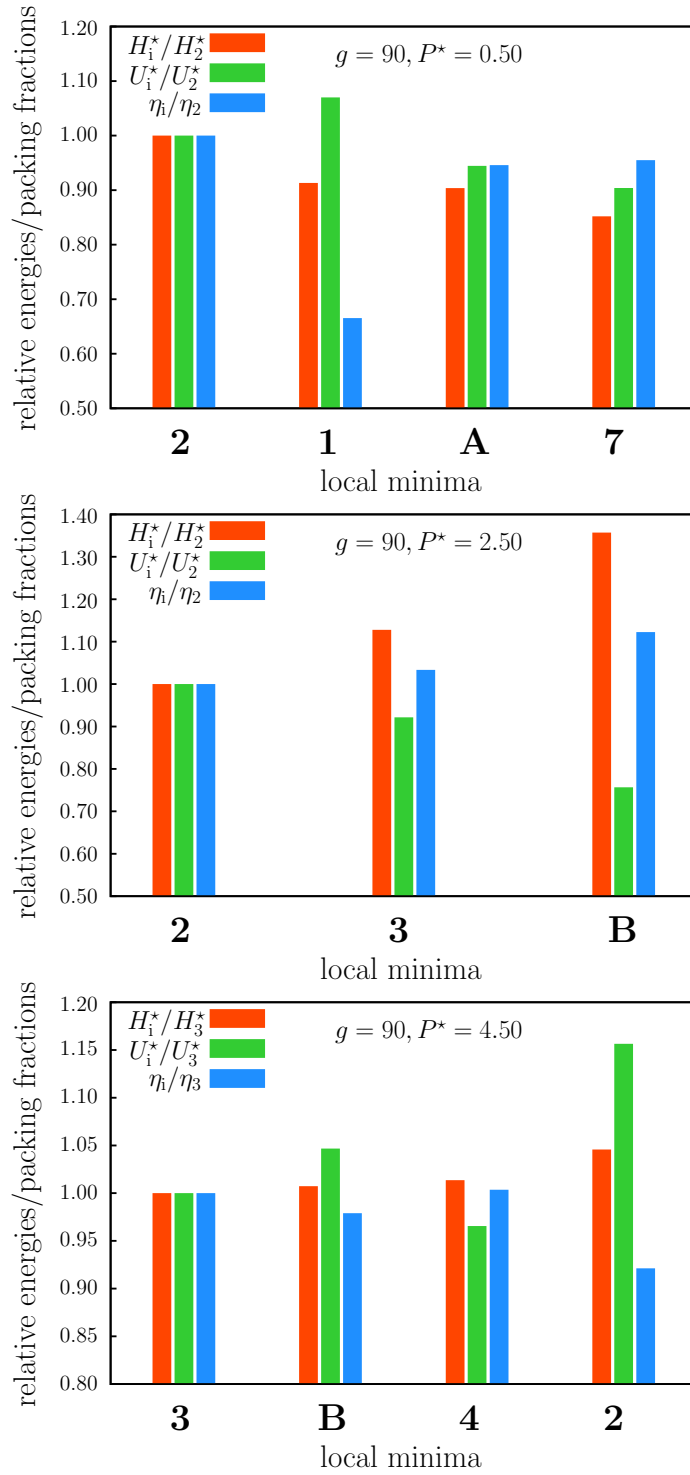
Figure 4.33.: Enthalpies $H_i^\star$, binding energies (*i.e.*, lattice sums) $U_i^\star$, and packing fractions η_i of the lowest, structurally different local enthalpy minima identified by the EA at $g = 90.00$ for different $P^\star$ values, where i stands for a structure label. Values are given in units of the respective values of the energetically most favorable lattice at each $P^\star$ value. At the lowest pressure, $H_i^\star < 0$, therefore high relative values are favorable, while for the higher $P^\star$ values the opposite is the case.
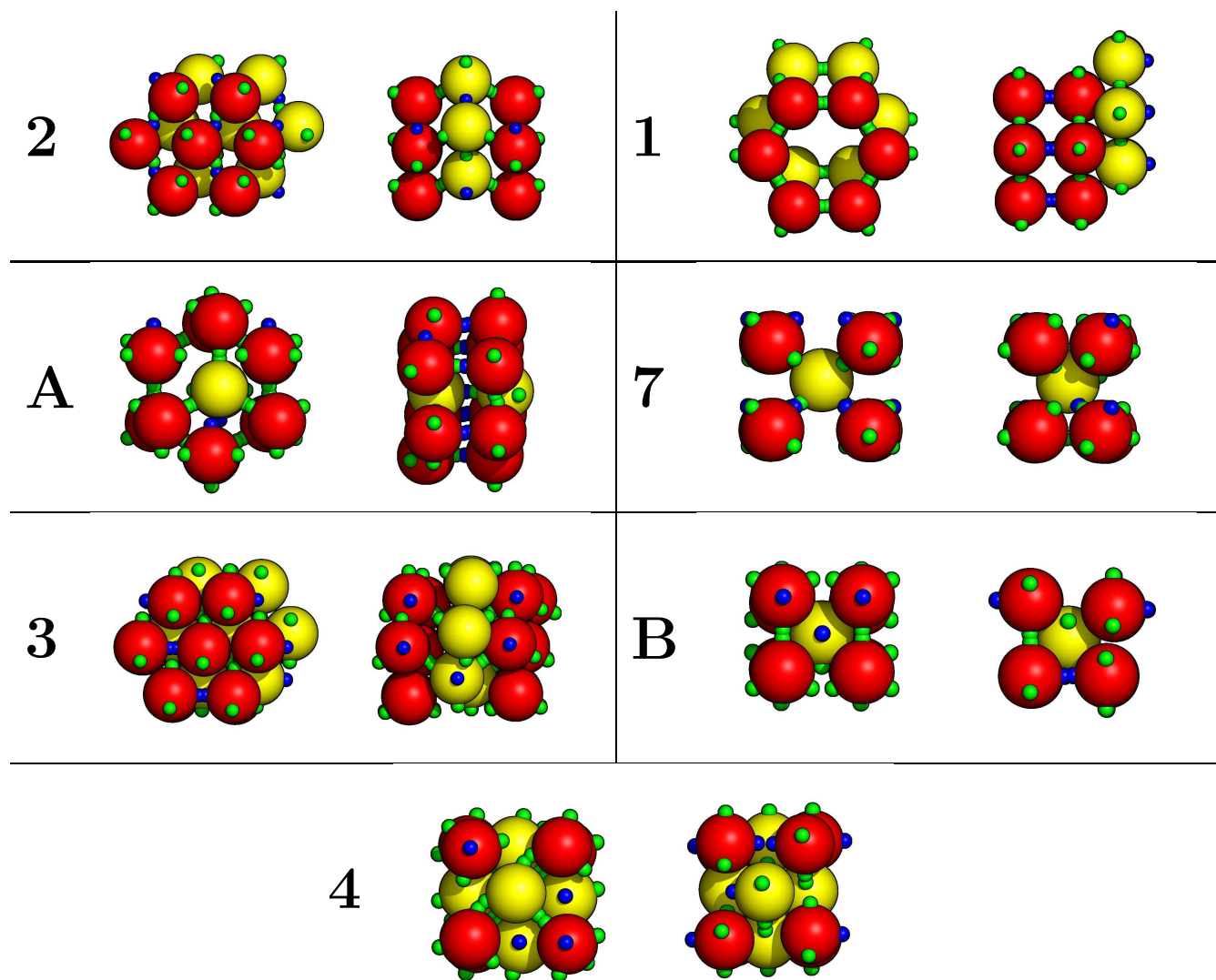
Figure 4.34.: Visualizations of the structures corresponding to local minima at $g = 90.00$. For the structure labels see text.

g = 109.47 (regular tetrahedral symmetry)

<u>$P^\star = 0.1$:</u> For the symmetrical tetrahedral geometry[*] and very low pressure, we observe four competing enthalpy minima, which are all fully bonded. The global minimum is represented by the shifted "bc I" configuration, which has a tiny advantage in binding energy over the fully symmetrical bcc structure. The third enthalpy minimum is structurally degenerate and is represented by both a cubic diamond and a hexagonal diamond structure. The structural difference between these configurations is illustrated in Fig. 4.36, labels C and D. In a cubic diamond, all bonds are of staggered type, *i.e.*, the projections[†] of two bonded particles are rotated by 60 degrees against each other about the axis defined by their mutual bond; in a hexagonal diamond, one out of four bonds is of eclipsed type, *i.e.*, the projections of two bonded particles exactly overlap (*cf.* Fig. 4.36, labels C and D, yellow particles). As mentioned in the previous section, the bcc-like structures can be interpreted as two interpenetrating, but virtually non-interacting cubic diamond configurations.

| index	classification	$H^\star$	$U^\star$	η
7_{sh}	bc I shifted	-1.92	-2.03	0.49
7_{sy}	bc I symmetrical	-1.91	-2.02	0.49
C	cubic diamond	-1.79	-2.01	0.24
D	hexagonal diamond	-1.79	-2.01	0.24

<u>$P^\star = 2.5$:</u> At intermediate pressure, we identify six competing minima with reduced enthalpy values between $H^\star \approx 0.53$ and $H^\star \approx 0.72$ shown in Fig. 4.36. Again, the global minimum is the shifted bcc-like structure, having a slightly lower enthalpy (by only 0.3 percent) than the perfectly symmetric bcc structure (both are categorized as "bc I" in Fig. 4.26). The third-lowest minimum is the – closely related – "bc broken" structure, which represents the global minimum for slightly higher pressure $3.2 \lesssim P^\star \lesssim 3.4$. For the lattice corresponding to the fourth-lowest local enthalpy minimum (*cf.* Fig. 4.36, label E) the discrepancy between bonding and packing is even more pronounced: we identify a relatively dense configuration consisting of hexagonally arranged particles. This configuration resembles the previously discussed "hexagonal layers I", with the notable difference that each layer is strongly bonded with one of its neighboring layers and unconnected with the other one. To be more specific, a tagged particle forms strong bonds *via* three of its patches: two of these bond with particles within the same layer, the third one connects the tagged particle to a neighboring layer. The remaining patch on each particle engages in a very wide-angle bond, contributing 7 % OBE to the energy. This lattice is not encountered as a global minimum for the symmetrical patch geometry. The structure corresponding to the local enthalpy minimum five is a non-close packed fcc-like structure (*cf.* Fig. 4.36, label F), where each particle has two saturated bonds. Additionally, there is a number of weaker bonds, with 4 to 52 % OBE within each unit cell. Within the fcc-picture, the particles located at the vertices of the cube differ in

---

[*]Due to the symmetry of the particles, it cannot be distinguished between NP and SH patches at this geometry.

[†]Onto a plane perpendicular to the axis defined by the bond.

their orientation from the particles that occupy the centers of the faces. Despite its high packing fraction, this structure is never stable at vanishing temperature due to the small number of saturated bonds. However, a slightly modified version of this lattice, where each particle is rotated in order to replace a single, fully saturated bond by two weaker bonds, is found to be stable at finite temperatures in the $(P^\star, T^\star)$-phase diagram for $T^\star \gtrsim 0.06$ over a pressure range steadily increasing with temperature [6, 7]. The sixth-lowest local enthalpy minimum at $P^\star = 2.5$ corresponds to the "fc II" structure, identified as global minimum for pressure values $P^\star \gtrsim 3.4$ in the previous section.

index	classification	$H^\star$	$U^\star$	η
7_{sh}	bc I shifted	0.53	-1.91	0.54
7_{sy}	bc I symmetrical	0.53	-1.90	0.54
8	bc broken	0.59	-1.63	0.59
E	hexagonal layers	0.66	-1.41	0.63
F	non close packed fcc-like	0.72	-1.22	0.68
6	fc II	0.72	-1.13	0.71

$\underline{P^\star = 4.5}$: The global minimum in enthalpy corresponds to "fc II", which is only the sixth-lowest minimum at the pressure value discussed before; its characteristic values* at $P^\star = 4.5$ are the same as at lower pressure. The second-lowest minimum on the enthalpy landscape corresponds to an hcp-like structure (*cf.* Fig. 4.36, label G): each particle forms two strong bonds – one with a particle within the same layer, the other connecting to a particle in a neighboring layer – similar as in the packed fcc-like case; however, here the bonding angles are found to be considerably closer to the ideal values (*i.e.*, the patches directly face each other), resulting, along with three weak bonds between nine and 31 % OBE in each unit cell, in the slightly lower $U^\star$ value. The lower packing fraction, however, renders it, in total, less favorable than "fc II". The structure corresponding to the third local enthalpy minimum is realized by another hcp-like configuration (*cf.* Fig. 4.36, label H). Similar to the hexagonal configuration (E) mentioned at $P^\star = 2.5$, each particle forms two strong intra-layer bonds; however, here, there are only very weak (4 % OBE) inter-layer bonds. This configuration reaches a packing fraction similar to the one of the global minimum structure; however, it has a considerably higher $U^\star$-value, making it thus unstable in the entire pressure region. Local minimum four corresponds to the non-close-packed fcc-like structure already identified at $P^\star = 2.5$.

index	classification	$H^\star$	$U^\star$	η
6	fc II	2.20	-1.13	0.71
G	hcp-like	2.23	-1.16	0.70
H	hcp-like	2.26	-1.06	0.71
F	non close packed fcc-like	2.26	-1.20	0.68

***I.e.*, binding energy and packing fraction.
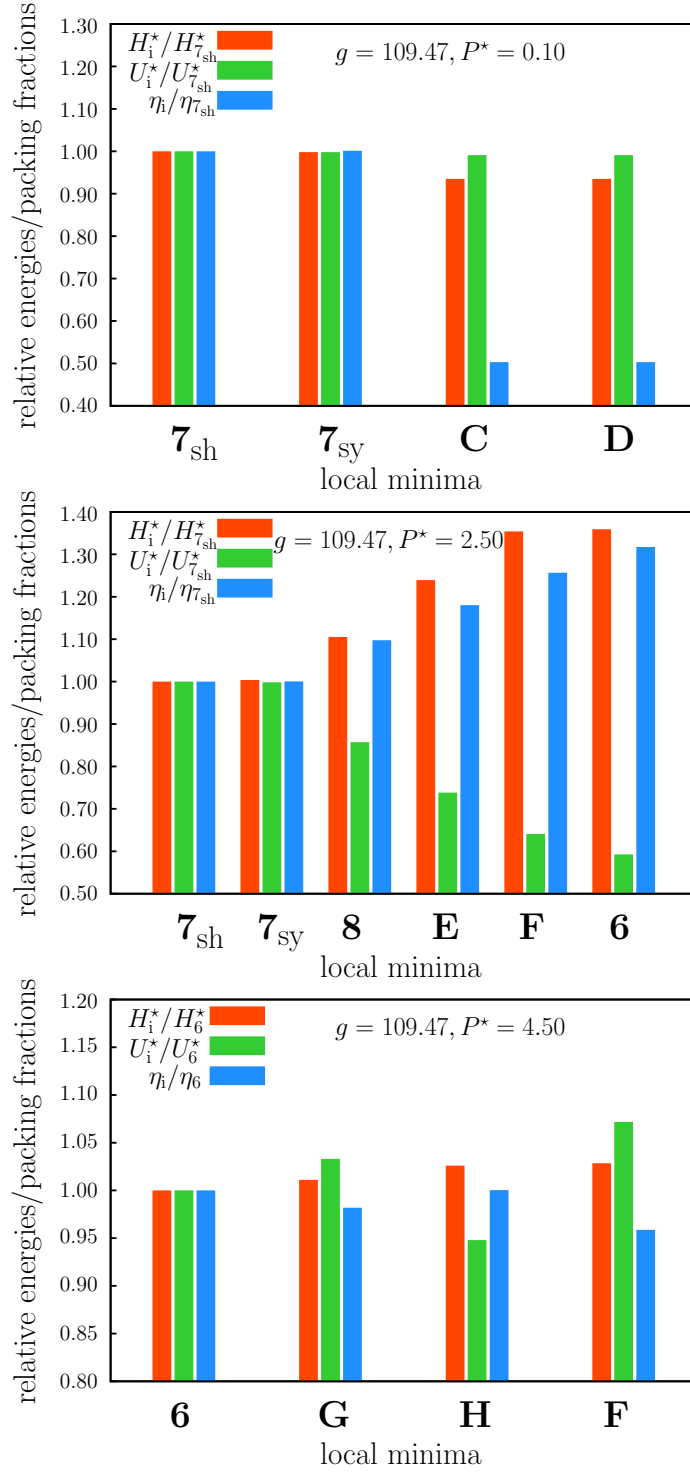
Figure 4.35.: Enthalpies $H_i^\star$, binding energies (*i.e.*, lattice sums) $U_i^\star$, and packing fractions η_i of the lowest, structurally different local enthalpy minima identified by the EA at $g = 109.47$ for different $P^\star$ values, where i stands for a structure label. Values are given in units of the respective values of the energetically most favorable lattice at each $P^\star$ value. At the lowest pressure, $H_i^\star < 0$, therefore high relative values are favorable, while for the higher $P^\star$ values, the opposite is the case.
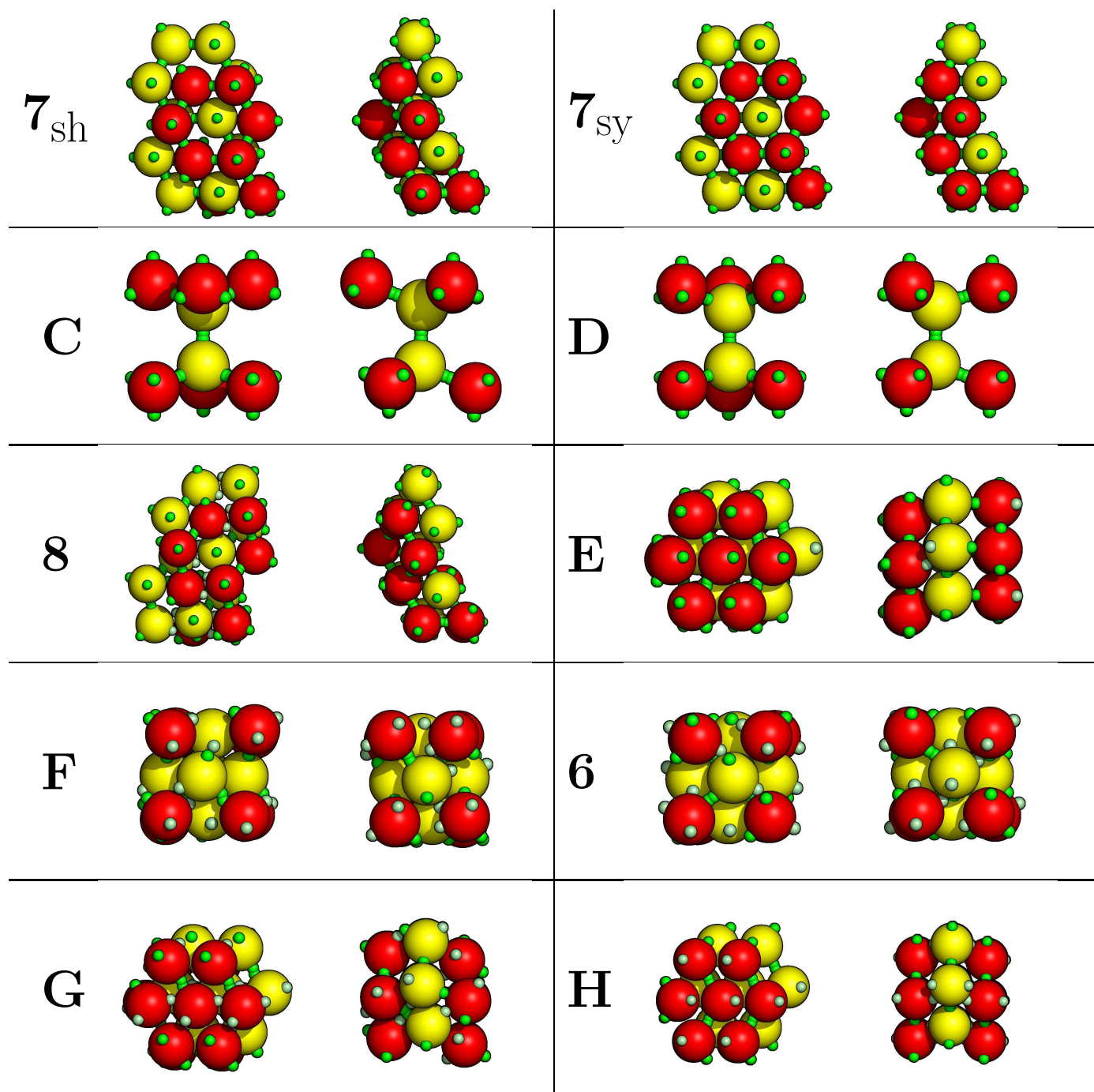
Figure 4.36.: Visualizations of the structures corresponding to local minima at $g = 109.47$. For the structure labels, see text.

g = 127.50

$\underline{P^\star = 2.5}$: At this elongated patch decoration and at intermediate pressure, we identify three competing minima. The global minimum corresponds again to the fully bonded "bc I" structure; all the bonds are slightly wide-angle and have binding energies around 90 % OBE. The second-lowest minimum is represented by the "bc II" structure. As the third minimum, having a much higher enthalpy value, we identify a previously not encountered non-close packed fcc-like structure. This lattice is much less perturbed from perfect fcc than the fcc-like structures usually encountered in this system.

index	classification	$H^\star$	$U^\star$	η
7	bc I	0.20	-1.87	0.63
9	bc II	0.23	-1.72	0.67
I	non close packed fcc-like	0.36	-1.64	0.65

$\underline{P^\star = 4.5}$: At intermediate pressure, the "bc II" structure is the most favorable one; here it is slightly more compressed than in the previous case. The "bc I" structure still has a competitive enthalpy value and corresponds to the second-lowest minimum at this pressure. The third-lowest minimum corresponds to the "fc III" structure, already described as the high pressure equilibrium structure for this system in the previous section; note that the orientation of two particles in the primitive cell differs in the low pressure version (*cf.* Figs. 4.38, label 10 and 4.31, center panel). Finally, the fourth minimum is represented by a denser, hcp-like structure, where the layers slightly deviate from hexagonal symmetry. All the patches engage in bonding: within the layers, there are slightly wide angle NP-SH bonds (82 % OBE), while the SH-SH inter-layer bonds are of wide-angle and long-distance type (51 % OBE).

index	classification	$H^\star$	$U^\star$	η
9	bc II	1.78	-1.66	0.68
7	bc I	1.84	-1.82	0.64
10	fc III	1.88	-1.54	0.69
J	hcp-like	1.94	-1.37	0.71

$\underline{P^\star = 6.5}$: Here, the "bc II" structure still corresponds to the global enthalpy minimum, with almost unchanged characteristic values. The "fc III" structure represents the second-lowest minimum; comparing the characteristic values shows that this configuration is more compressible than "bc II" and explains why it represents the global minimum for $P^\star \gtrsim 8.8$. As the "bc I" structure is no longer competitive at this pressure, the third-lowest minimum corresponds to the hcp-like structure mentioned above.

| index	classification	$H^\star$	$U^\star$	η
9	bc II	3.31	-1.66	0.68
10	fc III	3.36	-1.48	0.70
J	hcp-like	3.42	-1.37	0.71
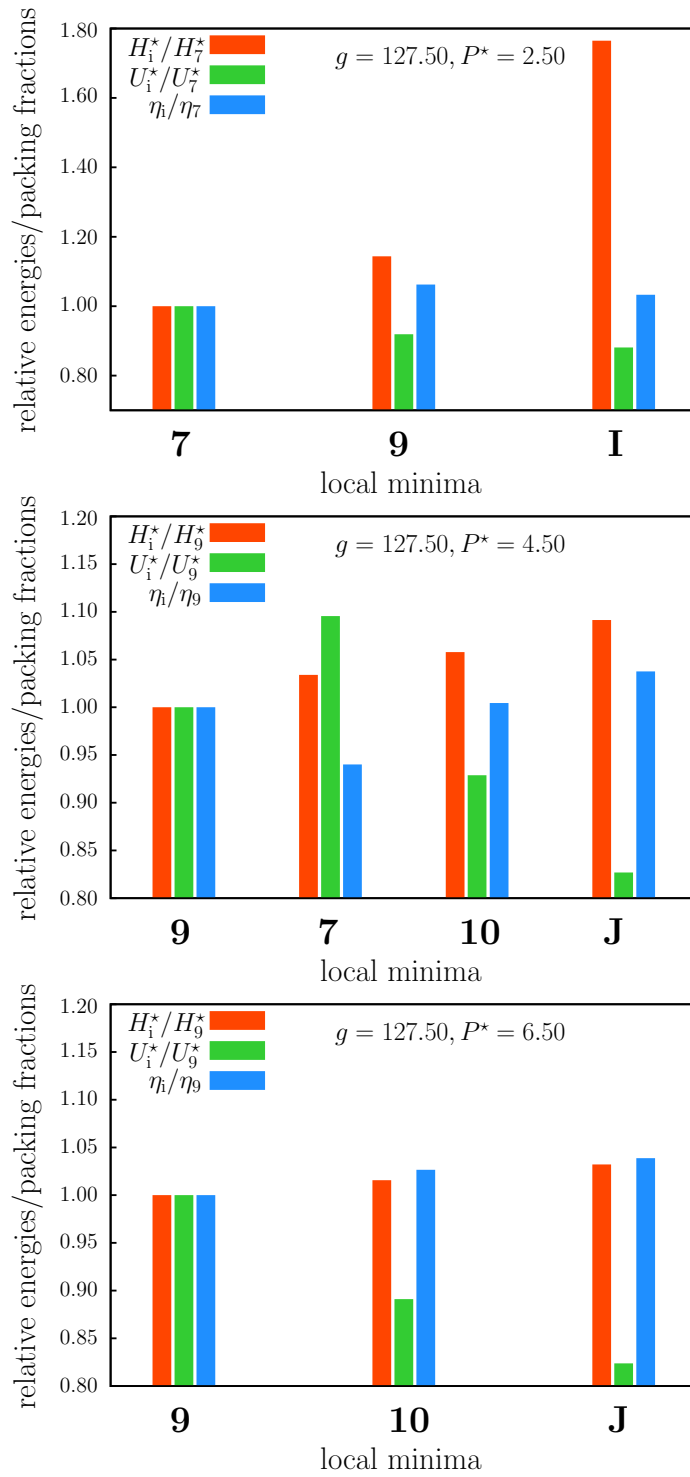
Figure 4.37.: Enthalpies $H_i^\star$, binding energies (*i.e.*, lattice sums) $U_i^\star$, and packing fractions η_i of the lowest, structurally different local enthalpy minima identified by the EA at $g = 127.50$ for different $P^\star$ values, where i stands for a structure label. Values are given in units of the respective values of the energetically most favorable lattice at each $P^\star$ value. At all $P^\star$ values, $H^\star > 0$, therefore, low relative values are favorable.
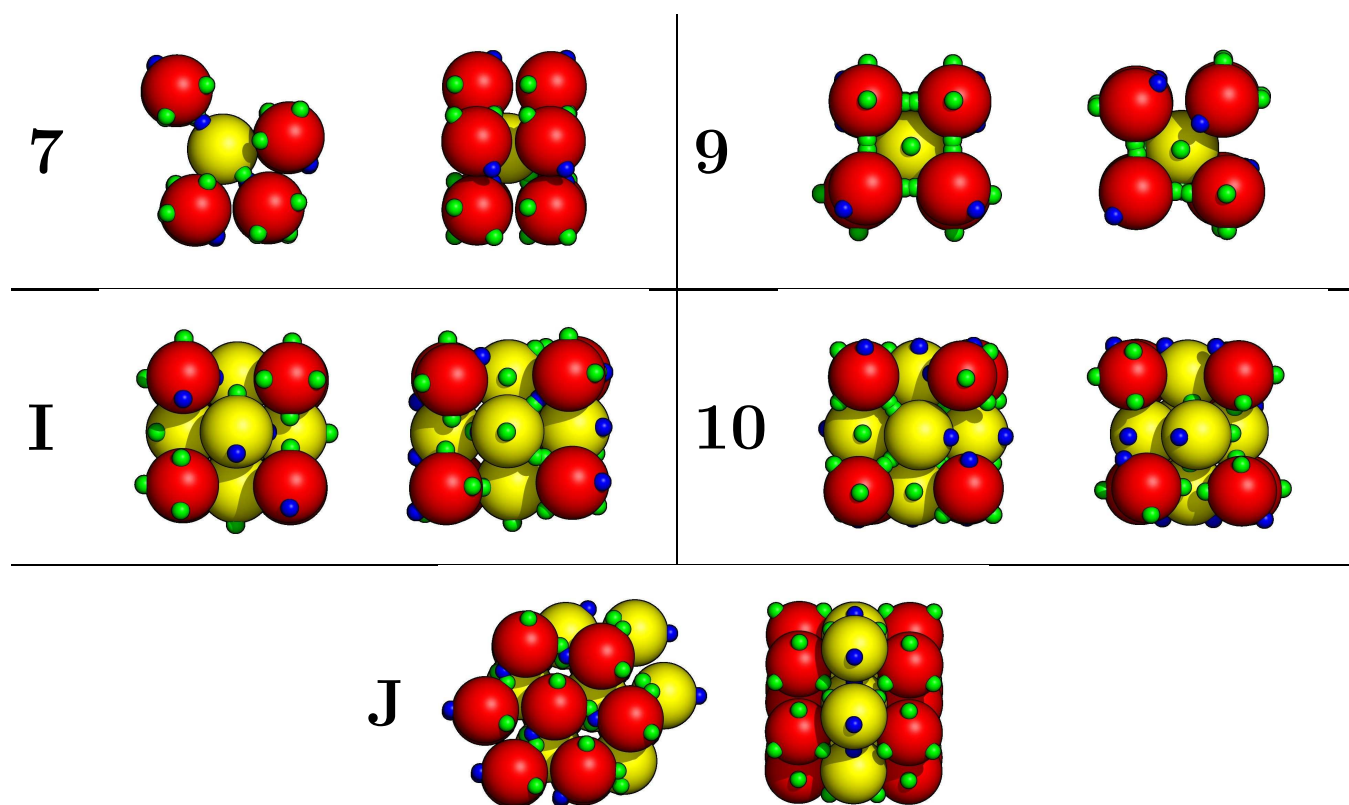
Figure 4.38.: Visualizations of the structures corresponding to local minima at $g = 127.50$. For the structure labels see text.

g = 150.00

$\underline{P^\star = 0.5}$: For the most elongated geometry and very low pressure, we observe three different fully bonded structures as the lowest-lying enthalpy minima. The global minimum corresponds to the "hexagonal layers III" configuration, where the bonds are of NP-NP and SH-SH types. This structure achieves the highest packing fraction of the fully bonded ones and has an extraordinarily low binding energy, due to a very large number of weak extra long-distance contributions (≈ 3 % OBE each). The next-lowest enthalpy minimum corresponds to another hexagonally layered structure, but here the particles do not have the same orientation within each layer, so that the bonds are of NP-SH and SH-SH types. Compared to the global minimum structure, the particles slightly rearrange in the direction perpendicular to the layers, so that the layers are not completely flat. This configuration achieves only slightly less favorable values for the binding energy and the packing fraction. The structure representing the third local minimum is also fully bonded, but has a considerably lower density. As for local minimum two, bonds of NP-SH and SH-SH type are formed, but different particle orientations lead to a rather peculiar lattice with voids (*cf.* Fig. 4.40).

index	classification	$H^\star$	$U^\star$	η
12	hexagonal layers III	-1.70	-2.15	0.58
K	hexagonal layers with different orientations	-1.69	-2.14	0.58
L	fully bonded lattice with voids	-1.63	-2.12	0.54

$\underline{P^\star = 2.5}$: At intermediate pressure, the first two minima are represented by the same structures as at the lower pressure value with almost identical binding energies and packing fractions. The configuration corresponding to the third local minimum is related to the "hexagonal layers I" structure; uniformly oriented particle are arranged in parallel layers. Compared to the "hexagonal layers I" structure, the present lattice reaches a higher packing fraction by breaking one bond per unit cell and rearranging the particles. Finally, the fourth local enthalpy minimum (with a relatively high enthalpy value) corresponds to the "hexagonal packed III" configuration.

index	classification	$H^\star$	$U^\star$	η
12	hexagonal layers III	0.08	-2.13	0.59
K	hexagonal layers with different orientations	0.10	-2.12	0.59
M	hexagonal layers broken	0.12	-1.93	0.64
14	hexagonal packed III	0.18	-1.71	0.69

$\underline{P^\star = 4.5}$: At this pressure value, the "hexagonal packed III" configuration with almost unchanged characteristic values corresponds to the global enthalpy minimum. The second minimum is represented by a very symmetrical, previously unobserved fcc-like structure where all the NP patches are unbonded, while the SH patches bond with their likes. The packing fraction of this configuration is only slightly lower than the value of the global minimum. Finally, the third-lowest minimum corresponds to the layered structure with broken bonds

already observed at lower pressure.

| index	classification	$H^\star$	$U^\star$	η
14	hexagonal packed III	1.69	-1.70	0.70
N	fcc-like	1.74	-1.68	0.69
M	hexagonal layers broken	1.76	-1.91	0.64
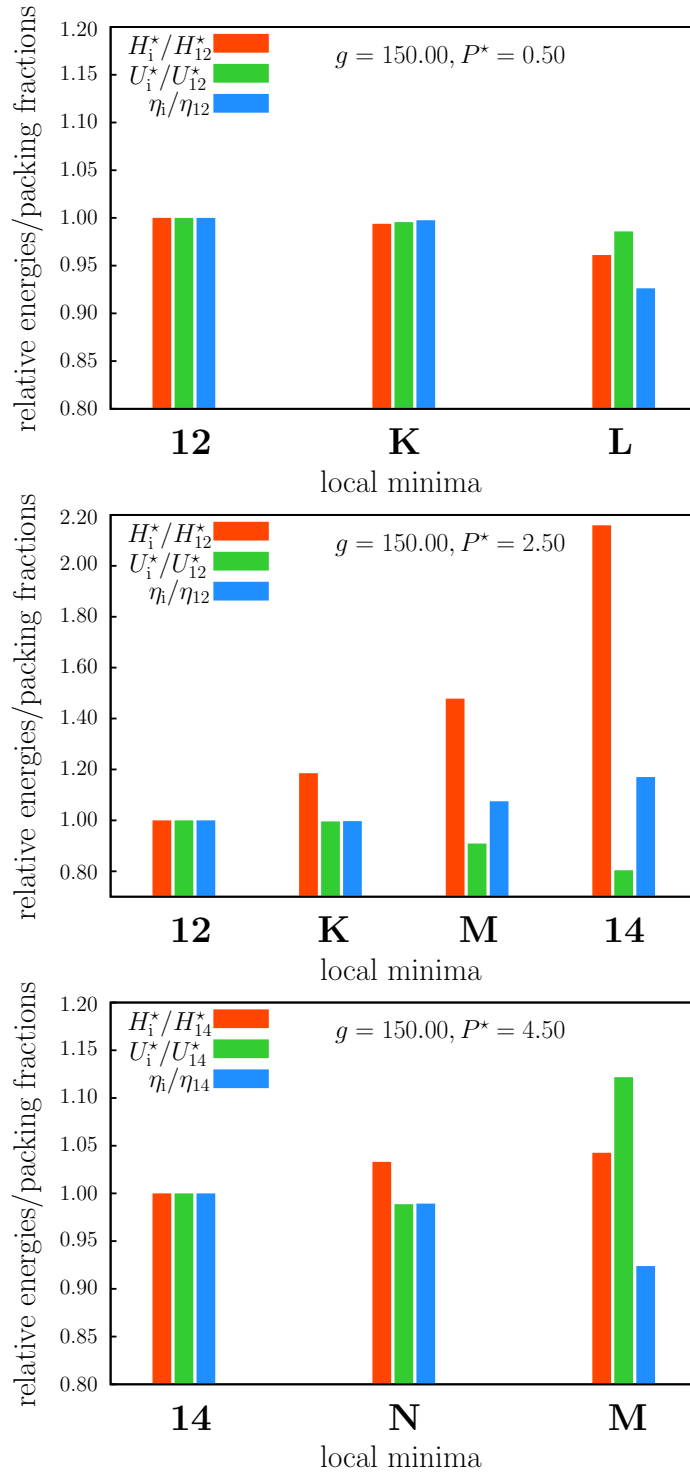
Figure 4.39.: Enthalpies $H_i^\star$, binding energies (*i.e.*, lattice sums) $U_i^\star$, and packing fractions η_i of the lowest, structurally different local enthalpy minima identified by the EA at $g = 150.00$ for different $P^\star$ values, where i stands for a structure label. Values are given in units of the respective values of the energetically most favorable lattice at each $P^\star$ value. At the lowest pressure, $H_i^\star < 0$, therefore high relative values are favorable, while for the higher $P^\star$ values the opposite is the case.
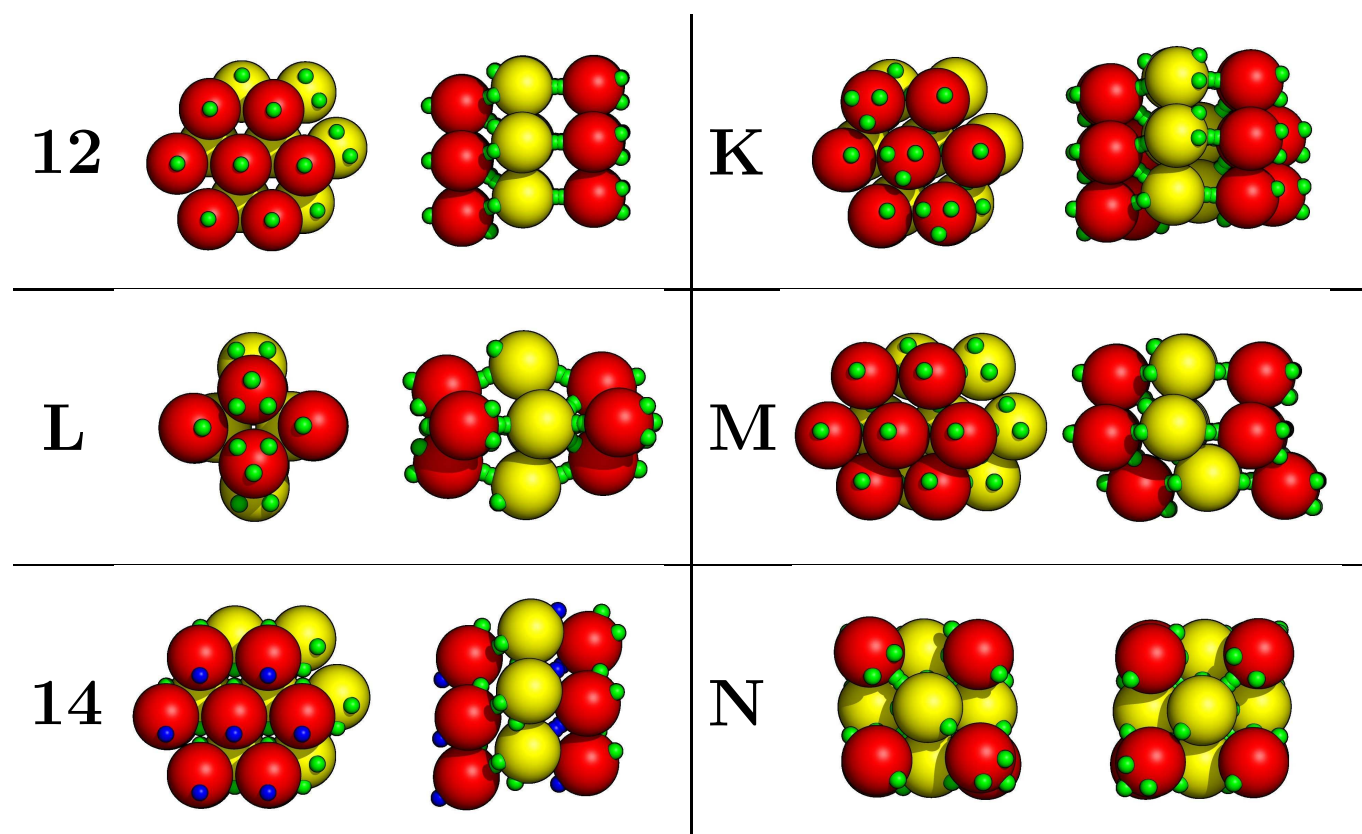
Figure 4.40.: Visualizations of the structures corresponding to local minima at $g = 150.00$. For the structure labels see text.

4.2.3. Inverse Patchy Colloids

We examine global minimum configurations formed by the model system for inverse patchy colloids described in Sec. 2.2.3. As the inverse patchy model has initially been introduced for two patches per particles, we restrict ourselves to that case in the present investigation. The parameters that specify the model are not completely independent from each other (for details see Ref. [47]). They are defined and compiled in Tab. 4.3. In this thesis, we fix all but two parameters to values as they are suggested from an experimental realization. In particular, we perform all calculations at low electrostatic screening conditions (specified by a low κ value and $\delta = 1/\kappa$), as this choice guarantees that the angle-dependent attractive and repulsive forces between the inverse patchy particles are of comparable orders of magnitude; in this system, the repulsive forces decrease much faster with increasing screening than the attractive ones. We expect considerably richer self-assembly scenarios if there is a strong competition between antipodal forces.

The two parameters that we vary are eccentricity e, which defines the patch size if all other spatial parameters (*i.e.*, the size of the colloids σ and the interaction range δ) are fixed, and the charge imbalance ΔZ_x (with $x \in \{c, p\}$), which defines the strength of the interactions, if all other paramters are fixed (*cf.* Tab. 4.3). For each pair $(e, \Delta Z_x)$, we perform the mapping procedure described in Ref. [47] in order to obtain the interaction parameters ϵ_i (*cf.* Tab. 4.4). Subsequently, we calculate the total interaction energy $U_{\text{pair}}^{\text{opt}}$ of an optimally aligned pair of inverse patchy particles (*i.e.*, a full BS overlap, *cf.* Sec. 2.2.3) and define $|U_{\text{pair}}^{\text{opt}}|$ as the unit of energy for the chosen combination $(e, \Delta Z_x)$. In each system, all reduced quantities $X^\star$ (*cf.* App. A) are calculated in terms of the respective units of energy and length[*].

As in the preceding sections, we vary the reduced pressure $P^\star$ for each system and identify the ordered equilibrium structures using our optimization algorithm. Due to computational limitations, we take lattices with up to eight basis particles into account. Some of the systems show surprisingly rich phase behavior, with some structures requiring indeed up to eight basis particles. Thus, we cannot completely rule out the possible existence of ordered configurations with even lower enthalpies, which could only be realized with larger basis particle numbers in some cases. The minimum enthalpy structures we identified are presented in the following. Visual representations of those structures can be found in Figs. 4.41 - 4.44. In these Figures, spheres arbitrarily colored red, yellow or blue represent the colloidal cores of the inverse patchy particles, corresponding to spheres C in the interaction model, *cf.* Sec. 2.2.3). Green spheres represent the polyelectrolyte star patches (*i.e.*, small spheres S in the interaction model), while the semitransparent coronae indicate the interaction range (*i.e.*, correspond to the large spheres B in the interaction model).

---

[*]In App. A, the unit of length is termed σ. This must not be confused with the parameter σ used in this section. In order to maintain consistency with the variables introduced in Ref. [47], the unit of length is defined as 2σ here (*cf.* Tab. 4.3).

[*]This system is completely repulsive, so the optimal alignment is a particle separation beyond the interaction range (*i.e.*, a configuration with zero energy). Thus, we do not normalize the energy values for this particular system.

Parameter	Value	Description	How obtained
Z_c	-300 - ΔZ_c	Electrostatic charge of the colloidal particles	can be chosen (experimental)
Z_p	$150 + \Delta Z_p/2$	Electrostatic charge of one adsorbed polyelectrolyte star	can be chosen (experimental)
$\Delta Z_c, \Delta Z_p$	vary	Charge imbalance	
κ	$2/\sigma$	Inverse Debye screening length	can be chosen (low screening)
σ	$1/2$	Radius of spheres representing colloidal particles	defines unit of length
δ	$1/\kappa$	Interaction range	natural choice
e	varies	Eccentricity of spheres representing adsorbed polyelectrolyte stars	
ρ	$\sigma + \delta/2 - e$	Radius of spheres representing adsorbed polyelectrolyte stars	given by Eq. (2.23)

Table 4.3.: Parameters of the inverse patchy model system: symbols, values chosen in this thesis and brief descriptions of the respective physical meanings and how the values were obtained.

Geometry	Interactions	Overcharge $Z_p = 60$	$Z_p = 30$	$Z_x = 0$	$Z_c = 30$	$Z_c = 60$
A – $e = 0.3$	ϵ_{BB}	21.49	24.00	32.75	55.82	88.17
	ϵ_{BS}	-113.47	-176.63	-226.59	-315.27	-403.95
	ϵ_{SS}	1844.76	1550.11	1281.08	1281.08	1281.08
	$U_{\text{Pair}}^{\text{Opt}}$	-5.50	-9.60	-12.10	-15.71	-18.30
B – $e = 0.2$	ϵ_{BB}	8.73	5.79	10.29	25.19	49.38
	ϵ_{BS}	12.76	-16.74	-41.08	-71.04	-101.00
	ϵ_{SS}	245.46	206.25	170.46	170.46	170.46
	$U_{\text{Pair}}^{\text{Opt}}$	0.00*	-0.52	-2.24	-3.27	-3.28

Table 4.4.: Interaction parameters obtained by the mapping procedure described in Ref. [47] for the cases (geometries A and B) investigated in this contribution.

Geometry A $-$ $e = 0.3$

For comparatively small patches (imposed by a comparatively larger value of the eccentricity e), we identified four different minimum enthalpy structures labeled A1 - A4. For each ΔZ_x value, we located at least one phase transition on the pressure coordinate of the zero-temperature phase diagram. In the following, different values for the patch overcharge (ΔZ_p) and colloid overcharge (ΔZ_c) are assumed.

Strongly overcharged patches - $\Delta Z_p = 60$: For this system, we observe two different zero-

temperature equilibrium structures: At low pressure, the particles arrange in parallel layers, with energetically favorable BS overlaps between the particles within each sheet. The layers, which are arranged in an ABCABC... pattern, are separated by relatively large inter-layer distances, in order to minimize unfavorable BB overlaps (*cf.* Fig. 4.41, label A2). With increasing pressure, this structure is slightly compressed by reducing this inter-layer distance. At higher pressure, a close packed structure, where the centers of mass of the particles are located on the sites of a perfect fcc lattice, is stable. Here, the particles are oriented in different directions in an alternating pattern (*cf.* Fig. 4.41, label A4).

stability	structure	binding energy	packing fraction
$P^\star \lesssim 1.73$	parallel layers (A2)	$-2.27 \lesssim U^\star \lesssim -2.24$	$0.515 \lesssim \eta \lesssim 0.568$
$P^\star \gtrsim 1.73$	fcc (A4)	$U^\star \approx -1.87$	$\eta \approx 0.741$

Moderately overcharged patches - $\Delta Z_p = 30$: For a smaller electrostatic overcharge value of the polyelectrolyte star patches, we identify a distinctly different self-assembly scenario: again, the particles form parallel layers, but between those sheets a number of additional particles are located at energetically favorable spots, connecting them thereby (*cf.* Fig. 4.41, label A1). Compared to the standard "parallel layeres" configuration (*i.e.*, A2), this bonding mechanism slightly lowers the total energy, but requires a considerably higher inter-layer distance and thus makes the the packing fraction smaller. Thus, this structure is stable only at very low pressures. At intermediate pressure, we encounter the standard "parallel layers" configuration (A2), while at high pressure the fcc structure (A4) is stable again.

stability	structure	binding energy	packing fraction
$P^\star \lesssim 0.05$	layers with interstitials (A1)	$U^\star \approx -2.36$	$\eta \approx 0.466$
$0.05 \lesssim P^\star \lesssim 0.14$	parallel layers (A2)	$U^\star \approx -2.25$	$\eta \approx 0.548$
$P^\star \gtrsim 0.14$	fcc (A4)	$U^\star \approx -2.32$	$\eta \approx 0.741$

Neutral particles - $\Delta Z_p = Z_c = 0$: For a balanced overall charge of the particles, we again identify three different ordered equilibrium structures. At very low pressure, the layers with interstitial particles (A1) correspond to the global enthalpy minimum again. On increasing the pressure to intermediate values, an arrangement of perpendicular sheets, forming a lattice penetrated by empty "channels" is stable. The particles making up those layers are not close-packed and show some deviation from a perfectly two-dimensional* configuration (*cf.* Fig. 4.41, label A3). In the region of stability of this rather complicated structure, the standard "parallel layers" configuration (A2) corresponds to a very close local minimum, as the respective enthalpy values differ by less than 0.5 %. At high pressure the close packed fcc structure is stable, as in all previous cases.

---

*In a sense that all centers of mass lie within a plane.

stability	structure	binding energy	packing fraction
$P^\star \lesssim 0.02$	layers with interstitials (A1)	$U^\star \approx -2.35$	$\eta \approx 0.463$
$0.02 \lesssim P^\star \lesssim 0.39$	perpendicular layers (A3)	$U^\star \approx -2.34$	$\eta \approx 0.556$
$P^\star \gtrsim 0.39$	fcc (A4)	$U^\star \approx -2.25$	$\eta \approx 0.741$

Moderately overcharged colloids - $\Delta Z_c = 30$: In this system, we encounter the same phase behavior as in the previous case of strongly overcharged patches: the two stable structures are "parallel layers" (A2) and fcc (A4), with a slightly lower coexistence pressure than in the previous case. This is due to the fact that here the fcc structure has a lower energy, relative to the layered structure. BB contacts, which are more abundant in the close packed structure, lead to a smaller energy penalty in systems with a smaller overcharge value.

stability	structure	binding energy	packing fraction
$P^\star \lesssim 1.30$	parallel layers (A2)	$-2.29 \lesssim U^\star \lesssim -2.27$	$0.545 \lesssim \eta \lesssim 0.564$
$P^\star \gtrsim 1.30$	fcc (A4)	$U^\star \approx -1.98$	$\eta \approx 0.741$

Strongly overcharged colloids - $\Delta Z_c = 60$: Again, we identified "parallel layers" (A2) and fcc (A4) as global enthalpy minima for low and high pressures, respectively. The higher value of overcharge of the colloids make the close packed structure less favorable, leading to a higher coexistence pressure than in the previous case.

stability	structure	binding energy	packing fraction
$P^\star \lesssim 2.83$	parallel layers (A2)	$-2.22 \lesssim U^\star \lesssim -2.15$	$0.546 \lesssim \eta \lesssim 0.577$
$P^\star \gtrsim 2.83$	fcc (A4)	$U^\star \approx -1.58$	$\eta \approx 0.741$

Geometry B $-\ e = 0.2$

For the geometry with a smaller value of the eccentricity e, leading to larger patches when all other parameters are fixed, we find a different scenario for the ordered equilibrium structures. For neutral inverse patchy particles as well as for moderate values of overcharge, close packed fcc structures represent the global enthalpy minima at all pressure values. For strongly overcharged patches as well as for strongly overcharged colloids, however, we find very rich phase behavior, with five or even more transitions along the pressure coordinate of the phase diagram. The identified configurations are labeled B1 - B11.

Strongly overcharged patches - $\Delta Z_p = 60$: As can be seen from the parameter values collected in Tab. 4.4, this system differs substantially from all the other ones investigated, as it has purely repulsive interactions. In this case, the need for compression caused by increasing system pressure leads to an interesting phase behavior.

At very low pressure values, an fcc structure which corresponds to close packing of the
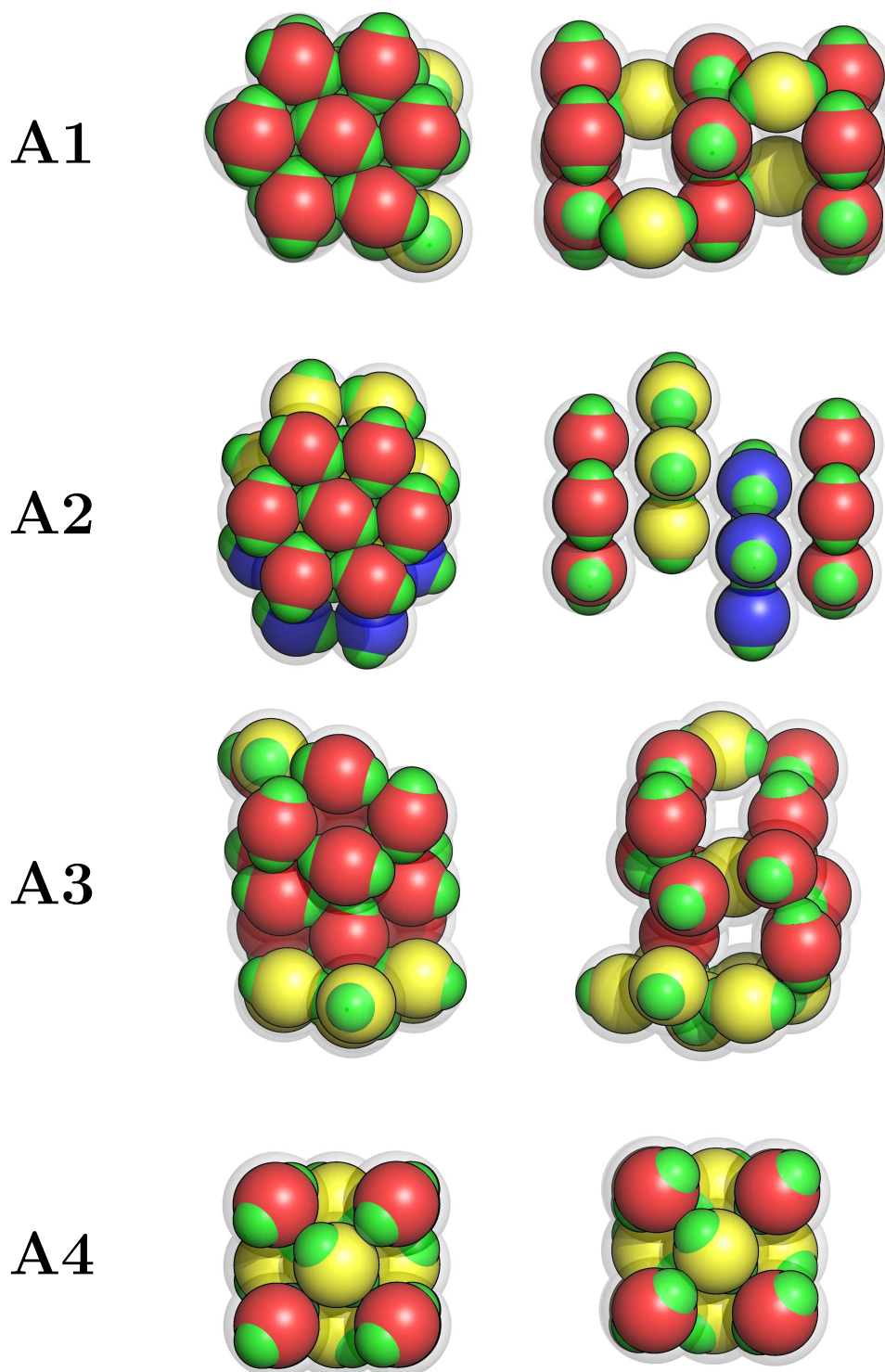
Figure 4.41.: Perpendicular views of the structures corresponding to global enthalpy minima for geometry A. For the labels and the color scheme, see text.

large spheres B, their diameter being the interaction range $\sigma + \delta/2$, minimize the enthalpy* (*cf.* Fig. 4.42, label B1). As in the model large sphere (BB) overlaps are energetically only slightly unfavorable, this structure is continuously, but anisotropically compressed with increasing pressure, forming an fct phase with uniform particle orientations (B2). This configuration is characterized by overlaps of the large spheres in two perpendicular direction, but avoids them in the third direction. At even higher pressure, a structurally different fct-like lattice (B3) with BB overlaps in all directions and a higher packing fraction is stable. In a tiny subsequent pressure region, yet another distorted fct-like structure (B4) represents the global enthalpy minimum, before an fcc configuration (B10) which corresponds to a close packing of the smaller central spheres C, representing the colloidal particles, becomes stable at the highest pressure values. In this configuration, the particle orientations are identical to the ones of structure A4. For visual representations of the four non-close packed lattices (B1-B4), see Fig. 4.42, for the close packed fcc lattice (B10), see Fig. 4.44, center panel.

stability	structure	binding energy	packing fraction
$P^\star \approx 0.00$	fcc range (B1)	$U^\star \approx 0.00$	$\eta \approx 0.380$
$P^\star \lesssim 34.20$	fct I (B2)	$0.00 \lesssim U^\star \lesssim 4.15$	$0.380 \lesssim \eta \lesssim 0.606$
$34.20 \lesssim P^\star \lesssim 52.10$	fct II (B3)	$7.37 \lesssim U^\star \lesssim 7.99$	$0.680 \lesssim \eta \lesssim 0.694$
$52.10 \lesssim P^\star \lesssim 53.80$	fct III (B4)	$U^\star \approx 8.77$	$\eta \approx 0.708$
$P^\star \gtrsim 53.80$	fcc colloids (B10)	$U^\star \approx 10.49$	$\eta \approx 0.741$

Moderately overcharged patches - $\Delta Z_p = 30$: For this system, the fcc structure (B10) corresponding to close packing of the central spheres C and the same particle orientations as the one identified for geometry A represents the global enthalpy minimum at all pressure values.

stability	structure	binding energy	packing fraction
$P^\star \gtrsim 0.00$	fcc colloids (B10)	$U^\star \approx -4.73$	$\eta \approx 0.741$

Neutral particles - $\Delta Z_p = Z_c = 0$: Here we encounter exactly the same situation as in the previously discussed model.

stability	structure	binding energy	packing fraction
$P^\star \gtrsim 0.00$	fcc colloids (B10)	$U^\star \approx -3.86$	$\eta \approx 0.741$

Moderately overcharged colloids - $\Delta Z_c = 30$: Again, an fcc-based close packing of the colloidal spheres has the lowest enthalpy value along the whole pressure coordinate (*cf.* Fig. 4.44, label B11). However, in the global minimum configuration the particle orientations show a pattern that is more complicated than the one of the fcc structure identified before (*i.e.*, B10), which corresponds to a very close local minimum for the present parameter values.

stability	structure	binding energy	packing fraction
$P^\star \gtrsim 0.00$	fcc colloids (B11)	$U^\star \approx -3.12$	$\eta \approx 0.741$

---

*Obviously, the orientations of the particles are arbitrary in this phase.

Strongly overcharged colloids - $\Delta Z_c = 60$:

In contrast to the case of strongly overcharged patches in the present geometry, a strong overcharge of the central colloids still leads to attractive interactions between the inverse patchy colloids. At very low pressure, a structure containing two perpendicular sets of parallel layers with almost perfect hexagonal symmetry (B5) corresponds to the global enthalpy minimum. This geometry leads to rather large "channels" with almost square cross-sections which penetrate the lattice in the direction perpendicular to the normal vectors of both sets of layers. On increasing pressure, a phase transition to a structure with only one set of parallel layers (B6) takes place. Within each layer, the hexagonal symmetry is strongly distorted, as the particles arrange in a zig-zag pattern in the direction perpendicular to the layers (*i.e.*, the layers are not completely flat). A further increase of pressure leads to a strongly distorted version (B7) of the perpendicular layers already encountered at low pressure to become stable. The distortion causes the packing fraction to increase by 16 %, as the empty "channels" penetrating the structure have a much smaller cross-section in this configuration. In a small region at even higher pressure, a lattice containing parallel layers with square symmetry corresponds to the global minimum. Here the particles are close packed in the direction perpendicular to the layers, but not in the plane of the layers. For visual representations of the aforementioned structures, see Fig. 4.43. On further increasing the pressure, we identify a configuration that corresponds to a perfect fcc lattice, with one lattice site unoccupied per two "cubic blocks" (*cf.* Fig. 4.44, top panel). At the highest pressure values, the close packed fcc structure, already identified for the system with $\Delta Z_c = 30$, corresponds to the global enthalpy minimum.

stability	structure	binding energy	packing fraction
$P^\star \lesssim 0.44$	perpendicular layers (B5)	$U^\star \approx -2.31$	$\eta \approx 0.536$
$0.44 \lesssim P^\star \lesssim 1.44$	distorted layers (B6)	$-2.29 \lesssim U^\star \lesssim -2.28$	$0.564 \lesssim \eta \lesssim 0.569$
$1.44 \lesssim P^\star \lesssim 2.50$	denser p. layers (B7)	$U^\star \approx -2.16$	$\eta \approx 0.625$
$2.50 \lesssim P^\star \lesssim 2.72$	square layers (B8)	$U^\star \approx -2.13$	$\eta \approx 0.635$
$2.72 \lesssim P^\star \lesssim 3.53$	fcc with defect (B9)	$U^\star \approx -2.08$	$\eta \approx 0.649$
$P^\star \gtrsim 3.53$	fcc colloids (B11)	$U^\star \approx -1.72$	$\eta \approx 0.741$

Figure 4.42.: Perpendicular views of structures corresponding to global enthalpy minima for geometry B. For the labels and the color scheme see text.
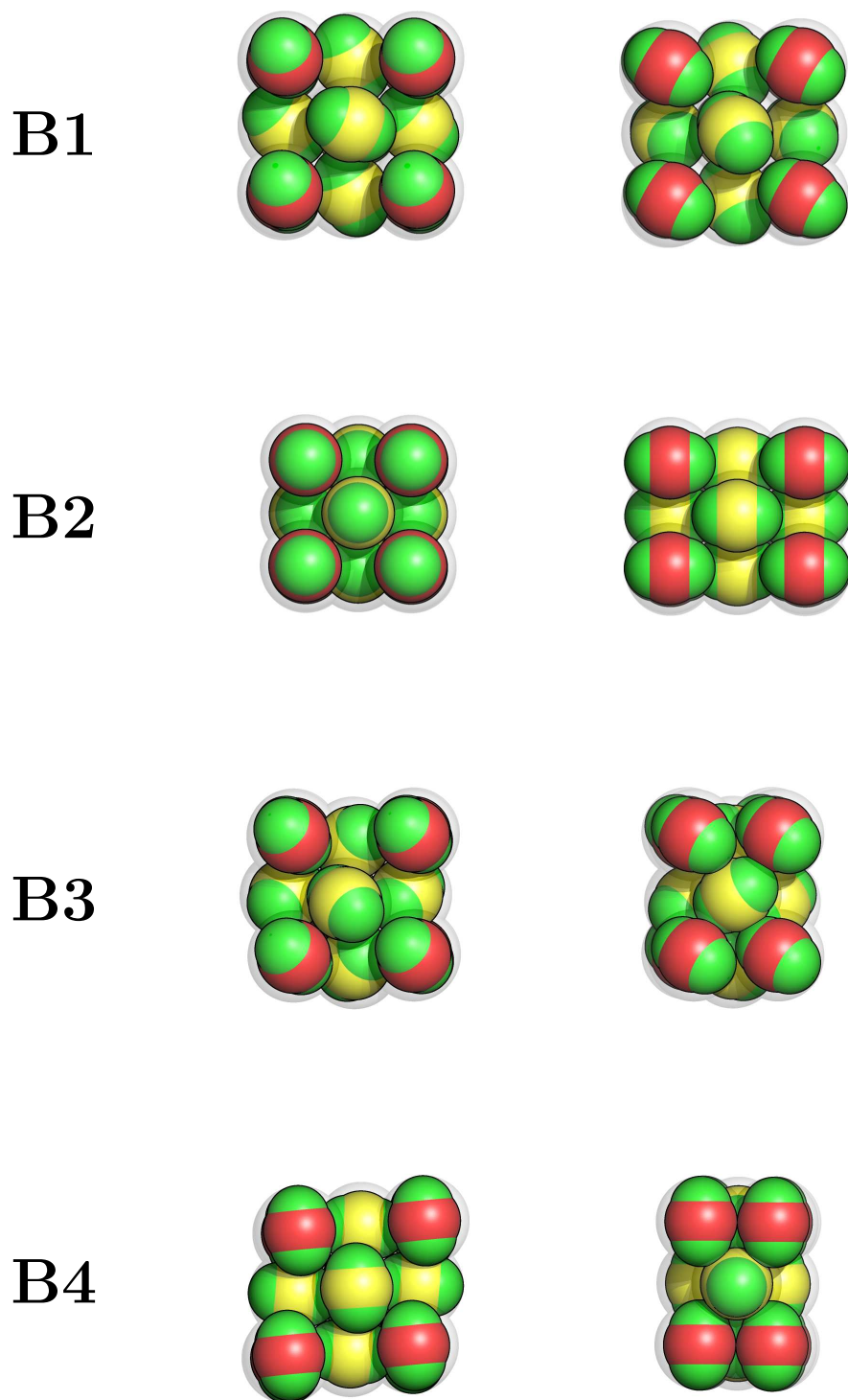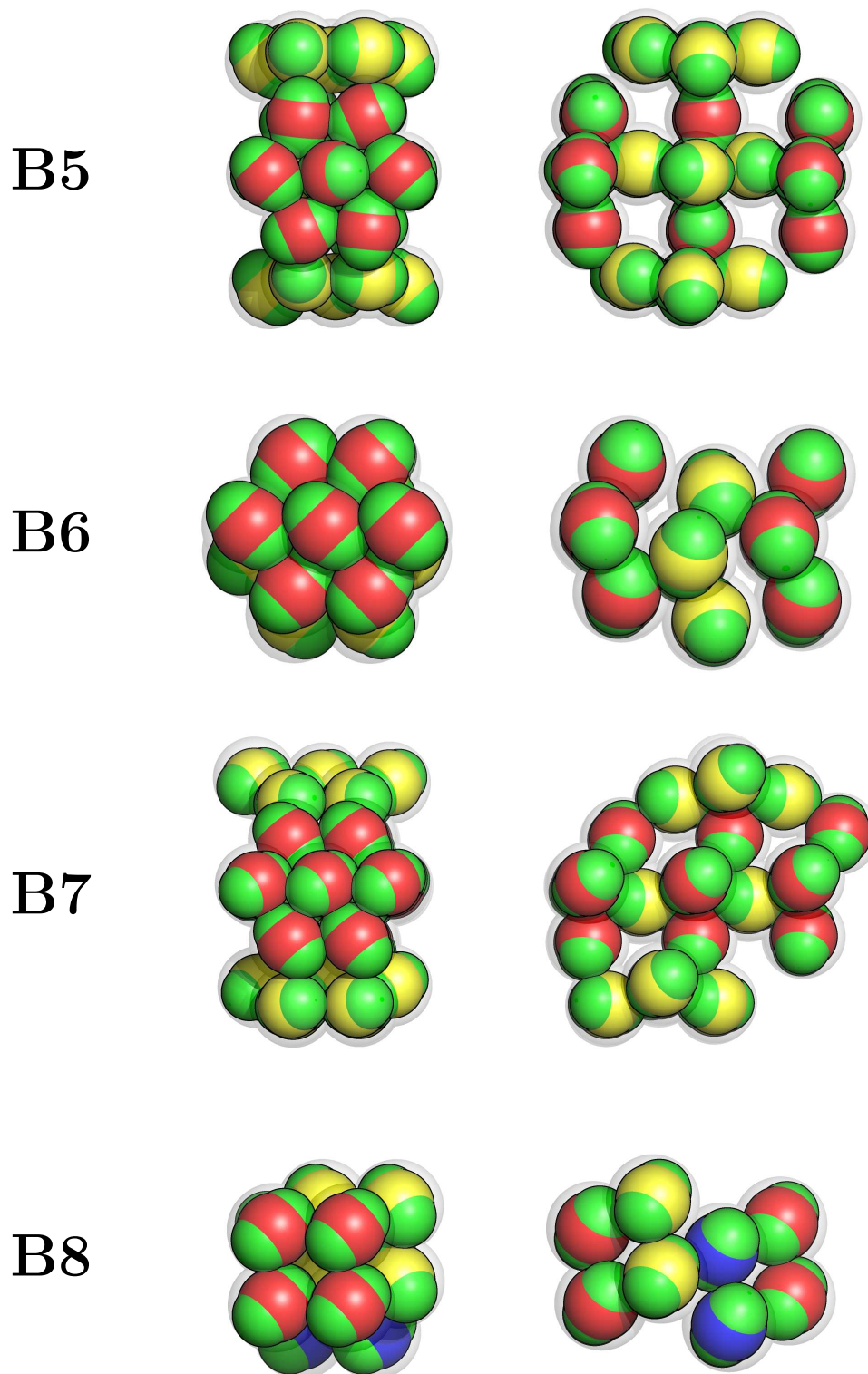
Figure 4.43.: Perpendicular views of structures corresponding to global enthalpy minima for geometry B. For the labels and the color scheme see text.
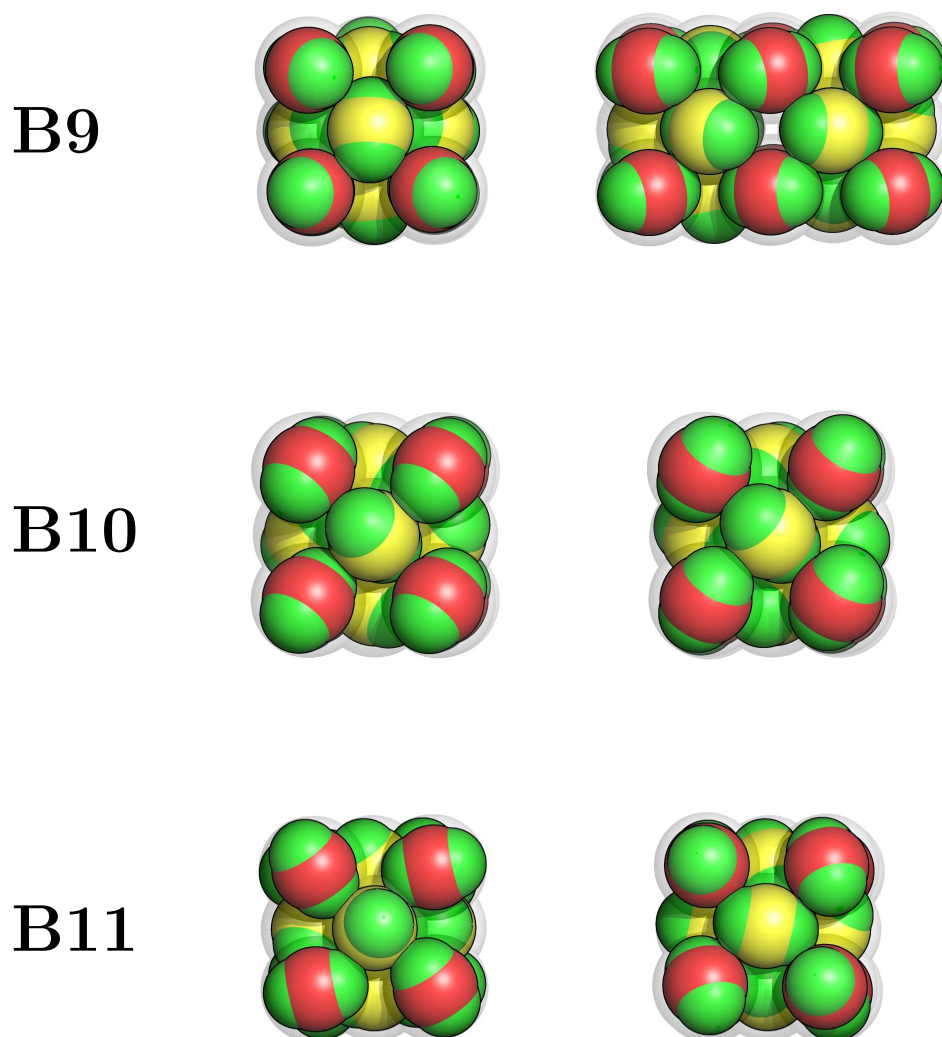
Figure 4.44.: Visualizations of structures corresponding to global enthalpy minima for geometry B. For the structure labels and the color scheme see text.

5. Conclusions

The investigations presented in this thesis focus on identifying ordered equilibrium structures (*i.e.*, energy-, enthalpy- or Gibbs free energy-minimizing configurations) of patchy colloids, a certain type of synthesized, anisotropic particles with very specific angle-dependent interactions. The identified configurations are relevant as macroscopic target structures of bottom-up self-assembly processes these mesoscopic particles can undergo.

The initial studies, performed at vanishing temperature, deal with two-dimensional systems of repulsive discs, decorated with mutually attractive as well as repulsive areas on their circumferences (see Sec. 4.1.1 and Ref. [43]). As the number, distribution and interaction-type of such patches varies, different sets of equilibrium structures, depending on the system pressure, are identified. These configurations emerge as a consequence of a delicate trade-off between optimizing the bonding-term and the packing-term in the enthalpy. At low pressure, minimal enthalpy values usually correspond to rather open structures, which strongly depend on the patch geometry; at high pressure values (almost) close packed (*i.e.*, triangular) lattices are optimal. For many systems, we identified additional intermediate structures, representing a suitable compromise between energy- and area-minimization in certain pressure regions.

The subsequent investigation takes a further step in the direction of bottom-up self-assembly of specifically designed particles: We give evidence that it is possible to decorate two-dimensional patchy particles in such a way that their equilibrium structures represent Platonic and Archimedean tilings of the plane (see Sec. 4.1.2 and Ref. [45]). We were able to show that all but one of the desired tilings can be stabilized at low to intermediate system pressure, in at least one of two proposed representations, either placing the particles at the centers or the vertices of the tiles. The realization of the tilings, especially the more complicated ones, tends to be more successful in the center representation, which has high packing fractions by definition; however this representation is expected to be more challenging in experimental implementations due to a generally rather large size disparity of the particles.

In three dimensional systems, we mainly focused on particles with four mutually attractive patches, modeled by the same potential. We first studied the minimum energy configurations of finite clusters consisting of three to 47 particles with a regular tetrahedral patch decoration (see Sec. 4.2.1). For these clusters, we identified two archetypal building units, namely rings, containing either five or six particles. As the six-rings have a lower energy per particle, they dominate the shapes of small clusters. The five-particle rings support a larger number of total bonds in bigger clusters and become dominant for particle numbers larger than 15. Examining the energy landscapes of selected cluster sizes by building databases of local minima and transition states and plotting disconnectivity graphs provided further insights into this competition.

The next topic covered in the present work are three-dimensional bulk systems of particles with four patches, arranged in geometries systematically varying from flat to strongly elongated pyramids (see Sec. 4.2.2 and Refs. [6, 7, 115]). Similar to the two-dimensional case, we identified a wide variety of zero-temperature equilibrium structures, balancing the bonding and packing terms in the enthalpy, as a function of the hydrodynamic pressure of the system. The low pressure equilibrium structures are based on a body-centered, "double-diamond" configuration for a large range of geometries. Only the most flat and the most elongated geometries have hexagonally layered low pressure configurations. In contrast to the two-dimensional systems, open low density structures correspond to the global enthalpy minimum only in rare cases and the often desired cubic "single" diamond structure is only metastable at very low pressure in this model. However, for certain intermediate geometries, we found a medium density bcc-like structure that is particularly stable with respect to close packed configurations at high pressure values. The remaining high pressure equilibrium structures frequently change between fcc-type and hcp-type configurations on varying the geometry. For these systems, we also investigated low-lying local enthalpy minima which might be stabilized by entropic effects at finite temperature. As such local minima with often only minute differences in enthalpy we encountered lattices that were already identified as global minima in other regions of the parameter space as well as previously unknown configurations.

In the final section of the results chapter (*i.e.*, Sec. 4.2.3), we presented an initial investigation on the ordered equilibrium structures formed by a recently proposed model for so-called inverse patchy particles. Exploring a comparatively small region of the available parameter space of this system, we already identified a very rich variety of self-assembly scenarios, depending on the hydrodynamic pressure as well as the geometry and the electrostatic charge of these particles. Along global enthalpy minima corresponding to close-packed and hexagonally layered structures, we also encountered global minima represented by lattices that are penetrated by channel-like voids with varying cross-sections in this system.

As the results obtained *via* optimization algorithms, minimizing binding energy or enthalpy, are valid at zero temperature only, it is of course very desirable to extend the investigations to finite temperature values, which can possibly be achieved using the methods presented in Sec. 3.3, eventually computing the $(P^\star, T)$-phase diagrams of the proposed systems. This is quite costly on a computational level, but can be handled with the tools at hand today. We have implemented such a framework for crystalline three-dimensional patchy particle systems in a collaborative effort. The finite temperature results provided by our collaborator (using the data presented in Sec. 4.2.2 as an input) are not covered in this thesis, but are presented in Refs. [6, 7].

An even further step would be to investigate kinetic pathways, *i.e.*, to check if the identified equilibrium structures are actually formed *via* self-assembly, starting from random non-equilibrium particle configurations at finite temperature or nucleate from an undercooled liquid phase [116]. For large systems, currently achievable simulation times in molecular

dynamics-based calculations suitable for this purpose might be too short for computing such pathways. Kinetic traps, which can often be avoided when using the optimization approaches described in this work, can make simulating these systems *via* molecular dynamics extremely hard.

Appendices

A. Reduced Quantities

We calculate energy U, pressure P, volume V and enthalpy H as reduced, dimensionless quantities $X^\star$. Additionally, we define the packing fraction

$$\eta = \frac{V_{\text{particles}}}{V} = \frac{N\frac{4\pi(\sigma/2)^3}{3}}{V} = \frac{N\pi\sigma^3}{6V},$$
(A.1)

considering the particles as hard spheres of diameter σ.

With the particle number N, the unit of energy ϵ and the unit of length σ (which are usually given as intrinsic parameters of the interaction potential), we arrive at

$$U^\star = \frac{U}{N\epsilon}$$
(A.2)

$$P^\star = \frac{P\sigma^3}{\epsilon}$$
(A.3)

$$V^\star = \frac{V}{N\sigma^3}$$
(A.4)

$$\eta = \frac{\pi}{6V^\star}$$
(A.5)

$$H^\star = \frac{H}{N\epsilon} = U^\star + \frac{\pi}{6}\frac{P^\star}{\eta}.$$
(A.6)

In the case of bulk systems, these quantities are all understood as per unit cell.

B. Doye Model: Derivatives of the Potential

The following convention will be used in this chapter: all occurring quantities will be denoted as indexed terms, where lower indices always refer to vector components ($1 \leq k \leq 3$), for which the Einstein summation convention (ESC) is used, while upper indices stand for particles (Latin, $1 \leq i \leq N$) and patches (Greek, $1 \leq \alpha \leq N_{\text{patches}}$)[*], for which we do not use the ESC. We employ the following symbols:

r_k^i	position vector of the center-of-mass (CMS) of particle i
$r_k^{i,j}$	$r_k^j - r_k^i$
$r^{i,j}$	$\sqrt{r_k^{i,j} r_k^{i,j}}$
$p_k^{i,\alpha}$	distance vector between center of patch α on particle i and CMS of particle i
$p_k^{0,\alpha}$	position vector of the center of patch α in the particle frame
o_k^i	orientation vector of particle i (in the angle-axis description, *cf.* Sec. 3.2.2)

The fundamental parameters of the central optimization problem (*i.e.*, minimizing the binding energy U of a system with respect to these parameters, *cf.* Sec. 3.2) are r_k^i and o_k^i. The following relations can be calculated in a straightforward way

$$\frac{\partial r_k^{i,j}}{\partial r_l^i} = -\frac{\partial r_k^{i,j}}{\partial r_l^j} = -\delta_{kl} \tag{B.1}$$

$$\frac{\partial r^{i,j}}{\partial r_k^{i,j}} = \frac{r_k^{i,j}}{r^{i,j}}, \tag{B.2}$$

while $o_k^i, p_k^{0,\alpha}$ and $p_k^{i,\alpha}$ are related by

$$p_k^{i,\alpha} = R_{km}(o_n^i) p_m^{0,\alpha} \tag{B.3}$$

$$\frac{\partial p_k^{i,\alpha}}{\partial o_l^i} = \frac{\partial R_{km}(o_n^i)}{\partial o_l^i} p_m^{0,\alpha}. \tag{B.4}$$

The rotation matrix $R_{km}(o_n^i)$ and its derivatives $\partial R_{km}(o_n^i)/\partial o_q^i$ are given in Sec. 3.2.2.

For a finite number of particles (and omitting arguments of the functions), the energy U of the system can be calculated as a sum over pair interactions (*cf.* Sec. 2.2.2),

$$U = \sum_{i,j>i;\alpha,\beta} V^{i,j,\alpha,\beta}. \tag{B.5}$$

---

[*]N represents the number of particles in the system, N_{patches} the number of patches on each particle.

In the patchy regime, *i.e.*, $r^{i,j} > \sigma$, the interaction potential $V^{i,j,\alpha,\beta}$ between patch α on particle i and patch β on particle j is given as a function of $r_k^{i,j}, p_k^{i,\alpha}$ and $p_k^{i,\beta}$:

$$V(r_k^{i,j}, p_k^{i,\alpha}, p_k^{i,\beta}) = V_{\text{LJ}}(r^{i,j}) V_{\text{ang}}(r_k^{i,j}, p_k^{i,\alpha}, p_k^{i,\beta}). \tag{B.6}$$

Hence, we need to calculate

$$\frac{\partial V}{\partial r_k^i} = \frac{\partial V}{\partial r_l^{i,j}} \frac{\partial r_l^{i,j}}{\partial r_k^i} = \tag{B.7}$$

$$= \left(\frac{\partial V_{\text{LJ}}}{\partial r^{i,j}} \frac{\partial r^{i,j}}{\partial r_l^{i,j}} V_{\text{ang}} + V_{\text{LJ}} \frac{\partial V_{\text{ang}}}{\partial r_l^{i,j}} \right) \frac{\partial r_l^{i,j}}{\partial r_k^i}$$

$$\frac{\partial V}{\partial r_k^j} = \frac{\partial V}{\partial r_l^{i,j}} \frac{\partial r_l^{i,j}}{\partial r_k^j} = \tag{B.8}$$

$$= \left(\frac{\partial V_{\text{LJ}}}{\partial r^{i,j}} \frac{\partial r^{i,j}}{\partial r_l^{i,j}} V_{\text{ang}} + V_{\text{LJ}} \frac{\partial V_{\text{ang}}}{\partial r_l^{i,j}} \right) \frac{\partial r_l^{i,j}}{\partial r_k^j}$$

$$\frac{\partial V}{\partial o_k^i} = \frac{\partial V}{\partial p_l^{i,\alpha}} \frac{\partial p_l^{i,\alpha}}{\partial o_k^i} = V_{\text{LJ}} \frac{\partial V_{\text{ang}}}{\partial p_l^{i,\alpha}} \frac{\partial p_l^{i,\alpha}}{\partial o_k^i} \tag{B.9}$$

$$\frac{\partial V}{\partial o_k^j} = \frac{\partial V}{\partial p_l^{j,\beta}} \frac{\partial p_l^{j,\beta}}{\partial o_k^j} = V_{\text{LJ}} \frac{\partial V_{\text{ang}}}{\partial p_l^{j,\beta}} \frac{\partial p_l^{j,\beta}}{\partial o_k^j}; \tag{B.10}$$

with

$$V_{\text{LJ}}(r^{i,j}) = 4\epsilon \left[\left(\frac{\sigma}{r^{i,j}} \right)^{12} - \left(\frac{\sigma}{r^{i,j}} \right)^6 \right] \tag{B.11}$$

$$V_{\text{ang}}(r_k^{i,j}, p_k^{i,\alpha}, p_k^{i,\beta}) = \exp \left[-\frac{(\theta^{i,\alpha})^2 + (\theta^{j,\beta})^2}{w^2} \right] \tag{B.12}$$

$$\frac{\partial V_{\text{ang}}}{\partial \theta^{i,\alpha}} = \exp \left[-\frac{(\theta^{i,\alpha})^2 + (\theta^{j,\beta})^2}{w^2} \right] \left(-\frac{2\theta^{i,\alpha}}{w^2} \right) \tag{B.13}$$

$$\theta^{i,\alpha} = \arccos \left(\frac{r_l^{i,j} p_l^{i,\alpha}}{r^{i,j} |p_l^{i,\alpha}|} \right) \tag{B.14}$$

$$\theta^{j,\beta} = \arccos \left(\frac{-r_l^{i,j} p_l^{j,\beta}}{r^{i,j} |p_l^{j,\beta}|} \right) \tag{B.15}$$

and the fact that $|p_l^{i,\alpha}|$ are constant values[*], we obtain

$$\frac{\partial V_{\mathrm{LJ}}}{\partial r^{i,j}} = -4\epsilon \left[12 \left(\frac{\sigma}{r^{i,j}} \right)^{13} - 6 \left(\frac{\sigma}{r^{i,j}} \right)^7 \right] \tag{B.16}$$

$$\frac{\partial V_{\mathrm{ang}}}{\partial r_k^{i,j}} = \frac{\partial V_{\mathrm{ang}}}{\partial \theta^{i,\alpha}} \frac{-1}{\sqrt{1 - \cos^2\left(\theta^{i,\alpha}\right)}} \frac{1}{r^{i,j}|p_k^{i,\alpha}|} \left[p_k^{i,\alpha} - \frac{r_l^{i,j} p_l^{i,\alpha}}{(r^{i,j})^2} r_k^{i,j} \right] + \tag{B.17}$$

$$\frac{\partial V_{\mathrm{ang}}}{\partial \theta^{j,\beta}} \frac{-1}{\sqrt{1 - \cos^2\left(\theta^{j,\beta}\right)}} \frac{-1}{r^{i,j}|p_k^{j,\beta}|} \left[p_k^{j,\beta} - \frac{r_l^{i,j} p_l^{j,\beta}}{(r^{i,j})^2} r_k^{i,j} \right]$$

$$\frac{\partial V_{\mathrm{ang}}}{\partial p_k^{i,\alpha}} = \frac{\partial V_{\mathrm{ang}}}{\partial \theta^{i,\alpha}} \frac{-1}{\sqrt{1 - \cos^2\left(\theta^{i,\alpha}\right)}} \frac{r_k^{i,j}}{r^{i,j}|p_l^{i,\alpha}|} \tag{B.18}$$

$$\frac{\partial V_{\mathrm{ang}}}{\partial p_k^{j,\beta}} = \frac{\partial V_{\mathrm{ang}}}{\partial \theta^{j,\beta}} \frac{-1}{\sqrt{1 - \cos^2\left(\theta^{j,\beta}\right)}} \frac{-r_k^{i,j}}{r^{i,j}|p_l^{j,\beta}|}. \tag{B.19}$$

Substituting these result in combination with Eqs. (B.1) and (B.4) in Eqs. (B.7) – (B.10), we obtain the desired derivatives with respect to the fundamental parameters.

When optimizing crystal structures, there are nine additional fundamental parameters, defining the three primitive lattice vectors a_k, b_k, c_k (k is the coordinate index and we will use a in a representative way for all three vectors in the following); furthermore the position and orientation vectors are given in fractional coordinates f_a^i and g_a^i, *i.e.*, also depend on the primitive lattice vectors (*cf.* Sec. 3.2.2) Therefore, the particle positions r_k^i become functions of f_a^i and a_k (we use the summation convention $f_a^i a_k = \sum_{a=1}^3 f_a^i a_k$). The particle index i now specifies the particles within the primitive cell and is, in the case of CMS position vectors, accompanied by a second upper index $\mathcal{C}(n_1, n_2, n_3)$, which specifies the image cell within the crystal. For the sake of brevity, we will not denote the explicit dependence of $\mathcal{C}$ in the following. We can compute the derivatives of the potential with respect to the fundamental parameters of the crystalline system using the protocol described above and the additional relations given below:

$$r_k^{i,\mathcal{C}}(f_a^i, a_k) = f_a^i a_k + n_a a_k \tag{B.20}$$

$$p_k^{i,\alpha}(f_a^i, a_k) = g_a^{i,\alpha} a_k \tag{B.21}$$

$$\frac{\partial r_k^{i,\mathcal{C}}}{\partial f_a^i} = a_k \tag{B.22}$$

$$\frac{\partial r_k^{i,\mathcal{C}}}{\partial a_l} = \delta_{kl}(f_a + n_a) \tag{B.23}$$

$$\frac{\partial o_k^i}{\partial g_a^i} = a_k \tag{B.24}$$

$$\frac{\partial p_k^{i,\alpha}}{\partial a_l} = \delta_{kl} g_a^{i,\alpha}. \tag{B.25}$$

---

[*]All patches are located on the surface of the particle, *i.e.* $|p_l^{i,\alpha}| = \sigma/2$.

When optimizing enthalpies $H = U + P\mathcal{V}$, we also need to take derivatives of the volume term[*]

$$\mathcal{V}(a_k, b_k, c_k) = |a_k \cdot (b_k \times c_k)|, \tag{B.26}$$

where the three primitive lattice vectors are termed a_k, b_k, c_k for clarity. With the signum function $\mathrm{sgn}(x)$ and the unimodular, real prefactor $A = \mathrm{sgn}(a_k \cdot (b_k \times c_k))$, the respective derivatives read

$$\frac{\partial \mathcal{V}}{\partial a_1} = A(b_2 c_3 - b_3 c_2) \qquad \frac{\partial \mathcal{V}}{\partial a_2} = A(b_3 c_1 - b_1 c_3) \qquad \frac{\partial \mathcal{V}}{\partial a_3} = A(b_1 c_2 - b_2 c_1) \tag{B.27}$$

$$\frac{\partial \mathcal{V}}{\partial b_1} = A(c_2 a_3 - c_3 a_2) \qquad \frac{\partial \mathcal{V}}{\partial b_2} = A(c_3 a_1 - c_1 a_3) \qquad \frac{\partial \mathcal{V}}{\partial b_3} = A(c_1 a_2 - c_2 a_1) \tag{B.28}$$

$$\frac{\partial \mathcal{V}}{\partial c_1} = A(a_2 b_3 - a_3 b_2) \qquad \frac{\partial \mathcal{V}}{\partial c_2} = A(a_3 b_1 - a_1 b_3) \qquad \frac{\partial \mathcal{V}}{\partial c_3} = A(a_1 b_2 - a_2 b_1). \tag{B.29}$$

---

[*]*I.e.*, the volume of the primitive cell.

C. IPCs: Derivatives of the Potential

If not stated otherwise, the symbols we use here have the same meanings as in App. B. Again, the fundamental parameters of the optimization problem are r_k^i and o_k^i; thus Eqs. (B.1) – (B.4) are also valid here.

The relevant inter-sphere distances for two given IPCs i, j (*cf.* Fig. 2.7, Sec. 2.2.3) read

$$r_{B^i B^j} = |r_k^j - r_k^i| \tag{C.1}$$

$$r_{B^i S^{j,\beta}} = |r_k^j + p_k^{j,\beta} - r_k^i| \tag{C.2}$$

$$r_{S^{i,\alpha} S^{j,\beta}} = |r_k^j + p_k^{j,\beta} - r_k^i - p_k^{i,\alpha}|. \tag{C.3}$$

It is straightforward to calculate the derivatives of these inter-sphere distances $r_{\mathcal{AB}}$ with respect to the fundamental parameters; the overlap volumes $\Omega_{\mathcal{AB}}$ given in Eq. (2.30) only depend on $r_{\mathcal{AB}}$. Thus, we need to compute

- $r_{\min} \leq r_{\mathcal{AB}} \leq r_{\max}$: $\tag{C.4}$

$$
\begin{aligned}
\frac{\partial \Omega_{\mathcal{AB}}}{\partial r_{\mathcal{AB}}} = \frac{\pi}{3} &\left[\left(1 - \frac{R_{\mathcal{A}}^2 - R_{\mathcal{B}}^2 + r_{\mathcal{AB}}^2}{2 r_{\mathcal{AB}}^2} \right) \left(R_{\mathcal{A}} - \frac{R_{\mathcal{A}}^2 - R_{\mathcal{B}}^2 + r_{\mathcal{AB}}^2}{2 r_{\mathcal{AB}}} \right)^2 + \right. \\
&\quad 2 \left(2 R_{\mathcal{A}} + \frac{R_{\mathcal{A}}^2 - R_{\mathcal{B}}^2 + r_{\mathcal{AB}}^2}{2 r_{\mathcal{AB}}} \right) \left(R_{\mathcal{A}} - \frac{R_{\mathcal{A}}^2 - R_{\mathcal{B}}^2 + r_{\mathcal{AB}}^2}{2 r_{\mathcal{AB}}} \right) \left(-1 + \frac{R_{\mathcal{A}}^2 - R_{\mathcal{B}}^2 + r_{\mathcal{AB}}^2}{2 r_{\mathcal{AB}}^2} \right) + \\
&\quad \left(-1 - \frac{R_{\mathcal{A}}^2 - R_{\mathcal{B}}^2 - r_{\mathcal{AB}}^2}{2 r_{\mathcal{AB}}^2} \right) \left(R_{\mathcal{B}} - \frac{R_{\mathcal{A}}^2 - R_{\mathcal{B}}^2 - r_{\mathcal{AB}}^2}{2 r_{\mathcal{AB}}} \right)^2 + \\
&\quad \left. 2 \left(2 R_{\mathcal{B}} + \frac{R_{\mathcal{A}}^2 - R_{\mathcal{B}}^2 - r_{\mathcal{AB}}^2}{2 r_{\mathcal{AB}}} \right) \left(R_{\mathcal{B}} - \frac{R_{\mathcal{A}}^2 - R_{\mathcal{B}}^2 - r_{\mathcal{AB}}^2}{2 r_{\mathcal{AB}}} \right) \left(1 + \frac{R_{\mathcal{A}}^2 - R_{\mathcal{B}}^2 - r_{\mathcal{AB}}^2}{2 r_{\mathcal{AB}}^2} \right) \right]
\end{aligned}
$$

- otherwise :

$$\frac{\partial \Omega_{\mathcal{AB}}}{\partial r_{\mathcal{AB}}} = 0$$

By combining these results, the derivatives $\partial V_{\text{IPC}}/\partial r_k^i$, $\partial V_{\text{IPC}}/\partial o_k^i$ can easily be evaluated.

D. Calculating Free Energies and Their Derivatives *via* Lattice Dynamics

D.1. Isotropic Potentials

We calculate the Gibbs free energy G of a given crystal configuration within the formalism of lattice dynamics in the quasi-harmonic approximation, as described in Ref. [104]. A configuration is characterized by geometric parameters $\{\mathbf{x}\}$, *i.e.*, a set of lattice vectors and coordinates of particles in the primitive cell and the temperature $T = T_0$ and the pressure $P = P_0$ are fixed. The Gibbs free energy reads

$$G(\{\mathbf{x}\}, T_0, P_0) = U(\{\mathbf{x}\})|_{T=T_0} - T_0 S(\{\mathbf{x}\}) + P_0 V(\{\mathbf{x}\}). \tag{D.1}$$

The difference in potential energy between the finite and the zero-temperature case, caused by temperature-driven particle fluctuations u_k^i, in combination with the entropic term* gives the vibrational part of the free energy

$$F_{\text{vib}}(\{\mathbf{x}\}, T_0) = U(\{\mathbf{x}\})|_{T=T_0} - U(\{\mathbf{x}\})|_{T=0} - T_0 S(\{\mathbf{x}\}). \tag{D.2}$$

With this quantity and the enthalpy H, the Gibbs free energy can be rewritten as

$$G(\{\mathbf{x}\}, T_0, P_0) = U(\{\mathbf{x}\})|_{T=0} + F_{\text{vib}}(\{\mathbf{x}\}, T_0) + P_0 V(\{\mathbf{x}\}) \tag{D.3}$$

$$= H(\{\mathbf{x}\}, P_0)|_{T=0} + F_{\text{vib}}(\{\mathbf{x}\}, T_0). \tag{D.4}$$

As all vibrational motions in the crystal can be written as a superposition of plane waves, $F_{\text{vib}}(\{\mathbf{x}\}, T_0)$ can be calculated as a sum

$$F_{\text{vib}}(\{\mathbf{x}\}, T_0) = \sum_{\mathbf{q}, s} F_{\mathbf{q}, s}(\{\mathbf{x}\}, T_0) \tag{D.5}$$

over terms corresponding to wave vectors $\mathbf{q}$ in the first Brillouin zone of the reciprocal lattice. In principle, the sum has to be taken over an infinite number of vectors $\mathbf{q}$, but there exist several approximation schemes involving only a finite sum, *e.g.* [117].

---

*We only treat the vibrational, not the configurational entropy here.

In the harmonic approximation, particle displacements from their equilibrium positions are treated as a superpositions of normal modes (phonons) with frequencies $\omega_{\mathbf{q},s}$. For each $\mathbf{q}$, s_{max} frequencies, corresponding to acoustic and optical phonon branches [103] can be obtained by solving an eigenvalue problem (see below). Treating the phonons as an ensemble of harmonic oscillators, the free energy contribution $F_{\mathbf{q},s}$ of each branch is given by [99, 103]

$$F_{\mathbf{q},s}(\{\mathbf{x}\}, T_0) = \frac{1}{2}\hbar\omega_{\mathbf{q},s}(\{\mathbf{x}\}) + k_B T_0 \ln\left[1 - \exp\left(-\frac{\hbar\omega_{\mathbf{q},s}(\{\mathbf{x}\})}{k_B T_0}\right)\right]. \tag{D.6}$$

In the classical limit $\hbar \to 0$, with

$$\exp\left(-\frac{\hbar\omega_{\mathbf{q},s}(\{\mathbf{x}\})}{k_B T_0}\right) \approx 1 - \frac{\hbar\omega_{\mathbf{q},s}(\{\mathbf{x}\})}{k_B T_0} \tag{D.7}$$

and $\ln(ab) = \ln a + \ln b$, we obtain

$$F_{\mathbf{q},s}^{\text{Classical}}(\{\mathbf{x}\}, T_0) \approx \text{const.} + k_B T_0 \ln[\omega_{\mathbf{q},s}(\{\mathbf{x}\})]. \tag{D.8}$$

The normal mode frequencies $\omega_{\mathbf{q},s}(\{\mathbf{x}\})$ correspond to the square roots of the eigenvalues $\lambda_{\mathbf{q},s}(\{\mathbf{x}\})$ of the so-called dynamical matrix $D_{kl}^{ij}(\mathbf{q}, \{\mathbf{x}\})$, where, as in the previous appendix chapters, upper indices correspond to particles in the primitive cell and lower indices correspond to Cartesian coordinates. With the eigenvectors $v_{k\mathbf{q},s}^i(\{\mathbf{x}\})$, the eigenvalue problem is given as

$$D_{kl}^{ij}(\mathbf{q}, \{\mathbf{x}\})v_{k\mathbf{q},s}^i(\{\mathbf{x}\}) = \lambda_{\mathbf{q},s}(\{\mathbf{x}\})v_{k\mathbf{q},s}^i(\{\mathbf{x}\}) \tag{D.9}$$

and can be solved using standard software like LAPACK [118].

The dynamical matrix is calculated as a Fourier transform from the direct lattice with vectors $\mathbf{a}$ to the reciprocal lattice with vectors $\mathbf{q}$, *i.e.*, a sum over all vectors $\mathbf{a}$

$$D_{kl}^{ij}(\mathbf{q}, \{\mathbf{x}\}) = \frac{1}{\sqrt{m_i m_j}}\sum_{\mathbf{a}} e^{i\mathbf{q}\mathbf{a}}\frac{\partial^2 U(\{\mathbf{x}\})|_{T=0}}{\partial u_k^{i,\mathbf{0}}\partial u_l^{j,\mathbf{a}}}. \tag{D.10}$$

m_i indicates the mass of particle i. $u_k^{i,\mathbf{a}}$ represents the k-th Cartesian component of the displacement of the image of particle i in the cell corresponding to lattice vector $\mathbf{a}$ from its equilibrium position $r_{\text{eq},k}^{i,\mathbf{a}}$ (*i.e.*, $r_k^{i,\mathbf{a}} = r_{\text{eq},k}^{i,\mathbf{a}} + u_k^{i,\mathbf{a}}$). Since only potentials with finite range are employed in this work, the sum always consists of a finite number of terms. In practice, the second derivatives of the interaction energy, which are given by the terms

$$\frac{\partial^2 U(\{\mathbf{x}\})|_{T=0}}{\partial u_k^{i,\mathbf{0}}\partial u_l^{j,\mathbf{a}}}, \tag{D.11}$$

can be calculated once and stored for a given configuration, so that it is computationally relatively cheap to compute the dynamical matrix for varying $\mathbf{q}$.

Even though the normal mode frequencies and thus the vibrational free energy do not depend

on the geometry parameters in a closed form, it is still possible to calculate derivatives with respect to the geometric parameters $\partial_{\{\mathbf{x}\}} F_{\text{vib}}$ *via* a perturbative approach [104]. Taking a derivative on both sides of the eigenvalue problem given in Eq. (D.9) leads to[*]

$$\partial_{\{\mathbf{x}\}}[D]\mathbf{v}_s + D\partial_{\{\mathbf{x}\}}[\mathbf{v}_s] = \partial_{\{\mathbf{x}\}}[\lambda_s]\mathbf{v}_s + \lambda_s\partial_{\{\mathbf{x}\}}[\mathbf{v}_s] \tag{D.12}$$

$$(\partial_{\{\mathbf{x}\}}[D] - \partial_{\{\mathbf{x}\}}[\lambda_s])\mathbf{v}_s = (\lambda_s - D)\partial_{\{\mathbf{x}\}}[\mathbf{v}_s]. \tag{D.13}$$

Since $\{\mathbf{v}_s\}$ is an orthonormal basis of the underlying vector space, we can write $\partial_{\{\mathbf{x}\}}[\mathbf{v}_s] = \sum_s c_s\mathbf{v}_s$; multiplying both sides with $\mathbf{v}_s^T$ and using orthogonality ($\mathbf{v}_s\mathbf{v}_t = \delta_{st}$) we find

$$\mathbf{v}_s^T\partial_{\{\mathbf{x}\}}[D]\mathbf{v}_s - \partial_{\{\mathbf{x}\}}[\lambda_s] = \lambda_s c_s - c_s\lambda_s \tag{D.14}$$

$$\partial_{\{\mathbf{x}\}}[\lambda_s] = \mathbf{v}_s^T\partial_{\{\mathbf{x}\}}[D]\mathbf{v}_s. \tag{D.15}$$

This equation is exact. Thus, once the eigenvalue problem is solved, derivatives of the eigenvalues and derivatives of the free energy

$$\partial_{\{\mathbf{x}\}}[F_{\mathbf{q},s}^{\text{Classical}}(\{\mathbf{x}\}, T_0)] \approx k_B T_0 \frac{1}{2\omega_{\mathbf{q},s}^2(\{\mathbf{x}\})}\partial_{\{\mathbf{x}\}}[\lambda_{\mathbf{q},s}(\{\mathbf{x}\})] \tag{D.16}$$

can effectively be obtained by taking first derivatives of the dynamical matrix (*i.e.*, third derivatives of the interaction energy) with respect to the geometric parameters. Although this procedure is quite cumbersome, it allows to perform quasi-Newton local optimization of structural parameters at finite temperature, as long as the harmonic approximation is valid.

D.2. Anisotropic Potentials

This formalism can be expanded to anisotropic potentials by including the rotational degrees of freedom in the dynamical matrix D_{kl}^{ij} [105]; then the indices k and l not only represent translational, but also rotational displacements (*i.e.*, derivatives are also taken with respect to infinitesimal rotations about the Cartesian coordinate axes). The rotation of a vector $p_l = \{p_1, p_2, p_3\}^T$ about an infinitesimal angle $d\phi$ and the third (z-) axis of the coordinate system is given by

$$p_k^{\text{rot}} = R_{kl}^3(d\phi_3)p_l \tag{D.17}$$

$$R_{kl}^3(d\phi_3) = \begin{pmatrix} 1 & -d\phi_3 & 0 \\ d\phi_3 & 1 & 0 \\ 0 & 0 & 1 \end{pmatrix}. \tag{D.18}$$

---

[*]We suppress the explicit dependencies and indices; $\partial[\ ]$ signifies that the partial derivative is only taken for the expression within the square brackets.

Hence, the derivative of the rotated vector with respect to this infinitesimal rotational displacement $d\phi_3$ is

$$\frac{\partial \mathbf{p}^{\mathrm{rot}}}{\partial \phi_3} = \begin{pmatrix} -p_2 \\ p_1 \\ 0 \end{pmatrix}. \tag{D.19}$$

Rotations about the remaining axes can easily be obtained by cyclical permutations

$$\frac{\partial \mathbf{p}^{\mathrm{rot}}}{\partial \phi_1} = \begin{pmatrix} 0 \\ -p_3 \\ p_2 \end{pmatrix} \qquad \frac{\partial \mathbf{p}^{\mathrm{rot}}}{\partial \phi_2} = \begin{pmatrix} p_3 \\ 0 \\ -p_1 \end{pmatrix} \qquad \frac{\partial \mathbf{p}^{\mathrm{rot}}}{\partial \phi_3} = \begin{pmatrix} -p_2 \\ p_1 \\ 0 \end{pmatrix}. \tag{D.20}$$

Thus, the derivatives of the interaction energy with respect to rotational displacements $\phi_k^{i,\mathbf{a}}$ are given by

$$\frac{\partial U(\{\mathbf{x}\})}{\partial \phi_k^{i,\mathbf{a}}} = \frac{\partial U(\{\mathbf{x}\})}{p_l^{i,\mathbf{a}}} \frac{\partial p_l^{i,\mathbf{a}}}{\partial \phi_k^{i,\mathbf{a}}}. \tag{D.21}$$

Further, in Eq. (D.10) the masses m_i, m_j have to be replaced by the moments of inertia I_i, I_j when the indices k, l correspond to rotational degrees of freedom.

E. Performance of the Evolutionary Algorithm

In this section, we measure convergence rates and runtimes of the evolutionary optimization algorithm in dependence of tunable parameters. As measurement techniques we employ graphs similar to the ones introduced in Ref. [119], sometimes called "Hartke plots". In such graphs, the performance of a (large) number of runs of an EA, applied on a certain optimization problem with a given set of parameters, is visualized by plotting

- the value of the cost function for the best individual of the best run (*i.e.*, the run which reached the global minimum within the smallest number of iterations[*])

- the value of the cost function for the best individual of the worst run (*i.e.*, the run, whose best individual has the highest enthalpy value after the given number of iterations)

- the average of the values of the cost function for the best individual of all runs

as functions of the number of individuals created so far. This method has been extended in Ref. [81] by fitting an exponential function of type

$$\bar{H}(i) = \left(\bar{H}_{\mathrm{random}} - H_{\mathrm{min}}\right)\, \exp(a\, i^b) + H_{\mathrm{min}} \tag{E.1}$$

to the average curve, where i is the number of individuals created so far, H_{random} represents the average cost function value of a large number randomly created, locally optimized candidate solutions, H_{min} is the cost function value of the (putative) global minimum and a, b are fitting parameters.

Here, we define the fitting function in a slightly different way: Since prior the evolutionary process the population is filled with random individuals, the EA effectively starts at

$$i_{\mathrm{start}} = N_{\mathrm{population}} \tag{E.2}$$

$$H_{\mathrm{start}} = \min \{H_1^{\mathrm{random}}, .., H_{N_{\mathrm{population}}}^{\mathrm{random}}\}. \tag{E.3}$$

Therefore, we fit the average curve to the function

$$\bar{H}(i) = (\bar{H}_{\mathrm{start}} - H_{\mathrm{min}})\exp(a(i - N_{\mathrm{population}})^b) + H_{\mathrm{min}}. \tag{E.4}$$

---

[*]Since we chose a rather simple benchmark problem, the best of 100 runs often reached the global minimum already at the first iteration.

We use three values to measure the suitability of the chosen parameters for the given benchmark problem:

- p_{success}, the percentage of algorithm runs which actually have reached the (putative) global minimum after a chosen number of iterations i_{max}.

- $i_{1/10}$, the average number of iterations it takes the EA to reach a cost function value below $\bar{H}(i_{1/10}) = 1/10(\bar{H}_{\text{random}} - H_{\text{min}}) + H_{\text{min}}$; this value can easily be calculated when the fitting function is known and provides complementary information to p_{success}: a comparatively low value of $i_{1/10}$ (*i.e.*, "good" solutions are found within few iterations) alongside a low success rate hints on the algorithm getting trapped in local minima and possibly a multi-funnel energy landscape.

- $\bar{t}_{\text{run}}$, the average runtime of the EA (in seconds, all tests performed in a parallel environment making use of 12 processor cores) to perform i_{max} iterations; this value is mostly governed by the runtime of the local optimizations, *i.e.*, better starting points provided by the crossover operation should lead to shorter runtimes.

In the following, we will present the results of benchmark tests we performed for several different parameters of the EA. As a test problem, we chose the identification of the zero-temperature equilibrium structure of the symmetrical tetrahedral Doye model, with four particles in the primitive cell. This optimization problem can usually be solved rather quickly, within 100 iterations; therefore we were able to perform at least 100 independent EA runs for each parameter setting. Based on the data presented in Tab. E.1, we calculate standard deviations for p_{success} of about $2-5$, based on several measurements averaged over 100 runs each; for $i_{1/10}$ we compute values around $1.7-2.5$ and for $\bar{t}$ the standard deviations are usually $0.1-0.3$. Here we list the parameters under investigation and the standard values we chose when varying other parameters:

parameter	value
lattice crossover type	(a)
unit cell volume (before local optimization)	0.8, adaptive
elitism	3 (population 10)
mutation rate	0.1

Crossover Type

As mentioned in Sec. 3.2.2, we have implemented two different protocols of performing a crossover for primitive lattice vectors. In type (a), the child individual's lattice vectors are computed as averages over the parents' lattice vectors, while in type (b), one parent is randomly chosen to directly pass on its lattice vectors to the child. The data from five independent benchmark tests consisting of 100 algorithm runs for each setting, provided in Tab. E.1, show that crossover type (a) leads to a distinctively superior performance with

respect to the values measuring the quality of the solutions (*i.e.*, success rates and $i_{1/10}$-values), while the algorithm runtimes are similar for both types.

lattice crossover type and run number	p_{success}	$i_{1/10}$	$\bar{t}$
(a) 1	84	24.82	35.72
(a) 2	85	22.87	35.34
(a) 3	80	26.43	35.56
(a) 4	84	22.20	36.20
(a) 5	84	23.41	35.70
(b) 1	61	39.73	36.02
(b) 2	73	35.45	36.07
(b) 3	71	35.29	36.34
(b) 4	65	40.39	36.17
(b) 5	73	35.86	36.24

Table E.1.: Benchmark values (as defined in the text) for two different versions of the lattice crossover operation (see text); five independent tests for crossover types (a) and (b) respectively, consisting of 100 EA runs each.

Initial Unit Cell Volume

In general, it seems to be natural to select an initial unit cell volume close to the expected value of the global minimum configuration*. However, our data (*cf.* Tab. E.2) suggests a different scenario for patchy particles, at least when using the Doye potential (*cf.* Sec. 2.2.2). Local optimizations of the interparticle distance in the isotropic repulsive regime of the potential are rather easy, while the particles do not "feel" each other's attraction at larger distances when they are not oriented in the proper way, which makes local optimizations in the patchy regime much less efficient. Thus, it is recommendable to choose a very small initial unit cell volume and to let the system relax to a energetically more favorable volume by the local optimization. In such a scenario, it is recommendable to keep the initial unit cell volume fixed during an EA run. However, the negative effect of choosing an adaptive V_{UC} is not very pronounced in the data provided below, since the benchmark runs use a comparatively small number of iterations. Notably, small initial unit cell volumes also decrease the average algorithm runtime, *i.e.* result in shorter local optimization cycles.

---

*In the test case, this would correspond to $V_{\text{UC}} \approx 0.97$.

V_{UC}	p_{success}	$i_{1/10}$	$\bar{t}$
0.1, fixed	100	35.29	27.86
0.2, fixed	98	26.49	29.87
0.4, fixed	92	21.91	33.06
0.6, fixed	92	21.67	34.80
0.8, fixed	85	25.89	35.83
1.0, fixed	86	25.49	36.63
0.1, adaptive	95	40.33	27.96
0.2, adaptive	98	26.88	30.09
0.4, adaptive	94	26.27	32.53
0.6, adaptive	86	20.85	34.67
0.8, adaptive	87	28.37	34.98
1.0, adaptive	82	25.69	36.44

Table E.2.: Benchmark values (as defined in the text) for different initial unit cell volumes V_{UC}, either fixed during the run or adaptive (see text). Note that $\bar{H}_{\mathrm{start}}$ – *cf.* Eq. (E.4) – depends on V_{UC}, influencing the $i_{1/10}$ values.

Elitism

According to our data (*cf.* Tab. E.3), the elitism parameter e has a much smaller influence on the performance of the algorithm than the options mentioned before. Employing a total population of ten individuals, we let e vary between 0 and 10. The only significant change we observe here is a somewhat lower success rate when using no elitism at all. Any e-value around half of the total population seems to be a good choice.

e	p_{success}	$i_{1/10}$	$\bar{t}$
0	84	25.76	35.62
3	87	22.88	35.74
5	87	22.74	36.11
7	86	23.44	35.98
10	86	24.76	36.00

Table E.3.: Benchmark values (as defined in the text) for different values of the elitism parameter e (see text).

Mutation Rate

As described in Sec. 3.2.2, we employ a mutation operator that performs a random strain on the primitive lattice vectors. The mutation rate p_{mut} is the probability of this operation acting on a newly created individual. Our benchmark tests (*cf.* Tab. E.4) show that rather low mutation rates around 10 percent have a beneficial effect on p_{success}, as compared to an algorithm without mutation, which seems to converge to low-enthalpy solutions faster

(*i.e.*, has a lower $i_{1/10}$-value) but gets stuck in local minima more easily. Higher p_{mut}-values, resulting in a much more stochastic search, negatively influence p_{success} as well as $i_{1/10}$.

p_{mut}	p_{success}	$i_{1/10}$	$\bar{t}$
0.0	83	24.81	35.70
0.1	89	25.06	35.70
0.2	84	29.61	35.89
0.3	75	32.67	36.12
0.4	70	29.92	35.28

Table E.4.: Benchmark values (as defined in the text) for different values of the mutation parameter p_{mut} (see text).
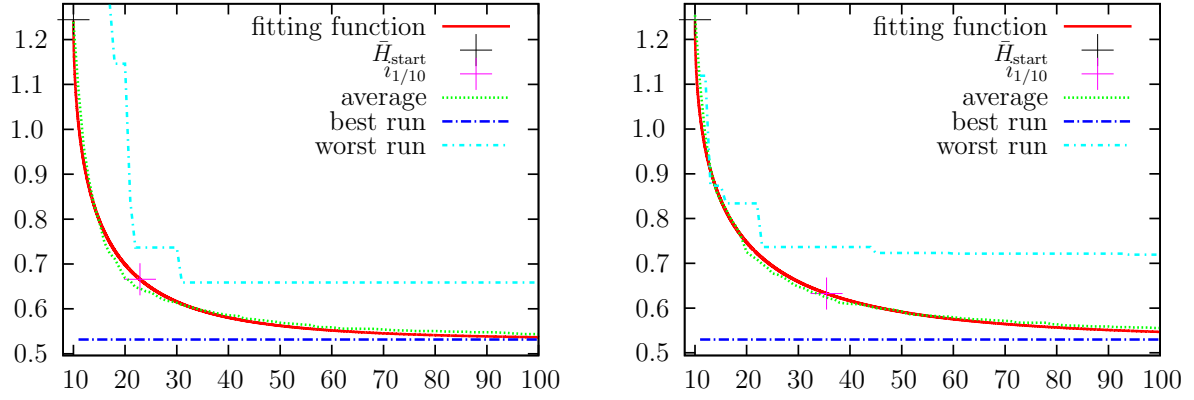
Figure E.1.: Hartke plots (see text) with a fitting function for the average curve as defined in Eq. (E.4). Left: Best out of five tests for lattice crossover type (a); right: best out of five tests for lattice crossover type (b).
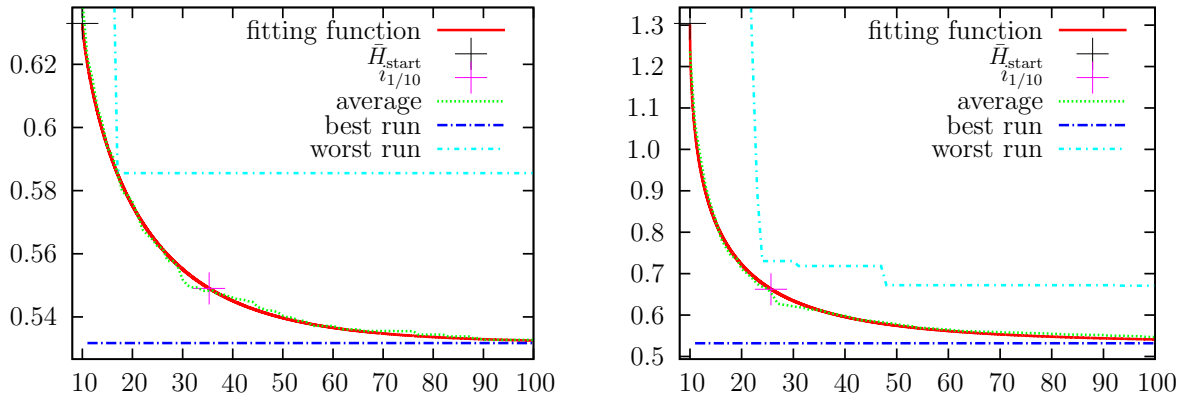

Figure E.2.: Hartke plots (see text) with a fitting function for the average curve as defined in Eq. (E.4). Best (left; $V_{\mathrm{UC}} = 0.1$, fixed) and worst (right; $V_{\mathrm{UC}} = 1.0$, adaptive) results among the tested initial unit cell volume parameter values.
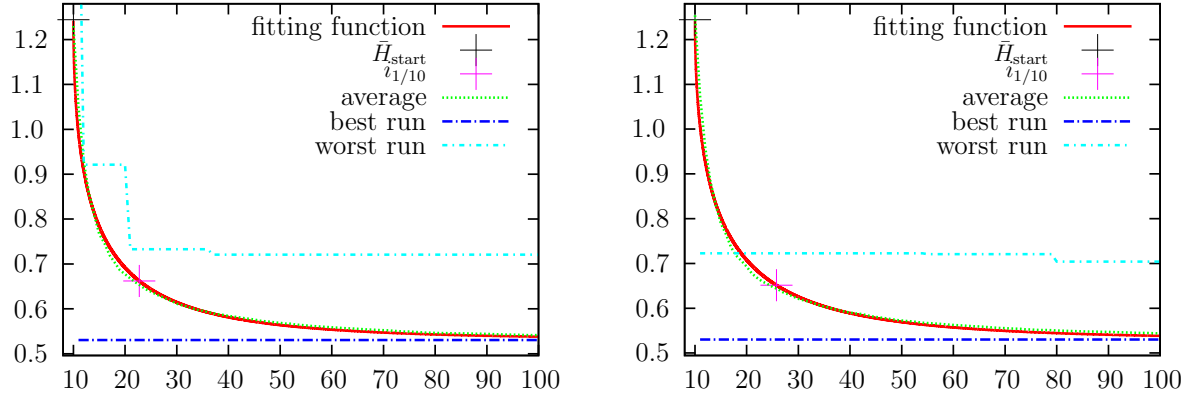
Figure E.3.: Hartke plots (see text) with a fitting function for the average curve as defined in Eq. (E.4). Best (left; $e = 5$) and worst (right; $e = 0$) results among the tested elitism parameter values.
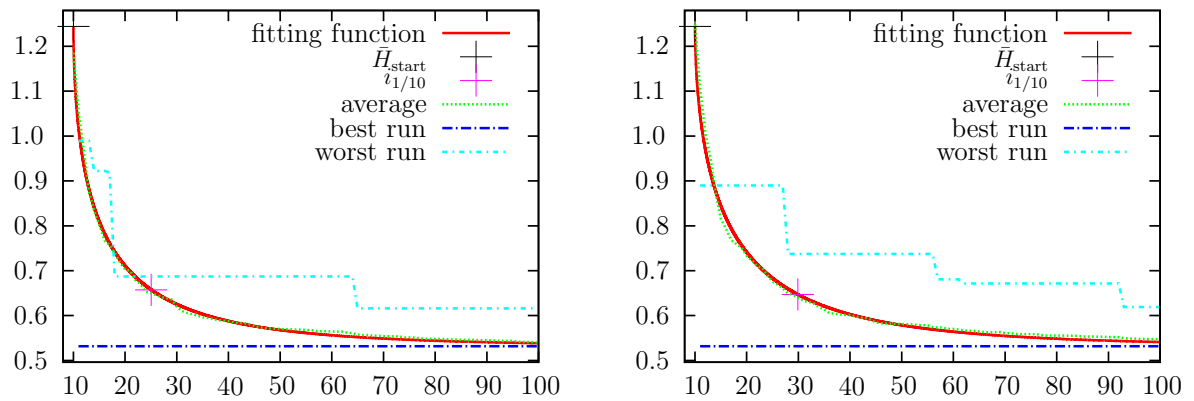

Figure E.4.: Hartke plots (see text) with a fitting function for the average curve as defined in Eq. (E.4). Best (left; $p_{\mathrm{mut}} = 0.1$) and worst (right; $p_{\mathrm{mut}} = 0.4$) results among the tested mutation rate values.

Bibliography

[1] Likos, C. N. Effective interactions in soft condensed matter physics. *Phys. Rep.* **348**, 267 (2001).

[2] Likos, C. N. Soft matter with soft particles. *Soft Matter* **2**, 478 (2006).

[3] deGennes, P. G. Soft matter (Nobel lecture). *Rev. Mod. Phys.* **64**, 645 (1992).

[4] Glotzer, S. C. & Solomon, M. J. Anisotropy of building blocks and their assembly into complex structures. *Nat. Mater.* **6**, 557 (2007).

[5] Li, F., Josephson, D. P. & Stein, A. Colloidal assembly: The road from particles to colloidal molecules and crystals. *Angew. Chem. Int. Ed.* **50**, 360 (2011).

[6] Doppelbauer, G., Noya, E. G., Bianchi, E. & Kahl, G. Self assembly scenarios of patchy particles. *Soft Matter* **8**, 7768 (2012).

[7] Doppelbauer, G., Noya, E. G., Bianchi, E. & Kahl, G. Competing ordered structures formed by particles with a regular tetrahedral patch decoration. *J. Phys.: Condens. Matter* **24**, 280401 (2012).

[8] Zhang, Z. & Glotzer, S. C. Self-assembly of patchy particles. *Nano Lett.* **4**, 1407 (2004).

[9] Bianchi, E., Blaak, R. & Likos, C. N. Patchy colloids: state of the art and perspectives. *Phys. Chem. Chem. Phys.* **13**, 6397 (2011).

[10] Pawar, A. B. & Kretzschmar, I. Fabrication, assembly, and application of patchy particles. *Macromol. Rapid. Commun.* **31**, 150 (2010).

[11] Maldovan, M. & Thomas, E. L. Diamond-structured photonic crystals. *Nat. Mater.* **3**, 593 (2004).

[12] Galisteo-López, J. F., Ibisate, M., Sapienza, R., Froufe-Pérez, L. S., Blanco, A. & López, C. Self-assembled photonic structures. *Adv. Mater.* **23**, 30 (2011).

[13] Langer, R. & Tirrell, D. A. Designing materials for biology and medicine. *Nature* **428**, 487 (2004).

[14] Graetzel, M. Photoelectrochemical cells. *Nature* **414**, 338 (2001).

[15] Hong, L., Jiang, S. & Granick, S. Simple method to produce janus colloidal particles in large quantity. *Langmuir* **22**, 9495 (2006).

[16] Böker, A., He, J., Emrick, T. & Russell, T. P. Self-assembly of nanoparticles at interfaces. *Soft Matter* **3**, 1231 (2007).

[17] Manoharan, V. N., Elsesser, M. T. & Pine, D. J. Dense packing and symmetry in small clusters of microspheres. *Science* **301**, 483 (2003).

[18] Kraft, D. J., Groenewold, J. & Kegel, W. K. Colloidal molecules with well-controlled bond angles. *Soft Matter* **5**, 3823 (2009).

[19] Pawar, A. B. & Kretzschmar, I. Patchy particles by glancing angle deposition. *Langmuir* **24**, 355 (2008).

[20] Chen, Q., Bae, S. C. & Granick, S. Directed self-assembly of a colloidal kagome lattice. *Nature* **469**, 381 (2011).

[21] Mirkin, C. A., Letsinger, R. L., Mucic, R. C. & Storhoff, J. J. A DNA-based method for rationally assembling nanoparticles into macroscopic materials. *Nature* **382**, 607 (1996).

[22] Park, S. Y., Lytton-Jean, A. K. R., Lee, B., Weigand, S., Schatz, G. C. & Mirkin, C. A. DNA-programmable nanoparticle crystallization. *Nature* **451**, 553 (2008).

[23] Nykypanchuck, D., Maye, M. M., van der Lelie, D. & Gang, O. DNA-guided crystallization of colloidal nanoparticles. *Nature* **451**, 549 (2008).

[24] Angioletti-Uberti, S., Mognetti, B. M. & Frenkel, D. Re-entrant melting as a design principle for DNA-coated colloids. *Nat. Mater.* **11**, 518 (2012).

[25] Mognetti, B. M., Leunissen, M. E. & Frenkel, D. Controlling the temperature sensitivity of DNA-mediated colloidal interactions through competing linkages. *Soft Matter* **8**, 2213 (2012).

[26] Rastogi, V., García, A. A., Marquez, M. & Velev, O. D. Anisotropic particle synthesis inside droplet templates on superhydrophobic surfaces. *Macromol. Rapid Commun.* **31**, 190 (2010).

[27] Likos, C. N., Blaak, R. & Wynveen, A. Computer simulations of polyelectrolyte stars and brushes. *J. Phys.: Condens. Matter* **20**, 494221 (2008).

[28] Jusufi, A. & Likos, C. N. Colloquium: Star-branched polyelectrolytes: The physics of their conformations and interactions. *Rev. Mod. Phys.* **81**, 1753 (2009).

[29] Bianchi, E., Largo, J., Tartaglia, P., Zaccarelli, E. & Sciortino, F. Phase diagram of patchy colloids: Towards empty liquids. *Phys. Rev. Lett.* **97**, 168301 (2006).

[30] Sciortino, F., De Michele, C., Corezzi, S., Russo, J., Zaccarelli, E. & Tartaglia, P. A parameter-free description of the kinetics of formation of loop-less branched structures and gels. *Soft Matter* **5**, 2571 (2009).

[31] Corezzi, S., De Michele, C., Zaccarelli, E., Tartaglia, P. & Sciortino, F. Connecting irreversible to reversible aggregation: Time and temperature. *J. Phys. Chem. B* **113**, 1233 (2009).

[32] Kern, N. & Frenkel, D. Fluid fluid coexistence in colloidal systems with short-ranged strongly directional attraction. *J. Chem. Phys.* **118**, 9882 (2003).

[33] Rho, K.-H., Martin, D. C. & Lahann, J. Biphasic Janus particles with nanoscale anisotropy. *Nat. Mater.* **4**, 759 (2005).

[34] Sciortino, F., Giacometti, A. & Pastore, G. Phase diagram of Janus particles. *Phys. Rev. Lett.* **103**, 237801 (2009).

[35] Romano, F. & Sciortino, F. Patchy from the bottom up. *Nat. Mater.* **10**, 171 (2011).

[36] Foffi, G. & Sciortino, F. On the possibility of extending the Noro Frenkel generalized law of correspondent states to nonisotropic patchy interactions. *J. Phys. Chem. B* **111**, 9702 (2007).

[37] Doye, J. P. K., Louis, A. A., Lin, I. C., Allen, L. R., Noya, E. G., Wilber, A. W., Kok, H. C. & Lyus, R. Controlling crystallization and its absence: proteins, colloids and patchy models. *Phys. Chem. Chem. Phys.* **9**, 2197 (2007).

[38] Noya, E. G., Vega, C., Doye, J. P. K. & Louis, A. A. Phase diagram of model anisotropic particles with octahedral symmetry. *J. Chem. Phys.* **127**, 054501 (2007).

[39] Noya, E. G., Vega, C., Doye, J. P. K. & Louis, A. A. The stability of a crystal with diamond structure for patchy particles with tetrahedral symmetry. *J. Chem. Phys.* **132**, 234511 (2010).

[40] Wilber, A. W., Doye, J. P. K., Louis, A. A. & Lewis, A. C. F. Monodisperse self-assembly in a model with protein-like interactions. *J. Chem. Phys.* **131**, 175102 (2009).

[41] Wilber, A. W., Doye, J. P. K., Louis, A. A., Noya, E. G., Miller, M. A. & Wong, P. Reversible self-assembly of patchy particles into monodisperse icosahedral clusters. *J. Chem. Phys.* **127**, 085106 (2007).

[42] Williamson, A. J., Wilber, A. W., Doye, J. P. K. & Louis, A. A. Templated self-assembly of patchy particles. *Soft Matter* **7**, 3423 (2011).

[43] Doppelbauer, G., Bianchi, E. & Kahl, G. Self-assembly scenarios of patchy particles in two dimensions. *J. Phys.: Condens. Matter* **22**, 104105 (2010).

[44] van der Linden, M., Doye, J. P. K. & Louis, A. A. Formation of dodecagonal quasicrystals in two-dimensional systems of patchy particles. *J. Chem. Phys.* **136**, 054904 (2012).

[45] Antlanger, M., Doppelbauer, G. & Kahl, G. On the stability of archimedean tilings formed by patchy particles. *J. Phys.: Condens. Matter* **23**, 404206 (2011).

[46] Sciortino, F., Bianchi, E., Douglas, J. F. & Tartaglia, P. Self-assembly of patchy particles into polymer chains: A parameter-free comparison between Wertheim theory and Monte Carlo simulation. *J. Chem. Phys.* **126**, 194903 (2007).

[47] Bianchi, E., Kahl, G. & Likos, C. N. Inverse patchy colloids: from microscopic description to mesoscopic coarse-graining. *Soft Matter* **7**, 8313 (2011).

[48] Debye, P. & Hückel, E. The theory of electrolytes. i. Lowering of freezing point and related phenomena. *Physikalische Zeitschrift* **24**, 185 (1923).

[49] Wales, D. J. *Energy Landscapes* (Cambridge University Press, Cambridge, 2003).

[50] Byrd, R. H., Lu, P. & Nocedal, J. A limited memory algorithm for bound constrained optimization. *SIAM J. Sci. Stat. Comp.* **16**, 1190 (1995).

[51] Zhu, C., Byrd, R. H. & Nocedal, J. Algorithm 778: L-BFGS-B: FORTRAN routines for large scale bound constrained optimization. *ACM Trans. Math. Software* **23**, 550 (1997).

[52] Morales, J. L. & Nocedal, J. Remark on Algorithm 778: L-BFGS-B: FORTRAN routines for large scale bound constrained optimization. *ACM Trans. Math. Software* **38**, 7 (2011).

[53] Becker, O. M. & Karplus, M. The topology of multidimensional potential energy surfaces: Theory and application to peptide structure and kinetics. *J. Chem. Phys.* **106**, 1495 (1997).

[54] Wales, D. J., Miller, M. A. & Walsh, T. R. Archetypal energy landscapes. *Nature* **394**, 758 (1998).

[55] Kohn, W. & Sham, L. J. Self-consistent equations including exchange and correlation effects. *Phys. Rev.* **140**, A1133 (1965).

[56] Creighton, T. E. *Protein Folding* (W. H. Freeman, San Francisco, 1992).

[57] Fersht, A. *Structure and Mechanism in Protein Science: A Guide to Enzyme Catalysis and Protein Folding* (Freeman, New York, 1999).

[58] Alberts, B., Johnson, A., Lewis, J., Raff, M., Roberts, K. & Walters, P. *The Shape and Structure of Proteins* (Garland Science, New York, 2007).

[59] Applegate, D. L., Bixby, R. E., Chvátal, V. & Cook, W. J. *The Traveling Salesman Problem: A Computational Study* (Princeton University Press, Princeton, 2007).

[60] Gross, J. L. & Yellen, J. *Graph Theory and Its Applications, Second Edition* (Chapman and Hall/CRC, Boca Raton, Florida, 2005).

[61] Neumaier, A. *Complete Search in Continuous Global Optimization and Constraint Satisfaction* (Cambridge University Press, Cambridge, 2004).

[62] Stillinger, F. H. & Weber, T. A. Nonlinear optimization simplified by hypersurface deformation. *J. Stat. Phys.* **52**, 1429 (1988).

[63] Pillardy, J. & Piela, L. Molecular dynamics on deformed potential energy hypersurfaces. *J. Phys. Chem.* **99**, 11805 (1995).

[64] Pillardy, J., Olszewski, K. A. & Piela, L. Performance of the shift method of global minimization in searches for optimum structures of clusters of Lennard-Jones atoms. *J. Phys. Chem.* **96**, 4337 (1992).

[65] Piela, L., Kostrowicki, J. & Scheraga, H. A. On the multiple-minima problem in the conformational analysis of molecules: deformation of the potential energy hypersurface by the diffusion equation method. *J. Phys. Chem.* **93**, 3339 (1989).

[66] Pappu, R. V., Hart, R. K. & Ponder, J. W. Analysis and application of potential energy smoothing and search methods for global optimization. *J. Phys. Chem. B* **102**, 9725 (1998).

[67] Wales, D. J. & Doye, J. P. K. Global optimization by basin-hopping and the lowest energy structures of Lennard-Jones clusters containing up to 110 atoms. *J. Phys. Chem. A* **101**, 5111 (1997).

[68] Moscato, P. On evolution, search, optimization algorithms and martial arts: Towards memetic algorithms. Tech. Rep., Caltech Concurrent Computation Program Report 826, California Institute of Technology, Pasadena (1989).

[69] Frenkel, D. & Smit, B. *Understanding Molecular Simulation, Second Edition* (Academic Press, San Diego, CA, 2002).

[70] Miller, M. A., Doye, J. P. K. & Wales, D. J. Structural relaxation in atomic clusters: Master equation dynamics. *Phys. Rev. E* **60**, 3701 (1999).

[71] Wales, D. J. & Bogdan, T. V. GMIN: a program for finding global minima and calculating thermodynamic properties from basinsampling. http://www-wales.ch.cam.ac.uk/GMIN/.

[72] Doppelbauer, G. *Development of a phenotype algorithm for particle geometry optimization.* Master's thesis, Vienna University of Technology (2009).

[73] Gibson, K. D. & Scheraga, H. A. Crystal packing without symmetry constraints. 1. Tests of a new algorithm for determining crystal structures by energy minimization. *J. Phys. Chem.* **99**, 3752 (1995).

[74] Goldberg, D. E. *Genetic Algorithms in Search, Optimization and Machine Learning* (Addison-Wesley, Boston, MA, 1989).

[75] Gottwald, D., Kahl, G. & Likos, C. N. Predicting equilibrium structures in freezing processes. *J. Chem. Phys.* **122**, 204503 (2005).

[76] Fornleitner, J. *Ordered equilibrium structures of two-dimensional soft matter systems.* Ph.D. thesis, Vienna University of Technology (2008).

[77] Fornleitner, J. & Kahl, G. Lane formation vs. cluster formation in two-dimensional square-shoulder systems A genetic algorithm approach. *Europhys. Lett.* **82**, 18001 (2008).

[78] Deaven, D. M. & Ho, K. M. Molecular geometry optimization with a genetic algorithm. *Phys. Rev. Lett.* **75**, 288 (1995).

[79] Glass, C. W., Oganov, A. R. & Hansen, N. USPEX - Evolutionary crystal structure prediction. *Comput. Phys. Commun.* **175**, 713 (2006).

[80] Abraham, N. L. & Probert, M. I. J. A periodic genetic algorithm with real-space representation for crystal structure and polymorph prediction. *Phys. Rev. B* **73**, 224104 (2006).

[81] Lonie, D. C. & Zurek, E. XtalOpt: An open-source evolutionary algorithm for crystal structure prediction. *Comput. Phys. Commun.* **182**, 372 (2011).

[82] Abraham, N. L. *A Genetic Algorithm for Crystal Structure Prediction.* Ph.D. thesis, University of York (2007).

[83] Oganov, A. R. & Glass, C. W. Crystal structure prediction using *ab initio* evolutionary techniques: Principles and applications. *J. Chem. Phys.* **124**, 244704 (2006).

[84] Bird, A. Perceptions of epigenetics. *Nature* **447**, 396 (2007).

[85] Dawkins, R. *The Selfish Gene* (Oxford University Press, Oxford, 1976).

[86] Goldstein, H., Poole, C. P. & Safko, J. L. *Classical Mechanics (3rd Edition* (Addison Wesley, New York, 2002).

[87] Chakrabarti, D. & Wales, D. J. Simulations of rigid bodies in an angle-axis framework. *Phys. Chem. Chem. Phys.* **11**, 1970 (2009).

[88] Belognie, S. Rodrigues' rotation formula. From MathWorld – A Wolfram Web Resource, created by Eric W. Weisstein.

[89] Hartke, B. Global cluster geometry optimization by a phenotype algorithm with Niches: Location of elusive minima, and low-order scaling with cluster size. *J. Comput. Chem.* **20**, 1752 (1999).

[90] Oganov, A. R. & Valle, M. How to quantify energy landscapes of solids. *J. Chem. Phys.* **130**, 104504 (2009).

[91] Abraham, N. L. & Probert, M. I. J. Improved real-space genetic algorithm for crystal structure and polymorph prediction. *Phys. Rev. B* **77**, 134117 (2008).

[92] Lonie, D. C. & Zurek, E. Identifying duplicate crystal structures: XtalComp, an open-source solution. *Comput. Phys. Commun.* **183**, 690 (2012).

[93] Steinhardt, P. J., Nelson, D. R. & Ronchetti, M. Bond-orientational order in liquids and glasses. *Phys. Rev. B* **28**, 784 (1983).

[94] The GNU Fortran Compiler, Version 4.7.0, Online Manual. http://gcc.gnu.org/onlinedocs/gcc-4.7.0/gfortran/.

[95] Messiah, A. *Quantum Mechanics, Volume II* (North-Holland, Amsterdam, 1962).

[96] Gropp, W., Lusk, E. & Skjellum, A. *Using MPI: Portable Parallel Programming with the Message Passing Interface* (MIT Press, Cambridge, MA, 1994).

[97] Fadda, A. & Fadda, G. An evolutionary algorithm for the prediction of crystal structures. *Phys. Rev. B* **82**, 104105 (2010).

[98] Bianchi, E. *Equilibrium Behavior of Patchy Particles: Thermo-reversible Gelation, Phase Separation and Self-Assembly.* Ph.D. thesis, Sapienza - Università di Roma (2008).

[99] Maradudin, A. A., Montroll, E. W., Weiss, G. H. & Ipatova, I. P. *Theory of Lattice Dynamics in the Harmonic Approximation* (Academic, New York, 1971).

[100] Evans, R. *Fundamentals of Inhomogeneous Fluids*, 85 (Dekker, New York, 1970).

[101] Kofke, D. A. & Cummings, P. T. Quantitative comparison and optimization of methods for evaluating the chemical potential by molecular simulation. *Mol. Phys.* **92**, 973 (1997).

[102] Born, M. & Huang, K. *Dynamical Theory of Crystal Lattices* (Oxford University Press, Oxford, 1954).

[103] Dove, M. T. *Introduction to Lattice Dynamics* (Cambridge University Press, Cambridge, 1993).

[104] Taylor, M. B., Barrera, G. D., Allan, N. L. & Barron, T. H. K. Free-energy derivatives and structure optimization within quasiharmonic lattice dynamics. *Phys. Rev. B* **56**, 14380 (1997).

[105] Venkataraman, G. & Sahni, V. C. External vibrations in complex crystals. *Rev. Mod. Phys.* **42**, 409 (1970).

[106] Kahl, G. & Löwen, H. Classical density functional theory: an ideal tool to study heterogeneous crystal nucleation. *J. Phys.: Condens. Matter* **21**, 464101 (2009).

[107] Frenkel, D. & Ladd, A. J. C. New Monte-Carlo method to compute the free energy of arbitrary solids. Application to the fcc and hcp phases of hard spheres. *J. Chem. Phys.* **81**, 3188 (1984).

[108] Vega, C., Sanz, E., Abascal, J. L. F. & Noya, E. G. Determination of phase diagrams via computer simulation: methodology and applications to water, electrolytes and proteins. *J. Phys.: Condens. Matter* **20**, 153101 (2008).

[109] Uche, O. U., Stillinger, F. H. & Torquato, S. Concerning maximal packing arrangements of binary disk mixtures. *Physica A* **342**, 428 (2004).

[110] Frank, F. C. & Kasper, J. S. Complex alloy structures regarded as sphere packings. II. Analysis and classification of representative structures. *Acta Cryst.* **12**, 483 (1959).

[111] Gruenbaum, B. & Shephard, G. C. *Tilings and Patterns* (W. H. Freeman, New York, NY, 1987).

[112] Kroto, H. W., Heath, J. R., O'Brien, S. C., Curl, R. F. & Smalley, R. E. C_{60}: Buckminsterfullerene. *Nature* **318**, 162 (1985).

[113] Taylor, P. R., Bylaska, E., Weare, J. H., Curl, R. F. & Kawai, R. C_{20}: fullerene, bowl or ring? New results from coupled-cluster calculations. *Chem. Phys. Lett.* **235**, 558 (1995).

[114] Vega, C. & Noya, E. G. Revisiting the Frenkel-Ladd method to compute the free energy of solids: The Einstein molecule approach. *J. Chem. Phys.* **127**, 154113 (2007).

[115] Bianchi, E., Doppelbauer, G., Filion, L., Dijkstra, M. & Kahl, G. Predicting patchy particle crystals: variable box shape simulations and evolutionary algorithms. *J. Chem. Phys.* **136**, 214102 (2012).

[116] Gasser, U. Crystallization in three- and two-dimensional colloidal suspensions. *J. Phys.: Condens. Matter* **21**, 203101 (2009).

[117] Monkhorst, H. J. & Pack, J. D. Special points for brillouin-zone integrations. *Phys. Rev. B* **13**, 5188 (1976).

[118] Anderson, E., Bai, Z., Bischof, C., Blackford, S., Demmel, J., Dongarra, J., Du Croz, J., Greenbaum, A., Hammarling, S., McKenney, A. & Sorensen, D. *LAPACK Users' Guide* (Society for Industrial and Applied Mathematics, Philadelphia, PA, 1999), third edn.

[119] Hartke, B. Global geometry optimization of clusters using genetic algorithms. *J. Phys. Chem.* **97**, 9973 (1993).

Acknowledgements

I would like to thank many people who have accompanied and aided me in the past years. These people include

Gerhard Kahl for his continuous support and guidance as a great supervisor and for making it such a pleasurable experience to work with him.

My colleagues in the soft matter theory group at the TU Wien for fruitful collaboration, help when it was needed and great company (in order of appearance): **Julia Fornleitner**, **Gernot J. Pauschenwein**, **Dieter F. Schwanzer**, **Daniele Coslovich**, **Jan Kurzidim**, **Emanuela Bianchi**, **Lukas Strauss**, **Camille Jouvie**, **Arash Nikoubashman**, **Moritz Antlanger**, **Giannis Georgiou**, **Martina Lechner**, **Ulf Rørbæk Pedersen**, **Andreas Tröster** and **Ismene Kolovos**.

David Wales, **Dwaipayan Chakrabarti**, **Bianca Mladek**, and **Mark Miller** for their hospitality during my visit to Cambridge.

Primož Ziherl for multiple suggestions concerning this thesis.

Johannes Strobl, **Georg Wachter**, **Daniela Klotz** and **Hanna & Yaniv Levy** for being very close friends during all the years of our studies.

My parents Maria and **Franz**, **my grandparents** and **my sister Eva-Maria** for support in many different ways.

Marta Montes Saralegui.

Curriculum Vitae

Personal Data

Name:	Günther Doppelbauer
Birth Date:	January 25th, 1984
Birth Place:	Grieskirchen, Austria
Citizenship:	Austria

Education

1990 - 1994	Volksschule I Grieskirchen
1994 - 1998	Hauptschule I Grieskirchen
1998 - 2002	Bundesoberstufenrealgynasium Grieskirchen
June 2002	Matura passed with distinction
2002 - 2009	Studies of Technical Physics at Vienna University of Technology
April 2009	all Diploma examinations passed with distinction
2009 - 2012	PhD studies in Technical Sciences at Vienna University of Technology, with a two month stay at the University of Cambridge